INAUGURAL - DISSERTATION

zur

Erlangung der Doktorwürde

der

Naturwissenschaftlich-Mathematischen

Gesamtfakultät

der

Ruprecht-Karls-Universität Heidelberg

Vorgelegt von
M.Sc. Alexandra Serena Burk
geboren in Bietigheim-Bissingen, Deutschland

Tag der mündlichen Prüfung: 30.10.2015

Dissertation

submitted to the

Combined Faculty of Natural Sciences and Mathematics

Heidelberg University, Germany

for the degree of

Doctor of Natural Sciences (Dr. rer. nat.)

Presented by
M.Sc. Alexandra Serena Burk
Born in Bietigheim-Bissingen, Deutschland

Date of oral examination: October 30, 2015

Quantifying Adhesion and Morphological Dynamics of Human Hematopoietic Stem and Progenitor Cells on Novel *In Vitro* Models of Bone Marrow Niche

1st Referee: Prof. Dr. Motomu Tanaka
2nd Referee: Prof. Dr. Anthony D. Ho

„Man braucht im Leben nichts zu fürchten,
man muss nur alles verstehen.“

Marie Skłodowska Curie (1867 – 1934)
Nobel Prize Winner in Chemistry and Physics

Zusammenfassung

Humane hämatopoietische Stamm- und Vorläuferzellen (HSPC) sowie Leukämie-auslösende Zellen (LIC) werden in der Stammzellnische vor zytotoxischen Effekten der Chemotherapie geschützt, da die Nische diese Zellen in der Ruhephase des Zellzyklus hält. Für die Entwicklung einer effektiven klinischen Therapie von Leukämie ist die quantitative Identifizierung des unterschiedlichen Adhäsionsverhaltens von HSPC im Kontrast zu LIC in der Knochenmarknische von großer Bedeutung. Das Hauptziel der vorliegenden Dissertation ist die Herstellung und Anwendung von festkörpergestützten Phospholipidmembranen als *in vitro* Modell der Knochenmarknische. Ein besonderes Augenmerk liegt auf der Untersuchung der Einflüsse von relevanten Ligand-Rezeptor-Paaren sowie der akuten myeloischen Leukämie (AML). Als Modellsystem der Stammzellnische wurden N-cadherin- und SDF1α-funktionalisierte, festkörpergestützte Phospholipidmembranen verwendet, um die unterschiedliche Bedeutung der beiden Liganden zu bestimmen.

In Kapitel 2 wurde unter Verwendung von hoch-energetischer, spekularer Röntgenreflektometrie (XRR) und Schwingquarzwaage mit Dissipationsaufzeichnung (QCM-D) die erfolgreiche Präparation der festkörpergestützten Phospholipidmembranen und derer quantitativen Funktionalisierung mit N-cadherin und SDF1α charakterisiert. Die Feinstrukturen sowie die Oberflächtendichte von membrangebundenden Proteinen wurden mittels XRR mit einer Auflösung im Ångström Bereich bestimmt. In-situ-Monitoring der Membranpräparation und deren Funktionalisierung bestätigte die Variierbarkeit des intermolekularen Abstandes $<d>$ der Proteine auf der Membran und charakterisierte ihre viskoelastischen Eigenschaften. Dazu gehörten das Viskoelastizitätsmodul und die Viskosität der Proteinschicht.

In Kapitel 3 wurde die Adhäsionsstärke mittels der Charakterisierung (a) des prozentualen Anteils an adhärenten Zellen, (b) der Adhäsionsfläche und (c) der kritischen Kraft zur Zellablösung als Funktion des intermolekularen Abstandes $<d>$ von N-cadherin und SDF1α von HSPC quantitativ bestimmt. Die Ergebnisse verdeutlichten, dass die Adhäsion von HSPC an die Modellnische ein positiv kooperativ-bindender Prozess ist. Außerdem konnte gezeigt werden, dass die SDF1α/CXCR4 vermittelte Adhäsion im Vergleich zur Adhäsion von HSPC an N-cadherin modifizierten Membranen stärker war. Die statistische Bildanalyse von stochastischen, morphologischen Zelldeformationen ergab, dass die Zellmotilität von HSPC auf SDF1α-funktionalisierten Modellnischen oszillierende Zellverformungen aufwies. Im Gegensatz dazu zeigten HSPC auf N-cadherin modifizierten Modellnischen nur geringe Zelldeformationen. Im Hinblick auf die klinische Relevanz wurde die Adhäsion von leukämischen Blasten (LB) eines AML Patienten untersucht. LB zeigten eine deutlich höhere Affinität an die Modellnische im Vergleich zu HSPC. Diese Ergebnisse sind ein Anzeichen für deren Resistenz gegen die Chemotherapie und die Schwierigkeit alle LIC durch gesunde allogen transplantierte HSPC zu ersetzen.

Die erzielten Ergebnisse zeigten, dass sich die Kombination von exakt definierten Modellsystemen der Stammzellnische mit neuartigen, nicht-invasiven Methoden zur Bestimmung der Zelladhäsionsstärke und statistischer Bildanalyse von HSPC im Fourier Raum hervorragend eignet, um verschiedene Funktionen von Zelladhäsionsmolekülen in der Stammzellnische quantitativ zu analysieren, welche durch phänomenologische Beobachtung nicht bestimmt werden können.

Summary

Since both healthy human hematopoietic stem and progenitor cells (HSPC) and leukemia initiating cells (LIC) are sustained in a dormant state in bone marrow niche, they are protected against cytotoxic effects of chemotherapy. Thus, quantitative identification of differential adhesion of HSPC vs. LIC to bone marrow niche would help for the development of an effective clinical therapy of leukemia. The main aim of the present thesis was the fabrication and application of self-assembled, planar phospholipid membranes on solid support as *in vitro* model of bone marrow niche. A special focus was put on the influences of relevant ligand-receptor pairs and acute myeloid leukemia (AML) on the adhesion and morphological dynamics of HSPC. As the model of bone marrow niche, supported lipid membranes functionalized with N-cadherin and SDF1α were utilized to study their relative significance.

In Chapter 2, the deposition of supported membranes and their quantitative functionalization with N-cadherin and SDF1α were confirmed by high energy specular X-ray reflectivity (XRR) and quartz crystal microbalance with dissipation monitoring (QCM-D). The fine structures perpendicular to the membrane surface and the lateral density of membrane-anchored proteins were determined by XRR with sub-Ångström resolution. Real-time monitoring by QCM-D of membrane deposition and functionalization demonstrated the quantitative variability of the average intermolecular distance $\langle d \rangle$ of proteins and elucidated their viscoelastic properties such as the shear elastic modulus and shear viscosity.

In Chapter 3, the strength of HSPC adhesion was quantitatively evaluated by the determination of (a) the fraction of adherent cells, (b) the area of tight adhesion and (c) the critical force of cell detachment as a function of the average intermolecular distance $\langle d \rangle$ of N-cadherin and SDF1α. The results clearly demonstrated that the binding of HSPC to the *in vitro* niche model was a positively cooperative process, and the adhesion mediated by the SDF1α/CXCR4 axis was stronger compared to adhesion mediated by the homophilic N-cadherin axis. The statistical image analysis of stochastic morphological dynamics unraveled that HSPC on *in vitro* niche models displaying SDF1α dissipated energy by undergoing oscillatory deformation, whereas cell locomotion mediated by the homophilic binding of N-cadherin was hardly impaired with morphological deformations. In order to verify the clinical relevance, the adhesion of leukemic blasts (LB) from AML patients was investigated in a systematic manner. In comparison to HSPC, LB exhibited a significantly higher affinity to the *in vitro* niche model reflecting the partial ineffectiveness of chemotherapy and the difficulties of replacing them by allogenic transplanted HSPC.

The obtained results demonstrated that the combination of precisely defined cell surface models, a novel non-invasive assay for evaluating the cell adhesion strength, and statistical analysis of live cell images in Fourier space is a powerful tool to quantitatively analyze different functions of ligand-receptor pairs in bone marrow niche, which cannot be assessed by phenomenological observation.

Acknowledgements

I would like to thank…

…**Prof. Dr. Motomu Tanaka** for giving me the possibility to work in his group, his generous support, his scientific guidance throughout my thesis and fruitful discussions. Furthermore, I would like to thank him for giving me the possibility to spend several months at the Institute of Integrated Cell Material Sciences in Kyoto, Japan to broaden my personal and scientific horizon.

…**Prof. Dr. Anthony D. Ho** who gave me the opportunity to join the interdisplinary project related to hematopoietic stem cells. His generous support and guidance was of particular importance for the success of my doctoral thesis.

…**Prof. Dr. Eiichi Nakamura** and **Assoc. Prof. Dr. Koji Harano** who kindly provided me with Rf8K vesicles.

…**BioInterfaces International Graduate School** at the Karlsruhe Institute of Technology, **Baden-Württemberg Scholarship Plus** and the **Heidelberg University** for their financial support.

…**Dr. Patrick Wuchter** and **Dr. Rainer Saffrich** for the introduction into the field of hematopoietic stem cells, fruitful discussions and experimental support.

…**Dr. Wasim Abuillan** and **Dr. Alexander Koerner** for the introduction into the field of biophysics, the great mentoring in all kind of questions and problems related to my doctoral thesis, proof-reading, fruitful experiments in Grenoble and humorous times in the lab.

…**Dr. Cornelia Monzel, Asst. Prof. Dr. Hiroshi Yoshikawa** and **Assoc. Prof. Ali Makky** for the great help in experiments, data evaluation and the continuous scientific exchange.

…**Dr. Akihisa Yamamoto, Dr. Stefan Kaufmann, Agatha Korytowski** and **Viktoria Frank** for proof-reading of the thesis and support in the lab.

…**Angela Lenze** for her excellent technical assistance during the isolation and preparation of HSPC samples.

…**Klaus Schmitt and his team** from the fine mechanical workshop for their excellent technical assistance.

…**Gabriele Fabry** and **Mieko Yoshida** for the assistance in all organizational issues in Heidelberg and Japan.

…**Saskia Krieg** for her supportive and reliable work in the lab.

…all other colleagues of the **Tanaka group** for the great time in the past years.

Special thanks go to my **family**, **Marcel Becker** and **my friends** for their great support, valuable advice and necessary distraction especially during the last months.

Table of Contents

1. Introduction

Hematopoietic stem and progenitor cells (HSPC) comprise a heterogeneous pool of progenitors of all blood lineages exhibiting a unique combination of self-renewal and multilineage potential[1-4]. A number of studies have identified the stem cell niche as main regulatory system which supports HSPC maintenance and hematopoiesis by sustaining the balance between their self-renewal and lineage commitment[5-9].

This specialized microenvironment is located in the bone marrow cavity consisting of several cellular and molecular determinants (Fig. 1.1)[10]. Early studies were performed in the murine system. For example, Calvi *et al.*[11] and Zhang *et al.*[12] suggested that spindle-shaped osteoblasts, which line along the endosteal surface of the bone, form the endosteal niche. Kiel *et al.* postulated the perivascular niche, in addition to the endosteum, which consists mainly of bone marrow endothelial cells (BMEC)[13]. Furthermore, Méndez-Ferrer *et al.*[14] and Katayama *et al.*[15] have demonstrated the importance of mesenchymal stem cells (MSC) which are stimulated by the sympathetic nervous system. Investigations of the human hematopoietic stem cell system are based on *in vitro* models such as feeder cell layers consisting of adherent cells which support long-term culture of HSPC or knockout and transgenic mouse models. Initial *in vitro* systems relied on a long-term culture system which consists of adherent bone marrow stromal cells, as described by Dexter *et al.*[16]. Due to the difficulties to dissect contributions of individual cell types, *in vitro* systems based on feeder layers which consisted of only one cell type were developed. For example, human osteoblasts promoted the *in vitro* expansion of human HSPC as reported by Taichman *et al.*[17]. Wagner *et al.* demonstrated the importance of direct cell contacts between human HSPC and a feeder layer consisting of human MSC for the long-term maintenance of HSPC by supporting asymmetric cell divisions[18, 19].

On molecular level, the niche regulates HSPC progression by several intrinsic and extrinsic factors. Cell extrinsic factors include cytokines, growth factors, chemokines, cell adhesion molecules (CAM), and oxygen tension. They merge into an interplay of intrinsic regulators such as signaling transduction pathways. For example, the cell adhesion molecule N-cadherin belongs to the family of classical type-1 cadherins and is expressed by HSPC[20], osteoblasts[11] and MSC[20]. Several studies suggested that the adhesion mediated by the homophilic N-cadherin axis supports the maintenance of the stem cell pool. Puch *et al.* suggested that N-cadherin is involved in the development and retention of HSPC in the bone marrow niche[21]. Zhang *et al.* reported that the number of HSPC in bone marrow niche is impaired with the number of N-cadherin expressing spindle-shaped osteoblasts[12].

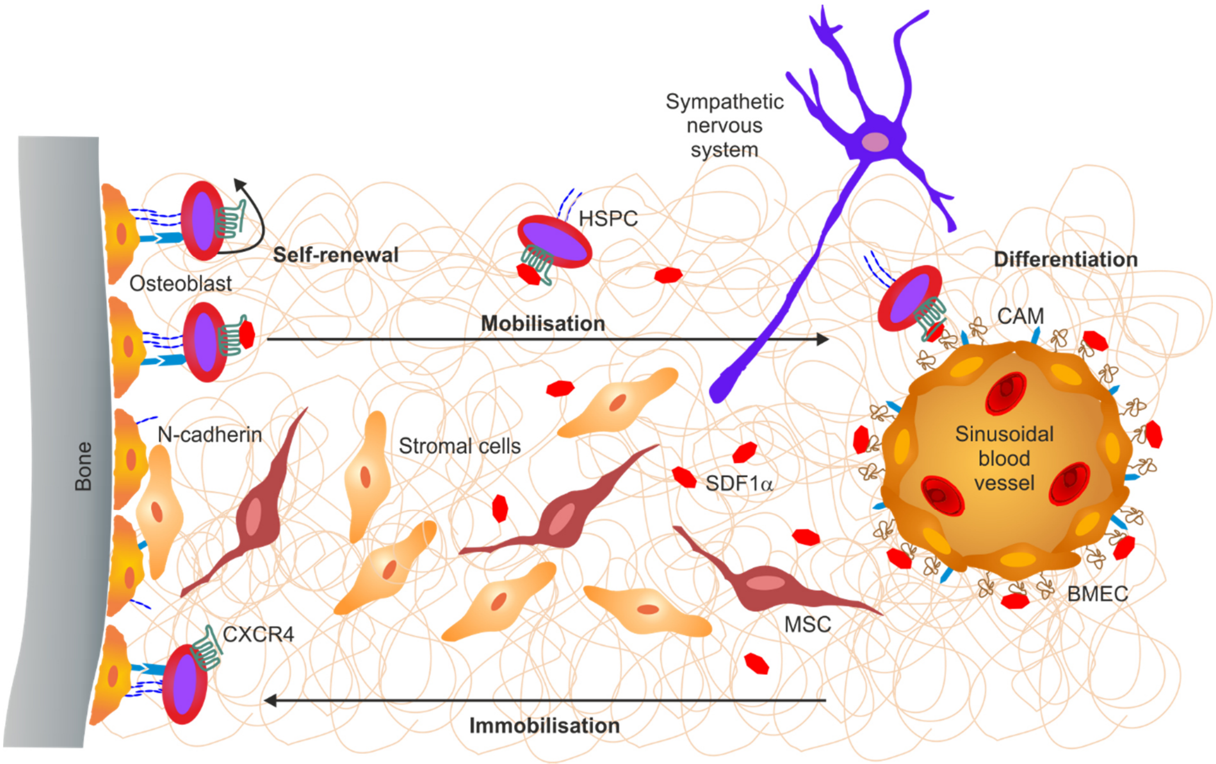

Figure 1.1 | The hematopoietic stem cell niche in bone marrow. Schematic illustration of the bone marrow niche including important cellular and molecular constituents. The interplay of different cell types, adhesion molecules and extracellular matrix components is supposed to regulate the immobilization and mobilization of HSPC in order to control their cell numbers and differentiation.

The knockdown of N-cadherin accelerates cell division *in vitro* and suppresses the homing of HSPC to the endosteal surface as demonstrated by Hosokawa *et al.*[22]. These findings are controversially discussed since other studies did not detect any significant role of N-cadherin[23-26]. Another important regulatory mechanism is the trafficking of HSPC from their niche across the bone marrow endothelium to the peripheral blood (PB) and *vice versa* which coincides with homing, differentiation and proliferation. The mobilization and immobilization of HSPC is regulated by circadian stimulation through the sympathetic nervous system which causes the secretion of the stromal cell-derived factor 1-alpha (SDF1α)[15, 27]. SDF1α is expressed by MSC[14, 28], BMEC[29] and reticular cells[30] and displayed as a dynamic gradient of both, soluble and immobilized molecule, in bone marrow niche. Lataillade *et al.* demonstrated that SDF1α affects HSPC proliferation[31]. Furthermore, the SDF1α/CXCR4 axis is supposed to be involved in the regulation of HSPC homing as reported by Hattori *et al.*[32]. Aiuti *et al.*[33] and Faber *et al.*[34] provided clear evidence for the directed locomotion of human HSPC towards a SDF1α gradient. However, the precise mechanisms of these interactions, especially in the human system, have remained mostly undefined due to the lack of relevant *in vitro* niche models whose composition is precisely defined

and fully controllable. Deeper understanding is of significant importance especially for the treatment of hematological disorders.
In acute myeloid leukemia (AML), HSPC have lost the ability to differentiate into cells of the myeloid lineage leading to the accumulation of undifferentiated leukemic blasts (LB)[35, 36]. Several studies implied that LB are derived from leukemia initiating cells (LIC) which are co-localized in the same microenvironment and exhibiting limitless self-renewing capacity[37, 38]. They are sustained in a dormant state due to adhesion to the bone marrow niche, and thus are resistant to chemotherapy which is the main reason for remission[39]. For example, Ishikawa *et al.* suggested that adhesion of dormant LIC to the endosteal niche prevents apoptosis induced by chemotherapy[39]. Although HSPC and LIC both reside in the same microenvironment, it is hypothesized that there are significant differences in their bidirectional interactions with the bone marrow niche[40]. For example, LIC are supposed to strengthen their interactions with the bone marrow niche by the upregulation of key ligands. Matsunaga *et al.* demonstrated that increasing expression levels of very late antigen-4 (VLA-4) are impaired with LIC drug resistance[41]. Furthermore, Rombouts *et al.* found that AML patients with a high CXCR4 expression level have a significantly reduced survival and a higher probability of AML relapse[42]. To improve the clinical therapy of AML patients, quantitative understanding of the differential adhesion of HSPC vs. LIC to the stem cell niche is very important. First, the selective mobilization of LIC to peripheral blood increases the cytotoxic effect of chemotherapy. Second, the optimization of allogeneic transplantation enhances HSPC engraftment. However, the definition of LIC is not precisely defined due to their heterogeneous phenotypes. Therefore, the CD34$^+$ subset is most suitable[43-45].

The primary aim of this thesis was the quantification of HSPC adhesion and morphological dynamics in order to understand the fundamental mechanisms underlying the immobilization and mobilization of HSPC as model for stem cell homing and trafficking in bone marrow niche. A special focus was laid on the development of a novel *in vitro* model of bone marrow niche based on self-assembled phospholipid membranes on solid support in order to study homophilic interactions of N-cadherin and heterophilic interactions between SDF1α and its receptor CXCR4. Furthermore, possible differences between the stem cell niche under healthy and malignant conditions were investigated.

Supported phospholipid membranes functionalized with N-cadherin and SDF1α were used as *in vitro* niche model (Fig. 1.2A-C). They consist of a phospholipid bilayer including different molar fractions of head group modified lipids which allow for the coupling of ligands (e.g. proteins) under non-denaturing conditions and in a defined orientation[46, 47]. Main advantages are their quasi two-dimensional structure, the possibility of tuning the average intermolecular distance <*d*> of neighboring ligands with nm-accuracy and the lateral mobility of lipids similar to those in biological membranes[48].

In Chapter 2, quantitative fabrication and functionalization of supported membranes with either N-cadherin or SDF1α were confirmed by a combination of the surface sensitive techniques high-energy specular X-ray reflectivity (XRR) and quartz crystal microbalance with dissipation monitoring (QCM-D). In Chapter 3, the adhesion and morphological dynamics of hematopoietic stem and progenitor cells (HSPC; $CD34^+$ cells) were characterized by the quantification of the fraction of adherent cells and the area of tight adhesion by reflection interference contrast microscopy (RICM). The mechanical strength of cell adhesion on *the in vitro* niche model was quantified by the pressure wave assay. This novel technique utilizes intense pressure waves in a non-invasive manner induced by ultrafast laser pulses (Fig. 1.2D)[49]. The stochastic morphological dynamics in the presence and absence of soluble SDF1α were assessed by power spectral analysis in order to determine the predominant mode of cell deformation and the corresponding total power as a measure of the energy dissipated through cell deformation. Furthermore, the differences in molecular mechanism leading to the adhesion and maintenance of LIC to the bone marrow niche were studied by the use of LB from an AML patient.

Details of the results are presented in the following chapters.

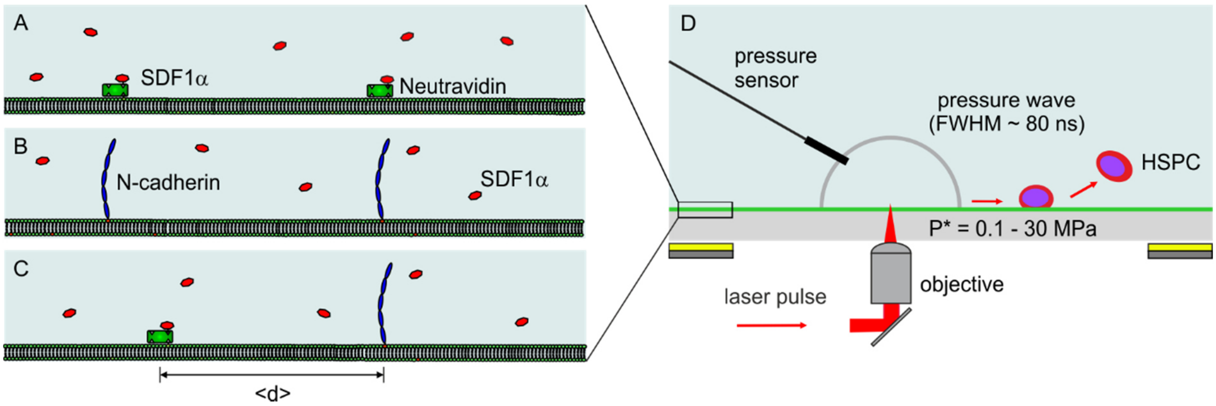

Figure 1.2 | The combination of *in vitro* models of bone marrow niche with novel experimental techniques and methods in statistical physics allowed for the quantification of the relative significance of HSPC-niche interactions. Supported membranes functionalized with either (A) SDF1α, (B) N-cadherin or (C) both ligands with precisely defined average intermolecular distances <*d*> were utilized as *in vitro* niche models. (D) Schematic illustration of the pressure wave assay. A novel technique which allowed for the quantification of the mechanical strength of cell adhesion.

2. Structural Characterization of the *In Vitro* Niche Model

The fabrication and application of the *in vitro* model of bone marrow niche could not have been feasible without the quantitative characterization of its structural parameters. The following chapter focuses on the determination of structural parameters of the *in vitro* model of bone marrow niche by two complementary surface-sensitive techniques. First, high-energy specular X-ray reflectivity (XRR) enabled the determination of the fine structures. By the use of supported membranes displaying either N-cadherin or SDF1α at a small average intermolecular distance $<d>$ = 4 nm, the thickness, roughness and scattering length density (SLD) profile along the surface normal of each layer with different electron density were obtained with sub-Å resolution. Second, the *in-situ* formation of the lipid bilayer and its functionalization with ligands were recorded by quartz-crystal microbalance with dissipation monitoring (QCM-D) which allowed for the determination of their electromechanical properties. In addition, the variability of the average intermolecular ligand distances was investigated by applying this technique to supported membranes functionalized with ligand molecules at different surface densities.

2.1 X-ray reflectivity study

2.1.1 Theoretical background

Since the discovery of electromagnetic radiation in the wavelength region of Ångström (10^{-10} m) by Röntgen in 1895[50], X-rays have become established as an important probe of the structure of matter. The total reflection of X-rays from stratified, solid substrates with smooth surfaces was first reported by Compton in 1923[51]. This finding marked the birth of the surface-sensitive technique XRR, which measures the reflected intensity R of a monochromatic X-ray beam as a function of the angle of incidence α_i. XRR is the method of choice for the determination of layer thickness, roughness and its electron density profile along the surface normal of thin single or multilayer systems [6, 52]. The high surface sensitivity arises from the fact that the index of refraction n of materials in the wavelength region of X-rays is smaller than unity which results in total external reflection at sufficiently small angles of incidence followed by a steep decay of the reflected intensity at higher angles. The dependency of the penetration depth according to the incident angle of X-rays enables the investigation of biological thin films with a thickness in the range of a few Ångströms up to several nanometers such as polymer films[53], Langmuir layers[54-56] and supported membranes[57]. In detail, the complex refractive index *n* of matter in the X-ray region is given by

$$n = 1 - \delta + i\beta \; . \tag{2.1.1}$$

The real part δ is associated with dispersion describing the strength of interaction between material and radiation. It is related to the electron density ρ_e, the classical electron radius r_e, and the wavelength λ as given by

$$\delta = \frac{\lambda^2}{2\pi} r_e \rho_e = \frac{\lambda^2}{2\pi} \mathrm{SLD} \; . \tag{2.1.2}$$

δ has typical values in the range of 10^{-5} - 10^{-6} and can be expressed in terms of SLD. The imaginary part β is more than ten times smaller and related to the attenuation coefficient $1/\mu$ of X-ray radiation in a material[6, 52]:

$$\beta = \frac{\mu\lambda}{4\pi}. \tag{2.1.3}$$

β is in the range of 10^{-8} for most biological matter. A refractive index *n* less than unity implies that below a material-dependent critical angle α_c the incident beam undergoes total external reflection. Snell's law describes the relationship between angle of incidence α_i and the angle of refraction α_r as given by

$$n_0 \cos \alpha_i = n \; \cos a_r \; , \tag{2.1.4}$$

where the critical angle α_c for total external reflection at a single vacuum/medium interface is defined as

$$\alpha_c \approx \sqrt{2\delta} \; . \tag{2.1.5}$$

For example, $\alpha_c = 0.22°$ for vacuum-silicon interface at 1.54 Å. Above the critical angle, reflection as well as refraction occurs leading to an exponential decrease of the reflected intensity *R.* In most cases, reflectivity profiles are given as a function of the wave vector transfer $q_z = \frac{4\pi}{\lambda} \sin \alpha$.

Fresnel Reflectivity

The basic description for reflection and transmission at interfaces is based on the Fresnel equations[58]. The incident X-ray beam is considered as plane wave polarized in the direction of the surface normal (s-polarization; denoted as *s*) (Fig. 2.1A)[59]. The electric field in a homogenous medium j for incident (i), reflected (r) and transmitted (tr) rays is given as

$$E_j = A_j e^{i(\omega t - k_j r)} \hat{e}_y \,, \qquad (2.1.6)$$

$$\text{with } k_o = |k_i| = |k_r| = 2\pi/\lambda = |k_{tr}|/n \,, \qquad (2.1.7)$$

and can be combined with the Maxwell equations for the description of the propagation equation of the electric field,

$$\Delta E + k_j^2 E = 0 \,, \qquad (2.1.8)$$

where k_j is the wave vector in medium j and $\hat{e}_y$ is a unity vector along the y-axis. Based on the assumptions that the tangential component of the electric field is continuous at the interface (z=0), the total field is the sum of the incident and reflected fields in air. Based on the assumption that the medium is sufficiently thick for the transmitted beam to be completely absorbed, the following equation becomes valid:

$$A_i e^{i(\omega t - k_0 i_1 x)} + A_r e^{i(\omega t - k_0 i_1 x)} = A_{tr} e^{i(\omega t - k_0 i_2 x)} \,. \qquad (2.1.9)$$

The angles i_1 and i_2 are defined as depicted in Figure 2.1A. Based on this mathematical statement, Snell's law is given by

$$\sin i_1 = n \, \sin i_2 \,, \qquad (2.1.10)$$

and results in

$$(A_i - A_r) \cos i_1 = n \, A_{tr} \cos i_2 \,. \qquad (2.1.11)$$

From the reflected, $r = A_r/A_i$, and the transmitted amplitude, $t = A_{tr}/A_i$, the following equations can be obtained,

$$1 + r = t, \qquad (2.1.12)$$

$$1 + r = nt \, \frac{\cos i_2}{\cos i_1}, \qquad (2.1.13)$$

which in summary leads to the reflected amplitude coefficient, as given by

$$r_{(s)} = \frac{\cos i_1 - n\cos i_2}{\cos i_1 + n\cos i_2} = \frac{\sin\alpha_i - n\sin\alpha_{tr}}{\sin\alpha_i + n\sin\alpha_{tr}}. \tag{2.1.14}$$

Note that in the geometry, as depicted in Figure 2.1A, *i* is the angle between the surface normal and the incident/reflected beam. Applying the Snell's' relationship, the coefficient of reflection is given by

$$r(\alpha_i) = \frac{\sin\alpha_i - \sqrt{n^2cos^2\alpha_i}}{\sin\alpha_i + \sqrt{n^2cos^2\alpha_i}} \tag{2.1.15}$$

In case of a small incident angle α_i in the absence of absorption, the Equation 2.1.15 can be written as

$$r(\alpha_i) = \frac{\alpha_i - \sqrt{\alpha_i^2 - \alpha_c^2}}{\alpha_i + \sqrt{\alpha_i^2 - \alpha_c^2}}. \tag{2.1.16}$$

The reflectivity corresponds to the square of the modulus of the reflection coefficient which is given by

$$R(\alpha_i) = rr^* = \left|\frac{\alpha_i - \sqrt{\alpha_i^2 - \alpha_c^2}}{\alpha_i + \sqrt{\alpha_i^2 - \alpha_c^2}}\right|^2. \tag{2.1.17}$$

Finally, the Fresnel reflectivity R_F is given by Equ. 2.1.18, taking into account the absorption of the X-ray beam by the material.

$$R_F = rr^* = \left|\frac{\alpha_i - \sqrt{\alpha_i^2 - \alpha_c^2 - 2i\beta}}{\alpha_i + \sqrt{\alpha_i^2 - \alpha_c^2 - 2i\beta}}\right|^2 = \left|\frac{q_z - \sqrt{q_z^2 - q_c^2 - \frac{32i\pi^2\beta}{\lambda^2}}}{q_z + \sqrt{q_z^2 - q_c^2 - \frac{32i\pi^2\beta}{\lambda^2}}}\right|^2 \tag{2.1.18}$$

The intensity profile according to the Fresnel reflectivity is depicted in Figure 2.1B and shows three distinct regions: The profile exhibits a plateau region at $0 < q_z < q_c$ due to total external reflection of the incident X-ray beam. At $q_z = q_c$, the reflectivity curve decays very rapidly as transmission occurs leading to an asymptotic dependence of R_F at $q_z > 3q_c$. In this last regime ($q_z > 3q_c$), the reflectivity R_F can be written as

$$R_F(q_z) = \frac{q_c^4}{16{q_z}^4}. \tag{2.1.19}$$

Based on Equations 2.1.12 and 2.1.18, the transmitted intensity is given as

$$T = tt^* = \left| \frac{2\alpha_i}{\alpha_i + \sqrt{\alpha_i^2 - \alpha_c^2 - 2i\beta}} \right|^2 = \left| \frac{2q_z}{q_z + \sqrt{q_z^2 - q_c^2 - \frac{32i\pi^2\beta}{\lambda^2}}} \right|^2 \tag{2.1.20}$$

The Fresnel coefficient for transmission *t* is given as

$$t_{j,j+1} = \frac{2k_{j,j}}{k_{j,j} + k_{j,j+1}}. \tag{2.1.21}$$

Specular reflections from layer structures

XRR is intensively used to investigate experimental systems consisting of either one or several layers with different electron densities where the mathematical description of the reflectivity profile is more complex and thus cannot be described by Equ. 2.1.18[6]. A simple approach is the kinematical theory which can be applied to systems consisting of an arbitrary number of homogeneous layers with sharp interfaces. It assumes that multiple reflections and refractions are negligible small. This approximation is only valid at higher angles ($q_z > 3q_c$) and in case of smooth surfaces where the reflection of X-rays is purely specular (in X0Z plane). The reflectivity is calculated for one layer and added up to the whole multilayer system taking into account the different phase factors. The reflectivity R_N from a system of *N* layers can be calculated using Equ. 2.1.20. It depends on the reflectivity R_1 for one layer, the average absorption per layer β, the layer thickness *d,* and ζ, defined by $Q = 2\pi\zeta/d$.

$$R_N(\zeta) = \sum_{v=0}^{N-1} r_1(\zeta) e^{i2\pi\zeta v} e^{-\beta v} = r_1(\zeta) \frac{1 - e^{i2\pi\zeta N} e^{-\beta N}}{1 - e^{i2\pi\zeta} e^{-\beta}} \tag{2.1.22}$$

The kinematical theory fails in describing reflectivity near the critical angle α_c and does not take into account surface roughness[6].

Another model relies on the Born approximation describing the ratio of the reflected intensity and the Fresnel reflectivity as a function of the absolute square of the Fourier transform of the normalized gradient of the electron density across the interface as given by

$$\frac{R(q)}{R_F(q)} = \left| \int_{-\infty}^{\infty} \left(\frac{df}{dz} \right) e^{iqz} \, dz \right|^2. \tag{2.1.23}$$

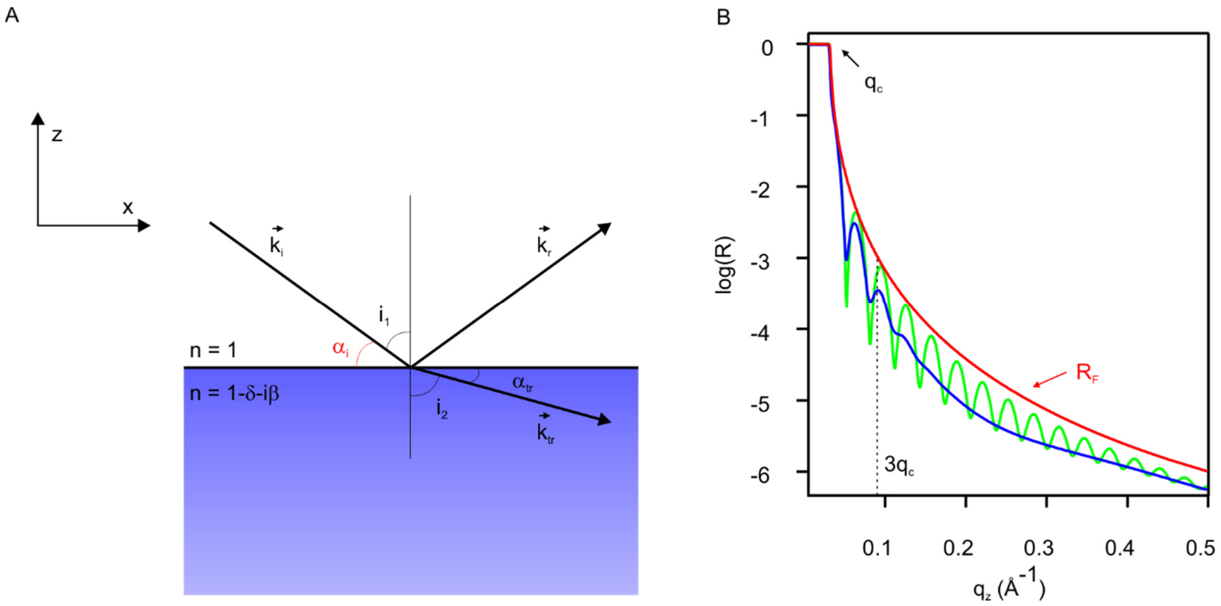

Figure 2.1 | Measurement geometry of XRR and typical reflectivity profiles. (A) Reflection and refraction of an incident plane wave at a solid, smooth surface. (B) Examples of reflectivity profiles: The reflectivity R_F was calculated according to Equ. 2.1.18 (red curve, 'specular' denotes that the reflected intensity is confined to the XZ-plane.); Reflectivity profile of a polymer film with a thickness of 200 nm without (green) and with interfacial roughness (blue).

This equation is referred to as Master formula and again only valid in the high q-range[6]. The models described above only deal with smooth interfaces. Since real interfaces are always rough to some extent, extensions have to be made. The effect of interfacial roughness causes a steeper decrease of the reflectivity profile with a simultaneous loss of information (Fig. 2.1B, blue curve) due to an additional diffuse component of the reflectivity referred to as off-specular reflectivity.

Further developments have been made by Parratt in 1954 introducing a recursive method to improve the description of the reflectivity profile in the small *q*-region[60]. The ratio X_j of the amplitude of the transmitted T_j and reflected X-rays R_j is given by the recursion formula

$$X_j = \frac{R_j}{T_j} = e^{2ik_{z,j}z_j} \frac{r_{j,j+1} + X_{j+1}e^{(-2ik_{z,j+1}z_j)}}{1 + r_{j,j+1}X_{j+1}e^{(-2ik_{z,j+1}z_j)}}, \tag{2.1.24}$$

with the Fresnel coefficient

$$r_{j,j+1} = \frac{k_{j,j} - k_{j,j+1}}{k_{j,j} + k_{j,j+1}}. \tag{2.1.25}$$

The specular reflected intensity R is obtained from Equ. 2.1.24 as given by

$$R = \left|X_j\right|^2. \tag{2.1.26}$$

The advantage of this method is that multiple reflections at different interfaces and refraction effects are taken into account. The interference between various reflections leads to oscillations in the reflectivity profile (so-called Kiessig fringes). The Parratt formalism is similar to the Abelès matrix method[61] and is the most widely used method to model data for layer structures. In case of a small roughness relative to the layer thickness, the Parratt formalism can be extended by introducing an idealized uncorrelated roughness, which is characterized by a mean standard deviation of the layer thickness $\sigma = \sqrt{\langle d^2 \rangle}$. The extended Fresnel coefficient is thus given by

$$R = R_F e^{-2\sigma^2 {q_z}^2}\,. \tag{2.1.27}$$

2.1.2 Experimental realization

XRR measurements were conducted at a sealed X-ray tube (D8 Discover, BrukerAXS, Karlsruhe, Germany), operating with Mo Kα radiation (E=17.48 keV, λ=0.0709 nm). The vertical beam size in the reflectivity plane was defined by an entrance slit to 0.2 mm. Before the beam reached the sample, it passed an automated 4-fold absorber to prevent the detector from beam damage. The reflected beam passed two slits with a horizontal width of 0.3 and 0.25 mm, respectively, to reduce the detection of diffuse scattering. A silicon strip detector (LynxEye Bruker AXS, Karlsruhe, Germany) was used. All measurements were performed at solid-liquid interface at T = 25 °C. For sample preparation, silicon substrates with native oxide (Si(100), 10 x 24 mm^2) from SiMat (Landsberg am Lech, Germany) were cleaned by a modified RCA protocol[62]. Briefly, substrates were sonicated in acetone, ethanol, methanol and water for 3 min, subsequently. Then, they were immersed in a solution of 1:1:5 (v/v/v) H_2O_2(30%)/NH_4OH(25%)/H_2O and sonicated at room temperature for 3 min, before soaking them at 60 °C for another 30 min. Thereafter, substrates were rinsed intensively with ultrapure water, dried at 70 °C and stored in a vacuum chamber at room temperature until their use. Finally, substrates were inserted into a self-manufactured liquid cell which consisted of a Teflon main body with kapton windows as depicted in Figure 2.2. Supported membranes were prepared by vesicle fusion. Specifically, small unilamellar vesicles (SUV; preparation described in Chapter 3.1.4) in buffer were injected onto the substrates and incubated for 30 min at 40 °C, followed by intensively rinsing with HBS buffer (150 mM NaCl, 10 mM Hepes, pH 7.5) to remove excess SUVs. Supported membranes doped with 5 mol% DOGS-NTA (Ni^{2+}) were incubated with nickel buffer (1 mM $NiCl_2 \cdot 6H_2O$, 150 mM NaCl, 10 mM Hepes, pH 7.5) for 45 min to saturate the nickel chelating nitrilotriacetic acid (NTA) head groups. The buffer was exchanged to calcium buffer (1 mM $CaCl_2 \cdot 2H_2O$, 150 mM NaCl, 10 mM Hepes, pH 7.5), then human recombinant His6 N-cadherin was added (10 µg/mL) and incubated for 12 h at room temperature. The reversibility of the protein coupling was probed by incubation with 100 mM aqueous EDTA for 1 h at r.t.. For the immobilization of SDF1α, a supported membrane doped with 5 mol% biotin-DOPE were incubated with neutravidin solution (40 µg/mL) for 8 h at room temperature. After removing neutravidin, biotinylated SDF1α (10 µg/mL) was added and incubated for 2 h. For both N-cadherin and SDF1α, excess proteins were removed by rinsing extensively with buffer. XRR profiles were recorded after (1) supported membrane preparation, (2) protein functionalization and, in case of a supported membrane functionalized with N-cadherin, (C) after removal of protein by 100 mM aqueous EDTA. Offset scans of the X-ray intensity ($\alpha_i \neq \alpha_r$) were carried out for the full angular scan range to correct the data for diffuse background. In order to ensure statistical reliability, three data sets were recorded and analyzed. Beside the instrument based normalization of the reflectivity profile to the intensity of the incident beam, the data was corrected for the beam footprint *F* in order to account for the beam size as given by

$$F = \frac{t_1}{w \cdot \sin \alpha_i}, \qquad (2.1.28)$$

where t_1 and w correspond to the vertical beam size and the sample width parallel to the beam, respectively. The best fit to the experimental data was determined for each sample by obtaining model intensity curves using the Parratt/Abelès formalism[60] implemented in the software package MOTOFIT[63] in IGOR Pro (WaveMetrics Inc., Portland, USA). Reasonable starting parameter values were initially set for each fit. SLD values for the silicon substrate, SiO_2 layer and water were calculated and set as constant.

Figure 2.2 Measurement chamber for XRR at solid-liquid interface. The liquid cell consisted of a self-made Teflon main body with Kapton windows. The silicon wafer was inserted prior the membrane preparation.

2.1.3 Structural characterization of membrane-coupled N-cadherin

XRR has been applied to probe the fine structures of a supported membranes prior and after its functionalization with His6 N-cadherin yielding values for the thickness, scattering length density and interfacial roughness of each layer. Figure 2.3 depicts the XRR profiles of a solid-supported membrane consisting of 5 mol% DOGS-NTA in SOPC before (blue) and after (red) its functionalization with His6 N-cadherin. The black solid lines correspond to the best fit of the reflectivity intensity $R(q_z)$. The resultant SLD profiles are shown as inset. Both data sets exhibit pronounced minima indicating the presence of layers with high SLD contrast. The shift of the position of the minima towards lower q_z values with a simultaneous decrease of the reflectivity curve after functionalization with N-cadherin indicates an increase of the total thickness and of the interfacial roughness caused by the protein coupling, respectively. The reflectivity profile of the supported membrane was fitted with a five-slab model representing the SiO_2 layer, the water layer separating the membrane and the substrate, and the alkyl side chains sandwiched by two layers consisting of phospholipid head groups. The thickness of the supported membrane was found to be d = 42.1 Å. This finding can be compared to the value of 38.7 Å for membranes with similar composition on Si-substrate at 25 °C, given by Koerner *et al.*[55]. Reich *et al.* reported a thickness of a pure SOPC bilayer of 48 Å[64]. Although the spatial resolution, as defined by $d_{min} = \pi/q_z$, was limited to 7.8 Å, a water layer of d = 3.9 Å was included into the fitting procedure as this approach led to better fitting results. A similar approach was utilized by Nováková *et al.* where a water layer with a thickness 4.3 Å was reported[65]. It is noteworthy to mention that their measurements were performed with a similar experimental setup using an in-house reflectometer with comparable spatial resolution. Furthermore, the obtained value is in good agreement with XRR studies by Miller *et al*. (d = 4.0 Å)[66]. The resulting thickness and SLD of the inner phospholipid head group layer differed from those obtained for the outer one. The inner head group layer was found to have a higher SLD ($\rho = 12.8 \cdot 10^{-6}$ Å^{-2}) accompanied by a smaller layer thickness (d = 7.6 Å) compared to the outer layer, where $\rho = 12.2 \cdot 10^{-6}$ Å^{-2} and d = 8.8 Å. Such differences arise from the close proximity between the inner leaflet and the substrate and are caused by van der Waals, electrostatic, hydration, and steric forces[67] resulting in viscous friction between the substrate and the supported membrane[68]. The obtained results were in good agreement to those obtained by Koerner *et al.* who reported a difference in thickness and SLD for the outer head groups of Δd = 0.2 Å and $\Delta\rho = 0.6 \cdot 10^{-6}$ Å^{-2}, respectively[55]. Hochrein *et al.* obtained similar tendencies[64]. The thickness and SLD of the inner layer consisting of alkyl chains were obtained to be d = 25.7 Å and $\rho = 7.5 \cdot 10^{-6}$ Å^{-2} and compared well to those obtained by others[55, 66, 69, 70]. The interfacial roughness of each layer was in the range of $3 < \sigma < 4$ Å.

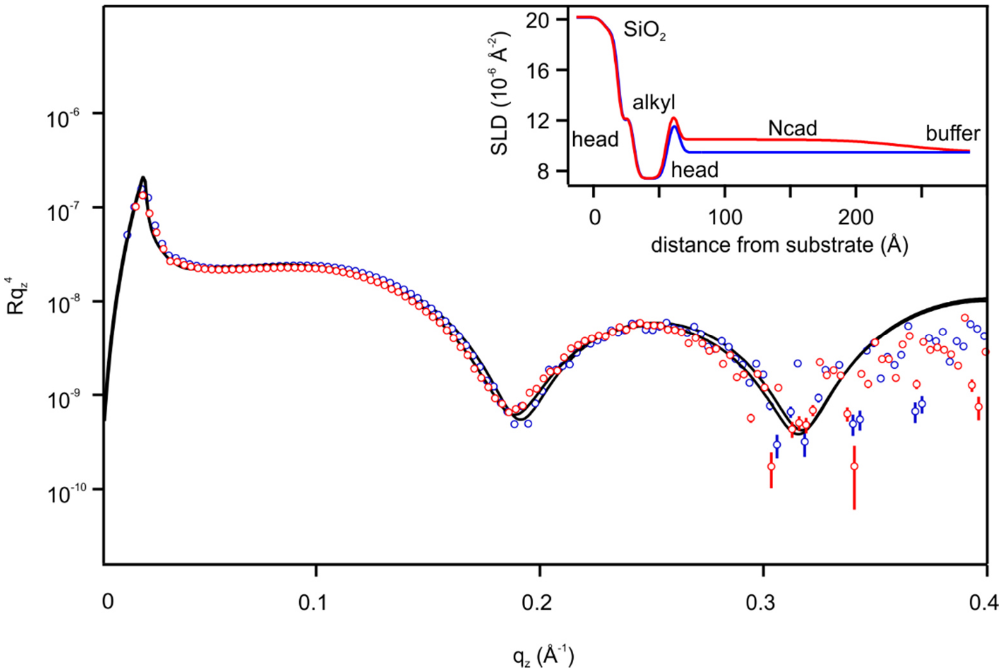

Figure 2.3 | Reflectivity profiles of the *in vitro* niche model prior and after its functionalization with His6 N-cadherin. Reflectivity profile of the *in vitro* niche model consisting of a supported membrane before (blue) and after functionalization with His6 N-cadherin (red). The protein coupling caused a shift of the minima to the lower q-range. The experimental errors are within the symbol size. The solid lines represent the best fits. The SLD profiles corresponding to the best fit results are presented as inset.

In a second step, the functionalization of the supported membrane with His6 N-cadherin was investigated. The coupling of His6 N-cadherin to the supported membrane was facilitated by the well-known coupling principle between a polyhistidine-tag and a nitrilotriacetic acid (NTA) moiety of the head group functionalized lipid DOGS-NTA, which is mediated by a nickel cation[71]. Data fitting of the corresponding reflectivity profile (Fig. 2.3, red) resulted in a thickness, d = 169.7 Å, and an interfacial roughness, σ = 41.0 Å, of the protein layer. Both values are reasonable as compared to the total length of N-cadherin and its flexible rod-like shape. X-ray crystallography experiments revealed a length of the strand-swapped dimer of N-cadherin to be 378 Å in the presence of Ca^{2+} ions[72], resulting in a length of one N-cadherin of around 189 Å. XRR measurements on other cadherins such as the recombinant protein Xenopus cadherin-11 yielded a thickness of d = 126 Å[55]. Deviations arose from the fact that this recombinant protein consists of only 3 EC whereas N-cadherin has a full length including 5 EC. Measurements performed by electron microscopy revealed a length of E-cadherin, which consisted of 5 EC, of 220 Å[73]. Thus, the obtained value in this study suggested that the proteins were not arranged perpendicular to the membrane but tilted by 40° with respect to the vertical direction. Martel *et al.* found a similar behavior with a mean tilt angle of 50° [74]. Furthermore, the current analysis resulted in a SLD of $10.1 \cdot 10^{-6}$ Å^{-2} for the N-cadherin layer which was slightly smaller compared to value found by Martel *et al.*[74]. They investigated the fine structures of a densely packed C-cadherin layer anchored to a Ni-NTA-DLGE monolayer by XRR resulting in values for thickness, d = 150 Å, and SLD, $\rho = 10.6 \cdot 10^{-6}$ Å^{-2}. Based on the obtained value for the SLD, the volume fraction Φ of the protein in its layer was calculated according to the following equation,

$$\rho_{tot} = \Phi\rho_{dry} + (1 - \Phi)\rho_{H2O} \,, \qquad (2.1.29)$$

where ρ_{tot}, ρ_{dry} and ρ_{H2O}, represent the obtained SLD of the protein layer, the calculated SLD for dry proteins and buffer, respectively. The SLD of the dry protein was estimated to be $\rho_{dry} = 12.5 \cdot 10^{-6}$ Å^{-2} based on the amino acid sequence of N-cadherin. This yielded a volume fraction of N-cadherin within the protein layer of 0.23. The functionalization of the supported membrane with His6 N-cadherin caused an increase of the SLD (3 %) of the outer head group layer. This finding can be attributed to the displacement of water molecules by the protein. All other layers were unaffected by the protein functionalization. Finally, the reversibility of the His6 N-cadherin functionalization was investigated. For this purpose, the *in vitro* niche model was incubated with 100 mM EDTA in HBS-buffer for 1 h in order to chelate the nickel cation by successive uncoupling of His6 N-cadherin.

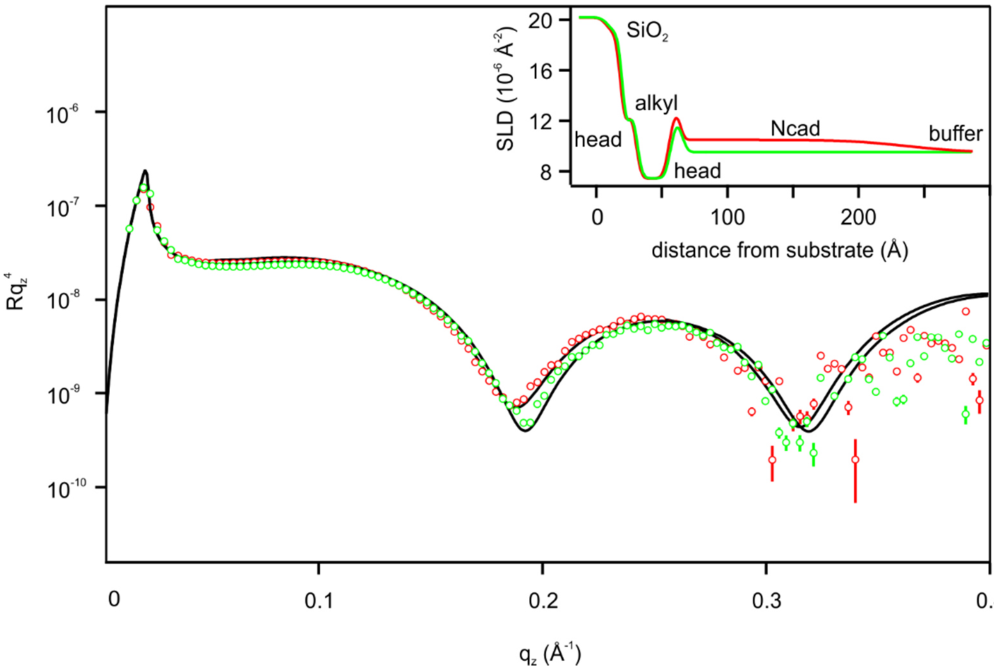

Figure 2.4 | Functionalization with His6 N-cadherin is reversible. Reflectivity profile of the *in vitro niche model* consisting of a supported membranes functionalized with His6 N-cadherin before (red) and after rinsing with 100 mM aqueous EDTA (green). The shift of the minima to a higher *q*-range indicates that His6 N-cadherin was successfully removed. The experimental errors are within the symbol size. The solid lines represent the best fits. The SLD profiles corresponding to the best fit results are presented as inset.

Figure 2.4 depicts the reflectivity profile of the *in vitro* niche model before (red) and after incubation with 100 mM EDTA in HBS-buffer (green). The black solid lines correspond to the best fit of the reflectivity intensity $R(q_z)$. The resultant SLD profiles are shown as inset. A shift of this minima towards higher q_z-values suggests the successful uncoupling of N-cadherin. Furthermore, the protein removal resulted in a lower roughness of the supported membrane as indicated by a steeper minima. A slight decrease of the thickness (-5 %) of the outer head group layer accompanied by a decrease in the SLD (-1 %) was a result of the removal of the Ni^{2+} cations from the NTA-modified headgroups.

Table 2.1 | Structural parameters. Thickness *d*, SLD and interfacial roughness σ obtained from fitting of three corresponding reflectivity profiles. Data is represented as mean value ± SD for n = 3 data sets.

	d [Å]	**SLD [$\cdot 10^{-6}$ Å^{-2}]**	**σ [Å]**
(I) Supported membrane before His6 N-cadherin coupling			
Outer head groups	8.8 ± 0.4	12.2 ± 0.1	3.5 ± 0.5
Alkyl side chains	25.7 ± 0.5	7.5 ± 0.2	3.5 ± 0.0
Inner head groups	7.6 ± 0.4	12.8 ± 0.0	3.1 ± 0.1
Aqueous buffer	3.9 ± 0.0	9.4*	3.1 ± 0.1
(II) Supported membrane after His6 N-cadherin coupling			
His6 N-cadherin	169.7 ± 6.6	10.1 ± 0.4	41.0 ± 5.7
Outer head groups	8.4 ± 0.5	12.6 ± 0.4	2.9 ± 0.2
Alkyl side chains	25.3 ± 0.1	7.5 ± 0.2	3.4 ± 0.5
Inner head groups	7.7 ± 0.2	12.8 ± 0.0	2.9 ± 0.5
Aqueous buffer	3.8 ± 0.1	9.4*	3.0 ± 0.0
(III) Supported membrane after 100 mM EDTA			
Outer head groups	8.4 ± 0.6	12.0 ± 0.1	3.2 ± 0.2
Alkyl side chains	25.3 ± 0.1	7.3 ± 0.0	3.2 ± 0.3
Inner head groups	7.6 ± 0.4	12.8 ± 0.1	2.9 ± 0.3
Aqueous buffer	3.9 ± 0.0	9.4*	3.0 ± 0.1
SiO_2 layer	11.4 ± 0.2	18.9*	3.2 ± 0.0
Si-substrate	∞	20.1*	4.1 ± 0.1

*Values were calculated and set constant.

2.1.4 Structural characterization of membrane-coupled SDF1α

After the successful determination of structural parameters of the *in vitro* niche model displaying N-cadherin, similar experiments were performed for the SDF1α functionalized supported membranes. As the functionalization of the supported membranes with biotin-SDF1α is mediated by the biotin-binding protein neutravidin, XRR measurements were performed first on a pure supported membranes consisting of 5 mol% biotin-DOPE in SOPC followed by similar experiments detecting the neutravidin and then the biotin-SDF1α functionalization. Figure 2.5 depicts the XRR profile of the supported membrane before (blue) and after the coupling of neutravidin (red). The black solid lines correspond to the best fit of the reflectivity intensity *R*(q_z). The resultant SLD profiles are shown as inset. In line with previous experiments, both data sets exhibit pronounced minima indicating the presence of layers with high SLD contrast. The shift of the position of the minima towards lower q_z values after functionalization with neutravidin is a result of the increase of the total thickness caused by the protein coupling. The coupling of neutravidin influenced not only the reflectivity intensity *R*(q_z) due to an increase in the interfacial roughness as it can be seen by lower intensity values of the corresponding XRR profile *R*(q_z), but the presence of an additional protein layer modulated the global shape of the reflectivity profile *R*(q_z) in the lower and middle q_z-range.

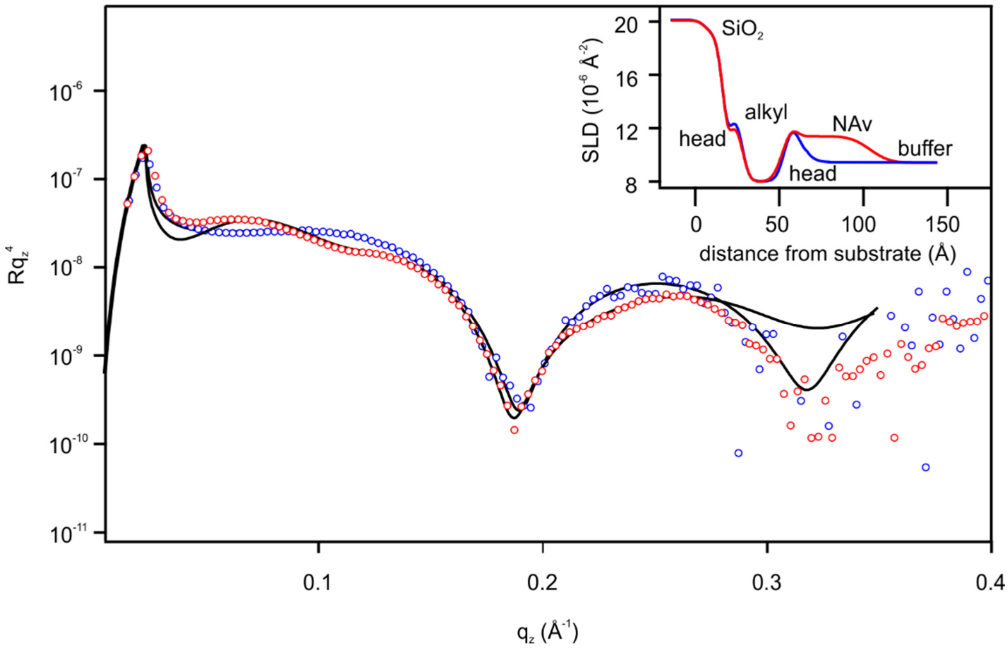

Figure 2.5 | Fine structures of a supported membrane functionalized with neutravidin. Reflectivity profile of a supported membrane before (blue) and after functionalization with neutravidin (red). The functionalization with neutravidin led to significant change of the XRR profile in low and middle *q*-range. The experimental errors are within the symbol size. The solid lines represent the best fits. The SLD profiles corresponding to the best fit results are presented as inset.

This finding was in well agreement to the data obtained by Abuillan *et al.* who performed similar experiments on the neutravidin coupling to phospholipid monolayers at the air/water interface[56]. Applying a six slab model, the corresponding fitting results revealed a thickness d = 43.5 Å perpendicular to the sample surface with an interfacial roughness σ = 7.1 Å. This value compared well to data published based on X-ray crystallography experiments. For example, X-ray diffraction experiments of crystalline tetrameric neutravidin revealed a cuboid structure with dimensions of $56 \times 50 \times 40$ Å^3, as reported by Rosano *et al.*[75]. The slight difference is attributable to protein hydration in case of the present XRR experiments at solid/liquid interface. Furthermore, a SLD of $\rho = 11.5 \cdot 10^{-6}$ Å^{-2} was obtained for the protein layer. Applying equation 2.1.29, a volume fraction of $\Phi = 0.69$ of the neutravidin layer was determined by using the SLD of the dry protein which was estimated to be $\rho_{dry} = 12.4 \cdot 10^{-6}$ Å^{-2} according to the amino acid sequence from crystallographic data (PDB:1AVE)[76]. It should be noted, that any protein aggregates in the neutravidin solution were removed by ultracentrifugation prior to membrane functionalization. Thus, such a high value suggests the *in situ* formation of protein clusters on the supported membrane due to electrostatic interactions. In order to enhance the quality of the membrane preparation, these clusters were removed by a similar approach to Orelma *et al*. using 100 mM aqueous glycine hydrochloride at pH 2.5[77]. The success of this procedure was proven by recording a second XRR profile of the neutravidin functionalized supported membrane.

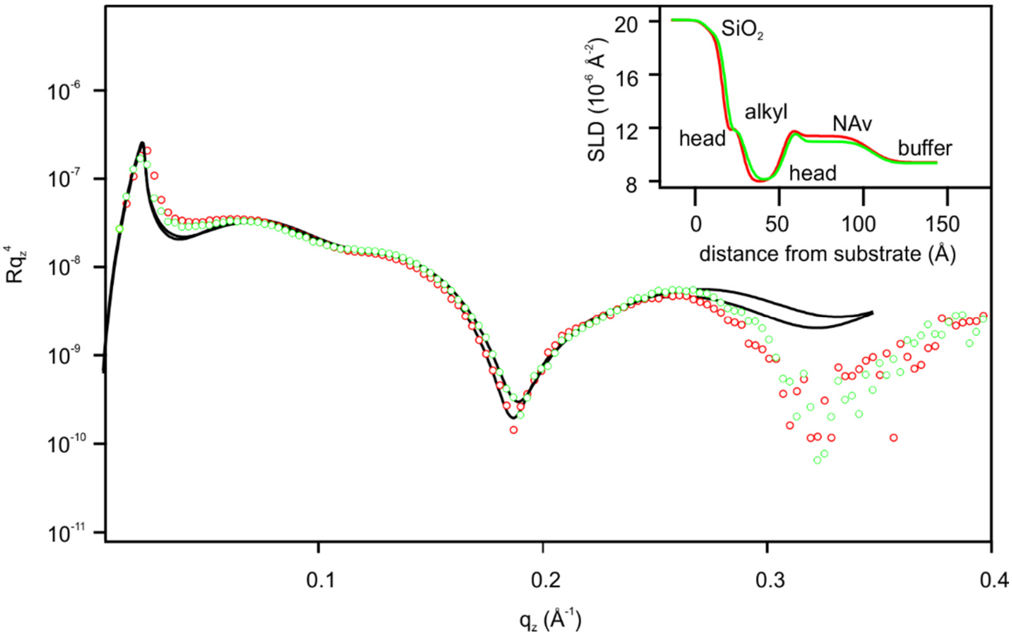

Figure 2.6 | Removal of protein clusters by 100 mM glycine hydrochloride. Reflectivity profile of a neutravidin functionalized supported membrane before (red) and after incubation with 100 mM glycine hydrochloride (green) at pH 2.5. The experimental errors are within the symbol size. The solid lines represent the best fits. The SLD profiles corresponding to the best fit results are presented in the insets.

Figure 2.6 depicts the reflectivity intensity $R(q_z)$ prior (red) and after the treatment with 100 mM aqueous glycine hydrochloride at pH 2.5 (brown). The corresponding fitting results (Table 2.2) revealed a decrease in the SLD by -5 % of the neutravidin layer without a simultaneous decrease in the layer thickness. Furthermore, the volume fraction was reduced by 42 %. Thus, multilayer formation can be excluded. Note, the incubation with 100 mM aqueous glycine hydrochloride solution at pH 2.5 had no influence on the structure of the supported membrane. The last step consisted of the structural analysis of the coupling of biotin-SDF1α to the neutravidin functionalized supported membrane. The obtained reflectivity profile (orange markers) and its best fit (black curve) are depicted in Figure 2.7. Data fitting was performed by applying again a six slab model. As the theoretically calculated SLD of the dry SDF1α (based on its amino acid sequence[78]) is similar to that one of neutravidin ($\rho_{dry} = 12.4 \cdot 10^{-6}$ Å^{-2}), it was not possible to distinguish both layers. The obtained SLD profiles are shown as inset. The coupling of biotin-SDF1α resulted in a total thickness of the protein layer of 79.4 Å corresponding to a thickness of the SDF1α layer of 35.3 Å. Furthermore, the interfacial roughness increased to 27.1 Å. This finding compared well to the value obtained from X-ray diffraction experiments on crystalline SDF1α. The crystal structure of chemically synthesized SDF1α revealed an almost globular structure consisting of four β–sheets and two alpha helices with a mean diameter of 32 Å[78, 79].

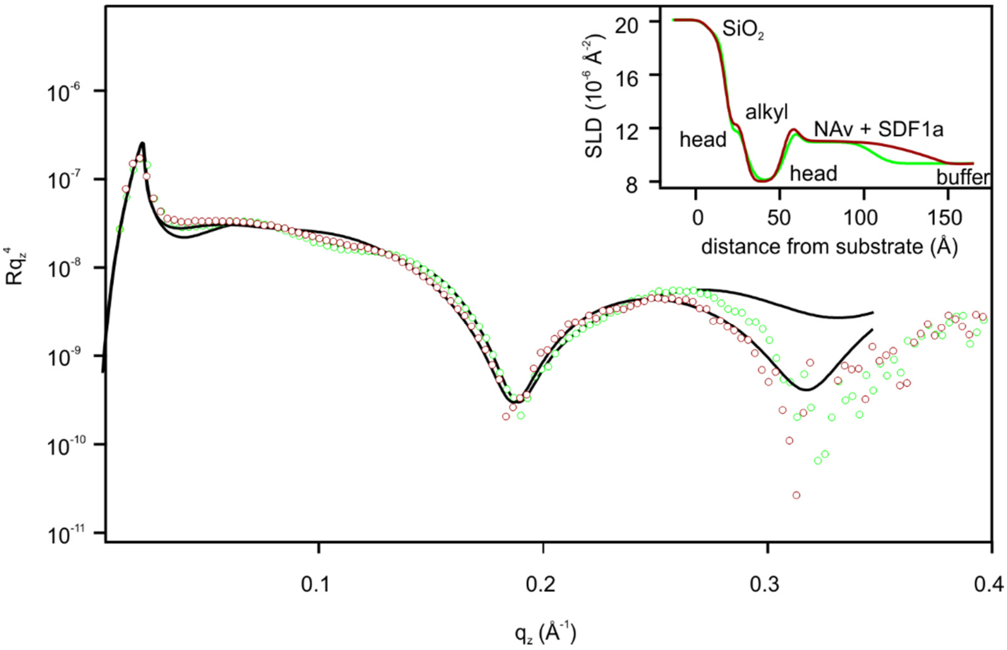

Figure 2.7 | Fine structures of the *in vitro* niche model functionalized with biotin-SDF1α. Reflectivity profile of the *in vitro* niche model consisting of a neutravidin functionalized supported membrane before (green) and after functionalization with biotin-SDF1α (brown). The functionalization with biotin-SDF1α led to a slight shift of the minima to the lower q-range. The experimental errors are within the symbol size. The solid lines represent the best fits. The SLD profiles corresponding to the best fit results are presented in the insets.

Furthermore, the SLD of the protein layer decreased to $\rho = 10.6 \cdot 10^{-6}$ Å^{-2} (-4 %) after coupling of biotin-SDF1α. This finding is attributable to the size differences of neutravidin and SDF1α. The dimensions of SDF1α are approximately 30 % smaller compared to neutravidin molecules as reported from crystallographic studies to be 56 × 50 × 40 Å^{3} [75]. As the current results did not give any information on the binding stoichiometry, further experiments were performed by QCM-D to address this important question.

Table 2.2 | Structural parameters. Thickness *d*, *SLD* and interfacial roughness ρ obtained by fitting of three corresponding reflectivity profiles. Data is represented as mean value ± SD for n = 3 data sets.

	d [Å]	**SLD [$\cdot 10^{-6}$ Å^{-2}]**	**σ [Å]**
(I) Supported membrane before neutravidin binding			
Outer head groups	8.1 ± 0.4	12.1 ± 0.0	3.5 ± 0.2
Alkyl side chains	24.8 ± 0.2	7.2 ± 0.0	3.5 ± 0.6
Inner head groups	7.3 ± 0.1	12.6 ± 0.2	2.9 ± 1.1
Aqueous buffer	4.3 ± 0.1	9.4*	2.5 ± 0.2
(II) Supported membrane after neutravidin binding			
neutravidin	43.5 ± 1.1	11.5 ± 0.1	7.1 ± 2.8
Outer head groups	7.5 ± 0.1	12.7 ± 0.1	2.9 ± 0.2
Alkyl side chains	24.2 ± 0.3	8.0 ± 0.0	3.4 ± 0.5
Inner head groups	7.4 ± 0.0	12.3 ± 0.4	2.9 ± 0.5
Aqueous buffer	3.9 ± 0.2	9.4*	3.0 ± 0.0
(III) Supported membrane with neutravidin after incubation with 100 mM glycine hydrochloride (pH 2.5)			
neutravidin	44.1 ± 0.7	11.0 ± 0.1	5.9 ± 2.2
Outer head groups	7.4 ± 0.2	12.6 ± 0.1	3.0 ± 0.0
Alkyl side chains	24.1 ± 0.1	8.2 ± 0.2	4.9 ± 1.0
Inner head groups	7.2 ± 0.0	12.4 ± 0.3	4.3 ± 0.2
Aqueous buffer	3.8 ± 0.1	9.4*	2.2 ± 0.3
(IV) Supported membrane with neutravidin after biotin-SDF1α binding			
Neutravidin/biotin-SDF1α	79.4 ± 6.1	10.6 ± 0.2	27.1 ± 7.3
Outer head groups	7.5 ± 0.1	12.7 ± 0.1	3.4 ± 0.4
Alkyl side chains	24.3 ± 0.2	7.3 ± 0.4	4.5 ± 0.6
Inner head groups	7.4 ± 0.1	12.2 ± 0.3	3.2 ± 0.4
Aqueous buffer	4.6 ± 0.3	9.4*	2.4 ± 0.1
SiO_2 layer	10.1 ± 0.5	18.9*	3.2 ± 0.0
Si-substrate	∞	20.1*	4.1 ± 0.2

*Values were calculated and set constant.

2.1.5 Summary

XRR measurements were utilized to reveal fine structures of *in vitro* models of bone marrow niche used for the mechanistic investigation of the adhesion and migration of HSPC. The structural characterization enabled a detailed analysis and thus improvement of the fabrication of N-cadherin and SDF1α functionalized supported membranes in order to ensure the high quality and reproducibility of the *in vitro* niche models. For this purpose, the stepwise deposition and functionalization of solid-supported membranes with either N-cadherin or biotin-SDF1α/Neutravidin at an average intermolecular distance $<d> \sim$ 4 nm were analyzed and evaluated by a applying an appropriate slab model implemented in the Parratt/Abelès formalism.

First, structural properties perpendicular to the membrane surface of N-cadherin functionalized supported membranes were investigated resulting in a thickness and SLD of the protein layer, d = 169.7 Å and $\rho = 10.1 \cdot 10^{-6}$ Å^{-2}, respectively, which are in good agreement to data published by others. These findings suggested that the proteins were not arranged perpendicular to the membrane but tilted by 40° with respect to the vertical direction. Second, similar experiments were performed for SDF1α functionalized supported membranes. Because the binding of biotin-SDF1α was mediated by the biotin binding protein neutravidin, XRR measurements on (1) neutravidin and (2) SDF1α/Neutravidin functionalized supported membranes were performed. In case of (1), the treatment of the neutravidin functionalized membranes with 100 mM aqueous glycine hydrochloride (pH 2.5) removed protein aggregates formed *in situ*. Data fitting revealed a thickness and SLD of the corresponding neutravidin layer of d = 44.1 Å and $\rho = 10.6 \cdot 10^{-6}$ Å^{-2}, respectively, which are in good agreement to values published by XRR and XRD measurements. The successive coupling of biotin-SDF1α resulted in an increase of the layer thickness of 35.3 Å at a simultaneous decrease of the SLD by 4 %. The obtained thickness compared well to crystallographic data of native SDF1α. The current findings demonstrated the successful fabrication of the *in vitro* niche model.

2.2 Quartz crystal microbalance study

2.2.1 Theoretical background

Quartz crystal microbalance (QCM) is an electromechanical, microgravimetric method which allows for the real-time detection of mass adsorption processes on a solid surface in liquid, gas or vapor phase [80-82]. This technique has been utilized since the 1960s[83] and relies on the piezoelectric properties of quartz which was first discovered in 1880 by Curie[84]. The experimental setup consists of a disc-shaped AT-cut quartz crystal with metal electrodes deposited on each side (Fig. 2.8A)[85]. By the application of an alternating current (AC) voltage across the electrodes in an oscillation circuit, the crystal starts to oscillate by shear deformation at its resonance frequency ω as given by

$$\omega = \frac{\upsilon_Q}{2d}, \tag{2.2.1}$$

where d and υ_Q correspond to the thickness of the quartz crystal and the velocity of the generated shear waves, respectively. This frequency is shifted by Δf in case of adsorption or desorption of mass Δm from the crystal surface. The linear relationship between the mass uptake Δm and the shift in frequency Δf was first claimed by Sauerbrey[86]

$$\Delta f = -\frac{\Delta d}{d}\omega = -\frac{\Delta m_Q}{\rho_Q \cdot d \cdot A}\omega = -\frac{2\omega^2}{\upsilon_Q \cdot \rho_Q \cdot A}\Delta m = -\frac{1}{C}\Delta m\,, \tag{2.2.2}$$

and is related to the intrinsic properties of the quartz crystal. The intrinsic properties comprise the mass of a slice of quartz Δm_Q with the thickness Δd and the area A. The mass density, ρ_Q as given as the value C by the manufacturer.

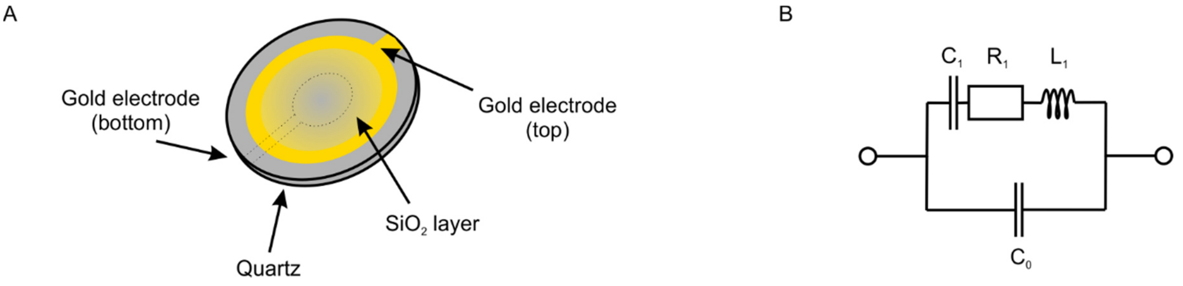

Figure 2.8 | Schematic illustrations of a QCM sensor and the electrical equivalence of the crystal unit. The sensor (A) is based on a piezoelectric, disc-shaped AT-cut quartz crystal with gold electrodes deposited on top and bottom of the disc. A thin, hydrophilic SiO_2 layer on top allows for the functionalization with polar molecules. The common electrical equivalence (B) near the principle resonance under the assumption that all undesired modes of vibration near the principle resonance are suppressed.

For an AT-cut quartz crystal at 5 MHz, C equals to 17.7 ng·cm^{-1}·Hz^{-1}. Prerequisites for the validity of this equation are the formation of a uniform, rigid layer with a much smaller mass compared to the quartz, i.e., $\Delta f/f << 1$. The theoretical predictions of Sauerbrey[86] were experimentally proven by Oberg and Lingensjo in 1956[87] and expanded towards the application in liquid by Nomura and Okuhara in 1982[88]. Due to the electromechanical properties of a quartz crystal, it can be described by an electrical circuit. Figure 2.8B depicts the common equivalent electrical circuit of a quartz crystal near the principle resonance frequency which can be applied based on the assumption that all undesired modes of vibration are suppressed[89, 90]. R_1 represent the electrical resistance. The mass sensitivity is related to the inductance L_1, which is considered as the mechanical energy storage of the crystal. The capacitance C_1 is a measure of its elasticity. The electrical connections of the experimental setup influences the system by their capacitance C_0. The deposition of a layer on the crystal surface changes its resonance frequency and dissipation according to its mechanical properties as depicted in Figures 2.9A and B. The reason for this change is an increase of the distance between the top and bottom antinodes of the wave causing an increased wavelength and, thus, a decreased frequency. In case of the adsorption of viscoelastic layers, Sauerbrey's equation loses its validity. A non-rigid layer with viscoelastic properties starts to self-oscillate on the substrate surface leading to additional dissipation of energy (Fig. 2.9, blue curve). In such a case, the mechanical properties of the layer are described by a parallel combination of a spring and a dashpot which is based on the Kelvin-Voigt model[91],

$$G^* = G' + iG'' = \mu_f + 2\pi i f \eta_f \, , \qquad (2.2.3)$$

where G^* represents the complex modulus which can be expressed in terms of shear storage and loss moduli, G' and G'', respectively. Thus, additional information about the elastic shear modulus η_f and the shear viscosity μ_f of the layer can be obtained. These findings caused the extension of the QCM method towards an experimental setup which allows for the periodic excitation of crystal oscillations by monitoring the decay of the oscillations as a function of time t. This approach is known as quartz crystal microbalance with dissipation monitoring (QCM-D)[82]. The dissipation factor D represents the reciprocal of the quality factor Q and is related to the energy which is dissipated during one period of oscillation $E_{dissipated}$ and the energy which is stored in the crystal E_{stored} as given by

$$D = \frac{1}{Q} = \frac{E_{dissipated}}{2\pi E_{stored}} = \frac{1}{\pi \omega \tau} \, . \qquad (2.2.4)$$

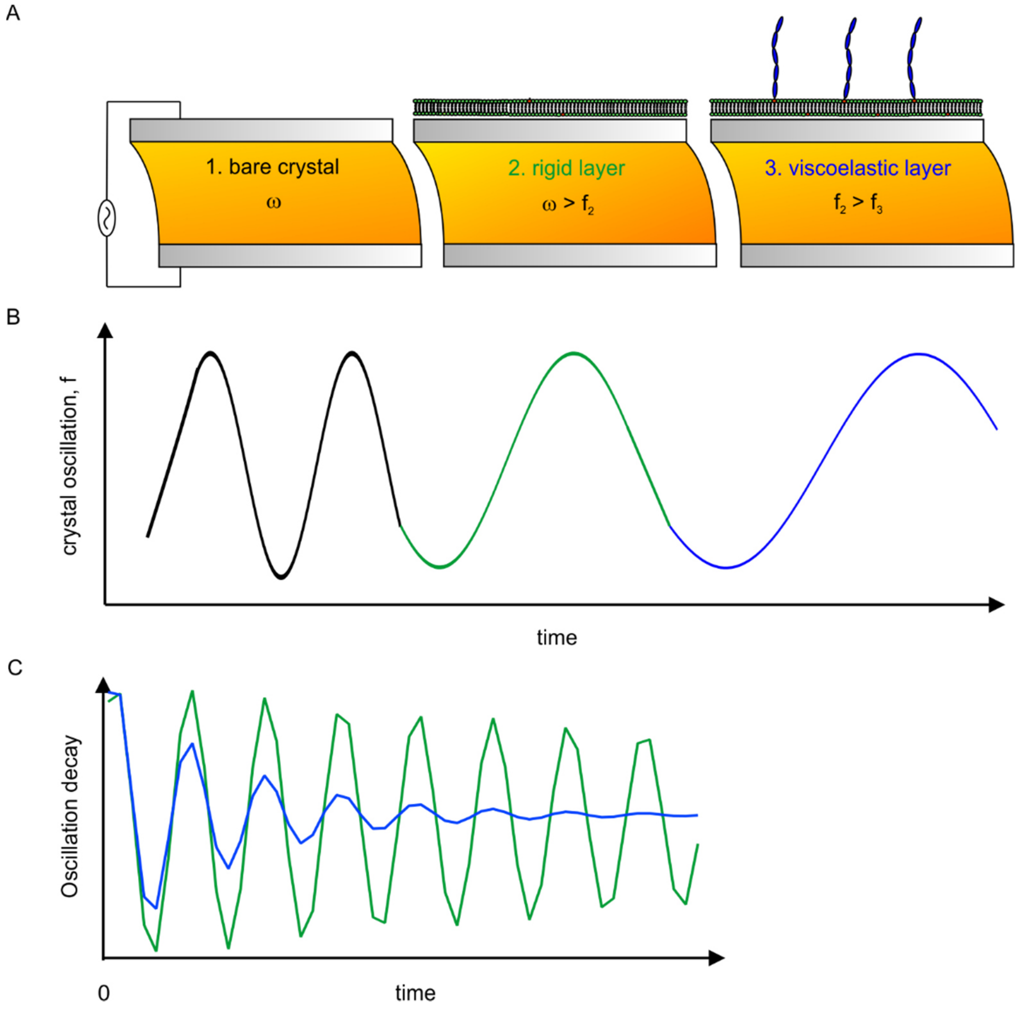

Figure 2.9 | Schematic illustrations of the response of a quartz crystal to the application of an electric field. The deposition of rigid or viscoelastic layer (A) on a bare crystal surface affects the frequency (B) in a characteristic manner. The decay of the quartz oscillations as a function of time distinguishes between rigid and viscoelastic layers (C).

τ represents the decay time constant of the oscillation. Based on the equivalent electrical circuit of the quartz crystal (Figure 2.8B), the dissipation factor is also given by

$$D = \frac{R_1}{\omega L_1}, \tag{2.2.5}$$

where ω represents the resonance frequency. Under the basic assumption that the oscillations are harmonic, the resonance frequency is influenced by the dissipation factor according to

$$\omega = \omega_0 \sqrt{1 - \frac{D^2}{2}} \approx \{D \ll 1\} \approx \omega_0 \,. \tag{2.2.6}$$

As $D \ll 1$, the resonance frequency is equal to its value for loss free oscillation ω_0. The crystal oscillates with the amplitude A which is related to B, the driven force divided by the force constant, and can be described as follows

$$A = \frac{B}{D\sqrt{1 - \frac{D^2}{4}}} \approx \{D \ll 1\} \approx \frac{B}{D}. \qquad (2.2.7)$$

The total energy loss in QCM is a sum of all losses in the system D_i and can be expressed as

$$D_{tot} = \sum_i D_i \, . \qquad (2.2.8)$$

QCM-D was applied as complementary method to XRR in order to investigate structural properties of the *in vitro* niche models as it allows for the determination of the mass uptake Δm and mechanical properties of the layer. Special attention was paid to the dependency of the mass uptake Δm from the molar concentration of head group functionalized lipids in the membrane in order to prove the assumption that the corresponding average intermolecular distance $\langle d \rangle$ of the coupled proteins can be tuned. The advantage of QCM-D is its high sensitivity (0.2 $\text{ng}\cdot\text{cm}^{-2}$ range) and the high temporal resolution of 0.5 s. Adding to the mass density determination, QCM-D allows also the investigation of the mechanical properties of the adsorbed layer. Thus, the combination of the QCM-D with XRR could be considered as a powerful tool to unravel the intermolecular interactions between the coupled proteins.

2.2.2 Experimental realization

QCM-D measurements were performed with AT-cut SiO_2 coated quartz crystals (LOT-QuantumDesign GmbH, Darmstadt, Germany) as sensors in a Q-Sense E4 system (Biolin Scientific, Stockholm, Sweden). For cleaning, QCM sensors were sonicated in 20 mM aqueous sodium dodecyl sulfate, ethanol and ultrapure water for 30 s, respectively. Thereafter, substrates were dried under a stream of nitrogen gas and placed into an UV-ozone cleaner ((UV/Ozone ProCleaner™220, Bioforce NanoSciences INC., Ames, USA) for 20 min. The instrument was operated at a temperature of T = 25 °C. After the freshly cleaned crystals were mounted in the instrument and the resonance frequency and its overtones were found, a constant buffer flow with a flow rate of 100 µL/min was applied by using a peristaltic pump (Ismatec IPC-N 4, IDEX Health & Science SA, Glattbrugg, Switzerland). Changes in frequency Δf and dissipation ΔD were measured at the fundamental frequency (n = 1) and six overtones (n = 3, 5...13), corresponding to resonance frequencies of $f_n \approx 5, 15, 25, ..., 65$ MHz. Once the drift in the resonance frequency, overtones and the dissipation factors had settled out, the measurement was started. Changes in dissipation ΔD and normalized frequencies $\Delta f_n/n$ are presented. Only the data from the overtones were used for further quantitative analysis, as at the fundamental frequency, the QCM-D response tends to be significantly affected by the mounting of the sensor, and small air bubbles which are trapped at the sensor periphery. Supported membranes were prepared by vesicle fusion[92]. In detail, SUV suspensions were injected onto the substrates and incubated for 15 min under continuous flow, followed by appropriate rinsing with HBS buffer (150 mM NaCl, 10 mM Hepes, pH 7.5) to remove excess SUVs. Supported membranes doped with different molar ratios of DOGS-NTA (Ni^{2+}) were incubated with nickel buffer (1 mM $NiCl_2 \cdot 6H_2O$, 150 mM NaCl, 10 mM Hepes, pH 7.5) for 15 min to saturate the nickel chelating nitrilotriacetic acid (NTA) head groups under continuous flow. The buffer was exchanged to calcium buffer (1 mM $CaCl_2 \cdot 2H_2O$, 150 mM NaCl, 10 mM Hepes, pH 7.5), then human recombinant His6 N-cadherin was added (10 µg/mL) and incubated until saturation was reached. For the immobilization of SDF1α, supported membranes doped with different molar ratios of biotin-DOPE were incubated with neutravidin solution (5 µg/mL) under continuous flow until saturation was reached. After removing the neutravidin, biotinylated SDF1α (10 µg/mL) was added and incubated. For both His6 N-cadherin and biotin-SDF1α, excess proteins were removed by rinsing extensively with buffer. For thin, rigid layers on a QCM-sensor surface such as the solid-lipid bilayer or neutravidin, the mass uptake was calculated according to the Sauerbrey equation (Equ. 2.2.2). In case of highly dissipative, thick layers (e.g. N-cadherin), the QCM-D data was modeled using least-squares curve fitting by Q-tools software 3.0.15.553. The data for the 5th, 7th and 9th overtone was fitted based on the Voigt-Voinova[91] model for viscoelastic layers. Parameters for the fluid density and viscosity were set constant as 1000 kg/m^3 and 0.001 kg/ms, respectively. The layer parameters to be fitted were forced to be between minimum and maximum estimates: layer density d (1000 – 1200 kg/m^3), shear viscosity μ_f (0.0001 – 0.1 kg/ms), elastic shear modulus η_f (0.1 – 0.5 MPa) and mass uptake Δm (100 – 2000 ng/cm^2) according to reasonable values for biological systems[93].

2.2.3 N-cadherin functionalized supported membranes

In vitro niche models consisting of functionalized supported membranes enable the precise control and variation of the ligand surface density (e.g. N-cadherin). The verification of this possibility was provided by systematic QCM-D measurements in order to ensure the quality of the *in vitro* niche model and reliability of the gained results for HSPC adhesion and migration. For this purpose, the deposition of supported membranes consisting of different molar fractions of DOGS-NTA (x = 0.05 – 2.00 mol%; corresponding to $<d_{N\text{-cadherin}}>$ ~ 6 – 36 nm) in SOPC and their subsequent functionalization with His6-N-cadherin were quantitatively investigated resulting in values for (1) the mass uptake by the QCM sensor, Δm, (2) viscoelastic properties of the N-cadherin layer such as (2) the elastic shear modulus η_f (3) the shear viscosity μ_f and (4) the binding stoichiometry between His6 N-cadherin and NTA-modified lipids. For further understanding, QCM-D data for the changes in frequency Δf and energy dissipation ΔD are discussed in detail for the deposition and functionalization of a supported membrane with His6 N-cadherin consisting of 2 mol% DOGS-NTA in SOPC ($<d_{N\text{-cadherin}}>$ ~ 6 nm) as representative result. Figure 2.10A displays the changes in resonant frequencies Δf and dissipations ΔD monitored at 25, 35 and 45 MHz (n = 5, 7, 9), respectively, caused by the formation of a lipid bilayer due to vesicle fusion. The complete QCM-D data set is shown in the Appendix 7.2.1. An abrupt decrease in the resonant frequency by $\Delta f_{n=7}$ = -60 Hz accompanied by an increase in the dissipation, $\Delta D_{n=7} = 4 \cdot 10^{-6}$, was caused by the adsorption of intact phospholipid vesicles on the sensor surface. After a critical density was reached, vesicles ruptured including the release of intravesicular water molecules and the formation of a stable supported membrane as indicated by a final $\Delta f_{n=7}$ = -26 Hz. A minor change in dissipation ($\Delta D_{n=7} = 0.2 \cdot 10^{-6}$) indicated rigid properties of the phospholipid bilayer. Thus, the mass uptake by the QCM sensor was calculated according to Sauerbrey, Δm = 470 ng/cm^2. This finding is in well agreement to Richter *et al.*[94] who reported a mass uptake of Δm = 434 ng/cm^2 and was also published by others[95, 96]. In order to remove remaining vesicles, a rinsing step was included until the curves remained stable (Δf < 0.04 Hz/min). Then, His6 N-cadherin (45 µM) was injected to the bilayer resulting in a further decrease of the resonant frequency, $\Delta f_{n=7}$ = -129 Hz caused by mass uptake of the QCM sensor during N-cadherin coupling as depicted in Figure 2.10B. For control measurements, the His6 N-cadherin solution was injected to a pure phospholipid bilayer resulting in no significant change of both measures ($\Delta f_{n=7}$ = -0.4, $\Delta D_{n=7}$ = 0). Thus, any non-specific binding could be excluded. Furthermore, membrane functionalization with His6 N-cadherin of NTA-doped lipids influenced the dissipation significantly. $\Delta D_{n=7} = 18 \cdot 10^{-6}$ suggested the formation of a viscoelastic layer. This finding prohibited the use of the Sauerbrey relation (Equ. 2.2.2).

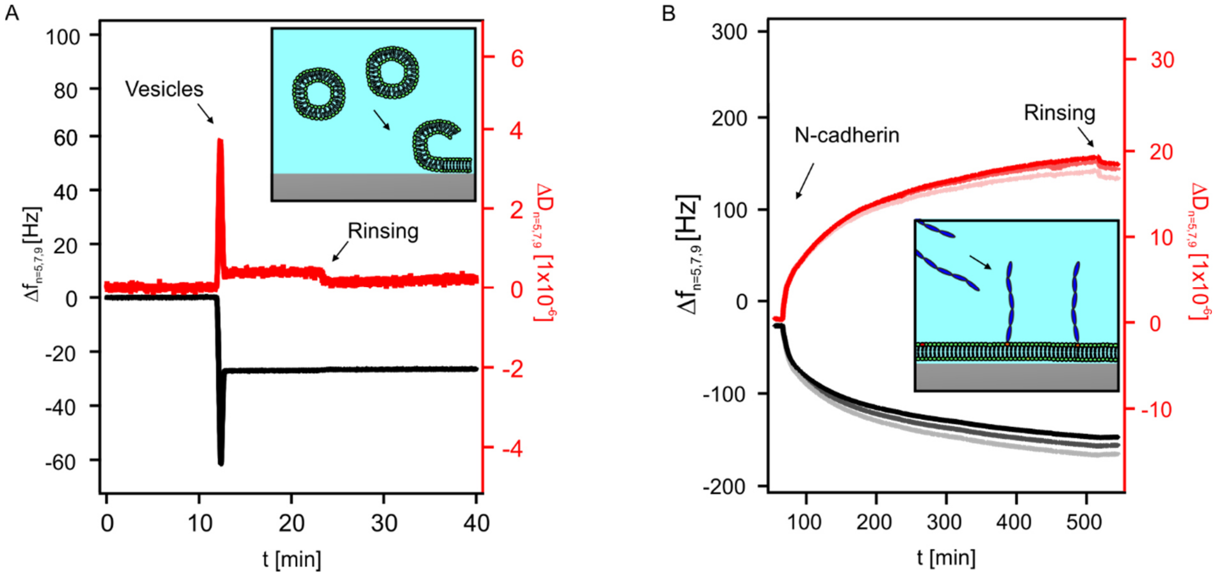

Figure 2.10 | Deposition of a supported membrane containing 2 mol% DOGS-NTA and functionalization with His6 N-cadherin. Changes in resonant frequencies *Δf* (light grey, grey, black) and dissipations *ΔD* (beige, light red, red) monitored at 25, 35 and 45 MHz (n = 5, 7, 9), respectively, during (A) formation of planar membrane consisting of 2 mol% DOGS-NTA in SOPC on SiO_2 substrates and (B) the subsequent functionalization with His6 N-cadherin (450 nM). The insets display a scheme of the corresponding deposition and functionalization step of the *in vitro* niche model.

Furthermore, the normalized changes in frequency (*Δf/n*) and dissipation (*ΔD*) for the three overtones (n = 5, 7, 9) did not overlap (Fig. 2.10B). Thus, calculation of the mass uptake *Δm* due to N-cadherin functionalization was performed by applying the Voigt-Voinova model in order to fit the data resulting in a mass uptake of Δm = 3457 ng/cm^2 at a layer density of ~1150 kg/m^3. This finding agrees well with results by Sakai *et al.*[97] who studied the formation of a dense layer of recombinant E-cadherin-IgG Fc fusion protein on a polystyrene substrate. Another study by Koerner *et al.* demonstrated that the membrane coupling of recombinant Xenopus cadherin-11, which consisted of only three EC, resulted in a mass change which was three orders of magnitude less compared to the value found in this study[55]. It should be pointed out that the mentioned studies performed data evaluation according to the Sauerbrey equation. Furthermore, the elastic shear modulus, μ_f = 0.6 MPa, and the shear viscosity, η_f = 3.2 mPa·s, of the protein layer was determined (Figure 2.12A and B). It should be noted that the shear viscosity of the N-cadherin layer is three times higher compared to the value for water (η_f = 1.0 mPa·s) and almost seven times lower than the value of the supported membrane (η_f > 20.0 mPa·s)[98]. This finding can be attributed to hydrating water present in the N-cadherin layer which was also reported for other proteins such as laminin[93]. For example, QCM-D measurements of hydrated laminin layers resulted in a shear elastic modulus of μ_f = 0.1 MPa and shear viscosity of η_f = 1.79 mPa·s. Höök *et al.* investigated layers of the mussel adhesive protein

Mefp-1 by a combination of surface sensitive techniques (QCM-D, surface plasmon resonance and ellipsometry)[99]. Mefp-1 forms layers with a high hydration (~94 %) and a shear elastic modulus and shear viscosity of μ_f = 0.7 MPa and η_f = 1.8 mPa·s, respectively. Layer formed by amphiphilic steroidal saponins coupled to a supported membrane revealed a shear elastic modulus and shear viscosity of μ_f = 0.4 MPa and η_f = 1.1 mPa·s, respectively[95]. Furthermore, previous XRR experiments with the same *in vitro* niche model (Chapter 2.1.3) support the finding of a high hydration state of the layer as there was a volume fraction of N-cadherin in the layer of 0.2 was obtained. Nevertheless, it should be noted that the direct comparison of QCM-D with XRR is hardly possible as XRR results do not account for coupled water molecules. The QCM-D experiments were then expanded in order to prove the variability of the average intermolecular distance based on the assumption that the mass uptake correlates with $<d_{N\text{-}cadherin}>$ ~ 6 – 36 nm in a linear manner. Table 2.3 summarizes the changes in frequency $\Delta f_{n=7}$ and energy dissipation $\Delta D_{n=7}$ caused by the coupling of N-cadherin to a supported membrane resulting in four different average intermolecular distances $<d_{N\text{-}cadherin}>$ ~ 6 – 36 nm. Both values exhibited a significant dependency on the composition of the supported membrane. Fitting the corresponding QCM-D data based on the Voigt-Voinova model revealed a linear dependency of the mass uptake Δm from $<d_{N\text{-}cadherin}>$ as displayed in Figure 2.11. This finding is in good agreement with results of Koerner *et al.*[55] who performed similar experiments with recombinant Xenopus cadherin-11 with hexa-histidine tag. Thus, the precise control of the ligand surface density was confirmed. Furthermore, by fitting the mass uptake Δm as a function of the molar ratio of DOGS-NTA lipids in SOPC by the empirical Hill equation as given by

$$\Delta m = \Delta m_{min} + \frac{\Delta m_{max} - \Delta m_{min}}{1 - \left({}^{c}/_{c^*}\right)^n}. \tag{2.2.9}$$

A Hill coefficient of n = 1.3 suggested a 1:1 binding between the protein and the NTA-group.

Table 2.3 | Changes in resonant frequency *Δf* and energy dissipation *ΔD* monitored at 35 MHz (n = 7), resultant from functionalization of supported membranes containing different molar fractions of DOGS-NTA in SOPC with 450 nM His6 N-cadherin. Errors are given as standard deviation.

c [mol% DOGS-NTA in SOPC]	$<d_{N\text{-}cadherin}>$ [nm]	$\Delta f_{n=7}$ [Hz]	$\Delta D_{n=7}$ [$\cdot 10^{-6}$]
2.00	6	-129.3 ± 12.3	17.6 ± 1.9
0.50	11	-62.0 ± 7.5	12.4 ± 1.2
0.20	18	-44.3 ± 4.1	9.6 ± 1.3
0.05	36	-11.4 ± 3.9	1.1 ± 0.4

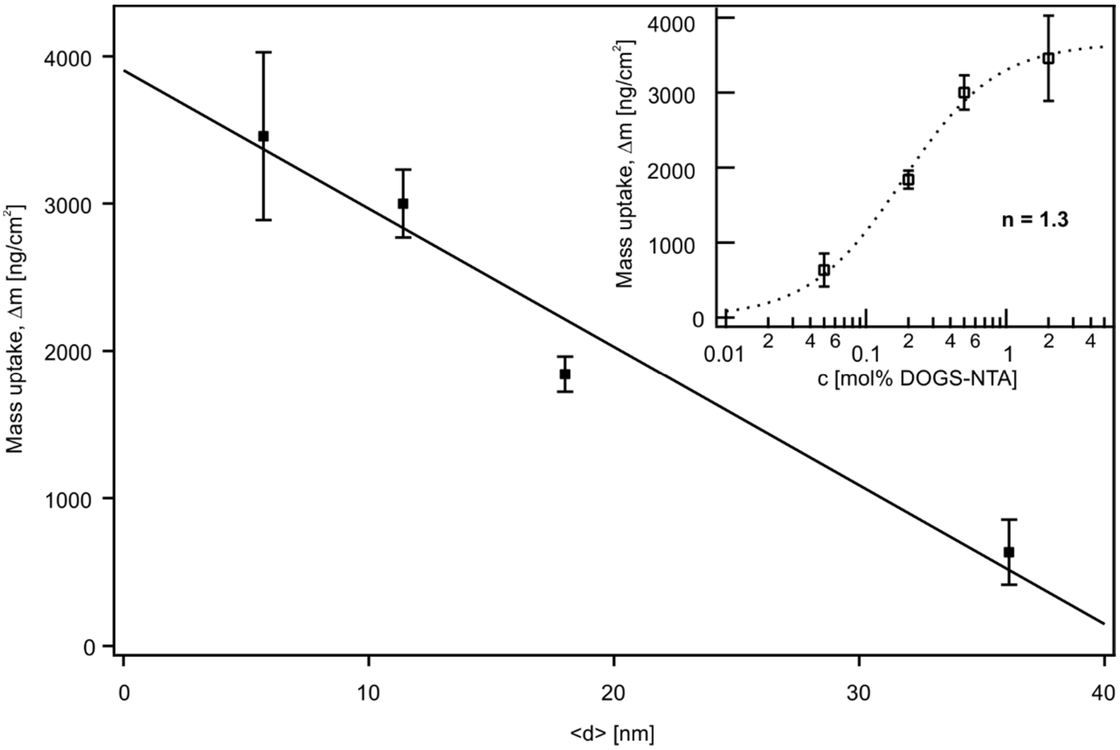

Figure 2.11 | Mass uptake by QCM sensor during the functionalization of supported membranes containing different molar concentration of DOGS-NTA with 450 nM N-cadherin. Determination of the mass uptake *Δm* as a function of the average intermolecular distance <$d_{N\text{-}cadherin}$> revealed a linear relationship (black line). The inset displays the mass uptake *Δm* as a function the molar fraction *x* of DOGS-NTA in the SOPC membrane. The dashed line represents the best fit according to the empirical Hill equation resulting in a 1:1 binding stoichiometry between His6-N-cadherin and the NTA-doped lipids as indicated by a Hill coefficient *n* ~ 1.

Finally, the dependency of the viscoelastic properties of the N-cadherin layer, η_f and μ_f, were investigated as a function of the ligand surface density. Figures 2.12A and B represent the shear elastic modulus μ_f and shear viscosity η_f as a function of the average intermolecular distance <$d_{N\text{-}cadherin}$>. Both values increased significantly at low <$d_{N\text{-}cadherin}$> which was accompanied to the increase in protein density on the membrane surface (d = 1020 kg/m^3 for <$d_{N\text{-}cadherin}$> ~ 36 nm up to d = 1150 kg/m^3 for <$d_{N\text{-}cadherin}$> ~ 6 nm). These values represent similar tendencies to those of hydrogel-like protein layers. In the study of Höök *et al.*, the crosslinking of a Mefp-1 layer with an antibody increased its density and caused a substantial increase of both viscoelastic properties, η_f and μ_f[99].

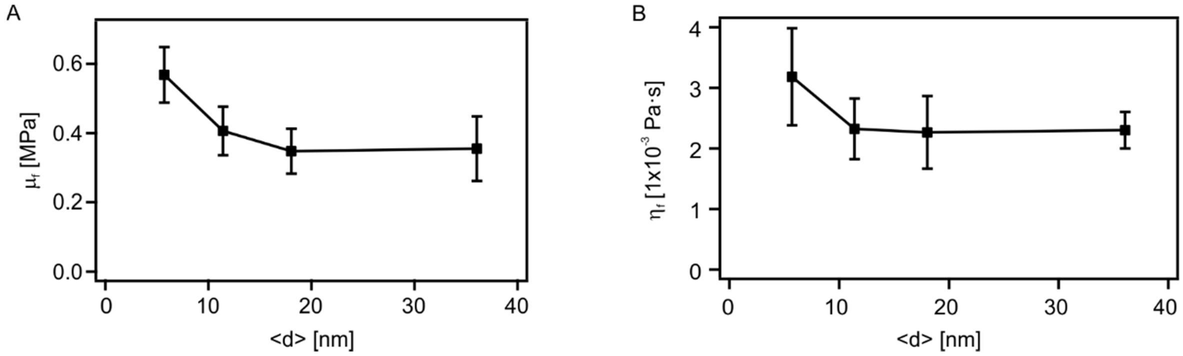

Figure 2.12 | Viscoelastic properties of the N-cadherin layer. (A) Shear elastic modulus μ_f and (B) shear viscosity η_f as a function of the average intermolecular distance $<d_{N\text{-}cadherin}>$.

2.2.4 SDF1α functionalized supported membranes

The successive functionalization of supported membranes with neutravidin and biotin-SDF1α was studied in order to determine (A) the mass uptake Δm depending on the average intermolecular distances $\langle d \rangle$ ($\langle d_{neutravidin/SDF1\alpha} \rangle$ ~ 4 – 36 nm; corresponding to $c_{biotin\text{-}DOPE}$ = 0.05 – 5.00 mol%;) and (B) the binding stoichiometry as already described for *in vitro* niche models displaying N-cadherin.

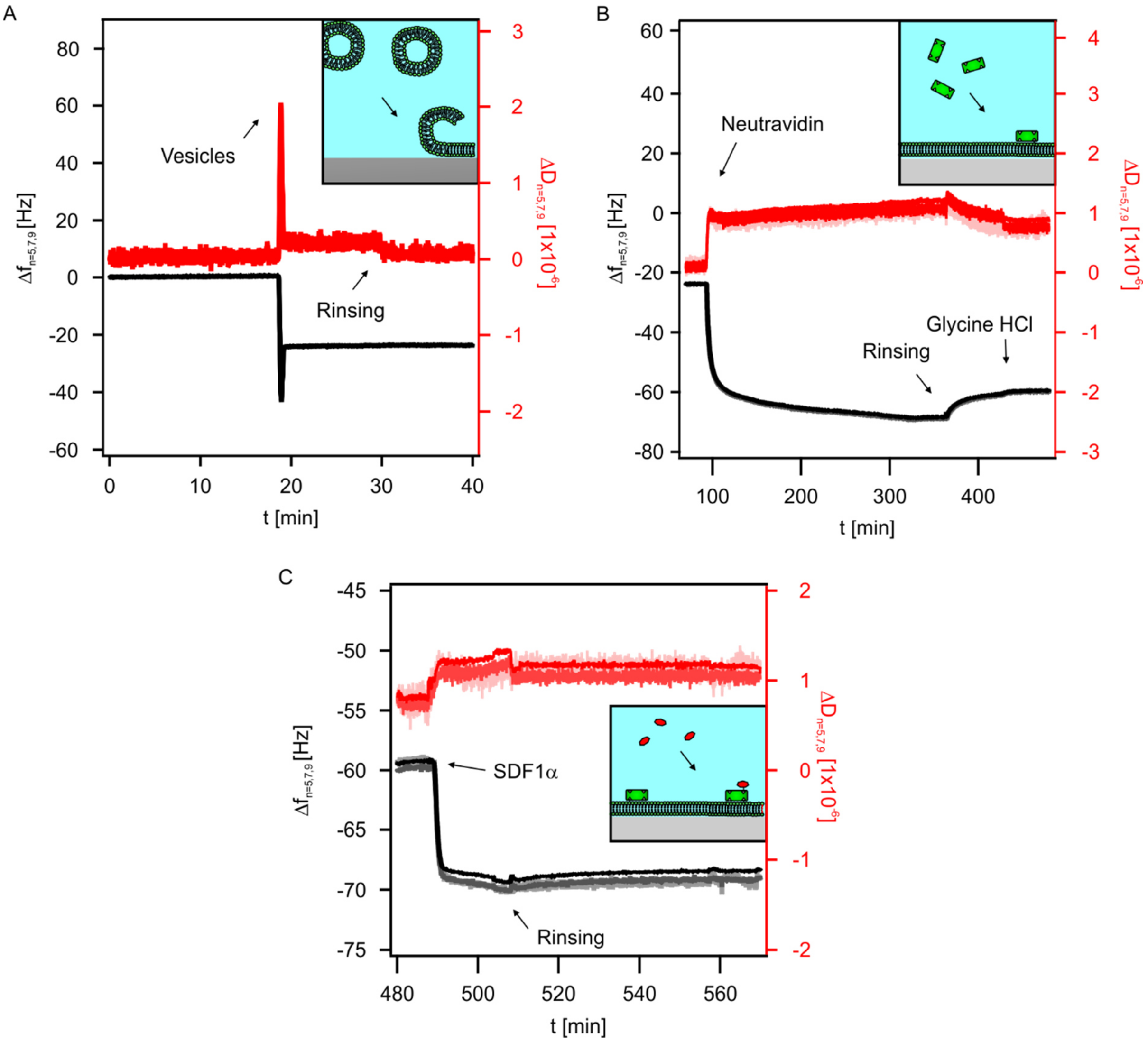

Figure 2.13 | Deposition of a supported membrane containing 0.5 mol% biotin-DOPE and successive functionalization with neutravidin and biotin-SDF1α. Changes in resonant frequencies Δf (light grey, grey, black) and dissipations ΔD (beige, light red, red) monitored at 35 MHz, during (A) formation of planar membrane consisting of 5 mol% biotin-DOPE in SOPC on SiO_2 substrates and the successive functionalization with (B) 83 nM neutravidin and (C) 1 µM biotin-SDF1α. The insets display a scheme of the corresponding deposition and functionalization step of the *in vitro* niche model.

Figure 2.13A displays changes in resonant frequencies Δf and dissipations ΔD monitored at 25, 35 and 45 MHz (n = 5, 7, 9), respectively, upon bilayer formation. The complete QCM-D data set is shown in the Appendix 7.2.2. The injection of phospholipid vesicles containing 0.5 mol% biotin-DOPE in SOPC caused a significant decrease of Δf (~-40 Hz) accompanied by an increase in ΔD (~ $2\cdot10^{-6}$) due to the adsorption of intact vesicles to the hydrophilic QCM sensor. Once, the critical density is reached, vesicles started to rupture and formed a stable, rigid bilayer as indicated by final frequency change $\Delta f_{n=7}$ = -25.5 Hz with a small $\Delta D_{n=7} = 0.2\cdot10^{-6}$. Thus, the QCM-D response was caused by a mass uptake of Δm = 460 ng/cm^2 due to bilayer formation, which was consistent with earlier reports[98, 100]. After a sufficient rinsing period to remove remaining vesicles, neutravidin solution (83 nM) was injected for t = 4 h (Fig. 2.13B). Thereafter, 100 mM glycine-HCl solution in Milli-Q-water (pH 2.5) was used to remove the electrostatically bound neutravidins[77]. The coupling resulted in a significant decrease of Δf (~-21 Hz) accompanied by an increase in ΔD (~ $2\cdot10^{-6}$) suggesting the formation of a rigid layer (Table 3.4). This finding was supported by the fact that all three overtones overlapped and did not show signs of viscoelasticity as it was found for N-cadherin layers. Thus, the mass uptake Δm could be calculated according to Sauerbrey equation (Equ. 2.2.2) and resulted in Δm = 378 ng/cm^2. Similar experiments on neutravidin coupling to supported phospholipid bilayer containing 5 mol% biotin-DOPE ($\langle d_{neutravidin} \rangle$ ~ 4 nm) performed by Wolny *et al.* resulted in changes of frequency and dissipation of Δf ~ -28 Hz and $\Delta D \sim 0.5\cdot10^{-6}$, respectively[100]. They used an extremely high concentration of 17 µM neutravidin which is 200 times higher compared to the present study in which the concentration of 83 nM was selected according to findings by Abuillan *et al.*. They reported the formation of a highly ordered neutravidin monolayer based on X-ray scattering by the use of a similar concentration. For control measurements, neutravidin was injected to a pure phospholipid membrane resulting in no remarkable change of both measures ($\Delta f_{n=7}$ = -0.2 Hz, $\Delta D_{n=7}$ = 0). Thus, any non-specific binding could be excluded. In a next step, 1 µM biotin-SDF1α was injected to the neutravidin functionalized supported membrane causing a decrease in frequency Δf ~ -6 Hz and an increase in dissipation of $\Delta D \sim 0.5\cdot10^{-6}$.

Table 2.4 | Changes in resonant frequency Δf and energy dissipation ΔD monitored at 35 MHz (n = 7), resultant from functionalization of a supported membrane containing different molar fractions of biotin-DOPE in SOPC with 83 nM neutravidin. Errors are given as standard deviation.

c [mol% biotin-DOPE in SOPC]	$\langle d_{neutravidin} \rangle$ [nm]	$\Delta f_{n=7}$ [Hz]	$\Delta D_{n=7}$ [$\cdot10^{-6}$]
0.05	36	-6.2 ± 0.4	0.9 ± 0.1
0.50	11	-21.0 ± 1.5	1.6 ± 0.2
1.00	8	-24.0 ± 1.8	1.2 ± 0.1
5.00	4	-38.2 ± 3.2	1.0 ± 0.7

The main advantage of QCM-D is the distinction of a second protein layer which was impossible by XRR. The corresponding mass uptake Δm was determined to be 114 ng/cm^2 as calculated according to Sauerbrey. It should be noted, that determinations of the protein layer thicknesses were avoided as their density was unknown. In other reports[98, 100], the layer density was assumed to be 1400 kg/m^3 which should results in an underestimation of the thickness as this is an average value for pure proteins[101]. In contrast to that, studies which were based on complementary methods such as surface plasmon resonance and QCM-D determined the layer density of proteins on a solid substrate to be close to the value of water ($\rho = 1000 - 1100$g/cm^3) due to high hydration[93]. There the layer density was obtained experimentally. In a next step, the current study was expanded to determine the mass uptake Δm as function of the average intermolecular distance of neutravidin molecules coupled to the supported membrane ($\langle d_{neutravidin} \rangle$ = 4 – 36 nm) and the corresponding different molar fractions of biotin-DOPE (x = 0.05 – 5.00 %). As it can be seen in Figure 2.14, the mass uptake Δm shows clearly a linear dependency on the $\langle d_{neutravidin} \rangle$ as indicated by the black line.

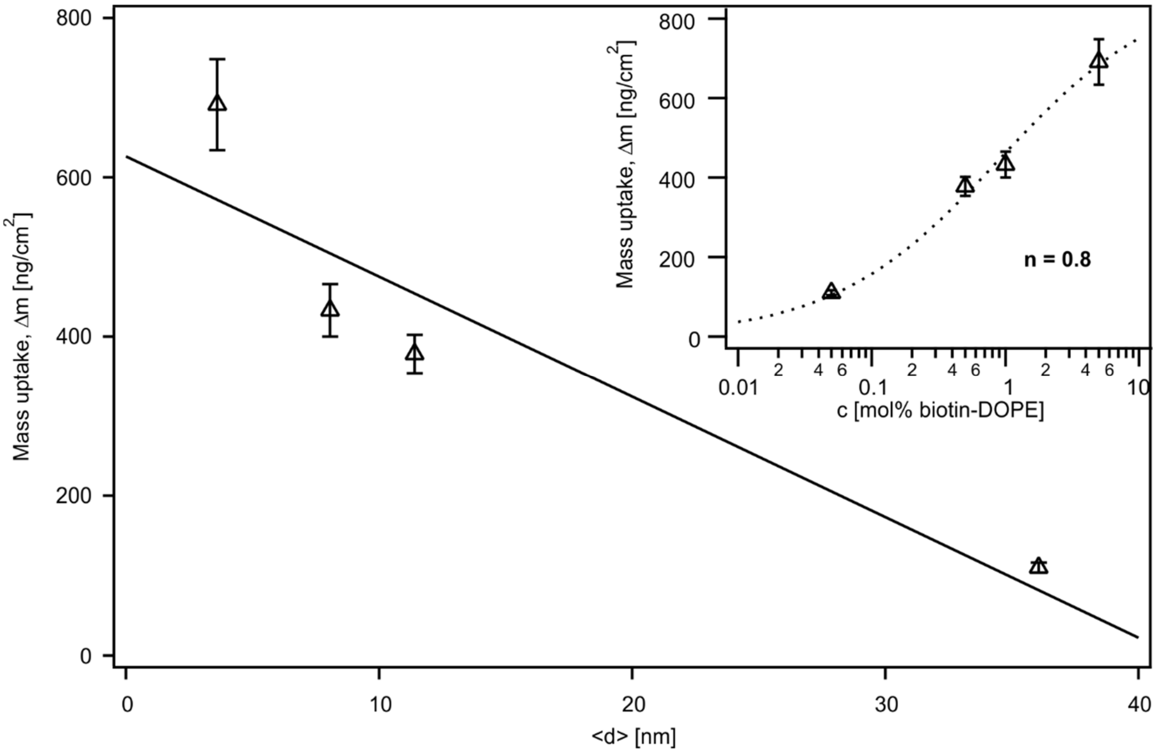

Figure 2.14 | Mass uptake by QCM sensor during the functionalization of supported membranes containing different molar fractions of biotin-DOPE with 83 nM neutravidin. Determination of the mass uptake Δm as a function of the average intermolecular distance $\langle d_{neutravidin} \rangle$ revealed a linear relationship (black line). The inset displays the mass uptake Δm as a function the molar fraction x of biotin-DOPE in the SOPC membrane. The dashed line represents the best fit according to the empirical Hill equation resulting in a 1:1 binding stoichiometry between neutravidin and biotin-DOPE as indicated by a Hill coefficient $n \sim 1$.

Table 2.5 | Changes in resonant frequency, *Δf*, and energy dissipation, *ΔD*, monitored at 35 MHz (n = 7), resultant from functionalization of a neutravidin functionalized phospholipid bilayer with 1 µM SDF1α.

c [mol% biotin-DOPE in SOPC]	$<d_{SDF1\alpha}>$ [nm]	$\Delta f_{n=7}$ [Hz]	$\Delta D_{n=7}$ [$\cdot 10^6$]
0.05	36	-1.0 ± 0.0	0.4 ± 0.1
0.50	11	-6.3 ± 1.0	0.5 ± 0.2
5.00	4	-9.5 ± 0.7	0.5 ± 0.2

The inset represents the mass uptake *Δm* as a function of the different molar fractions of biotin-DOPE (x = 0.05 – 5.00 %). The best fit according to the empirical Hill equation (dashed line) revealed a Hill coefficient n close to 1 indicating a binding stoichiometry of 1:1 between neutravidin and the biotin-tagged head groups although neutravidin exhibits four biotin binding sites[76]. Due to the two-dimensional geometry of planar supported membranes, two binding-sites are accessible as neutravidin was found to couple vial its long axis parallel to the surface[100]. Fukuto *et al.*[102] reported a surface density dependence of the binding stoichiometry. They provided a clear evidence for a binding stoichiometry of 1:1 for streptavidin to lipid monolayers at concentrations similar to those used in this study by utilizing X-ray scattering and Brewster angle microscopy.

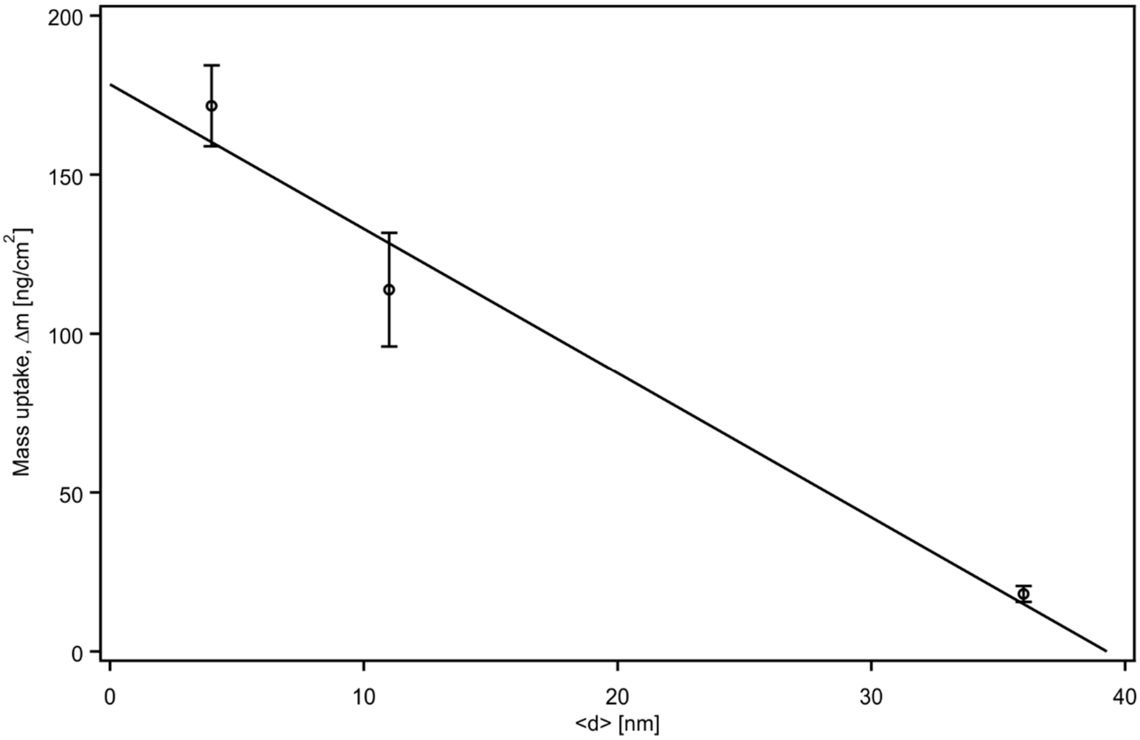

Figure 2.15 | Mass uptake by QCM sensor during the coupling of biotin-SDF1α (1 µM) to supported membranes functionalized with neutravidin. Determination of the mass uptake *Δm* as a function of the average intermolecular distance $<d_{SDF1\alpha}>$ revealed a linear relationship (black line).

Finally, similar considerations were made for the last functionalization step with biotin-SDF1α. Table 2.5 summarizes the changes in frequency Δf and dissipation ΔD monitored at 35 MHz (n = 7) caused by the coupling of biotin-SDF1α to neutravidin functionalized supported membranes at different molar ratios of biotin-DOPE in SOPC (x = 0.05 – 5.00 %). The mass uptake Δm linearly decreased when plotted as function of the $<d_{SDF1\alpha}>$ as depicted in Fig. 2.15. As the crystal structure of SDF1α revealed an almost globular structure with a mean diameter of 32 Å[78, 79], similar tendencies for the binding stoichiometry would be expected between SDF1α and neutravidin although neutravidin would have the capacity to bind two SDF1α molecules. Nevertheless, it was avoided to fit the data by the Hill equation as it was done for neutravidin due to fact that the SDF1α binding is only indirectly dependent on the molar concentration of biotin-DOPE in the supported membrane.

2.2.5 Summary

In this chapter, the deposition of supported membranes and their subsequent functionalization with ligand molecules such as N-cadherin and SDF1α was investigated by real-time detection with QCM-D. Special attention was paid to quantify the mass adsorption as a function of the surface density of ligand molecules in order to demonstrate the possibility to vary their average intermolecular distances $<d>$ dependent on composition of the supported membrane.

In case of pure supported membranes, no coupling of neither His6 N-cadherin nor Neutravidin/biotin-SDF1α occurred confirming specific coupling of the proteins. His6-N-cadherin was successfully anchored to supported membranes displaying NTA-tagged lipids. Variations of the molar fraction x of DOGS-NTA in SOPC, which is related to the average intermolecular distances $<d_{N\text{-}cadherin}>$, resulted in a linear dependency of the mass uptake Δm by the QCM sensor from $<d_{N\text{-}cadherin}>$. Furthermore, the QCM-D response revealed a $<d_{N\text{-}cadherin}>$-dependent change of both viscoelastic measures. In case of $<d_{N\text{-}cadherin}> \sim 6$ nm (x = 2 mol% biotin-DOPE), the elastic shear modulus and the shear viscosity were determined to be $\mu_f = 0.6$ MPa and $\eta_f = 3.2$ mPa·s, respectively. At lower average intermolecular distances, both values decreased by approximately 30 %. In contrast, neutravidin as well as SDF1α formed a rigid layer, after the successful coupling to the supported membrane displaying biotin-tagged lipids resulting in mass uptake which decrease linear with increasing $<d_{N\text{-}cadherin}>$. Finally, the data for N-cadherin and neutravidin coupling revealed a binding stoichiometry of 1:1. The obtained results demonstrated the successful fabrication of both *in vitro* niche models.

3. Adhesion and Dynamics of Human Hematopoietic Stem and Progenitor Cells

3.1 Materials and experimental techniques

This chapter comprises a detailed summary of all materials and experimental techniques which were applied for experiments with HSPC in this work. It lists all buffer systems, phospholipids and proteins which were necessary for the preparation of the *in vitro* niche models. The method section includes descriptions of the basic procedures including vesicle preparation, deposition of supported membranes and their functionalization with proteins. The isolation of HSPC from CB and PB as well as LB cells is described. Finally, the experimental procedure for HSPC adhesion, migration studies and cell viability tests is outlined. Detailed descriptions of the main techniques used for adhesion and migration studies (e.g. RICM, pressure wave assay) follow in the topic-specific sub-chapters.

3.1.1 Buffers

All aqueous solutions were prepared with ultrapure water (Millipore, Molsheim, France) with a resistivity $R > 18$ MΩcm^{-1}. As most experimental techniques used for this work need a buffered, aqueous environment, the following buffer solutions were prepared:

HBS – buffer:
10 mM 4-(2-hydroxyethyl)-1-piperazineethanesulfonic acid (HEPES, Karl Roth, Karlsruhe, Germany) and 150 mM sodium chloride (NaCl, Karl Roth, Karlsruhe, Germany), pH 7.5.

Ni^{2+} - buffer:
5 mM nickel(II)chloride ($NiCl_2$, Karl Roth, Karlsruhe, Germany), 10 mM 4-(2-hydroxyethyl)-1-piperazineethanesulfonic acid (HEPES, Karl Roth, Karlsruhe, Germany) and 150 mM sodium chloride (NaCl, Karl Roth, Karlsruhe, Germany), pH 7.5.

Ca^{2+} - buffer:
1 mM calcium(II)chloride ($CaCl_2$, Karl Roth, Karlsruhe, Germany), 10 mM 4-(2-hydroxyethyl)-1-piperazineethanesulfonic acid (HEPES, Karl Roth, Karlsruhe, Germany) and 150 mM sodium chloride (NaCl, Karl Roth, Karlsruhe, Germany), pH 7.5.

3.1.2 Lipids and proteins

1-stearoyl-2-oleoyl-*sn*-glycero-3-phosphocholine (SOPC, Fig. 3.1A), 1,2-dioleoyl-*sn*-glycero-3-[(N-(5-amino-1-carboxypentyl)iminodiacetic acid) succinyl] (nickel salt) (DOGS-NTA (Ni^{2+}), Fig. 3.1B) and 1,2-dioleoyl-*sn*-glycero-phospho-ethanolamine-3-N-(cap biotinyl) (biotin-DOPE, Fig. 3.1C) were purchased from Avanti Polar Lipids (Alabaster, USA).

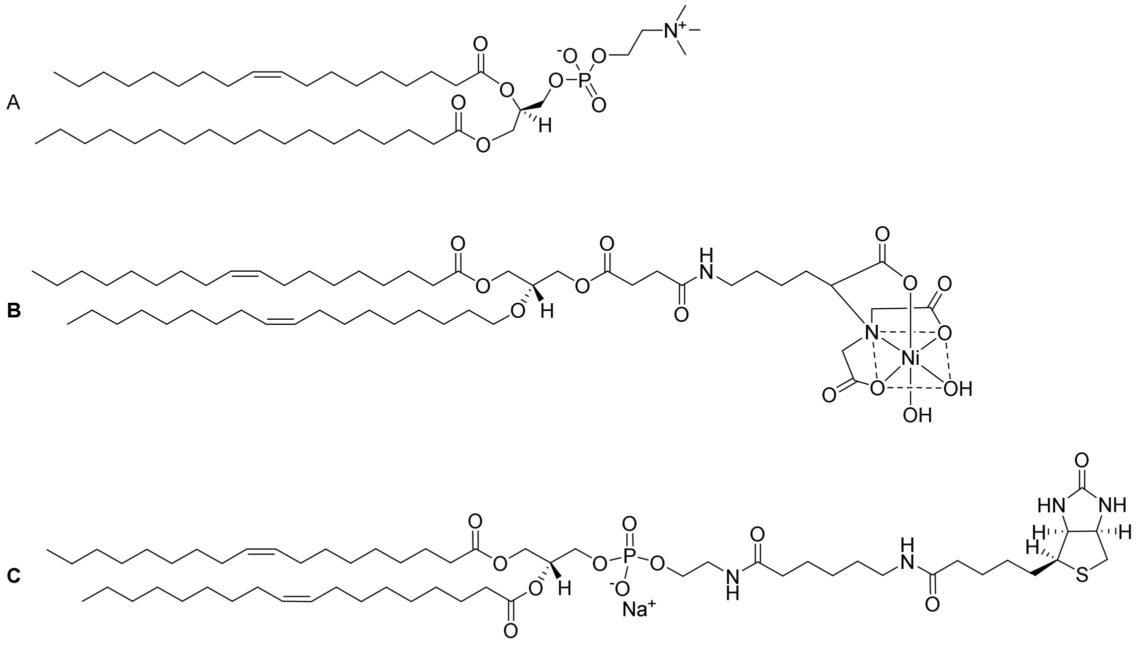

Figure 3.1: Synthetic phospholipids. Solid-supported membranes are prepared with SOPC (A) as matrix lipid and either DOGS-NTA (Ni^{2+}-salt) (B) or biotin-DOPE (C) as lipid anchors in different molar concentrations.

Neutravidin (Life Technologies GmbH, Darmstadt, Germany) was purified by ultracentrifugation to remove protein clusters prior membrane functionalization. Recombinant stromal cell-derived factor-1α (SDF1α) with and without biotin tags and human N-cadherin with histidine tag with 6 repetitions (His6-N-cadherin) were purchased from Almac Group (Craigavon, UK) and R&D Systems Inc. (Wiesbaden, Germany), respectively. For all cell experiments, Iscove's Modified Dulbecco's Media from Life Technologies was used.

3.1.3 Substrates and liquid chambers

Unless otherwise mentioned, all substrates were cleaned by a modified RCA protocol[62]. Therefore, substrates were sonicated in acetone, ethanol, methanol and water for 3 min, subsequently. Then, they were immersed in a solution of 1:1:5 (v/v/v)

H_2O_2(30%)/NH_4OH(25%)/H_2O and sonicated at room temperature for 3 min, before soaking them at 60 °C for another 30 min. Thereafter, substrates were rinsed intensively with ultrapure water, dried at 70 °C and stored in a vacuum chamber at room temperature. For high-energy specular X-ray reflectivity experiments, a silicon wafer with native oxide (Si(100), 8 x 23 mm^2, SiMat, Landsberg am Lech, Germany) was placed into a self-built liquid chamber. Prior the measurements, the liquid chamber was cleaned by sonication for 30 min at 60 °C in a 2 % aqueous solution of Hellmanex II (Hellma, Müllheim, Germany). Afterwards, the cleaned liquid chamber was rinsed intensively with ultrapure water and dried using a stream of nitrogen gas. Cell incubation chambers for RICM and time-lapse imaging were prepared by sealing microscopic grade 256 × 75 mm^2 glass slides from Gerhard Menzel GmbH (Braunschweig, Germany) to bottomless plastic fluidic channels (μ-Slide $VI^{0.4}$) from Ibidi (Martinsried, Germany). For picosecond laser pulse detachment assays, round microscopic grade glass slides with a diameter of 28 mm from Gerhard Menzel GmbH were bonded to bottomless culture dishes from Ibidi. Polydimethylsiloxane produced from base and curing agent (SYLGARD184, Dow Corning Co., USA) served as bonding agent for both chambers.

3.1.4 Vesicle preparation

Stock solutions of phospholipids in $CHCl_3$ (1 or 5 mg/mL) were mixed to obtain the desired concentration of either DOGS-NTA (Ni^{2+}) or biotin-DOPE in SOPC. After evaporation of $CHCl_3$ under a gentle nitrogen stream and storage under vacuum overnight, the lipids were re-suspended in HBS and sonicated with a titanium microtip sonicator S3000 (Misonix Inc., Farmingdale, USA) for 30 min to obtain small unilamellar vesicles (SUVs). To remove any residual titanium particles, vesicle suspensions were centrifuged (Eppendorf, Hamburg, Germany) for 10 min at 13400g. Thereafter, SUV suspensions (0.5 mg/mL) were stored at 4 °C.

3.1.5 Deposition of supported membranes

Solid-supported membranes were prepared by vesicle fusion. Specifically, SUV suspensions were injected onto the substrates and incubated for 30 min at 40 °C, followed by intensively rinsing with HBS buffer (150 mM NaCl, 10 mM Hepes, pH 7.5) to remove excess SUVs.

3.1.6 Functionalization of supported membranes with ligands

Supported membranes doped with DOGS-NTA (Ni^{2+}) were incubated with nickel buffer (1 mM $NiCl_2 \cdot 6H_2O$, 150 mM NaCl, 10 mM Hepes, pH 7.5) for 45 min to saturate the nickel chelating nitrilotriacetic acid (NTA) head groups. The buffer was exchanged to calcium buffer (1 mM $CaCl_2 \cdot 2H_2O$, 150 mM NaCl, 10 mM Hepes, pH 7.5), then human recombinant His6 N-cadherin was added (10 µg/mL) and incubated for 12 h at room temperature. For the immobilization of SDF1α, supported membranes doped with biotin-DOPE were incubated with neutravidin solution (40 µg/mL) for 2 h at room temperature. After removing the neutravidin, biotinylated SDF1α (10 µg/mL) was added. Since the anchor lipids are monomerly incorporated into the matrix lipids, the average lateral distance between lipid anchors $<d>$ and thus proteins can be estimated from the molar fraction x of lipid anchors by inserting the value of the lipid area of $A_{\text{lipid}} \sim 65$ Å^2 [55, 103] in the following equation:

$$< d > = \sqrt{\frac{A_{lipid}}{x}} \,. \tag{3.1.1}$$

In vitro niche models displaying SDF1α and N-cadherin at $<d> \sim 13$ nm were prepared by the deposition of supported membranes doped with 0.4 mol% head group modified lipids containing different proportions of DOGS-NTA (Ni^{2+}) and biotin-DOPE [0.4 : 0.0 mol%, 0.32 : 0.08 mol%, 0.2 : 0.2 mol%, 0.08 : 0.32 mol%, 0.0 : 0.4 mol% of DOGS-NTA (Ni^{2+}) : biotin-DOPE in SOPC]. In a first step, supported membranes were functionalized with N-cadherin followed by the successive functionalization with neutravidin and SDF1α as described above. Finally, excess proteins were removed by rinsing extensively with cell culture medium prior to the cell adhesion experiments, and the samples were equilibrated at 37 °C.

3.1.7 Isolation of hematopoietic stem and progenitor cells

All samples of primary cells were collected from voluntary donors after obtaining informed consent using guidelines approved by the Ethics Committee on the Use of Human Subjects at Heidelberg University. Human HSPC ($CD34^+$ cells) were derived from umbilical cord blood (CB) or from healthy allogeneic stem cell donors. The latter had received a mobilization regimen with G-CSF (10 µg/kg bw per day subcutaneously for 5 days) and a sample of 60 ml of peripheral blood (PB) was taken for this study prior to leukapheresis. Mononuclear cells (MNCs) were isolated by density gradient centrifugation using the Ficoll–

Hypaque technique (Merck KGaA, Darmstadt, Germany). CD34$^+$ cells from the MNC fraction were enriched by labelling with magnetic microbeads and sorted twice using an affinity column with the AutoMACS system (all Miltenyi Biotec GmbH, Bergisch-Gladbach, Germany). The cells were allowed to rest for at least 2 hours at 37 °C and 5% CO2 before further use and were stored in long-term bone marrow culture (LT-BMC) medium, a basal HSPC culture medium described by Dexter *et al.* consisting of 75% Iscove's modified Dulbecco's medium (IMDM; Life Technologies Inc., Carlsbad, USA), 12.5% FCS, 12.5% horse serum (both Stemcell Technologies Inc., Vancouver, Canada), 2 mM L-glutamine, 100 U/ml penicillin/streptomycin (Life Technologies) and 0.05% hydrocortisone 100 (Sigma–Aldrich Co., St. Louis, USA)[104]. Staining with propidium iodide was performed to exclude non-viable cells. Reanalysis of the isolated cells by flow cytometry revealed a purity of > 95% CD34$^+$ cells.

3.1.8 Isolation of leukemic blasts

CD34$^+$ leukemic blasts (LB) were collected from a patient with newly diagnosed acute myeloid leukemia (AML) after obtaining informed consent using guidelines approved by the Ethics Committee on the Use of Human Subjects at Heidelberg University. LB from PB were isolated as described above for HSPC from CB. After the isolation, the cells were stored in liquid nitrogen at 77 K.

3.1.9 Cell adhesion and migration measurements

HSPC cell sample in LT-BMC was separated, one portion was supplemented with dissolved SDF1α (5 ng/mL) and both samples were pre incubated for 2 h at 37 °C and 5 % CO_2. Before cell adhesion and migration experiments, culture medium was exchanged to pre-warmed IMDM and cells were seeded at a density of 1 × 105 cells/cm^2 into cell incubation chambers in the absence and presence of dissolved SDF1α (5 ng/mL). Cell adhesion and migration experiments were conducted at 37 °C in μ-slides VI$^{0.4}$ from Ibidi.

3.1.10 Cell viability and apoptosis test

The viability of HSPC was assessed before seeding and after 2 h and 4 h of seeding HSPC on the *in vitro* niche model by performing a dye exclusion test using the diazo dye trypan blue. Additionally, cells were stained using Annexin V for apoptosis. In both cases and for all time points a cell viability of ~ 90 % was obtained, which did not change during the time period of the experiments.

3.1.11 Statistics

The underlying number of experiments per data point corresponds to three experiments. In summary, the fraction of adhered cells χ, the adhesion area A_{Adh} and the critical pressure for cell detachment P^* were calculated for a total number of 50 cells per data point and data included in the corresponding figures represent means $\pm$ standard deviation. Data characterizing the morphological dynamics of HSPC, comprise a total number of 30 cells per data point and represent means $\pm$ standard deviation of the mean.

3.2 Quantitative analysis of cell adhesion and morphological dynamics

3.2.1 Quantification of cell adhesion by microinterferometry

3.2.1.1 Theoretical background

Adhesion plays an important role in immune response[105], embryological development[106] and cell differentiation[55] and is based on the binding between two cells through the formation of homophilic or heterophilic ligand-receptor pairs. In case of HSPC, the adhesion of cells to the bone marrow niche is an important aspect for the maintenance of the stem cell pool. As the direct assessment of cell adhesion *in vivo* is rather complicated, *in vitro* investigations by the use of a suitable model system in combination with an appropriate technique allows to clarify important mechanistic questions.

Physics of cell adhesion

Based on the classical description of cell adhesion, which was formulated by Bell, Dembo and Bongrand in 1984, the adhesion process is controlled by a competition of different forces caused by generic and specific interactions (Fig. 3.2)[107]. A further refinement of this theory was developed by Bruinsma, Behrisch and Sackmann in 2000 by interpreting the adhesion in terms of a double-well intermembrane potential[108]. In detail, a balance of short range attractive forces, medium range repellant forces and the elastic stresses due to the deformation of the cell membrane leads to the formation of an adhesion area A_{Adh}, which is dependent on the type of ligand-receptor pair but also on intrinsic properties of the cell (e.g. mechanical properties of the cell membrane, glycocalix)[107, 109, 110]. The elastic free energy of adhesion ΔG_{Adh} for an elastic shell such as biological cells can be expressed as

$$\Delta G_{Adh} \sim \omega A_c + \int \left[\frac{\kappa}{2}(\nabla^2 h(x))^2 + \frac{\sigma}{2}(\nabla h(x))^2 + V(h(x))\right] dx\,, \tag{3.2.1}$$

which consists of the following terms[108, 111, 112]: The first term describes the free energy of adhesion due to the formation of specific ligand-receptor pairs (specific interactions) and is based on the product of the binding energy per unit area ω and the contact area A_c where the bond is located. The second term arises from the Helfrich repulsion and is a consequence of the thermal excitation of bending undulation (bending modulus $\kappa \sim 25\ k_BT$) as given by

$$V_{und}(h(x)) = \frac{(k_BT)^2}{\kappa h^2}\,. \tag{3.2.2}$$

The required freezing of the membrane fluctuations is entropically unfavorable, which counteracts the adhesion process. The third term describes the membrane tension[113]. The last term (generic interactions) accounts for the intermembrane potential energy per unit area $V(h(x))$ and consists of

$$V(h(x)) \cong V_{hyd}(h(x)) + V_{vdW}(h(x)) + V_{rep}(h(x))\,. \tag{3.2.3}$$

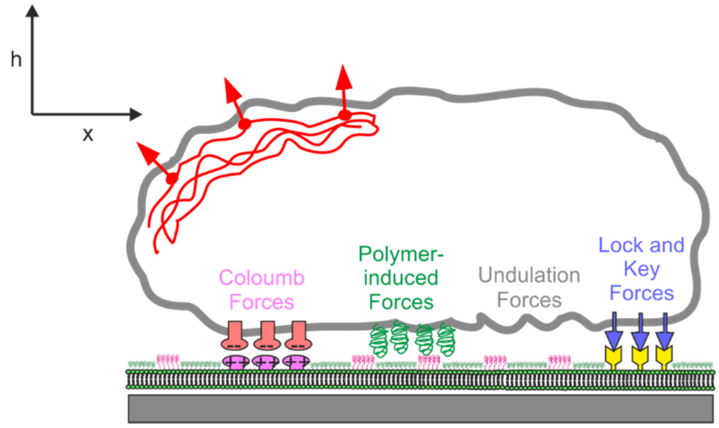

Figure 3.2 | Cell adhesion is controlled by a complex interplay of specific and generic forces. Schematic illustration of the interaction of a cell with an *in vitro* model mimicking the surface of a target cell. Specific forces are induced by the binding of ligand-receptor pairs. Generic forces comprise repulsive undulation forces due to thermally activated bending undulations of the cell membrane, electrostatic interactions between for example charged glycoproteins (Coulomb forces), polymer-induced forces caused by steric repulsion of molecules of the ECM and attractive van-der-Waals interactions.

The short-range steric repulsion V_{hyd} can be represented as

$$V_{hyd}\big(h(x)\big) = V_0 e^{-h/\lambda}\,, \tag{3.2.4}$$

with V_0 and the characteristic decay length λ in the range of <30 mJ·m^{-2} and 1 nm, respectively. The second term describes the van der Waals (vdW) interactions between induced or permanent dipoles of two layers and is given by

$$V_{vdW}\big(h(x)\big) = -\frac{H_A}{12\pi}\left(\frac{1}{(h+2\delta)^2} + \frac{1}{(h)^2} - \frac{1}{(h+\delta)^2}\right), \tag{3.2.5}$$

where H_A corresponds to the Hamaker constant (~ 10^{-21} J for pure membranes). Biopolymers of the glycocalix act as repellers and can be described as a neutral polymer with a radius of gyration R_g. The repeller-induced steric repulsion can be approximated by

$$V_{rep}\big(h(x)\big) \cong \begin{cases} \frac{\pi}{6} k_B T \sigma_0 \left(\frac{R_g}{h(x)}\right)^2 e^{-1.5(h/R_g)^2}, & h \gg R_g\,, \\ k_B T \sigma_0\,, \ h \ll R_g\,, \end{cases} \tag{3.2.6}$$

where σ_0 corresponds to the lateral density of repeller molecules.

This generic potential $V(h(x))$ can be approximated by a harmonic form as given by

$$V(h(x)) \cong V_0 + \frac{1}{2}\gamma(h-h_0)^2\,, \tag{3.2.7}$$

where γ represents the curvature at the equilibrium position $h = h_0$[108, 112].

Reflection interference contrast microscopy

For the quantification of cell adhesion, it is desirable to investigate living cells in their natural environment (e.g. label-free, non-invasive). A prominent choice for this purpose is reflection interference contrast microscopy (RICM), which is a microinterferometry technique enabling the detection of the adhesion area by analyzing the contour of the adherent cell near the substrate surface[114, 115]. The principle of RICM is based on detection of interference patterns, which arise from light reflections at interfaces with different refractive indices. For example, in case of a system with two interfaces, the reflected intensity I under quasi-normal incidence is given by[116]

$$I = I_1 + I_2 + 2\sqrt{I_1 I_2}\cos[2kh(x,y) + \phi] \tag{3.2.8}$$

with $k = 2\pi n_1/\lambda$ and the phase shift ϕ. *h(x,y)* corresponds to the distance which separates the two interfaces at the lateral position *(x,y)*. I_1 and I_2 represents the reflected intensity at interface 1 and 2, respectively. Thus, recording of the reflected intensity I is a direct probe of the separation distance between the interfaces which allows for the detection of adhesion area. Beside the analysis of the adhesion area, this method can be applied additionally to investigate wetting phenomena, the formation of ligand-receptor domains, and to quantify the underlying forces. The application of RICM in cell adhesion experiments was firstly demonstrated by Abercrombie and Ambrose in 1958 and Curtis in 1964. Sackmann and co-workers further developed this technique to gain quantitative results in the 1980s[117]. Nowadays, the newest RICM setups even enable the determination of absolute heights of cells on a substrate[118].

RICM instrumental setup

The RICM setup consists of an inverted microscope equipped with an oil-immersion antiflex objective and a partial incoherent, monochromatic light source (Fig. 3.3A). The presence of an aperture and field diaphragm and a collector lense allows for Köhler illumination[114]. The development of the antiflex technique[119] by Ploem in 1975 led to a drastical improvement of the image quality and is based on the insertion of three additional components in the light path compared to a standard setup of an inverted microscope: A polarizer, a λ/4-plate and an analyzer. Due to the additional components, linear polarized light with a preferred direction is first filtered, and then circular polarized by the built-in λ/4-plate of the objective. The reflection of the light at interfaces with different refractive indices causes a phase shift of π of the two electrical field components (perpendicular and parallel) of the circular polarized light which is then converted into linearly polarized light after passing through the λ/4-plate. Due to the insertion of an analyzer, only the reflected light with a linear polarization state is detected by the camera by a simultaneous reduction of stray light intensity resulting in a high contrast. Additional prerequisites for the visibility of interference patterns are sufficient temporal and spatial resolution which are given by a monochromatic, partial incoherent light source. Temporal coherence describes the correlation between rays observed at different time points. In RICM, a metal halide lamp in combination with an interference filter emits a quasi-monochromatic light with a wavelength distribution of λ = 546 ± 10 nm. Thus, a high temporal coherence is given. Spatial coherence is based on the correlation between rays at different points in space. The spatial coherence length for a metal halide lamp corresponds approximately to 200 µm which exceeds the measured distances in this method. Consequently, spatial coherence is sufficient but due to the finite extension of the light source, full spatial resolution cannot be achieved.

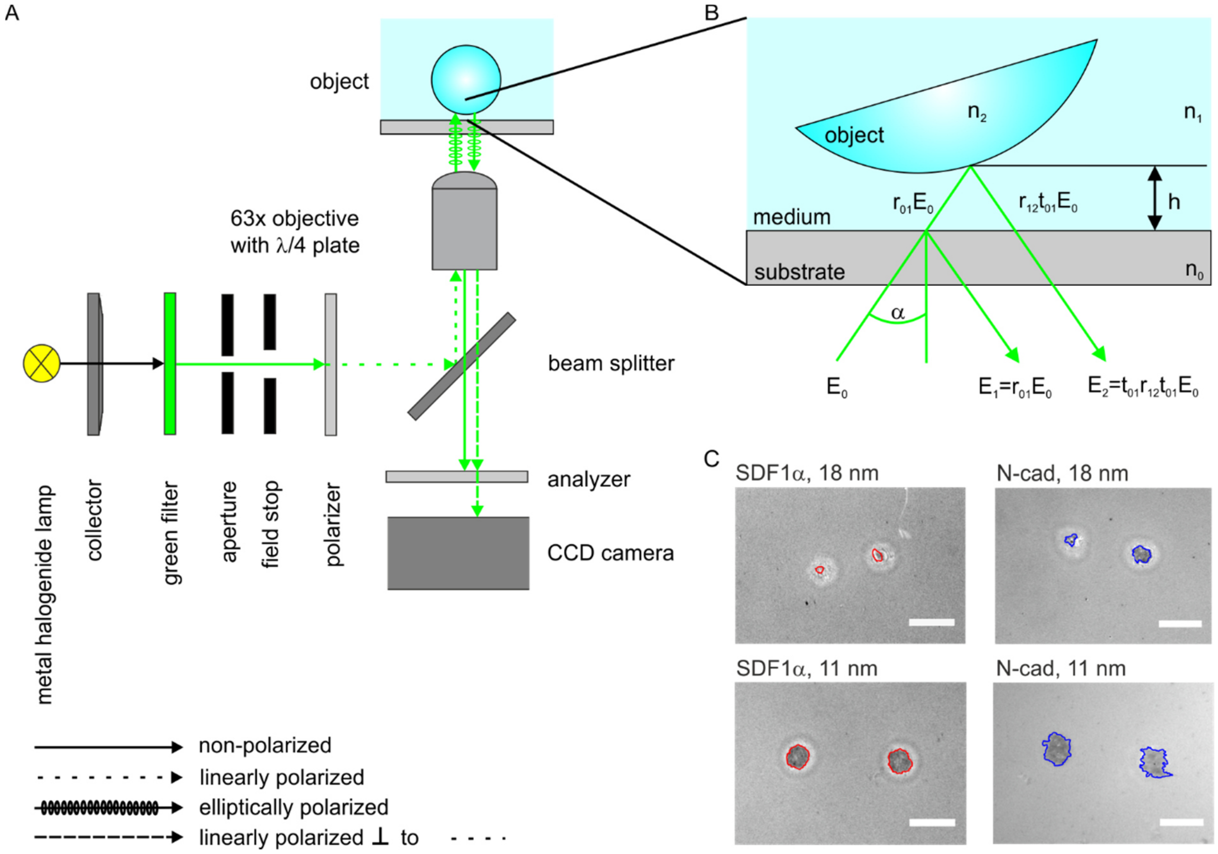

Figure 3.3 | Typical experimental setup of a RIC microscope and image formation in microinterferometry. The main components of the optical path include a bandpass filter ($\lambda = 546 \pm 10$ nm), two adjustable diaphragms, a polarizer, an analyzer and a 63x objective with built-in $\lambda/4$ plate (A). This setup allows for Köhler illumination under quasi-normal incidence of light. Monochromatic incident rays are reflected at interfaces with different refractive indices and can interfere constructively and destructively leading to the formation of Newton fringes (B). The adhesion area of HSPC on membranes displaying N-cadherin and SDF1α at different average intermolecular distances can be distinguished from non-adhered parts of the cell (C).

As the light source is considered as point source, the illuminated area has different degrees of coherence. Full spatial coherence occurs at an illumination area with a diameter *d* of

$$d \leq \frac{0.16\lambda}{n\sin(\alpha)}. \tag{3.2.9}$$

At larger diameters, only partial coherence is achieved which has to be taken into account during image analysis. The size of the light source plays also an important role and can be tuned by the aperture of the microscopy setup (Fig. 3.3A). A different opening of the aperture diaphragm results in an interplay between lateral resolution vs. focus depth. In case of an opened aperture diaphragm, the illumination aperture INA,

$$INA = n\sin(\alpha), \tag{3.2.10}$$

is increased resulting in a high lateral resolution with a limited depth in focus.

Image formation

The image formation relies on the detection of interference patterns formed by constructive and destructive interferences of reflected rays due to their differences in the optical path lengths *Δ*. Subsequently, contrast variations of the recorded image refers to differences in the sample height (*h* ~ in the order of nm). Typical patterns from various objects are depicted in Fig. 3.4[116]. Dark and bright rings correspond to minimal and maximal intensity, subsequently, and are referred to Newton rings. The mathematical description of image formation in RICM was described by Wiegand *et al.*[120]*.* The intensity of the incident light experiences multiple reflections and refraction at interfaces of layers with different refractive indices *n*. The reflected intensity *I(x,y)* corresponds to the average of the squared electric field *E(r,t)* and is related to the phase *Φ(r)* as given by

$$I(x,y) = \langle E^2 \rangle_t \,, \tag{3.2.11}$$

$$E(r,t) = E(r,t) \cdot e^{[i(\Phi(r)+\omega t)]} \,. \tag{3.2.12}$$

The electric field vector E_r includes the sum of all electric field vectors, $E_r = \sum_i E_{r,i}$, of the reflected light at different layers of the specimen (Fig. 3.3B) and can be expressed a function of the electric field vector E_o of the incident light.

$$E_r = r_{01}E_0 + (1 - r_{01}^2) r_{12} E_0 \, e^{(-ik\Delta_1)} + \cdots + \tag{3.2.13}$$

$$= RE_0 \,, \tag{3.2.14}$$

r_{ij} corresponds to the reflection coefficient which relies on the Fresnel coefficients r_{ij}^p and r_{ij}^s which establish a connection to the refractive indices of the successive layers n_i and n_j and the angle of incidence α as given by

$$r_{ij}^p(\alpha) = \frac{n_j \cos\alpha_i - n_i \cos\alpha_j}{n_j \cos\alpha_i + n_i \cos\alpha_j} \,, \tag{3.2.15}$$

$$r_{ij}^s(\alpha) = \frac{n_i \cos\alpha_i - n_j \cos\alpha_j}{n_i \cos\alpha_i + n_j \cos\alpha_j} \,. \tag{3.2.16}$$

p and *s* denote the polarization of the reflected wave parallel or perpendicular to the plane of incidence, respectively. The transmission coefficient, t_{ij}, is described by the following equation:

$$t_{ij} = \sqrt{1 - r_{ij}^2}\,. \tag{3.2.17}$$

The phase shift caused by the reflection of light at layer *i* is a product of the wave number $k = 2\pi/\lambda$ and the optical path length *Δ*. The resulting reflection coefficients of all interfaces can be summarized to an effective reflection coefficient *R*, which is expressed by

$$R = r_{01} + \sum_{i=1}^{m} \left[\prod_{s=1}^{i} \left(1 - {r_{s-1,s}}^2\right) \exp(-ik\Delta_s) \right] r_{i,i+1}\,, \tag{3.2.18}$$

$$I(x,y) = R^* R E_0^2 = R^* R I_0\,, \tag{3.2.19}$$

where *m* corresponds to the number of layers. This assumption is only valid if multiple reflections are small and negligible. The optical path length Δ_i of the reflected ray traversing layer *i* is given by

$$\Delta_i = 2 n_i d_i(x,y)\,, \tag{3.2.20}$$

where *$d_i(x,y)$* represents the thickness of layer *i* at its position *(x,y).*

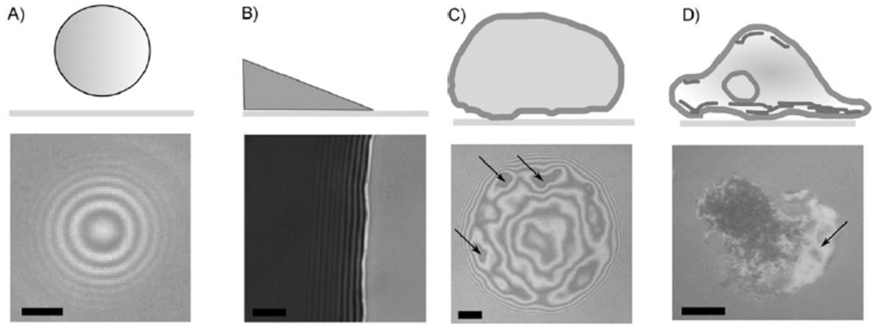

Figure 3.4 Typical samples and their RICM pattern The figure displays RICM pattern of (A) a sphere above a glass substrate, (B) a layer coated on glass substrate, (C) a vesicle with unspecific binding to a substrate and (D) an adherent cell (adopted from Sengupta *et al.*[116]).

Cell-mimetic in vitro model systems

Self-assembled phospholipid membranes on solid support (supported membranes), which are functionalized with proteins or carbohydrates are ideal models of cell surfaces[47, 92]. These cell mimetic systems can be utilized to study the adhesion and migration of cells with various techniques which require a two-dimensional surface (e.g. microscopy). They consist of a phospholipid bilayer including different molar fractions *x* of head group modified lipids which allow for the anchoring of ligands (e.g. proteins, polysaccharides) at defined average intermolecular distances <*d*>, as given by

$$< d > = \sqrt{\frac{A_{lipid}}{x}}, \tag{3.2.21}$$

where $A_{lipid} = 65$ Å^2 corresponds to the molecular area of single phospholipid[55, 103].

A few studies have utilized these cell mimetic systems in the past to study cell adhesion. Brian and McConnell utilized supported membrane for allogeneic stimulation of cytotoxic T cells in 1984[121]. The adhesion of leukocytes in immunological and inflammatory reactions based on intercellular adhesion molecule-1 (ICAM-1) and lymphocyte function-associated antigen-1 (LFA-1) was investigated using supporting membranes[122]. Furthermore, the adhesion of lymphocytes to endothelial cells via similar interactions was studied by Dustin and Springer in 1988[123]. These early studies opened up new possibilities to study cellular behavior *in vitro*[55, 124-126]. Nevertheless disadvantages arise from the close proximity between the lipid bilayer and the underlying substrate leading to the denaturation of transmembrane proteins. Thus, further developments were made by introducing polymer supported membranes[47]. By mimicking the generic role of the extracellular matrix with a thin polymer layer, the membrane is separated from the substrate reducing the frictional coupling between transmembrane proteins and the solid support[46]. Phospholipid membranes can be deposited on a solid substrate via vesicle fusion[105, 121]. The coupling of desired ligands (e.g. proteins, polysaccharides) is achieved by the use of molecules which comprise a functional group with a high affinity to head group modified lipids. Recombinant or synthetic proteins are usually modified with either a polyhistidine tag (His-tag) or a biotin group and can be directly coupled to the supported membrane or via linker proteins such as biotin-binding proteins (Fig. 3.5). Biotin binding proteins such as avidin and its analogues neutravidin and streptavidin have four biotin binding pockets. Avidin is a glycoprotein with a molecular weight of 66 kDa and was isolated from egg white of chickens by Snell in 1941[127]. Its quartiary structure consists of eight β-strands including four biotin binding pockets[128]. The avidin-biotin interaction is the strongest non-covalent biological bond with a Gibbs-free energy of 35 k_BT and a K_d of 10^{-15} M[129]. Polyhistidine-tagged proteins can be coupled by incorporating nickel-chelating lipids into the supported membrane[130, 131]. The reversibility of this coupling can be triggered by competitors (e.g. histidine, imidazole), by shifting the pH value, or by loading or unloading the chelate complex[132]. In contrast to the avidin-biotin interaction, the coupling of polyhistidine-tagged proteins to the supported membrane has a Kd of 10^{-7} M[131].

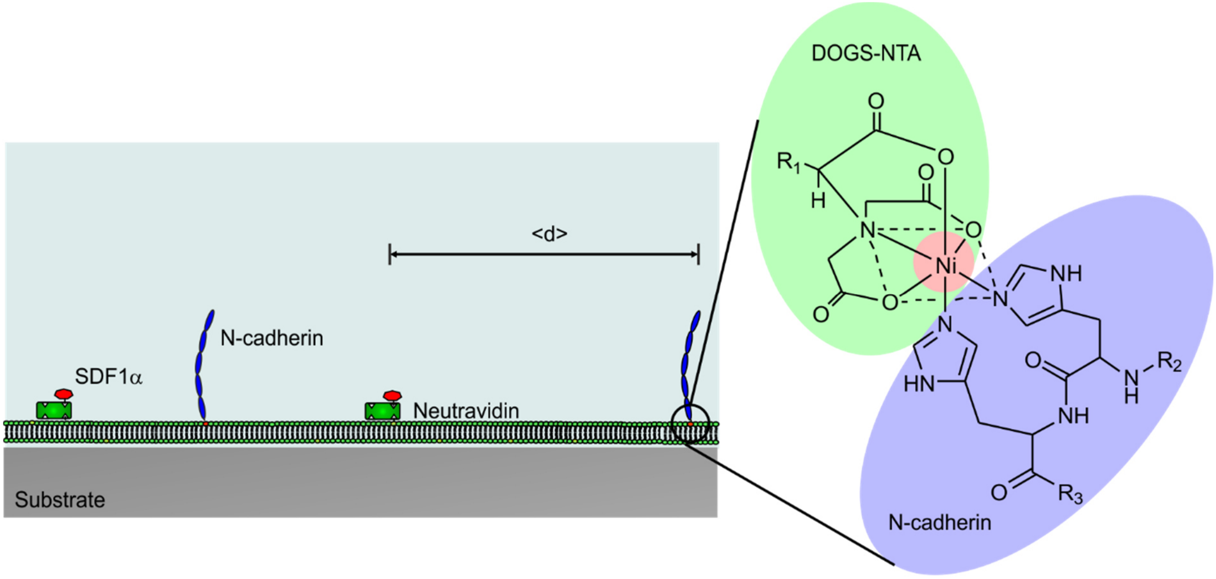

Figure 3.5 | Supported membranes as cell mimetic models. Schematic illustration of a supported membrane functionalized with proteins via neutravidin/biotin binding or nickel-chelating lipids. The molecular structure depicts the complex formation and specific binding of histidine-tagged N-cadherin to the NTA group of the chelator lipids. The average intermolecular distance <*d*> can be tuned with nm-accuracy by variation of the lipid composition.

In the present study, the bone marrow niche was mimicked by supported membranes which were functionalized with the ligands (1) His6 N-cadherin, (2) biotin-SDF1α or (3) both ligands.

N-cadherin belongs to the family of classical type-1 cadherins[133]. These transmembrane proteins are expressed in multiple tissues and involved in cell adhesion and migration[134, 135]. Their tertiary structure is dependent on the presence of calcium ions which rigidify the protein structure. Above a Ca^{2+}-concentration of 40 μM, they have a rod-like shape with a short axis of 5 nm to 8 nm and a long axis of 25 nm to 28 nm[136]. Cadherins are composed of five extracellular domains (EC) with a size of ~4.5 nm, a transmembrane region and a highly conserved cytoplasmic tail (Fig. 3.6 left)[137]. The EC repeats are labeled EC1–EC5, with EC1 being the most distant from the membrane. Cadherins mediate Ca^{2+} concentration dependent adhesion via homophilic binding in an anti-parallel conformation ($K_D = 0.7$ mM at 1 mM Ca^{2+}, $K_D = 0.17$ mM at 10 mM Ca^{2+})[136, 138]. The mechanism of homophilic binding is still under debate and is suggested to proceed in a two-step process[135]. The first step comprises the formation of a cis-dimer on the same cell[139-141]. Thereafter, cell-cell adhesion is initiated by binding between two *cis* dimers on opposing cell surfaces[135, 139]. This process can be described by the strand-swapping model and is based on the swapping of the N-terminal *β*-strands of the EC1 domains[142].

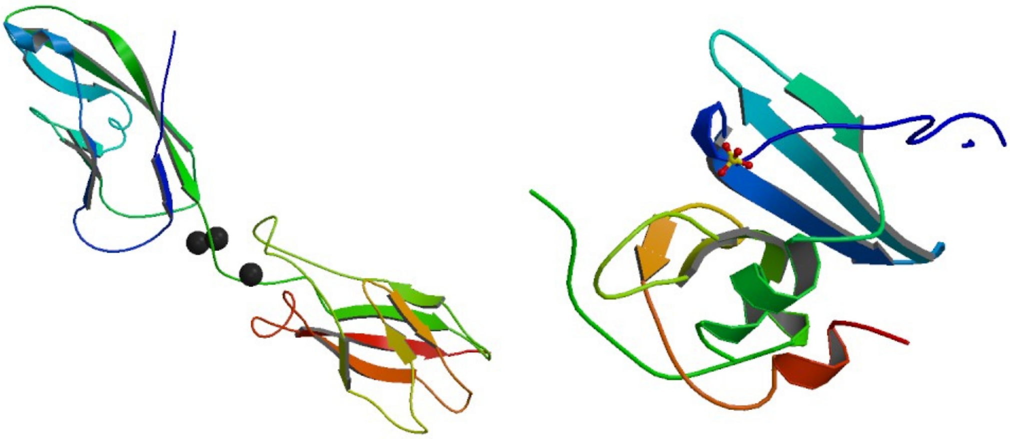

Figure 3.6 | Crystal structures of N-cadherin and SDF1α. Crystal structures of N-cadherin domains EC12 (2QVI, left) including three calcium ions and SDF1α (1A15[143], right) including a sulfate ion. Protein chains are colored from the N-terminal to the C-terminal using a rainbow color gradient.

Another important aspect of cadherin mediated adhesion is their indirect connection to actin filaments of the cytoskeleton via a catenin complex[144] allowing for mechanotransduction[145]. Several studies, which relied on force measurements, quantified binding strength between single cadherin molecules as well as between integral proteins during cell adhesion. Surface force apparatus measurements of cadherin-mediated binding (Xenopus C-cadherin mutants) between cadherin functionalized lipid bilayers revealed a normalized binding force of -1.8 ± 0.6 mN/m between EC1-EC1 domains[146]. Single-molecule measurements utilized the biomembrane force probe resulting in a weak bond rupture force of 32 pN for EC1-2 fragments of Xenopus C-cadherin mutants[147]. By comparison, the avidin-biotin rupture force was determined to be ~200 pN[148]. In case of cell adhesion, the homophilic binding of cadherins conveys mechanical information to cells due to mechanosensing of their microenvironment (e.g. rigid vs. soft surfaces) resulting in e.g. cytoskeletal rearrangements[149]. For example, traction forces of muscle cells mediated by N-cadherin-based adhesion to N-cadherin coated micropillars increased with the substrate stiffness. This behavior is caused by endogenous actomyosin contractility[150].

SDF1α is a member of the CXC chemokine ligand superfamily. Its tertiary structure consists of three anti-parallel β-strands and an overlapping α-helix (Fig. 3.6 right)[151]. The binding to CXCR4 is suggested to proceed via a two site model as suggested by Crump *et al.*[151]*.* First, residues 12-17 (referred to as RFFESH motif) couple to CXCR4. Then, the first eight N-terminal residues activate the receptor. The receptor CXCR4 is a transmembrane G-coupled receptor protein[152, 153] consisting of seven transmembrane domains. Several studies have indicated that the main binding site for SDF1α is located at the N-terminal region of CXCR4 whereas it is activated via the EADD motif at the second extracellular loop[151]. Furthermore, Zhou *et al.* have suggested that the third extracellular loop plays also a significant role in SDF1α binding and signaling[154]. In contrast to N-cadherin, there is no linkage to the cytoskeleton reported. Therefore, mechanotransduction plays no role for SDF1α/CXCR4 axis. Surface plasmon resonance-based investigations of SDF1α binding using CXCR4 functionalized lentiviral particles immobilized to the sensor surface revealed a dissociation constant of $K_D = 3.47 \pm 0.05 \times 10^{-8}$ M[155]. A ^{125}Iod binding assay performed by Staudinger *et al.* resulted in a dissociation constant of $K_D = 5.33 \pm 1.03 \times 10^{-9}$ M[156].

3.2.1.2 Experimental realization and image analysis

The quantification of HSPC adhesion to the *in vitro* niche model was performed by phase contrast microscopy and RICM. Image acquisition was performed on an Axiovert 200 inverted microscope (Carl Zeiss AG, Oberkochen, Germany) equipped with a PlanNeofluar 63x/1.25 Antiflex oil-immersion objective with a built-in λ/4-plate, a filter cube with crossed polarizers and a cell incubation chamber from Ibidi. For RICM, light emerging from a metal halogenide lamp (X-Cite 120 PC, Lumen Dynamics Group Inc., Ontario, Canada) was filtered using a green filter ($\lambda_{ex} = 546 \pm 10$ nm) and passed perpendicular oriented polarizers before and after the first and second transmission across the λ/4-plate, respectively. Single phase contrast images and sequences of 20 consecutive RICM frames were acquired for at least 10 positions per condition using an Orca ER CCD camera (Hamamatsu Photonics, Hamamatsu, Japan) with an exposure time set to 0.1 s after 1 – 4 h of cell seeding. The image analysis was based on a routine written in Matlab (R2008b, The MathWorks, Natick, MA) by Dr. C. Monzel and performed for four hours after cell seeding on the following steps: First, the cell of interest was identified in the phase contrast image by an image segmentation process in order to gain information about cell aspect ratio but also to facilitate the identification of the adhesion area in the corresponding RICM image sequence. In a second step, each image of the RICM sequence was corrected for the parabolic illumination profile. The average background intensity I_{bkg} was measured and the entire image sequences was normalized according to

$$I_{norm} = \frac{I - I_{Bkg}}{I_{Bkg}}. \tag{3.2.22}$$

The normalized intensity was converted into heights, applying the RICM theory for finite INA and multiple reflecting layers[114]. Briefly, reflections from five interfaces were taken into account for the analysis of the interference patterns. The first reflection took place at the glass substrate/cell medium interface due to the use of an oil immersion objective. Then, additional four reflections occurred at each interface with different refractive index as depicted in Fig. 3.7. The refractive indices corresponded to $n_0 = 1.525$ (glass substrate[157]), $n_1 = 1.335$ (IMDM medium), $n_2 = 1.486$ (lipid membrane) and $n_3 = 1.37$ (cytosol[158]). It should be pointed out that multiple reflection effects are negligible small due to a slight opening of the aperture diaphragm (illumination numerical aperture (INA) ~ 0.64) and, thus, they were not included in the height reconstruction. Consequently, the intensity distribution I(x,y) of the RICM pattern can be described by the following equation:

$$I(x,y) = R * RE_0^2 = R * RI_0 \tag{3.2.23}$$

with $$R = r_{01} + \sum_{i=1}^{4}\left[\prod_{s=1}^{i}\left(1 - r_{s-1,s}^2\, exp(-ik\Delta_s)\right)\right] r_{i,i+1} \tag{3.2.24}$$

In order to quantify height fluctuations caused by membrane fluctuations, the image sequence was additionally corrected for shot noise of the camera. Finally, adhesion was detected from the average height and standard deviation of heights in each pixel, whenever the pixel lay within the cell contact area enclosed by the interference fringe pattern and when the standard deviation of heights was ≤ than the height variation due to noise.

In addition to the cell adhesion area A_{Adh}, the fraction of adherent HSPC χ normalized by cells seeded on surrogate niche models was determined by counting the surface densities of adherent cells.

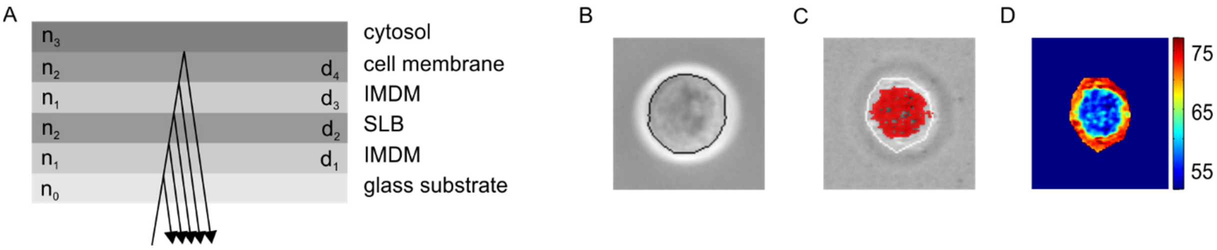

Figure 3.7 | RICM analysis. (A) The RICM analysis is based on a five layer model. Reflections at five interfaces with different refractive indices *n* and thicknesses *d* were taken into account for the analysis of interference patterns. (B) The first step is based on an image segmentation procedure to detect the cell in a phase contrast image. (C) In the second step, the contact zone of the cells (white line) and its adhesion area is calculated (red). (D) Finally, the height map is reconstructed not as absolute values, but constructed as fluctuation maps to judge the adhesion state.

3.2.1.3 Results and discussion

The adhesion of HSPC was quantitatively investigated *in vitro* by a combination of phase contrast microscopy and RICM yielding values for (1) the fraction of adherent cells χ, (2) the adhesion area A_{Adh} and (3) the aspect ratio as a measure for cell polarization. As *in vitro niche model* of bone marrow niche, a solid-supported membrane functionalized with different surface densities of either SDF1α or N-cadherin was utilized (Fig. 3.8).

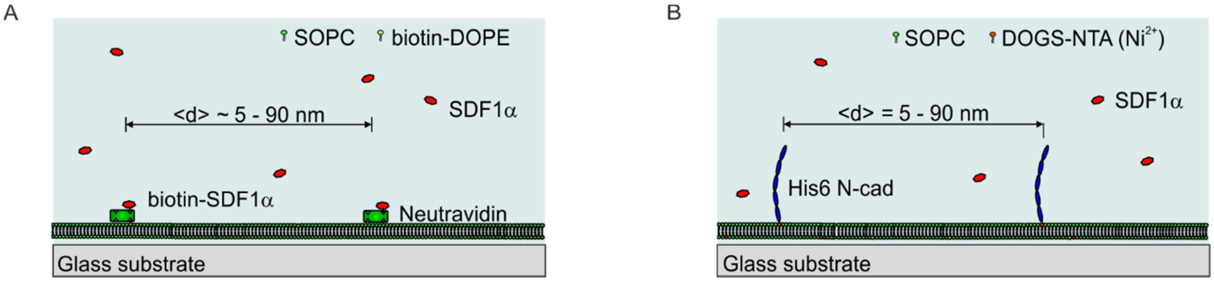

Figure 3.8 | *In vitro* models of bone marrow niche. Supported membranes functionalized with either (A) biotin-SDF1α or (B) His6 N-cadherin were used as *in vitro* niche models which exhibited the advantages of planar geometry and precise variability of the average intermolecular distances <*d*> of ligand molecules between 5 and 90 nm. The counterplay of soluble vs. immobilized SDF1α was studied by the addition of 5 ng/mL SDF1α in the cell medium.

This approach allowed for the mechanistic characterization of differential roles of ligand-receptor pairs in bone marrow niche. Figures 3.9A and B represent phase contrast images of HSPC on *in vitro* niche models displaying either SDF1α or N-cadherin at <*d*> ~ 18 nm (top) and 11 nm (bottom) two hours after cell seeding, respectively. In a first step, the fraction of adherent cells was determined by dividing the number of adherent cells, which were identified by RICM, by the total number of cells visible on phase contrast images. To exclude any non-specific binding of cells to the supported membrane, adhesion measurements of HSPC on non-functionalized membranes were performed (Fig. 3.9C, black data point). The data clearly revealed that HSPC specifically bound to the ligand molecules via the homophilic interaction of N-cadherin molecules or the heterophilic binding of SDF1α/CXCR4. The fraction of adherent cells χ increased significantly according to a decrease of the average intermolecular distances $\langle d_{N\text{-}cadherin} \rangle$ and $\langle d_{SDF1\alpha} \rangle$. This finding suggests that there is a distinct transition from the "bound" state (close to 100%) to "unbound" state (close to the base line) including a cooperative effect of the ligand-receptor binding. Thus, both data sets were fitted according to the empirical Hill equation:

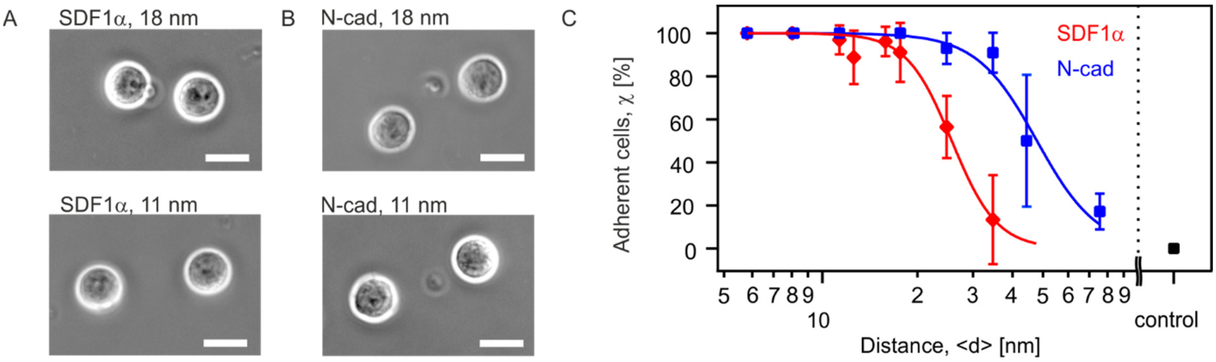

Figure 3.9 | HSPC specifically detect changes in intermolecular ligand distance in the nm regime. Phase contrast images of HSPC on membranes displaying (A) SDF1α at <*d*> = 18 nm (top) and <*d*> = 11 nm (bottom) and (B) N-cadherin at <*d*> = 18 nm (top) and <*d*> = 11 nm (bottom) at *t* = 2 h (scale bar: 10 µm). (C) The fraction of adherent HSPC on supported membranes, plotted as functions of $<d_{\text{N-Cadherin}}>$ (blue) and $<d_{\text{SDF1}\alpha}>$ (red) could be characterised by an empirical Hill equation (solid lines), identifying a difference in the transition point. Data points represent means ± SD for n = 50 cells.

$$\chi = \chi_{min} + \frac{\chi_{max} - \chi_{min}}{1 - \left({}^{d}/_{d^*}\right)^{n}}, \tag{3.2.25}$$

where χ_{min} and χ_{max} stand for the minimum and maximum levels. This equation is primarily used for the characterization of the binding of a ligand to a macromolecule (e.g. enzyme) and was firstly introduced by Hill to characterize the sigmoidal O_2 binding curve of hemoglobin[159]. A Hill coefficient *n* of 1 indicates the independent binding between a ligand-receptor pair, regardless of how many pairs are already formed. A coefficient greater than 1 indicates positive cooperativity, whereas a coefficient less than one indicate negative cooperativity. Additionally, the unbinding/binding transition is determined by the average intermolecular distance <*d**>, characterizing <*d*> at which a fraction of adherent cells of $\chi \sim 50$ % is reached. In case of the adhesion mediated by SDF1α/CXCR4 (Fig. 3.9C, red curve), the unbinding transition could be characterized by the critical distance $<d^*_{SDF1\alpha}> \sim 27$ nm and the cooperativity coefficient n ~ 3. In contrast, the corresponding results for N-cadherin (Fig. 3.9C, blue curve) exhibited a broader tail to a larger critical distance $<d^*_{N\text{-}cadherin}> \sim 50$ nm with a cooperativity coefficient $n \sim 2$. These results suggested that HSPC specifically detected slight changes in <*d*> with nm accuracy, and the adhesion mediated by both SDF1α/CXCR4 and homophilic N-cadherin axes could be classified as cooperative binding processes. This study was further extended as the results obtained from the fraction of adherent cells vs. <*d*> were based on an "ensemble counting" where cells were either classified as adherent or non-adherent. Therefore, the second step of the presented approach consisted of a detailed image analysis of RICM image sequences in order to gain additional information of the adhesion area A_{Adh} of HSPC based on the two different types of *in vitro* niche models in order to distinguish between weak and strong adhesion. Figures 3.10A and B represent the RICM images obtained for HSPC on supported membranes displaying either SDF1α or N-cadherin at $\langle d \rangle$ ~ 18 nm and 11 nm, respectively. Changes of $\langle d \rangle$ from 18 to 11 nm caused a significant change in the adhesion area A_{Adh} of HSPC. Thus, RICM permitted the quantitative analysis of minor changes of A_{Adh} dependent on the different average lateral distances $\langle d \rangle$. Figure 3.10C represents the adhesion area A_{Adh} dependent on the average intermolecular distance $\langle d_{SDF1\alpha} \rangle$ (red) and $\langle d_{N\text{-}cadherin} \rangle$ (blue). The sigmoidal progression of the data set revealed a significant decrease from 16 µm^2 to 7 µm^2 for HSPC on SDF1α functionalized supported membranes at average intermolecular distances $\langle d_{SDF1\alpha} \rangle$ ~ 11 nm to 18 nm. Almost no adhesion area could be detected for HSPC on an *in vitro* niche model displaying SDF1α at $\langle d_{SDF1\alpha} \rangle$ ~ 34 nm, which consistent with the results for the fraction of adherent cells. The corresponding results on membranes displaying N-cadherin exhibited a similar tendency. There was no signs of adhesion at $\langle d_{N\text{-}cadherin} \rangle$ ~ 80 nm. The direct comparison between both data set (Fig. 3.9C and 3.10C) is a clear evidence that the determination of the fraction of adherent cells is not as precise as the calculation of the adhesion area in characterizing the adhesion of HSPC. The first method underestimates the characteristic transition point between unbinding and binding of cells. Here, fitting of the data with the Hill equation by replacing χ to A_{Adh} in Equ. 3.2.25 resulted in the critical distance $\langle d^*_{SDF1\alpha} \rangle$ ~ 14 nm and the cooperativity coefficient n ~ 1.9. In contrast, the corresponding results for the adhesion mediated by the homophilic interaction of N-cadherin (blue curve) are $\langle d^*_{N\text{-}cadherin} \rangle$ ~ 31 nm with a cooperativity coefficient n ~ 1.4. This finding implied that the detailed analysis of RICM data was much more sensitive for assessment of the difference in cell adhesion.

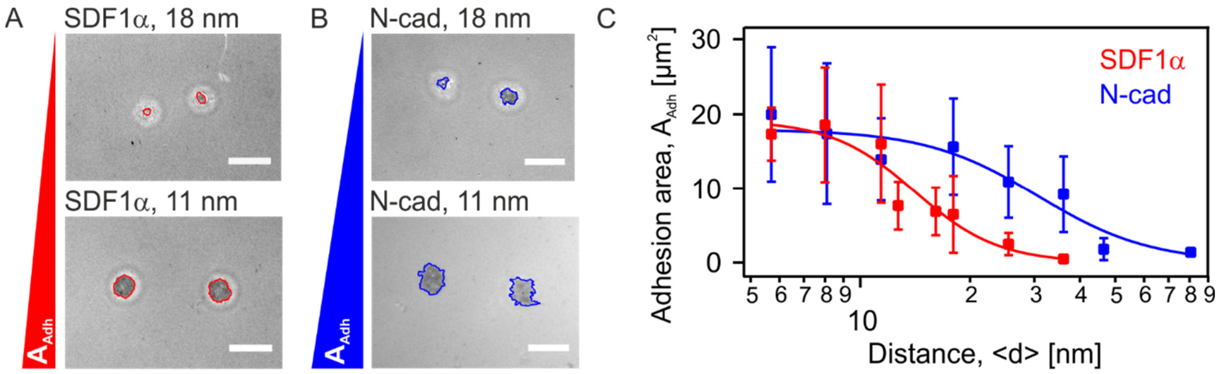

Figure 3.10 | The determination of the adhesion area revealed characteristic differences of the binding between the two ligand-receptor pairs. Micro-interferometry images of HSPC on membranes displaying either (A) SDF1α at $\langle d \rangle$ = 18 nm (top) and $\langle d \rangle$ = 11 nm (bottom) or (B) N-cadherin at $\langle d \rangle$ = 18 nm (top) and $\langle d \rangle$ = 11 nm (bottom) at t = 2 h (scale bar: 10 µm). (C) The average adhesion area plotted vs. $\langle d_{\text{N-Cadherin}} \rangle$ (blue) and $\langle d_{\text{SDF1}\alpha} \rangle$ (red) could be characterised by an empirical Hill equation (solid lines) by replacing χ with A. Data points represent means ± SD for n = 50 cells.

Since SDF1α is not only expressed as immobilized molecule but also released in the extracellular space of the bone marrow microenvironment, the fraction of adherent HSPC χ and the area of tight adhesion A_{Adh} were determined in the presence and absence (as control) of 5 ng/mL SDF1α, which corresponded to the physiological level of SDF1α in human bone marrow. Table 3.1 summarizes the corresponding data at <$d_{SDF1\alpha}$> ~ 11 and 18 nm. A decrease in the fraction of adherent cells χ and adhesion area A_{Adh} was observed in the presence of soluble SDF1α at t = 2 h. For example, at <$d_{SDF1\alpha}$> ~ 11 nm, the area of tight adhesion A_{Adh} was reduced almost by a factor of two in the presence of soluble SDF1α. This finding suggested that soluble SDF1α was able to shift the dynamic equilibrium between bound and unbound states of CXCR4/SDF1α. The decrease in the HSPC adhesion area A_{Adh} was much more pronounced compared to that observed in previous experiments on substrates coated with fibronectin, where no significant difference in cell adhesion could be observed until soluble SDF1α was applied at concentrations. The SDF1α concentrations used in these studies were 1–2 orders of magnitude higher than the physiological concentration, which was used in this study. However, as these studies investigated interactions between HSPC and cell feeder layer and thus cannot discriminate different ligand-receptor pairs, the direct comparison with the current results is practically invalid. Furthermore, the effect of soluble SDF1α on N-cadherin mediated adhesion was investigated at <$d_{N\text{-}cadherin}$> ~ 11 and 18 nm. The results clearly demonstrated that soluble SDF1α did not affect the fraction of adherent HSPC χ and the average area of tight adhesion A_{Adh} (Table 3.1).

Table 3.1 | SDF1α shifts the dynamic equilibrium between bound and unbound states of CXCR4/SDF1α but did not affect N-cadherin mediated adhesion. The fraction of adherent HSPC χ and the average area of adhesion A_{Adh} in the presence and absence of 5 ng/mL SDF1α at t = 2 h. The experiments were performed at two different average lateral distances, <$d_{SDF1\alpha}$> and <$d_{N\text{-}cadherin}$> ~ 11 nm and 18 nm. The values represent means ± SD for n = 50 cells.

	χ [%]		**A_{Adh} [µm^2]**	
(I) HSPC on membranes displaying SDF1α				
<$d_{SDF1\alpha}$> [nm]	**11**	**18**	**11**	**18**
without SDF1α	97.0 ± 6.7	94.0 ± 14.1	16.0 ± 8.0	6.5 ± 2.0
with SDF1α	93.1 ± 6.7	52.0 ± 24.4	9.5 ± 6.4	2.0 ± 1.9
(II) HSPC on membranes displaying N-cadherin				
<$d_{N\text{-}cadherin}$> [nm]	**11**	**18**	**11**	**18**
without SDF1α	100.0 ± 0.0	100.0 ± 0.0	13.9 ± 5.5	15.6 ± 6.5
with SDF1α	100.0 ± 0.0	100.0 ± 0.0	15.0 ± 4.9	13.3 ± 5.0

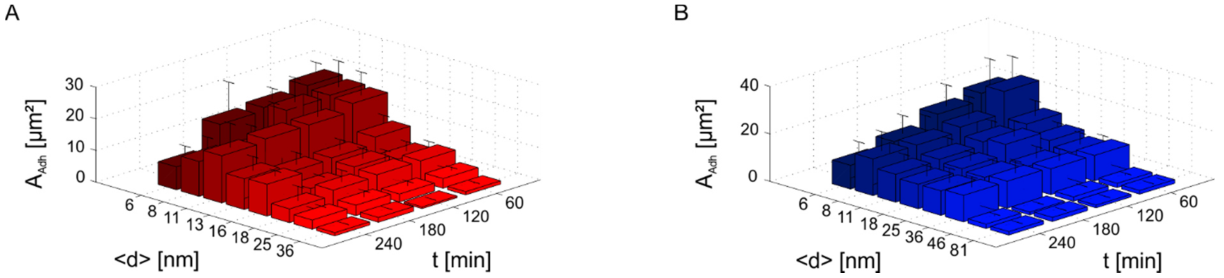

Figure 3.11 | High surface densities of SDF1α and N-cadherin caused a significant, time-dependent decrease of the adhesion area. The adhesion area A_{Adh} as function of the average intermolecular distance $\langle d \rangle$ of (A) SDF1 and (B) N-cadherin is plotted for t = 1 – 4 h after seeding of cells on the *in vitro* niche model. Significant reductions of the adhesion area over time occurred for $\langle d \rangle$ ~ 6 and 8 nm for both data sets. The bars represent means ± SD for n = 50 cells.

Thereafter, the current approach was extended to analyze time-dependent changes in the adhesion area A_{Adh}. For this purpose, RICM experiments were performed for the first four hours of adhesion (Fig. 3.11). As shown in Figures 3.11A and B, high surface densities of both ligands led to a significant reduction of the adhesion area A_{Adh} over time. In case of HSPC on membranes displaying SDF1α at an average intermolecular distance $\langle d_{SDF1\alpha} \rangle$ ~ 6 nm, the adhesion area A_{Adh} was reduced by the factor of three within the first four hours of adhesion. HSPC on membranes displaying N-cadherin at the same ligand distance exhibited a similar behavior. The adhesion area was reduced by a factor of two. These changes were less pronounced at average intermolecular distance $\langle d \rangle$ ~ 11 nm, but still significant. At higher distances of both ligands ($\langle d \rangle$ > 11 nm), no reduction occurred. This finding implied that the contact between HSPC and the *in vitro* niche models displaying high surface densities of SDF1α and N-cadherin stimulate the cell to detach. This finding implies the active downregulation of the surface expression of the two receptors by for example receptor internalization or asymmetric re-distribution along the adhesion site, which is known for the receptor CXCR4 on other hematopoietic cells. Förster *et al.* demonstrated that the incubation of leukocytes with SDF1α induces downregulation of up to 60% of surface-expressed receptors[160]. A similar behavior was also observed for N-cadherin. In neurons, N-cadherins are subject of a dynamic traffic between the cell membrane and the cell interior by endo- and exocytosis[161]. This provides flexibility for regulating adhesive forces and cellular signaling in response to neuronal activity. In case of HSPC, the internalization of both receptors was not yet proven and should play a central role in future investigations. Nevertheless, the current experimental setup did not allow for investigations whether the receptors CXCR4 and N-cadherin can be internalized by HSPC due to the exposure of high surface concentrations of the ligands.

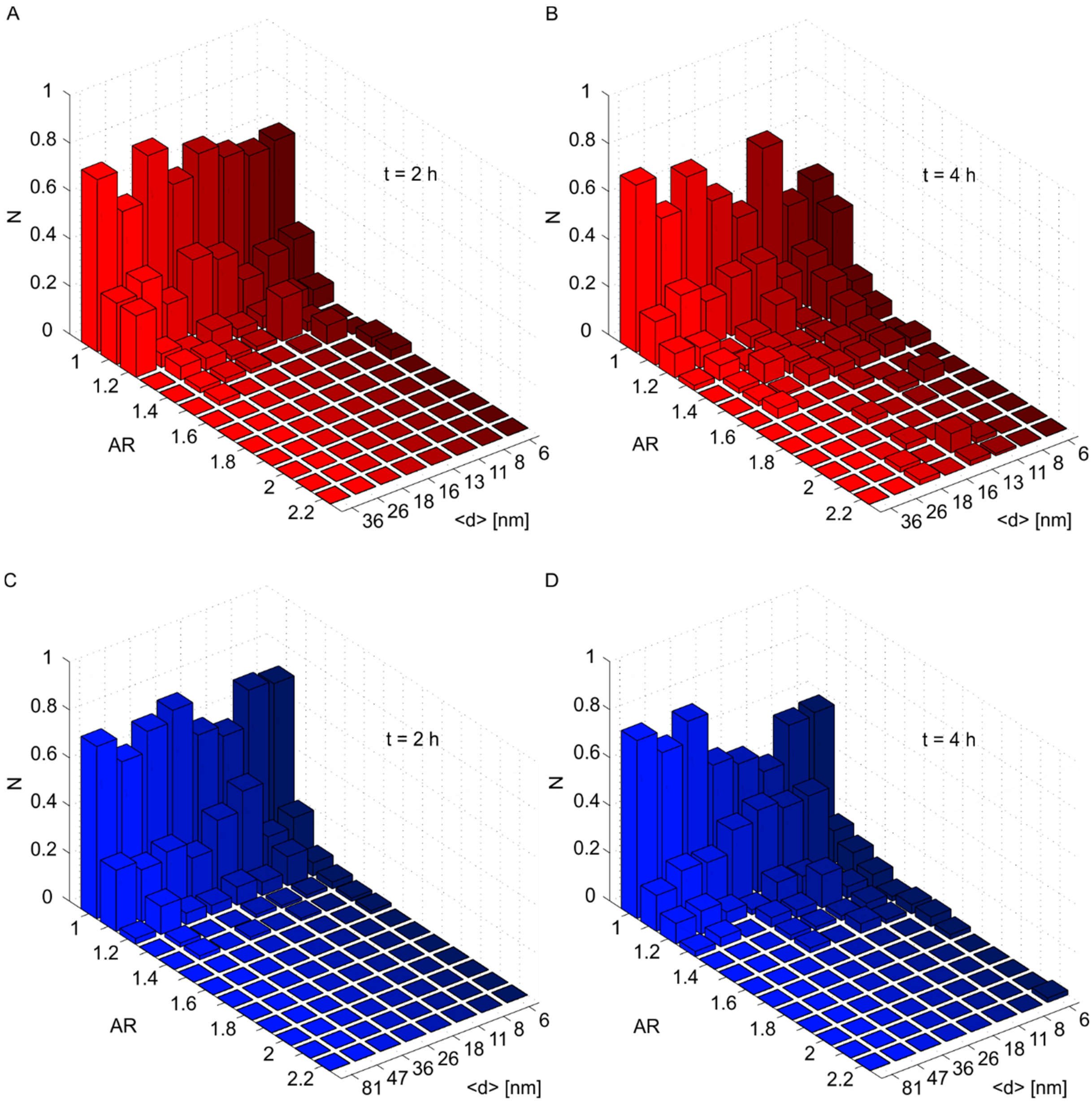

Figure 3.12 | Time-dependent increase in cellular polarization indicates HSPC motility. Three-dimensional plot of the fraction *N* of HSPC with aspect ratio *AR* as function of the average intermolecular distance <*d*> of (A, B) SDF1α and (C, D) N-cadherin is plotted for *t* = 2 and 4 h after seeding of cells on the *in vitro* niche model. Data is shown for n = 50 cells per timepoint and *in vitro* niche model.

Finally, further investigations focused on time-dependent polarization of HSPC induced by the adhesion to the *in vitro* niche models. Thus, the aspect ratio *AR* of HSPC was quantified as measure for cell polarization for the first four hours after seeding as given by

$$AR = \frac{L_1}{L_2}, \tag{3.2.26}$$

where L_1 and L_2 correspond to the ratio of the longest axis to the shortest axis of the cell periphery. Figure 3.12 displays *AR* of HSPC on membranes displaying either SDF1α or N-cadherin for t = 2 and 4 h after cell seeding as identified from the phase contrast images. After the initial adhesion process, cells on membranes displaying SDF1α were significantly polarized. Surprisingly, HSPC did not follow similar tendencies as identified for the time-dependent analysis of the adhesion. Here, they showed a significant increase in AR at intermediate average intermolecular distances $<d_{SDF1\alpha}>$ ~ 11 – 18 nm. Surprisingly, these ligand spacings are in the range of the transition point of binding/unbinding as identified by microinterferometry. At small intermolecular distances, e.g. $<d_{SDF1\alpha}>$ ~ 6 nm, HSPC did not polarize as indicated by a minor change in the *AR* distribution. This finding coincides with the identified reduction of the adhesion area A_{Adh}. HSPC on N-cadherin modified membranes hardly polarized. There, the *AR* of HSPC increased only in the presence of *in vitro* niche models with a high surface density of N-cadherin molecules. The current findings can be attributed to the different functional roles of SDF1α and N-cadherin. Whereas the latter one serves as CAM anchoring HSPC to the bone marrow niche[12], SDF1α is a chemoattractant which induces actin polymerization and cell polarization[33, 162]. Furthermore, the current findings indicate cellular motility as an active response of HSPC to the *in vitro* niche models.

3.2.1.4 Summary

The current approach demonstrated the specificity of HSPC in detecting different ligands molecules in their microenvironment. The fraction of adherent cells χ and the adhesion area A_{Adh} of HSPC varied according to the *in vitro* niche model. Whereas the adhesion molecule N-cadherin immobilizes HSPC at already an average intermolecular distance $<d_{N\text{-}Cadherin}>$ ~ 80 nm, the chemokine SDF1α needs to be present at $<d_{SDF1\alpha}>$ ~ 34 nm to efficiently bind HSPC. These findings were in clear contrast to studies which could not detect N-cadherin as an important adhesion molecule and simultaneously supports a previous report of Wein *et al.* on intercellular junctions between HSPC and MSC formed by the homophilic interaction between N-cadherin molecules[20]. The characterization of both binding curves by the Hill equation identified significant differences but also characteristic similarities between both ligand-receptors pairs: First, both ligand-receptor pairs mediate a positively cooperative binding. Second, the characteristic transition points between unbinding and binding of cell corresponds to $<d^*_{SDF1\alpha}>$ ~ 27 nm and $<d^*_{N\text{-}Cadherin}>$ ~ 50 nm in case of the fraction of adherent cells. As the underlying data set represents an "ensemble counting" of different densities of adherent cells, the adhesion study was extended towards the quantification of the adhesion area as a function of the average intermolecular distance $<d>$ of ligand molecules. The characteristic transition points between unbinding and binding of cell corresponds to $<d^*_{SDF1\alpha}>$ ~ 14 nm and $<d^*_{N\text{-}cadherin}>$ ~ 31 nm as only adherent cells were considered. Third, the effect of soluble SDF1α on HSPC adhesion mediated by the heterophilic SDF1α/CXCR4 axis and the homophilic binding of N-cadherins was investigated. As the mobilization/homing mechanism is regulated by a dynamic stimulation of the SDF1α level in bone marrow, differences in the adhesion indicated that the niche was able to regulate homing versus mobilization by changing the ratio of soluble versus immobilized SDF1α. This finding was supported by the fact that the adhesion mediated by N-cadherin was not affected by the presence of the physiological concentrations of soluble SDF1α. Fourth, time-dependent changes of the adhesion area A_{Adh} were investigated. The exposure of HSPC to *in vitro* niche models displaying SDF1α and N-cadherin at average intermolecular distances $<d>$ ~ 6 – 11 nm led to a significant decrease of the adhesion area A_{Adh} within the first four hours of adhesion. This finding implied that the presence of high surface densities of ligand molecules caused an active response of the cell. Possible effects like e.g. receptor internalization or asymmetric re-distribution should play a central role in further investigations as the experiments performed for the current study did not allow any conclusions. Finally, HSPC polarization indicated cell motility which was more pronounced for the SDF1α/CXCR4 axis. Whereas HSPC on membranes displaying SDF1α exhibited a significant time-dependent increase of the aspect ratio, such an increase could hardly be identified for cells on N-cadherin functionalized membranes. Surprisingly, the increase in *AR* was most pronounced at intermediate ligand spacings, $<d_{SDF1\alpha}>$ ~ 11 – 18 nm. This finding was in well agreement with the transition point for binding/unbinding as identified by microinterferometry. In summary, the quantitative investigations on the immobilization of HSPC on *in vitro* niche models of bone marrow niche resulted in deep insights into the function of different ligand-receptors pair which could not identified by previous in vitro studies using cell feeder layer as model system.

3.2.2 Evaluation of the cell adhesion strength

3.2.2.1 Theoretical background

An important parameter in the context of cell adhesion is the mechanical strength of binding between the cell and its environment (e.g. adjacent cell, ECM, *in vitro* niche model). In the past, various methods have been developed to study the cell adhesion strength. These methods comprise the pulling of the adherent cells by micropipette aspiration[163, 164], atomic force microscopy (AFM)[165-167] or magnetic tweezers[168, 169]. Although all these techniques address the same question, there are significant differences in the force range which can be applied to the cell due to instrumental limitations (Table 3.2). In micropipette aspiration, an adherent cell is detached from a substrate or cell by sucking it into a micropipette[163]. The limiting factors of this method are the cell size, which should fit into the micropipette without adhering to it, and the forces which can be applied are inverse proportional to the micropipette diameter. For example, the use of a micropipette with a diameter of 10 µm limits the force range to 10 pN to 1 nN. Therefore, this method can be only utilized to measure the adhesion strength of relatively small cells (e.g. neutrophils, red blood cells) whereas other cell types like e.g. fibroblasts or keratinocytes which have usually a size of several tenth of micrometer cannot be detached. Another method is based on the dislodgement of an adherent cell by an atomic force microscope (AFM) cantilever [165-167] and was developed by Sagvolden *et al.* in 1999[170]. By recording the laser beam deflection vs. the lateral cantilever displacement, a force-distance curve is obtained from which the adhesion strength can be calculated. Due to the contact of the cantilever with the cell of interest, the cantilever can be contaminated and has to be replaced frequently. Another approach based on AFM was developed by Benoit *et al.*[166] in 2000. They have quantified de-adhesion forces between a cell attached to the AFM cantilever and a cell which adhered to a substrate. Both AFM based techniques enable the application of forces up to 100 nN and are limited to a minimal value of 10 pN due to thermal noise of the setup[171]. Force spectroscopy measurements on cell adhesion can be also performed using magnetic tweezers[168, 169]. The experimental setup consists of a magnetic particle which is covalently bound to the cell adhering to a substrate. In the presence of a magnetic field, the particles experiences a force which is proportional to the gradient of the square of the exerted magnetic field. By lifting up the magnetic particle, the adherent cell is detached from its substrate. The advantage is that high forces can be achieved due to a broad range of field strengths. Disadvantages arise from the used magnets which limits the manipulation ability and can cause substantial heating of the samples[168]. All of the mentioned techniques have three characteristics in common: The main disadvantages are (1) the non-contact-free measurement of the cell adhesion strength with (2) low statistics (1 – 10 cells/h) and (3) the obtained results include inelastic responses of the cells, due to their small loading rates.

Table 3.2| Overview of techniques for the determinination of the cell adhesion strength. Different techniques are available to determine the cell adhesion strength. They vary according to the applied force range and the amount of cells which can be measured per hour (statistics).

Technique	Minimum force	Maximum force	Statistics [cells/h]
Micropipette aspiration	10 pN	1 nN	5 -10
AFM peeling	10 pN	100 nN	1 - 5
Magnetic tweezers	0.01 pN	1 nN	5 -10

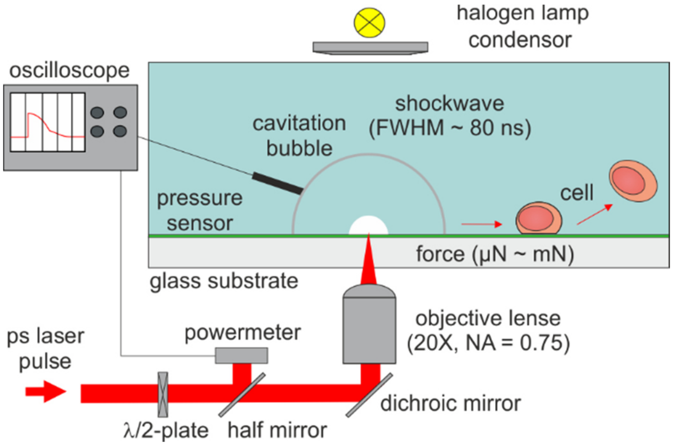

Figure 3.13 | Pressure wave assay. Schematic illustration of the experimental setup of the pressure wave assay.

Recently, Yoshikawa *et al.* developed a new technique which overcame these disadvantages[49, 172]. In the pressure wave assay, cells are detached by hydrodynamic pressure waves which are generated by intense picosecond laser pulses in the surrounding medium of adherent cells. The experimental setup consists of a picosecond laser which is coupled to an inverted microscope and allows, therefore, to focus the laser pulse into the cell incubation chamber (Fig. 3.13). At the focal point, the aqueous medium is evaporated forming a cavitation bubble. The formation and collapse of this cavitation bubble generates intensive pressure waves. By tuning the pulse energy, the strength of the pressure wave can be tuned (0.1 – 30 MPa; µN - mN), which is approximately 6 orders of magnitude larger compared to the methods mentioned above. The main advantages of this technique are the contact-free determination of the required pressure for cell detachment with high statistics (~ 100 – 200 cells/h) and the high velocity of the pressure wave. Due to the fact that the first pressure wave has a supersonic velocity of approximately 1640 $m \cdot s^{-1}$ and a full width at a half-maximum of 80 ns, any inelastic response of the cell is suppressed[49]. A disadvantage arise from the necessity to perform calibration measurements prior to each series of experiments. As depicted in Fig. 3.14, the pressure generated by a shock wave has to be calibrated by the laser pulse energy and the distance from the focus using a pressure sensor.

3.2.2.2 Experimental realization

The determination of the critical pressure for cell detachment as a measure for the cell adhesion strength of HSPC on the *in vitro* niche model was performed by the pressure wave assay. The experimental setup consisted of a Nd:YAG laser system ($\lambda = 1064$ nm, $\tau_L = 60$ ps, PY 61C-20, Continuum, Santa Clara, CA, USA) which was coupled to an inverted microscope (Eclipse TE2000-U, Nikon Europe) and equipped with a self-built cell incubation chamber. Pressure waves were induced by focusing picosecond laser pulses with a PlanApo 20×/0.75 objective into the measurement chamber. The measurement chamber was based on a round glass bottom dish (µ-Dish, 35 mm, Ibidi, Martinsried, Germany). The *in vitro* niche model was prepared as described in chapter 3.1.4 – 3.1.9). All experiments were performed at a time point $t = 2$ h after cell seeding. This position of the laser focal point inside the cell incubation chamber was selected due to the following reasons: As the irradiation of an intensive, short laser pulse leads to the generation of a cavitation bubble at the position of the focal point, a measurement position was carefully chosen at a distance where potential damage to HSPC can be excluded. First, the distance between cells and the focal point of the laser (1.5 mm) was set to a value larger than the maximal possible radius of the cavitation bubble ($R_{max} < 1.4$ mm), which is at the same time larger than any damage observed on the *in vitro* niche model (with a maximal radial distance of $R_{damage} < 300$ µm). Second, the short separation distance between the focal point of the ps laser pulse and the substrate (~0.1 mm) suppresses any adverse effects due to hydrodynamic liquid jet impacts. Thus, the target cells are not exposed to hot gaseous water.[173] Nevertheless, the impact of heating caused by the intensive laser pulse and the formation of the cavitation bubble was estimated to ensure the quality of the experiment. Based on the experimental conditions, which were mentioned above, the increase in temperature at this position was estimated according to the following two assumptions. First, the laser energy with a maximum value of 10 mJ is assumed to be fully converted to heat. As the heat transfer to the cell culture medium occurs via multiphoton absorption of which the efficiency is much less than for single photon absorption, this assumption is apparently an overestimation. Second, the medium (volumetric heat capacity ~ 4.2 $\mathrm{mJ \cdot mm^3 \cdot K^{-1}}$) is uniformly heated within the radius of 1.5 mm from the focal point. The resultant temperature increase can be calculated according to

$$\Delta T = \frac{1\times\ 10^{-2}[J]}{4.2\times\ 10^{-3}\ \left[\frac{J}{mm^3\cdot K}\right]\times\frac{4\pi\times(1.5\ [mm])^3}{3}\times\frac{1}{2}} = 0.34[\mathrm{K}]\,. \tag{3.2.27}$$

Although the underlying assumptions should result in an overestimation of the effect, the calculated temperature increase is negligibly small. Consequently the temperature increase by the laser irradiation do neither affect measurements of cell adhesion strength nor influence the cell viability. To confirm the stability and statistical reliability of the assay, calibration measurements were performed as described previously. Briefly, before and after several series of experiments the relationship between the pulse energy E_{pulse} and the hydrodynamic pressure P of the generated wave was determined. For this purpose, a piezoelectric hydrophone (Müller-Platte Needle Probe, Dr. Müller Instruments, Oberursel, Germany) was placed 1.5 mm away from the focal point of the ps laser pulse and 0.1 mm above the substrate. A data set was recorded displaying the hydrodynamic pressure P as a function of the laser pulse energy E_{pulse}. Figure 3.14 represents the hydrodynamic pressure P plotted as a function of E_{pulse}, yielding $P \propto (E_{pulse})^{0.47}$. In cell detachment assay, the laser pulse energy E_{pulse} was increased until all cells were detached. The successful detachment of HSPC was distinguished from remaining adherent cells by recording phase contrast images before and after the pressure wave was generated. A significant displacement of the detached cell of around 10 µm was observed. Four positions per cell incubation chamber were selected to get sufficient statistics. Thereafter, the pressure affecting HSPC can be deduced from the obtained calibration curve. Finally, the critical pressure P^* for cell detachment was determined by fitting the obtained data with a sigmoidal curve with P^* corresponding to the detachment of 50 % of adherent cells.

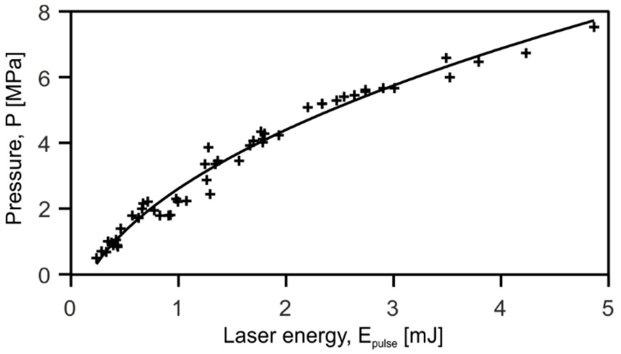

Figure 3.14 | Pressure-energy relationship of the pressure wave assay. The calibration curve depicts the hydrodynamic pressure P as a function of the laser pulse energy E_{pulse}, yielding $P \propto (E_{pulse})^{0.47}$. It was recorded prior each series of experiments by using a piezoelectric hydrophone.

3.2.2.3 Results and discussion

In Figure 3.15A, single HSPC adhering to the *in vitro* niche models displaying SDF1α at different average lateral distances $<d_{SDF1\alpha}>$ are shown before and after their successful detachment illustrating their viability after detachment. Figure 3.15B represents the critical pressures P^* for the detachment of HSPC plotted as a function of $<d_{N\text{-}Cadherin}>$ (blue) and $<d_{SDF1\alpha}>$ (red). The pressure wave assay was performed within the range of $<d>$ ~ 5.5 – 25 nm, at which the majority of cells were identified as "adherent" (Fig. 3.9C). The critical pressure P^* showed a clear decrease corresponding to an increase in the average intermolecular distance $<d>$ of ligand molecules within this range. In contrast to the results on the adhesion area (Fig. 3.11C), this assay magnified differences in the strength of HSPC adhesion to the *in vitro* niche model displaying SDF1α and N-cadherin at small $<d>$. For example, the critical pressure P^* to detach HSPC from the *in vitro* niche model functionalized with SDF1α at $<d_{SDF1\alpha}>$ ~ 11 nm (P^* ~ 6.4 MPa) was more than two times higher compared to the corresponding value on membranes displaying N-cadherin at $<d_{N\text{-}cadherin}>$ ~ 11 nm (2.8 MPa). The comparison between the two binding axes yielded significant differences in the binding strength. Adhesion strength of HSPC based on the CXCR4/SDF1α axis was significantly higher compared to the homogeneous interaction between two N-cadherin molecules. This difference indicate the different binding affinities of single ligand-receptor pairs. Furthermore, this finding suggests differences in the surface expression of the receptors.

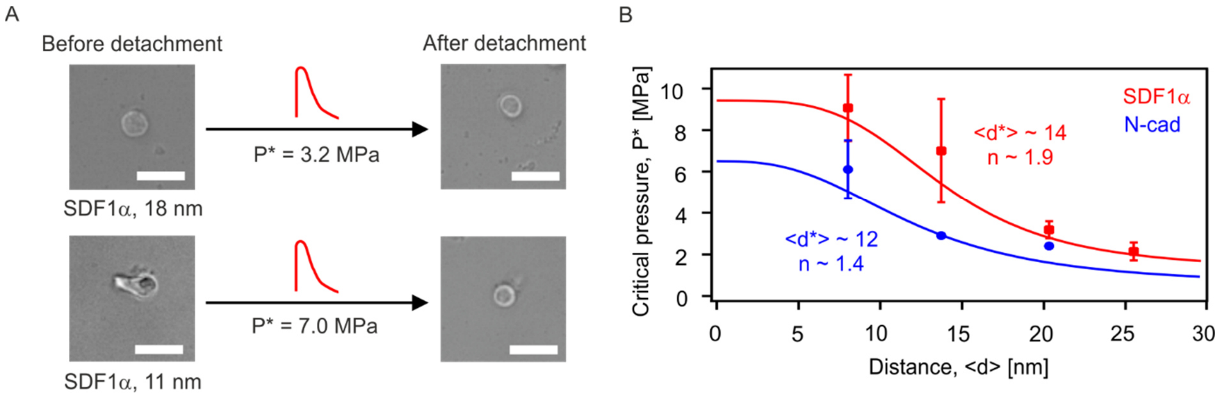

Figure 3.15 | SDF1α mediates a higher adhesion strength compared to N-cadherin. (A) Bright-field images of individual HSPC on membranes displaying SDF1α at $<d>$ ~ 18 nm (upper) and $<d>$ ~ 11 nm (lower) before and after its detachment by pressure waves (red waves) at t = 2 h (scale bar: 10 μm). Applying a laser-induced pressure wave, HSPC were displaced from the substrate and shifted by about 10 μm. Subsequently, HSPC were able to adhere again to the *in vitro* niche model niche as evidence for its viability. (B) Critical detachment pressures P^* determined for HSPC on supported membranes at t = 2 h, plotted as functions of $<d_{N\text{-}cadherin}>$ (blue) and $<d_{SDF1\alpha}>$ (red). Data points represent means ± SD for n = 50 cells.

Nevertheless, as the exact amount of the receptors on the HSPC surface is not known, further discussions would be speculative.

In line with previous experiments, the influence of soluble SDF1α on the adhesive strength of HSPC, which adhered to *in vitro* niche models displaying SDF1α at $<d_{SDF1\alpha}>$ ~ 11 nm and 18 nm, was investigated (Table 3.3). The presence of the physiological concentration of soluble SDF1α caused a significant reduction of the adhesive strength. For example, the critical pressure for cell detachment was reduced by factor of two at $<d_{SDF1\alpha}>$ ~ 11 nm. These findings agrees well with the data, which is presented in Chapter 3.2.1.3. Finally, it should be noted that the direct comparison between the P^* values obtained here and those obtained by other experiments (e.g. micropipette aspiration, AFM, magnetic tweezers) was not possible due to differences in the experimental setup. The reason for this is a difference in the characteristic time window for the bond rupture by several orders of magnitude. As demonstrated by Merkel *et al.*, the rupture force for individual bonds is strongly dependent on the loading rate which corresponds to the applied force in a certain time window. In the pressure wave assay, HSPC are exposed to the pressure wave only for 80 ns which is more than 10^7 times shorter than loading rates utilized in other assays[174-176]. In fact, such a short exposure to pressure waves eliminates both inelastic deformation of cells and remodeling of cytoskeleton during the cell detachment from our assays.

Table 3.3 | Soluble SDF1α decreased the strength of cell adhesion. The critical pressure P^* for cell detachment in the presence and absence of 5 ng/mL SDF1α at t = 2 h. The experiments were performed at two different average lateral distances, $<d_{SDF1\alpha}>$ ~ 11 nm and 18 nm. The values represent means ± SD for n = 50 cells.

	P^* [MPa]	
$<d_{SDF1\alpha}>$ [nm]	**11**	**18**
without SDF1α	7.0 ± 2.5	3.2 ± 0.2
with SDF1α	3.6 ± 0.7	2.2 ± 0.4

3.2.2.4 Summary

The pressure wave assay revealed significant differences in the adhesion strength of HSPC to the *in vitro* models of bone marrow niche and, therefore, delivered complementary results to the microinterferometry experiments.

First, the obtained results showed significant differences between the two ligand-receptor axes at low average intermolecular distances <d> ~ 5 - 25 nm, which could not be identified by RICM. Second, the adhesion mediated by the SDF1α/CXCR4 axis is significantly stronger compared to the binding of HSPC to N-cadherin functionalized supported membranes. The differences can result from different amounts of the receptors on the cell membrane of HSPC which are not known until now but can be deduced from quantitative fluorescence activated cell sorting experiments (FACS).

As already mentioned above, cellular adhesion is based on a counter play of different kind of forces. The formation of ligand-receptor pairs leads to force generation by the adherent cell towards the substrate and provides a basis for mechanosensing of the cells which itself regulates various cellular responses on molecular level[177]. Mechanoresponse of the adherent cell requires the active involvement of the cytoskeleton (e.g. actin) at the adhesion site[178]. As CXCR4 is not connected to the cytoskeleton, but intracellularly associated with heterotrimeric G proteins[179], this process does not involve any direct participation of the cytoskeleton. In contrast, N-cadherin is coupled to the actin network of the cell via a catenin complex including α-, β-, γ- and p120-catenin[144, 180]. There, it has been reported that the cell adhesion on substrates displaying immobilized N-cadherin leads to the formation of adherens junctions resulting in mechanotransduction[145]. Although the extracellular domains of N-cadherin anchored on supported membranes via lipid anchors can undergo lateral diffusion on membrane surfaces, we observed no distinct change in the cellular adhesion patterns for the first two hours after cell seeding.

3.2.3 Statistical image analysis of stochastic morphological dynamics[*]

3.2.3.1 Theoretical background

Cell migration plays a fundamental role in many biological processes. It orchestrates morphogenesis[181], wound healing[182], tumor invasion[183] and immune response[184] and can be usefully conceptualized as a cyclic process[185]. The initial step of a migrating cell is to polarize due to actin polymerization forming protrusions (e.g. lamellipodia or filopodia) in the direction of motion (Fig. 3.16). Then, the leading edge is stabilized due to ligand-receptor pairs with adjacent cells which are linked to the cytoskeleton. At these focal adhesions, the cell is able to produce traction forces allowing it to move forward. Finally, ligand-receptor pairs are disassembled at the trailing edge. This dynamic process depends on several external factors. The geometry and elasticity of the microenvironment is one of the important aspects[186]. For example, cancer cells show a broad variety of migration mechanisms by sensing their environment which allow them to invade different tissues.

---

[*] Data and figures displaying the morphological dynamics of HSPC on SDF1α functionalized membranes are property of Dr. Cornelia Monzel and are inserted for comparison.

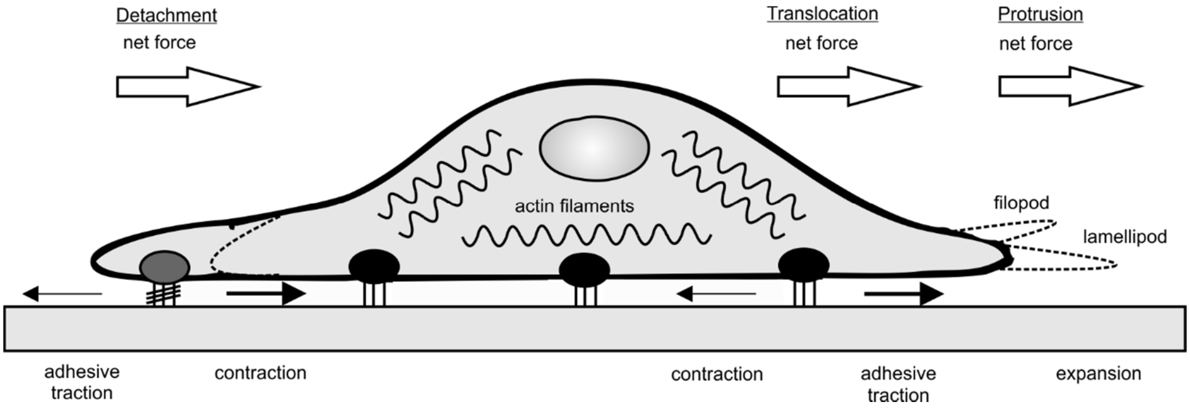

Figure 3.16 | Schematic illustration of different forces involved in cell migration. [adopted from Lauffenberger & Horwitz[185]]

They can migrate as individual cells, or expand in cell clusters by collective cell migration dependent on their environment[187]. Beside mechanical stimuli, cells are enforced to migrate due to molecular stimuli such as chemokines[188, 189]. The secretion of these soluble factors is dynamically up- and downregulated due to signals from the sympathetic nervous system and usually present as a gradient[15]. After binding to cell receptors, they trigger various signaling pathways connected to cell migration such as those mediated by Rho family proteins[190, 191]. Rho family small guanosine triphosphate (GTP) binding proteins are regulators of actin polymerization and adhesion sites and thus control the formation of lamellipodia and filopodia.

Physics of cell migration

Besides the biological mechanisms, it is also important to understand the physical background of cell migration in a quantitative manner. [It should be noted that in the following discussions, all physical descriptions are based on non-chemotactic migration.] Especially, the relationship between cell shape and motility should be determined to be able to interconnect biological signaling with physical principles (e.g. force generation). First descriptions were based on a simple random walk model which describes the motion of a particle as uncorrelated and unbiased, meaning that every migration step is independent from the former one and its direction. In 1905, Albert Einstein provided one of the first physical descriptions for the diffusive random walk model as he introduced his theory on Brownian motion which describes the mean square displacement $<d(t)^2>$ of a particle as a diffusive motion[192, 193]. As depicted in Fig. 3.17A, molecules or small particles with the mass m and the radius r diffuse randomly in a medium with the viscosity η driven by thermal energy k_bT according to the equation

$$\langle d(t)^2 \rangle = 2n_{dim}Dt\ , \tag{3.2.28}$$

where n_{dim} corresponds to the dimension in space in which the motion takes place. According to Einstein's theorem, *D* represents the diffusion coefficient which connects the Brownian motion with the Stokes drag coefficient γ_o as given by

$$D = \frac{k_B T}{\gamma_o} = \frac{k_B T}{6\pi\eta r}. \tag{3.2.29}$$

The Austrian biologist Przibram[194] and the German physicist Fürth[195] first applied this theory towards the description of the motion of protozoa. Fürth discovered that the motion of cells has a certain persistence in directionality and thus cannot be described by Equ. 3.3.28. He demonstrated that Equ. 3.3.28 has to be modified to

$$\langle d(t)^2 \rangle = 2 n_{dim} D \left(t - P \left(1 - e^{-\frac{t}{P}} \right) \right), \tag{3.2.30}$$

where *P* denotes the persistence time (Fig. 3.17B). According to this finding, Gail and Boone interpreted their data on the motion of murine fibroblasts according to this equation[196]. Afterwards, several studies have been published using the model of a persistent random walk to analyze cell migration[197-200]. Nevertheless, many studies detected a deviant migration behavior. Whereas in a typical diffusive random walk, the mean square displacement $<d(t)^2>$ is linearly related to time, some cases were identified where $<d(t)^2>$ may not be diffusive, causing a power-law relationship of $<d(t)^2>$ from time:

$$\langle d(t)^2 \rangle \sim t^{\beta}\,. \tag{3.2.31}$$

This type of migration can be described anomalous diffusion and is categorized in four distinct cases[201, 202]: (1) In case of $\beta = 0$, no movement occurred over the period of observation. (2) A value of β smaller than 1 describes subdiffusion since $<d(t)^2>$ increases at a slower rate than in the case of standard diffusion (Fig. 3.17C, blue). Such situations typically occur when waiting times between each step of motion are included. The standard relation between $<d(t)^2>$ and time for diffusive motion has a β value of 1 (Fig. 3.17C, red). (3) When the step lengths of the walk are based on a distribution with infinite variance, a β value between 1 and 2 is obtained (Fig. 3.17C, green). Such a motion is referred to as Lévy walk[203] and most applicable to the migration of biological cells although its general applicability is still open to debate. (4) In case of ballistic movement, $<d(t)^2>$ increases quadratically with *t* ($\beta = 2$).

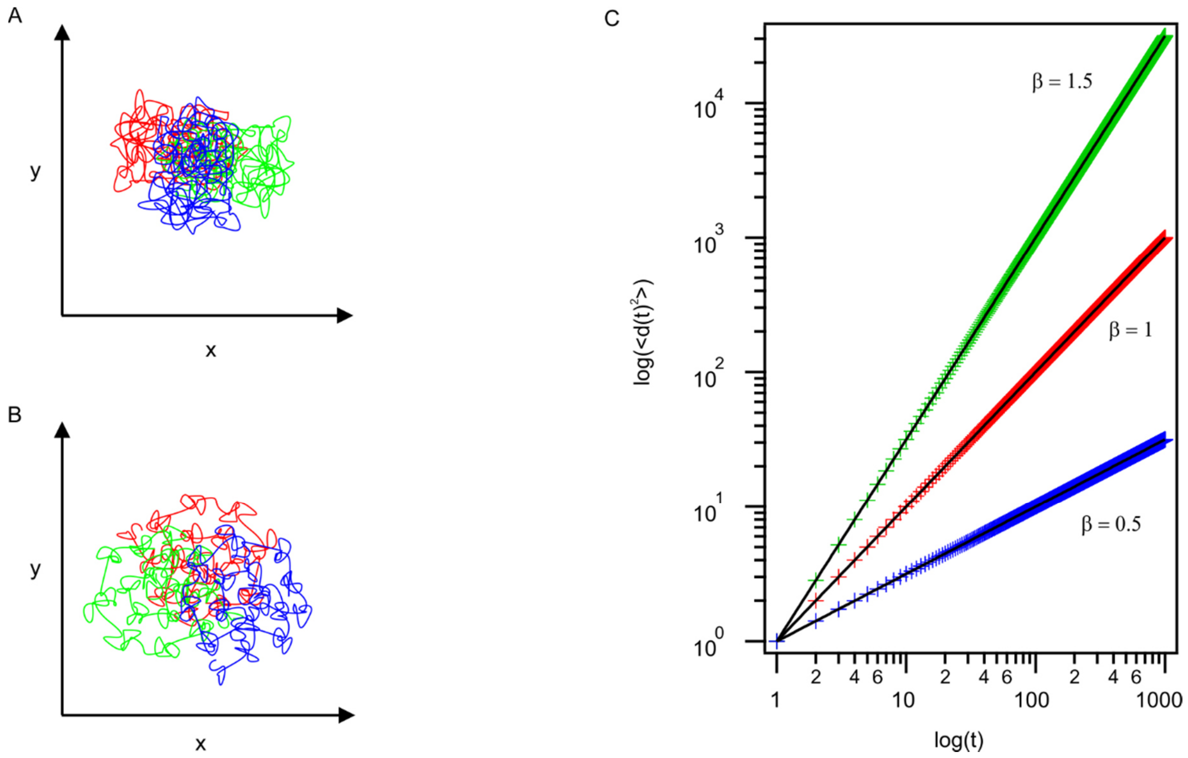

Figure 3.17 | Exemplary presentations of cell migration behavior. Sample tracks illustrate (A) diffusive random walk and (B) persistent random walk. (C) Cell migration in the framework of anamolous diffusion. The linear relation between $<d(t)^2>$ and t is obtained in case of Brownian motion with $\beta = 1$ (red). For $\beta < 1$, $<d(t)^2>$ increases at a slower rate than in the case of standard diffusion referred to as subdiffusion (blue). In case of superdiffusion, $\beta > 1$ caused by step lengths which are based on a distribution with infinite variance. (green). The black lines correspond to the best fits based on Equ. 3.2.31.

However, cellular motion is based on an active process triggered by external stimuli causing actin polymerization inside the cell and thus cannot be described only by diffusive motion driven by thermal energy. In such cases, the cellular motion is correlated and biased as it has a certain degree of memory and persistence. Thus, further developments on the physical description of cell migration were made by introducing the theory of deformable self-propelled particles[204, 205] which arises from theory of non-linear dynamics and non-equilibrium statistical physics. In the simplest case, deformable self-propelled particles produce an active motile force of a fixed magnitude which acts along the same direction for an average duration (persistence time). Additionally, they are able to change their shape during migration. Although several studies have been published dealing with the theoretical description of the motion of deformable self-propelled particles[205-207], only a few studies have investigated the correlation of migration and shape deformation in single eukaryotic cells experimentally[197, 208-210]. For example, Partin *et al.* analyzed cell motility of cancer cells, and found that different types of shape deformation correlated with increasing metastatic potential[211]. Cell migration plays an important role in the maintenance of the

HSPC pool and in the regeneration of blood. Deep knowledge of the underlying mechanisms is necessary to improve the enforced mobilization of HSPC for stem cell donation and chemotherapy. HSPC are unique in their ability to migrate to various sites during embryonic development as well as post-natal, ensuring the safety and integrity of their regenerative potential. Already in 1950, Jacobsen and co-workers demonstrated that HSPC from spleen were able to recover the stem cell pool in murine bone marrow after a lethal dose of irradiation[212]. Such and comparable studies demonstrated that HSPC spontaneously "home" and thus opened the path to the development of stem cell transplantation. HSPC migration is a complex process which is regulated by the nervous system and enabled by the vasculature which permeates the bone marrow. The main steps include homing, lodgment and retention, and circadian release[213]. A central role in the process of mobilization and immobilization plays the chemokine stromal-derived factor-1α (SDF1α) which interacts with the G-protein coupled receptor CXCR4 expressed on the HSPC surface. SDF1α is present as dissolved molecule as well as on the surface of endothelial cells triggering the coordinated action of several CAM and downstream pathways leading to adhesion and chemotaxis of HSPC. Aiuti *et al.* were the first who demonstrated that SDF1α is displayed as a gradient in bone marrow and triggers the migration of HSPC[33]. Levels of SDF1α in bone marrow follow a circadian pattern and are regulated by rhythmic release of noradrenaline by the sympathetic nervous system[15, 27]. The number of peripheral HSPC fluctuate in antiphase with SDF1α expression in bone marrow. Additionally to SDF1α, also CAM regulate trafficking of HSPC. For example, van Buul *et al.* demonstrated that HSPC migration across bone marrow endothelium is regulated by vascular endothelial cadherin[214]. Although N-cadherin is a dominant molecule in the osteoblastic sub-niche in bone marrow[11, 12] and was found in close proximity to HSPC, the role of N-cadherin for the migration of HSPC was not yet investigated. Until now, it is not clear how the interplay of SDF1α and CAM, such as N-cadherin, orchestrate the maintenance of the HSPC and their progenitor cells. Recent studies suggest that such ligand-receptor interactions may work together in a complex network within which the SDF1α-CXCR4 axis appears to play a prominent role. Further studies are needed to understand the differential roles not only for a deeper understanding of the trafficking between stem cell niche and periphery but also to understand the migration between different sub-niches in bone marrow.

In the present study, HSPC migration was analyzed by calculating the autocorrelation maps and corresponding power spectra in Fourier space in order to extract characteristic spatio-temporal patterns from the morphological dynamics of HSPC in response to either SDF1α or N-cadherin functionalized supported membranes. In line with previous studies on the adhesion of HSPC (Chapters 3.2.1 and 3.2.2), the influence of dissolved SDF1α was investigated in addition. Similar analyses have been applied extensively to characterize the mainly thermal fluctuations in model membranes and erythrocytes[211]. As the dynamic fluctuations of nucleated cells comprise mostly active processes, the power spectrum analyses yield additional insight into the energy dissipation through cellular deformation and give experimental evidence for the theory of deformable self-propelled particles.

3.2.3.2 Experimental realization

HSPC were seeded on *in vitro* niche models displaying either SDF1α or N-cadherin at average intermolecular distances $<d_{SDF1\alpha}>$ ~ 6, 18 and 34 nm, and $<d_{N\text{-}cadherin}>$ ~ 18, 34 and 47 nm, respectively, according to the procedures described in Chapters 3.1.4 – 3.1.9. Time-lapse movies were recorded with a Keyence BZ-9000 microscope (Keyence, Osaka, Japan), equipped with a Plan Fluor 40x/0.6 air objective. 1-2 positions per condition were chosen and recording of phase contrast images was undertaken over 6 hours with a frame rate of 0.025 Hz. Acquired movies were drift corrected utilizing cross-correlation analysis implemented in ImageJ[215]. Further image analysis was based on a routine written in Matlab by Dr. C. Monzel and performed according to the following steps: Each image of the time-lapse movies was analysed by an image segmentation algorithm to determine the peripheral edge of individual cells by pixel intensity (Fig. 3.18A) and the x-y coordinates of the center of mass. The x-y coordinates for each of the 90 individual contours were summarized to display the cell trajectory. Second, the radial distance r originating from the center of mass was plotted in polar coordinates θ (Fig. 3.19B). An amplitude map $r(\theta,t)$ was obtained by displaying the time evolution of the radial distances for 60 min (Fig. 3.18C). Finally, the corresponding autocorrelation map $\Gamma_{rr}(\theta,t)$ was calculated according to

$$\Gamma_{rr}(\theta,t) = \frac{\langle r(\theta+\Delta\theta, t+\Delta t)\cdot r(\theta,t)\rangle}{\langle [r(\theta,t)]^2\rangle} \qquad (3.2.32)$$

as depicted in Fig. 3.18D. Finally, a Fourier analysis was performed to assess temporal changes in the cell morphology during migration in a similar way to Partin *et al.* but calculated in the inertial frame with the origin being the center of mass (i.e. translational motion was not assessed).

$$\hat{\Gamma}_{r,r}(\theta,t) = \langle FT\big(r(\theta,t)\big) * FT\big(r(\theta,t)\big)\rangle \qquad (3.2.33)$$

These calculations enabled the quantitative determination of the predominant mode of deformation.

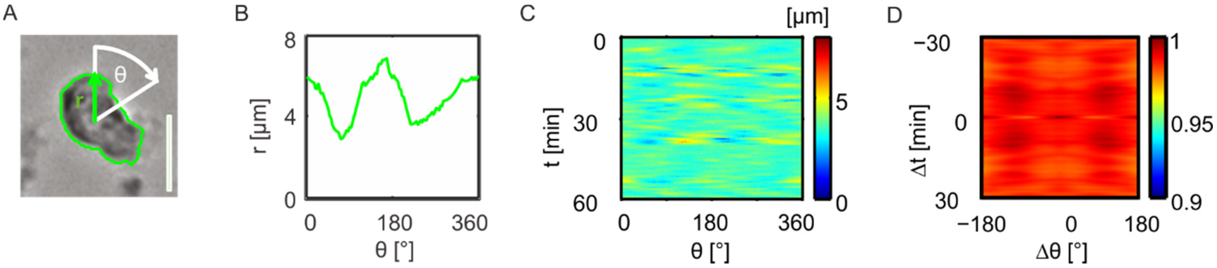

Figure 3.18 | Image analysis performed to quantifiy morphological dynamics and the mode of deformation of HSPC on the *in vitro* niche model. (A) Phase contrast image of individual HSPC on the *in vitro* niche model. The peripheral edge of the cell (green line) was determined by the contrast in pixel intensity. Scale bar: 10 µm. (B) The radial distance *r* plotted in a polar coordinate *θ*. (c) The amplitude map *r(θ,t)* as a function of angle θ over time. (D) The autocorrelation $\Gamma_{r,r}(\theta,t)$ corresponding to the amplitude map in panel (C).

3.2.3.3 Results and discussion

After detailed investigations of HSPC adhesion, the morphological dynamics of HSPC during cell migration on *in vitro* niche models of bone marrow niche were assessed by time-lapse imaging in combination with statistical image analysis. Thereby, the differences between both ligand-receptor pairs could be quantified and thus complemented previous findings made by microinterferometry and pressure wave assay. The underlying image analysis was in line with previous reports describing cell motion as an active process where active morphological dynamics correlate with translational motion[210, 211]. Ligand spacings were selected in the transition region for HSPC binding/unbinding as identified by adhesion experiments.

First, migration and morphological dynamics of HSPC on membranes displaying SDF1α at different average intermolecular distances $<d_{SDF1\alpha}>$ were analyzed. Figure 3.19 depicts phase contrast images including the trajectory of HSPC at t = 120 – 210 min after cell seeding (A-C), the amplitude maps (D-F) and the corresponding autocorrelation maps (G-I). The analysis revealed that the migration behavior of HSPC can be subdivided into three main categories: (1) At small average intermolecular distances of SDF1α, e.g. $<d_{SDF1\alpha}> \sim 6$ nm, a featureless amplitude map was obtained suggesting that the morphology of HSPC remained round (Fig. 3.19D). Furthermore, a quick decay of autocorrelation over time (Fig. 3.19G) implied that HSPC dynamics are dominated by rotational motion. As a small average intermolecular distance $<d_{SDF1\alpha}>$ coincided with a high adhesion area A_{Adh} and strength (Chapters 3.2.1 and 3.2.2), HSPC were strongly pinned to the *in vitro* niche model and thus had little degree of freedom to deform their shape and the translational motion was blocked. (2) At an intermediate average intermolecular distance $<d_{SDF1\alpha}> \sim 18$ nm, HSPC started to polarize by the formation of protrusions, followed by a similar extension in the perpendicular direction (Fig. 3.19B, E, H). Such an oscillatory deformation could be identified from the periodic appearance of peaks at $\Theta = 0/180°$ and $90/270°$ in the autocorrelation map (Fig. 3.19H). This finding suggested that HSPC first stretched pseudopods along the long axis to find new binding spots, followed by a retraction towards a round shape, and, thereafter, the formation of pseudopods in a perpendicular direction. (3) When the average intermolecular distance was further increased, e.g. $\langle d_{SDF1\alpha} \rangle \sim 34$ nm, shape deformations became less prominent. This finding was accompanied by a high translational displacement of the cell (Fig. 3.19C, F, I) and can be explained as a results of weak adhesion.

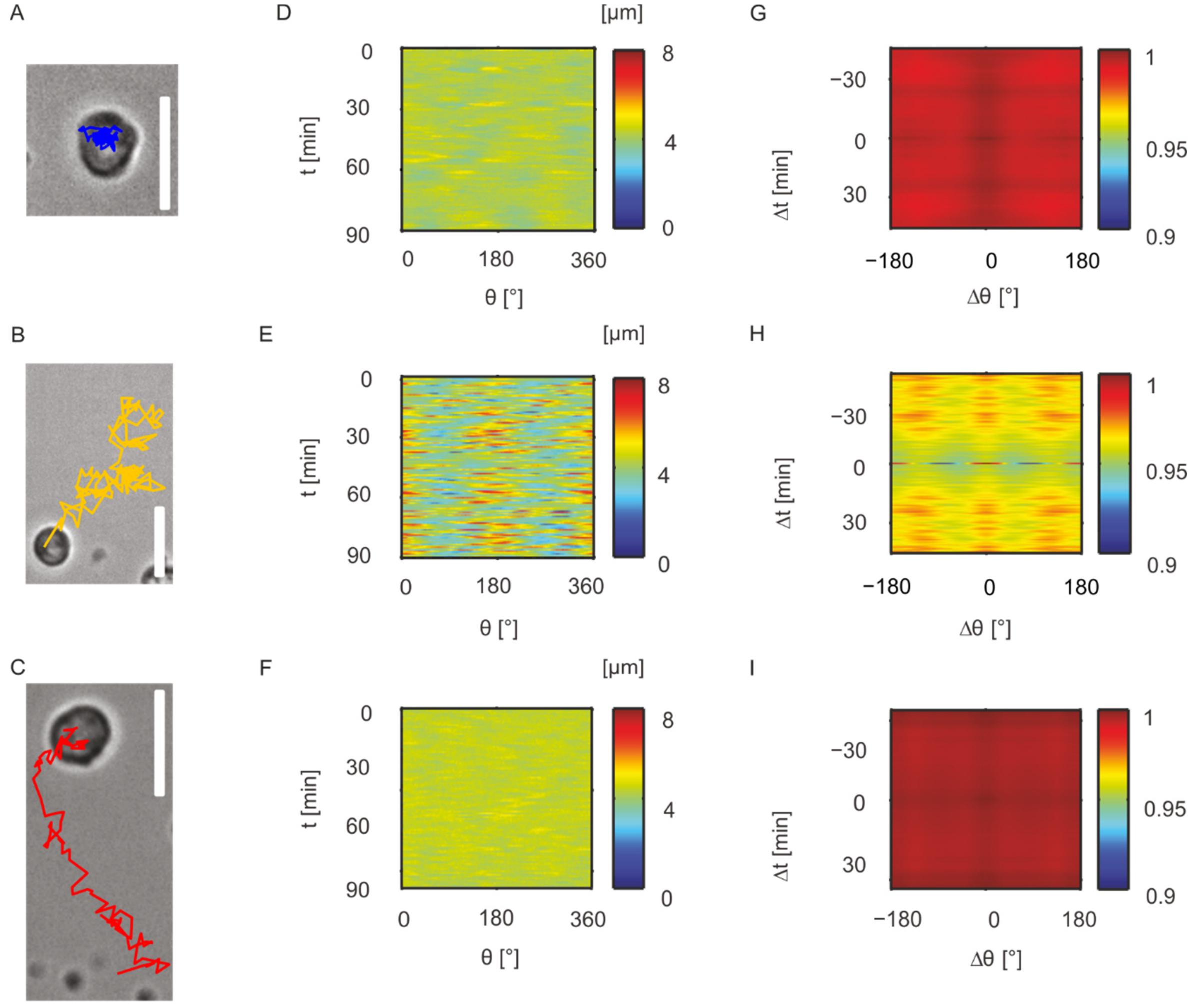

Figure 3.19 | HSPC motion can be categorized into three major classes. Morphological dynamics of HSPC on supported membranes displaying SDF1α: (A – C) phase contrast images and trajectories over 90 min for $t = 2$ h (scale bars: 10 µm), (D - F) amplitude $r(\theta,t)$ maps, and (G - I) the corresponding autocorrelation $\Gamma_{r,r}(\theta,t)$ maps. The patterns could be classified into three representative cases as a function of $\langle d_{SDF1\alpha} \rangle \sim 6$ nm (A,D,G), 18 nm (B,E,H) and 34 nm (C,F,I).

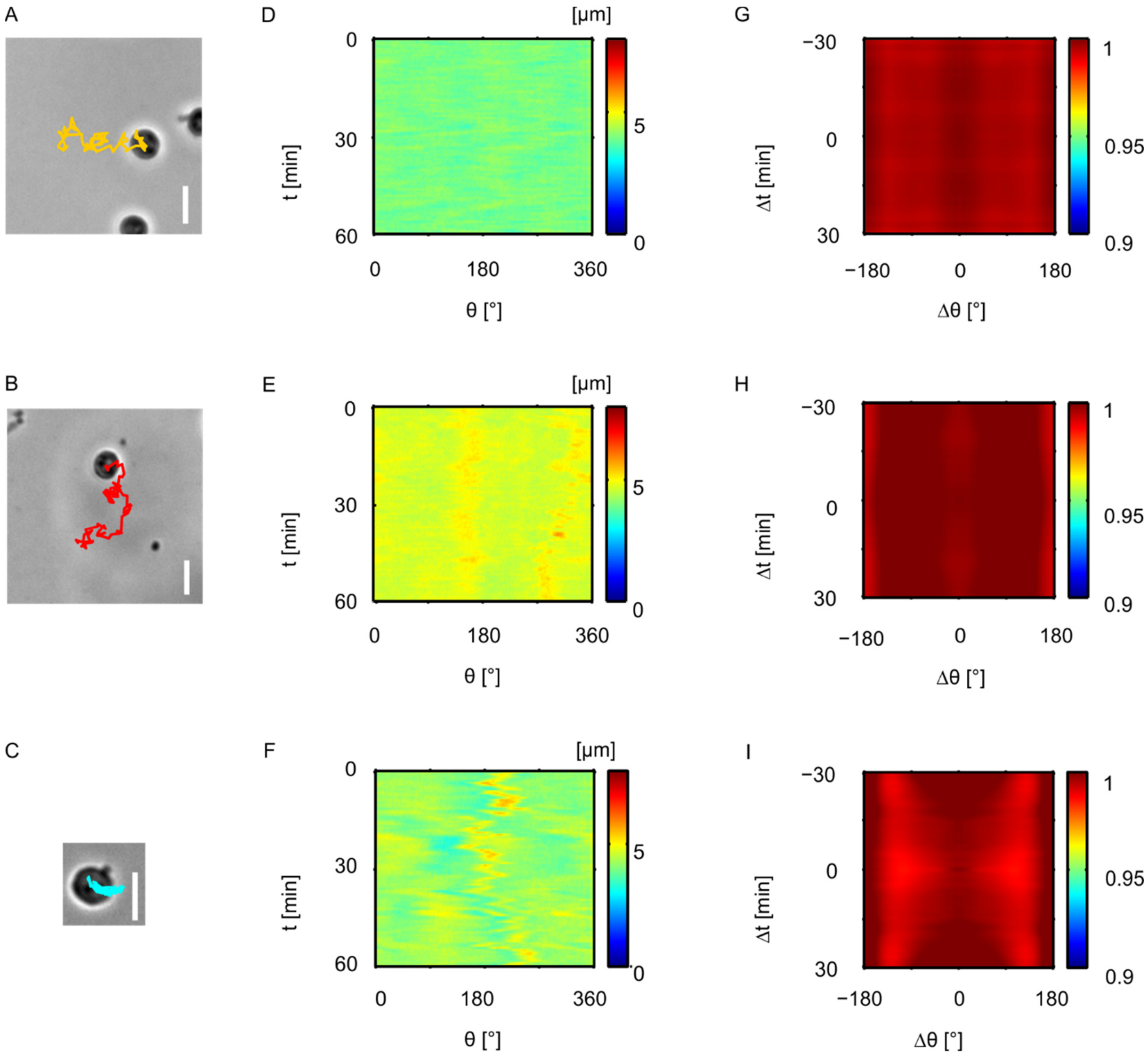

Figure 3.20 | Morphological dynamics of HSPC on membranes displaying N-cadherin. HSPC were observed on membranes displaying N-cadherin at <$d_{N\text{-}cadherin}$> ~ 18 (yellow track), 34 (red track) and 47 nm (cyan track): (A-C) Phase contrast images and trajectories over 60 min (scale bar: 10 µm), (D-F) amplitude maps $r(\theta,t)$, and (G-I) the corresponding autocorrelation maps $\Gamma_{r,r}(\theta,t)$ (t = 2 h).

Second, the morphological dynamics of HSPC on *in vitro* niche models displaying N-cadherin at <$d_{N\text{-}cadherin}$> ~ 18, 34 and 47 nm were assessed. A significantly different migration mechanism could be identified (Fig. 3.20). First, the trajectory length decreased with increasing <$d_{N\text{-}cadherin}$>. This finding suggests that the translational motion of HSPC on membranes displaying N-cadherin increases with stronger pinning to the substrate. Second, at low <$d_{N\text{-}cadherin}$>, a featureless amplitude and autocorrelation map was identified. Third, at intermediate average intermolecular distances, e.g. <$d_{N\text{-}cadherin}$> ~ 34 nm, HSPC showed mainly oscillatory deformations, which were much less pronounced compared to HSPC on SDF1α functionalized membranes. Additionally, there was no formation of protrusions observed. These findings suggests that the migration of

HSPC mediated by the homophilic N-cadherin axis follow a different mechanism compared to the migration mediated by the heterophilic SDF1α/CXCR4 axis. Whereas the translational motion of HPSC on SDF1α functionalized membranes was accompanied by the formation of protrusions in order to 'find' new binding spots, HSPC on N-cadherin functionalized membranes migration behavior suggested a rolling motion. Previous studies demonstrated that SDF1α is present as soluble and immobilized molecule in bone marrow niche. Therefore, the impact of soluble SDF1α on HSPC motility was investigated. Figure 3.22 depicts the results of the statistical analysis of stochastic morphological dynamics for three experimental conditions: HSPC on *in vitro* niche models displaying SDF1α at $<d_{SDF1\alpha}> \sim$ 6, 18 and 34 nm in the presence of dissolved SDF1α (5 ng/mL). The counterplay between dissolved vs. immobilized SDF1α decreases the trajectory lengths (Fig. 3.22A-C) and dampens the maxima in the autocorrelation maps (Fig. 3.22H).

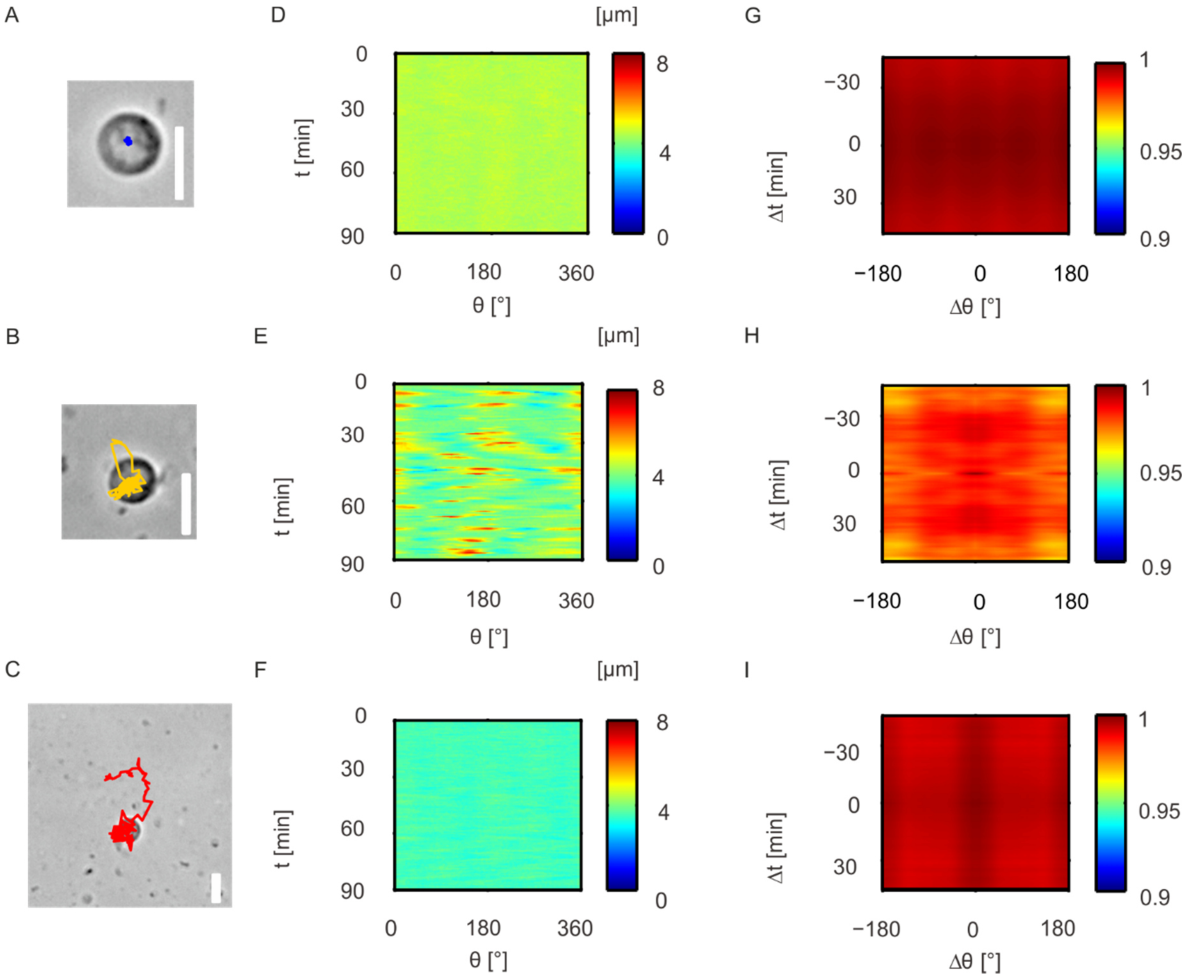

Figure 3.21 | The counterplay between soluble and immobilized SDF1α dampened morphological dynamics. HSPC were observed on membranes displaying SDF1α at $<d_{SDF1\alpha}> \sim$ 6 (blue track), 18 (orange track) and 34 nm (red track) in the presence of dissolved SDF1α: (A-C) Phase contrast images and trajectories over 90 min (scale bar: 10 μm), (D-F) amplitude maps $r(\theta,t)$, and (G-I) the corresponding autocorrelation maps $\Gamma_{r,r}(\theta,t)$ (t = 2 h).

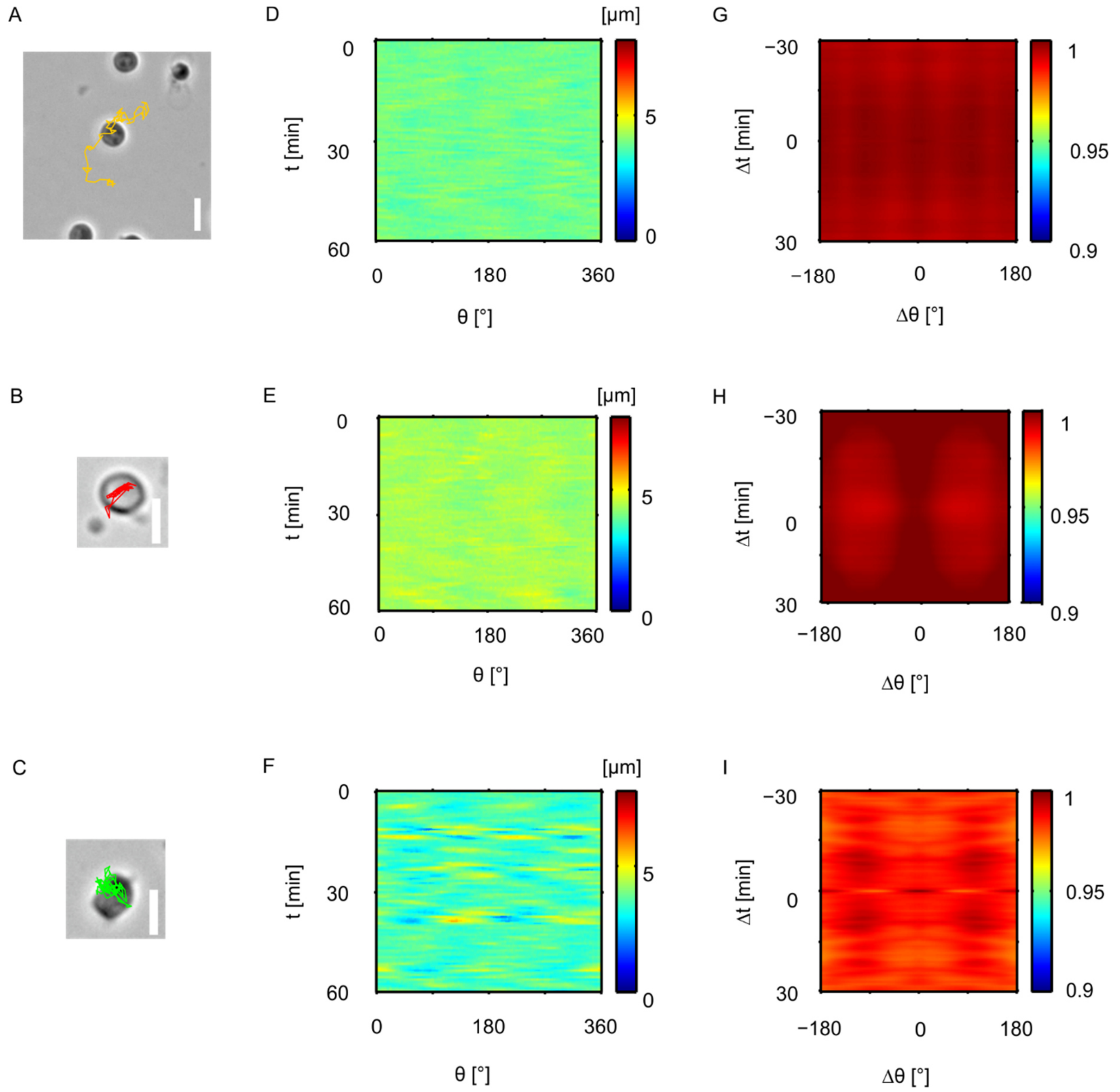

Figure 3.22 | Soluble SDF1α did not affect morphological dynamics of HSPC on N-cadherin functionalized *in vitro* niche models. HSPC were observed on membranes displaying N-cadherin at $<d_{N\text{-}cadherin}>$ ~ 18 (blue track), 34 (orange track) and 47 nm (red track) in the presence of soluble SDF1α: (A-C) Phase contrast images and trajectories over 60 min (scale bar: 10 µm), (D-F) amplitude maps $r(\theta,t)$, and (G-I) the corresponding autocorrelation maps $\Gamma_{rr}(\theta,t)$ (t = 2).

Although SDF1α was found to increase actin polymerization[162], shape deformations were less pronounced when the total amount of SDF1α (immobilized + soluble) was higher. This finding can be attributed to the partial blocking of the receptor CXCR4 causing a decrease in adhesion strength, as already identified by RICM and pressure wave assay. The question arises, if there is also an effect of soluble SDF1α on the morphological dynamics of HSPC which adhere to N-cadherin functionalized supported membranes. Therefore, the influence of soluble SDF1α (5 ng/mL) on the migration and morphological dynamics of HSPC on N-cadherin modified membranes was analyzed. The presence of dissolved SDF1α hardly affected the strength of deformations (Fig. 3.23). This finding supports the aspect that SDF1α specifically binds to CXCR4 and is a competitor of the interaction between CXCR4 and immobilized SDF1α whereas the homophilic interaction of N-cadherin is not involved in this competition. Finally, active cell motion was quantified by mode analysis and calculations of the energy which is dissipated during shape deformations. For this purpose, a mode analysis of the power spectrum from the Fourier transform of amplitude maps $FT(r(\theta,t))$ for m = 0, 1, 2, 3,… was performed as reported by Partin *et al.*[211]. Exceptionally, the calculation was carried out in the inertial frame with the origin being the center of mass (i.e. the translational mode was not assessed). By the use of a Fourier analysis, spatial harmonics of the sinusoidal frequency of shape deformation were extracted. It should be emphasized that the power spectrum analysis in Fourier space enables the discrimination of different modes (m) of deformation and energy consumption of HSPC in the presence and absence of soluble SDF1α at various $<d_{\mathrm{SDF1}\alpha}>$, which cannot be assessed by the shape analysis in real space. This analysis allowed for the determination of the predominant mode of deformation followed by the quantification of the power dissipation. Figure 3.24 depicts the power spectra (A,C) and total power of cell deformation (B,D) for HSPC on SDF1α and N-cadherin functionalized supported membranes at various average intermolecular distances $<d>$. In case of both ligand-receptor axes, the calculated power spectrum of HSPC exhibited peaks at mode number m = 2 for various $<d>$, implying that the mode of HSPC deformation was predominantly oscillatory (inset). Such deformation occurred independently from the type of ligands as well as their average intermolecular distances $<d>$. Shape deformations by shrinking or expansion were suppressed for both axes as indicated by a negligible small fraction of mode m = 1. Figure 3.23B and D represent the calculated total power integrated over all modes as a function of $<d_{\mathrm{SDF1}\alpha}>$ and $<d_{\text{N-Cadherin}}>$, respectively, in order to highlight the impact of different ligand spacings on the total energy consumed by HSPC in the presence (crosses) and absence (circles) of soluble SDF1α. HSPC on *in vitro* niche models displaying SDF1α exhibited a higher energy consumption during shape deformation compared HSPC on N-cadherin functionalized membranes (Fig. 3.23B and D). In addition, the amount of energy dissipated by the cell through shape deformation did not monotonically follow the changes in the average intermolecular distance $<d_{SDF1\alpha}>$, reaching the maximum around the successive ligand spacing $<d_{\mathrm{SDF1}\alpha}>$ = 11 and 18 nm. This finding suggests that the magnitude of energy consumed by the deformation of HSPC is not only determined by the intermolecular distance of ligand molecules, but also by the frictional coupling with the contact substrates. Remarkably, this range agrees well with the characteristic average intermolecular distances for binding/unbinding transition determined by the pressure wave assay, $<d_{\mathrm{SDF1}\alpha}>$ = 14 nm.

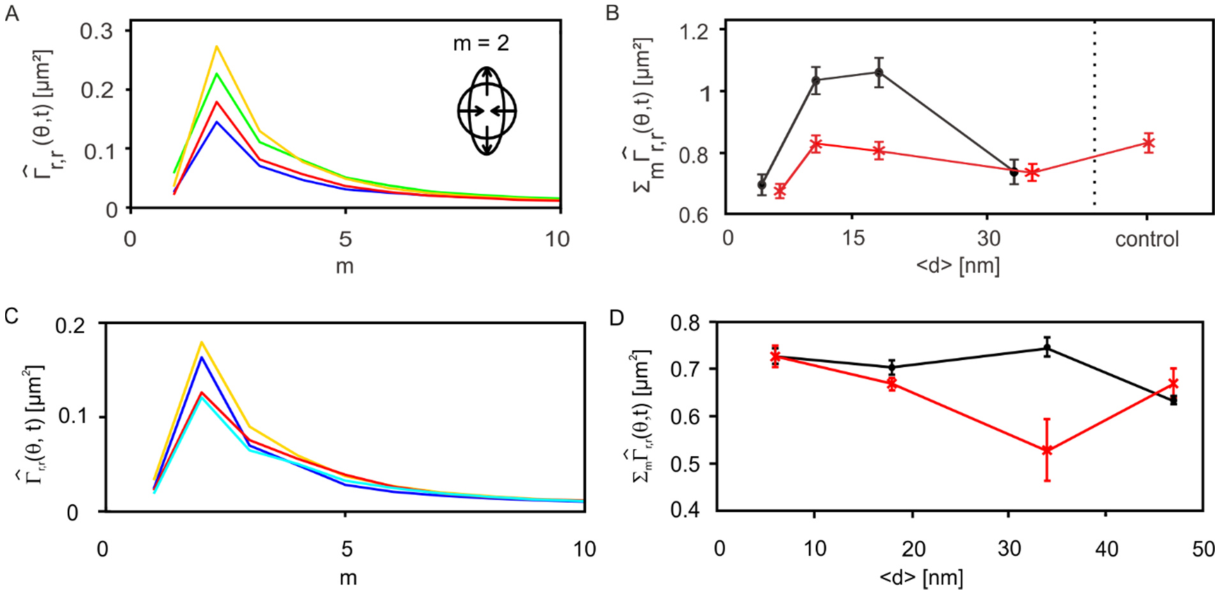

Figure 3.23 HSPC locomotion was mostly based on oscillatory cell deformations. (A) Power spectrum of HSPC at various <$d_{\text{SDF1}\alpha}$> = 6 nm (blue), 11 nm (green), 18 nm (orange) and 34 nm (red). (B) Total power in the presence (crosses) and absence (circles) of dissolved SDF1α plotted vs. <$d_{SDF1\alpha}$>. (C) Power spectrum of HSPC at various <$d_{N\text{-}cadherin}$> = 18 nm (blue), 34 nm (green) and 47 nm (red). (D) Total power in the presence (crosses) and absence (circles) of dissolved SDF1α plotted vs. <$d_{N\text{-}Cadherin}$>. Data points represent means ± SEM for n = 30 cells of three individual experiments.

In contrast, the total power exhibited no maximum over the whole range of <$d_{\text{SDF1}\alpha}$> in the presence of 5 ng/mL dissolved SDF1α (Fig. 3.23, red), suggesting that consumption of energy by HSPC was significantly suppressed in the presence of dissolved SDF1α. The total power $\sum_m \hat{\Gamma}_{r,r}(\theta,t)$, which was dissipated by HSPC on membranes displaying N-cadherin, was much less pronounced compared to those on SDF1α functionalized membranes. Moreover, the total power $\sum_m \hat{\Gamma}_{r,r}(\theta,t)$ was hardly influenced by <$d_{\text{N-Cadherin}}$> or by the presence of dissolved SDF1α. This finding can be attributed to the different role of N-cadherin from SDF1α. The former serves as CAM necessary for the anchorage of HSPC to the bone marrow niche[11], while the latter functions as chemoattractant for HSPC migration[33]. Thus, the dynamic motion of HSPC mediated by N-cadherin is not directly influenced by soluble SDF1α.

3.2.3.4 Summary

The morphological dynamics of HSPC on *in vitro* niche models were assessed by statistical analysis of time-lapse images. Several important findings were made: (1) SDF1α and N-cadherin induced a different migration mechanism. HSPC, which adhered to SDF1α functionalized supported membranes, underwent oscillatory deformations during cell locomotion, which were most pronounced at intermediate average intermolecular distances, $<d_{SDF1\alpha}>$ ~ 18 nm. Cell motility of HSPC on *in vitro* niche models displaying N-cadherin was only weakly accompanied by morphological deformations, suggesting a migration mechanism based on cell rolling. Moreover, the energy dissipation for shape deformations of HSPC on SDF1α functionalized membranes was significantly higher in comparison to deformations of HSPC on N-cadherin functionalized membranes. Furthermore, the power spectra exhibited peaks at around $<d_{\mathrm{SDF1}\alpha}>$ ~ 11 and 18 nm corresponding to the transition points for binding/unbinding. These findings were in line with previous results on the adhesion area and strength. (2) The trajectory length of migrating HSPC decreased with increasing $<d_{SDF1\alpha}>$ which was the opposite for HSPC on N-cadherin functionalized supported membranes. These findings can be attributed to the differential roles of N-cadherin and SDF1α in bone marrow niche. (3) The presence of soluble SDF1α dampened the morphological dynamics of HSPC on *in vitro* niche models displaying SDF1α, but had no influence on the motility of HSPC on N-cadherin functionalized supported membranes. Thus, it can be concluded that the morphological dynamics of HSPC mediated by the homophilic N-cadherin axis is not directly influenced by SDF1α.

The current results demonstrated that the analysis of morphological dynamics of HSPC by Fourier analysis is a very powerful tool to extract the non-equilibrium fluctuation dynamics of HSPC, which are hidden behind the noise and thus cannot be detected by the conventional image analysis in real space.

3.3 Synergistic effect of N-cadherin and SDF1α

3.3.1.1 Theoretical background

Although numerous molecules have been identified in close proximity at the cell-cell contact site between HSPC and bone marrow stromal cells[11, 12, 18, 33], their ability to control stem cell functions via cross-talk are not fully clarified yet. Figure 3.24A depicts a simplified illustration of the role of N-cadherin and SDF1α in the bone marrow niche. Whereas N-cadherin is suggested as important CAM which anchors HSPC to the bone marrow niche[11, 12], SDF1α functions as a chemokine and thus regulates the mobilization and immobilization of HSPC[33, 162]. Signals from SDF1α and N-cadherin may co-regulate processes like adhesion and migration, but little is known about their relative importance in this interplay. Both SDF1α and N-cadherin are involved in actin dynamics which provide the basis for cell motility[216-218]. N-cadherin is indirectly linked to F-actin via a cadherin/catenin complex including β-catenin, α-catenin and several other proteins[144, 180]. Previous studies demonstrated that the formation of adherens junctions by cadherins is correlated with the decease of RhoA and elevation of Rac1 activity. Both RhoA and Rac1 are small GTPases belonging to the Rho family and are central regulators of actin polymerization and cell motility[219]. Moreover, Rho family small GTPases have been implicated in HSPC shape, adhesion, and motility[220, 221]. They act as a mediator of G protein-coupled receptor signaling. In HSPC, SDF1α binding to CXCR4 induces actin polymerization in HSPC resulting in pronounced cell polarization and the induction of HSPC migration[162, 222]. Moreover, SDF1α enhances the association and phosphorylation of proteins involved in the formation of focal adhesions such as paxilin. Paxilin is a focal-adhesion adaptor protein which couples the cytoskeleton to the cell adhesion area and is suggested to play an important role in several signaling pathways[223]. Although paxilin is involved in integrin-regulated signaling, Yano *et al.* reported that this protein participates in processes regulating N-cadherin mediated cell adhesion in HeLa cells[224]. Nevertheless, the interplay between both ligands is still poorly understood.

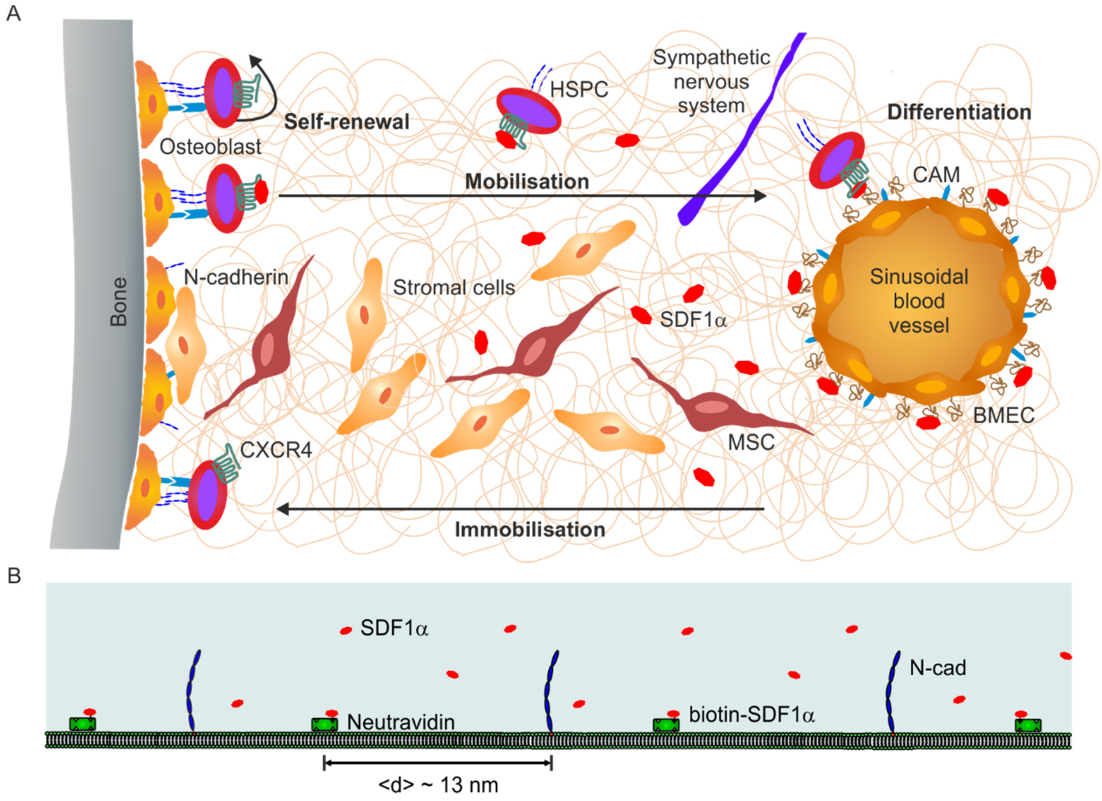

Figure 3.24 | Differential role of SDF1α and N-cadherin in bone marrow niche. (A) Simplified illustration the bone marrow niche depicting of the regulatory process underlying the immobilization and mobilization of HSPC in the bone marrow niche. (B) Supported membranes functionalized with different fraction of SDF1α and N-cadherin at <*d*> ~ 13 nm were used as *in vitro* niche models to investigate synergistic effects of both ligands.

Therefore, the present study was further expanded to elucidate possible synergistic effects of both ligands on adhesion and morphological dynamics of human HSPC. For this purpose, HSPC from CB were seeded on *in vitro* niche models displaying SDF1α and N-cadherin at different ligand fractions with a constant average intermolecular distance <*d*> ~ 13 nm (Fig. 3.24B). Microinterferometry and time-lapse experiments were performed as described in Chapters 3.2.1.2 and 3.2.3.2.

3.3.1.2 Results and discussion

Four different cell morphological characteristics were quantified: (1) The cell aspect ratio as measure of cell polarization. (2) The fraction of adherent cells χ and (3) adhesion area A_{Adh} disclosing any differences between the adhesion behavior of HSPC on membranes with one or two ligands. (4) The morphological dynamics including cell trajectories, modes of deformation *m* and total power of shape deformations, $\sum_m \hat{I}_{r,r}(\theta,t)$, in order to characterize the cell motility. The combination of these measures gave a better understanding of the synergistic effect of different ligand-receptor pairs in the bone marrow niche. Figures 3.25A and B depict phase contrast and RICM images of single HSPC on *in vitro* niche models displaying different fractions of SDF1α and N-cadherin, respectively. The polarization of HSPC were quantified by measuring the cell aspect ratio AR (Fig. 3.25C)

$$AR = \frac{L_1}{L_2}, \tag{3.3.1}$$

which corresponds to the ratio of the longest axis L_1 and the shortest axis L_2. After 2 h of seeding, HSPC became elongated on membranes displaying two ligands but kept their round shape when they were exposed to only one type of ligand. The latter finding was in good agreement with the data obtained before (Chapter 3.2.1). Cell polarization was most pronounced on membranes displaying SDF1α and N-cadherin at a fraction of 1:4 and was accompanied by the formation of a cell protrusion. The formation of these pseudopods (Fig. 3.25A and B, red arrows) is driven by actin filament bundles that polymerize underneath the cell membrane in order to overcome the bending rigidity of the cell membrane[225]. Intriguingly, this behavior was hardly visible for HSPC on membranes displaying only N-cadherin although the intracellular domain of this CAM is indirect linked to the actin cytoskeleton. These findings implied that SDF1α and N-cadherin induce cell polarization in a synergistic effect. The sole presence of N-cadherin seems to be not enough to induce cell polarization. But the coexistence with SDF1α further enhances HSPC polarization as it supports actin polymerization[162]. The formation of pseudopods was also reported migrating leukocytes[226].

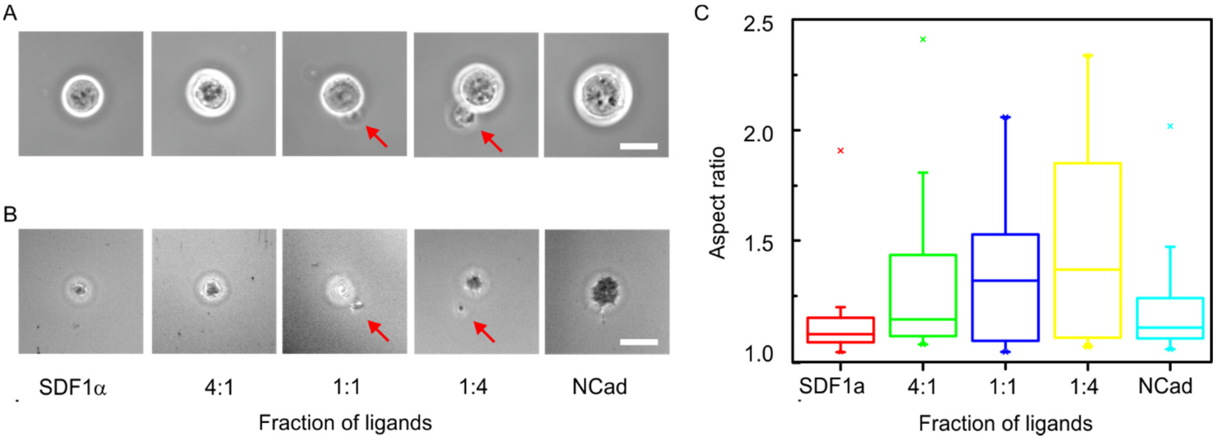

Figure 3.25 | HSPC polarization was enhanced by the simultenous presence of SDF1α and N-cadherin. (A) Phase contrast and (B) RICM images of HSPC on membranes displaying different fractions of SDF1α and N-cadherin at <*d*> ~ 13 nm at t = 2 h: Pure SDF1α (red), SDF1α:N-cad [4:1] (green) SDF1α:N-cad [1:1] (blue), SDF1α:N-cad [1:4] (yellow), pure N-cadherin (cyan). Scale bar corresponds to 10 µm. The red arrows indicate cell protrusions. (C) The corresponding HSPC aspect ratios reveal a significant cell polarization in the presence of two ligands. Box plots show the median and percentiles (box: 0.25 and 0.75, whiskers: 0.05 and 0.95) including extreme values for n = 30 cells.

Similar morphological changes were identified during *in vitro* studies of migrating HSPC and correlated with the redistribution of cell receptors such as CXCR4 and CD44[227]. Then, the adhesion of HSPC was quantified by microinterferometry. Figures 3.26A and B represent the fraction of adherent cells χ and the corresponding adhesion area A_{Adh} of HSPC on membranes displaying different fractions of SDF1α and N-cadherin at <*d*> ~ 13 nm. Neither the fraction of adherent cells χ nor the adhesion area A_{Adh} showed pronounced differences in the presence of two ligands as revealed by a test for statistical significance test. Nevertheless, a slight increase in the adhesion area A_{Adh} was obtained for HSPC on membranes functionalized with SDF1α and N-cadherin towards a fraction of 1:4. This finding implies that the formation of a pseudopod does not alter the adhesion area A_{Adh} of the cell. Instead, it induces a displacement of the adhesion area by the formation of a new adherent spot below the pseudopod with a simultaneous retraction of the former adhesion spot under the cell main body. Moreover, such a behavior implies enhanced cellular motility with similar characteristics of migrating leukocytes. Therefore, further experiments were performed to study possible synergistic effects of SDF1α and N-cadherin on the morphological dynamics and modes of motion of HSPC. Additional attention has been attributed to the influence of soluble SDF1α. Figure 3.27 illustrates cell trajectories of migrating HSPC on *in vitro* niche models displaying different fractions of SDF1α and N-cadherin at <*d*> ~ 13 nm in the absence (upper row) and presence (lower row) of 5 ng/mL SDF1α in solution.

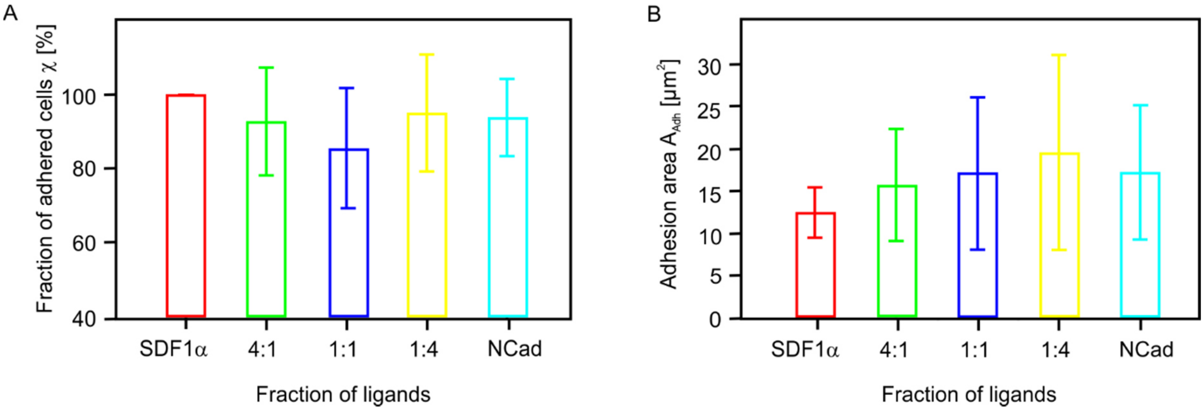

Figure 3.26 | Microinterferometry measurements revealed only a slight effect of the presence of two ligands . (A) Fraction of adherent cells χ and (B) the corresponding values for the adhesion area A_{Adh} of HSPC on membranes displaying different fractions of SDF1α and N-cadherin at <*d*> ~ 13 nm: Pure SDF1α (red), SDF1α:N-cad [4:1] (green) SDF1α:N-cad [1:1] (blue), SDF1α:N-cad [1:4] (yellow), pure N-cadherin (cyan). Bars represent means ± SD of n = 30 cells.

In the absence of soluble SDF1α, the trajectory length increases slightly with increasing proportion of N-cadherin. The presence of soluble SDF1α always dampens the cell motility. This finding implies that the bone marrow niche can regulate the migratory response of HSPC by up- and down-regulation of the concentration of SDF1α. According to these qualitative findings, the cell motility and dynamics of shape deformation were quantified as described in section 3.2.3. Figure 3.28 depicts phase contrast images including the trajectory of HSPC at t = 120 – 180 min (A- E), the amplitude maps (F-J) and the corresponding autocorrelation maps (K-O). The analysis revealed three pronounced tendencies: (1) Translational motion of HSPC on membranes displaying pure SDF1α at <$d_{SDF1\alpha}$> ~ 13 nm was less pronounced (Fig. 3.28A) due to strong adhesion to the *in vitro* niche model. In addition, cells deformed in an oscillatory manner which could be identified from the periodic appearance of peaks at Θ = 0/180° and 90/270° in the autocorrelation map (Fig. 3.28K). These findings support previous data (presented in Fig. 3.19). (2) Oscillatory deformations with simultaneous spinning motion were identified for HSPC on membranes with two ligands as it can be seen by a continuous shift of the peak positions with separations of 90° in the corresponding amplitude maps (Fig. 3.28G-I). This behavior was most pronounced at a ligand mixture of 4:1 [SDF1α:N-cadherin]. This finding implied that the simultaneous presence of both ligands caused a superposition of the migration mechanisms, which were identified for both ligands. Additionally, time-lapse movies showed the enhanced formation of pseudopods which seemed to function as an anchor for the cell (data not shown here). Third, HSPC on membranes displaying N-cadherin showed almost no shape deformations as indicated by a featureless amplitude and autocorrelation map (Fig. 3.29E, J, O). This finding implied that there are significant differences in the mechanism of migration of HSPC adhering to N-cadherin vs. SDF1α.

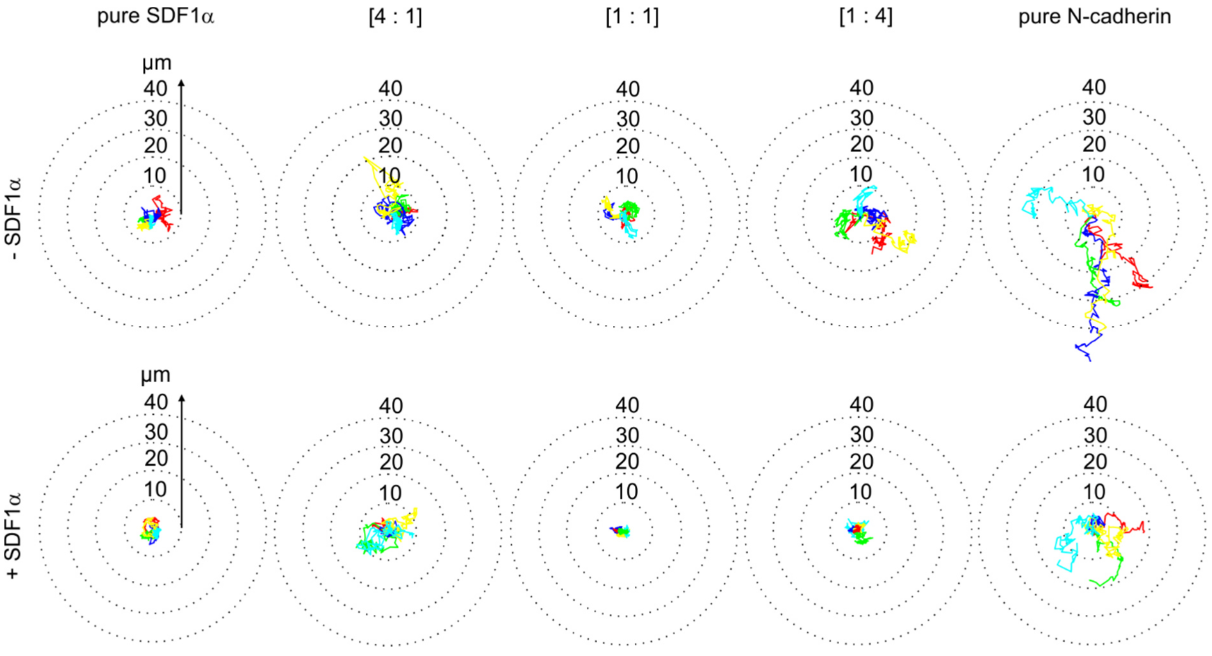

Figure 3.27 | Cell trajectories implies differential roles of the ligands SDF1α and N-cadherin. Cell trajectories of HSPC on membranes displaying different fractions of SDF1α and N-cadherin at <*d*> ~ 13 nm in the absence and presence of dissolved SDF1α. n = 5 cells.

In a next step, active cell motion was quantified by mode analysis as described in Chapter 3.2.3. By the use of a Fourier analysis, spatial harmonics of the sinusoidal frequencies of shape deformations were extracted. This analysis allowed for the determination of the predominant mode of deformation followed by the quantification of the power dissipation during shape deformations. Figure 3.29 depicts the power spectra (A) and total power dissipated during cell deformation (B) for HSPC on membranes displaying different fractions of SDF1α and N-cadherin at an average intermolecular distance <*d*> ~ 13 nm. Independently from the underlying substrate, oscillatory deformations of HSPC were the most pronounced shape deformation as it was identified by a maximum in the power spectrum which corresponds to m=2. In contrast to HSPC on membranes displaying either SDF1α or N-cadherin showing similar tendencies as described previously (Chapter 3.3.3), the oscillatory deformation was even stronger for cells on membranes displaying different fractions of the two ligands. Shape deformations by shrinking or expansion were suppressed at all different fractions as indicated by a negligible small fraction of mode m = 1. Figure 3.29B represents the calculated total power integrated over all modes as a function of the different fractions of SDF1α and N-cadherin, in order to highlight the impact of different ligands fractions on the total energy consumed by HSPC in the presence (red) and absence (black) of soluble SDF1α (5 ng/mL). The total power dissipated during shape deformations was higher in case of HSPC on membranes displaying different fractions of ligands.

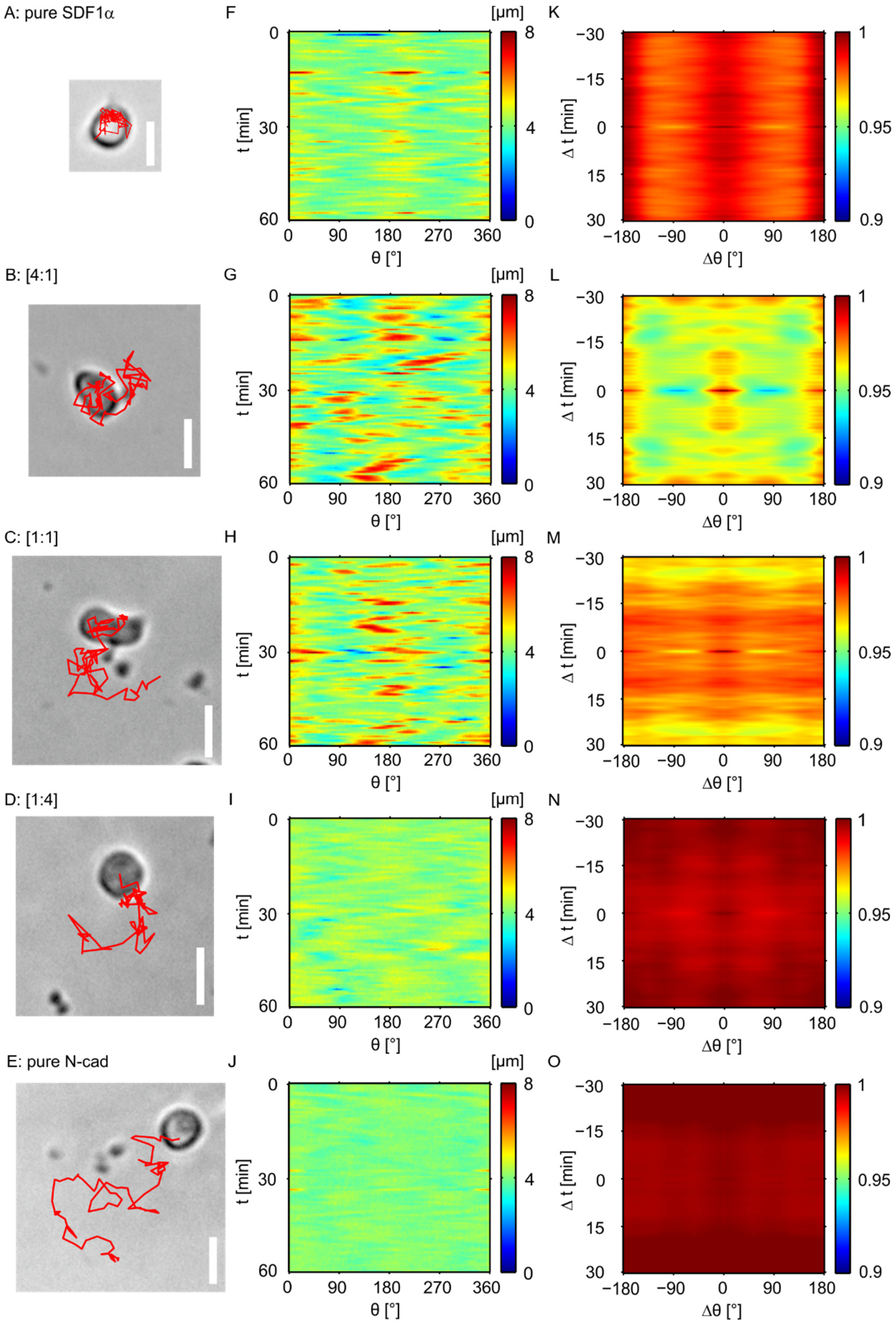

Figure 3.28 | Morphological dynamics of HSPC on supported membranes displaying SDF1α and N-cadherin with different fractions at <*d*> ~ 13 nm: (A - E) phase contrast images and trajectories over 60 min, (F - J) amplitude $r(\theta,t)$ maps, and (K - O) the corresponding autocorrelation $\Gamma_{r,r}(\theta,t)$ maps. Pure SDF1α (A,F,K), SDF1α:N-cad [4:1] (B,G,L) SDF1α:N-cad [1:1] (C,H,M), SDF1α:N-cad [1:4] (D,I,N), pure N-cadherin (E,J,O) (scale bars: 10 µm).

A maximum was reached for HSPC on an *in vitro* niche model functionalized with SDF1α:N-cadherin [4:1]. The presence of soluble SDF1α (5 ng/mL) caused a reduction of the energy consumption which was most pronounced for HSPC on *in vitro* niche models displaying increasing proportions of N-cadherin. For example, the total power of HSPC in the presence of a fraction of SDF1α:N-cadherin [1:4] was reduced by 40 % and showed a similar value as for HSPC on pure N-cadherin functionalized membranes. In contrast to that, the total power for HSPC on membranes displaying SDF1α:N-cadherin [4:1] was reduced by only 20 %.These findings reflect back to the fact that the adhesion and migration of HSPC via the CAM N-cadherin leads to the direct involvement of the cytoskeleton as N-cadherin is indirectly coupled to F-actin via a cadherin/catenin complex including β-catenin, α-catenin and several other proteins[144, 180]. The coupling of the cytoskeleton to the adhesion site dampens shape deformations. The simultaneous presence of immobilized SDF1α causes a strong increase in shape deformations which supports the role of SDF1α as trigger of actin polymerization and thus active cell motility[162]. Although the sole presence of SDF1α resulted already in a higher cell motility, the shape deformations are less pronounced without the participation of N-cadherin and actin cytoskeleton.

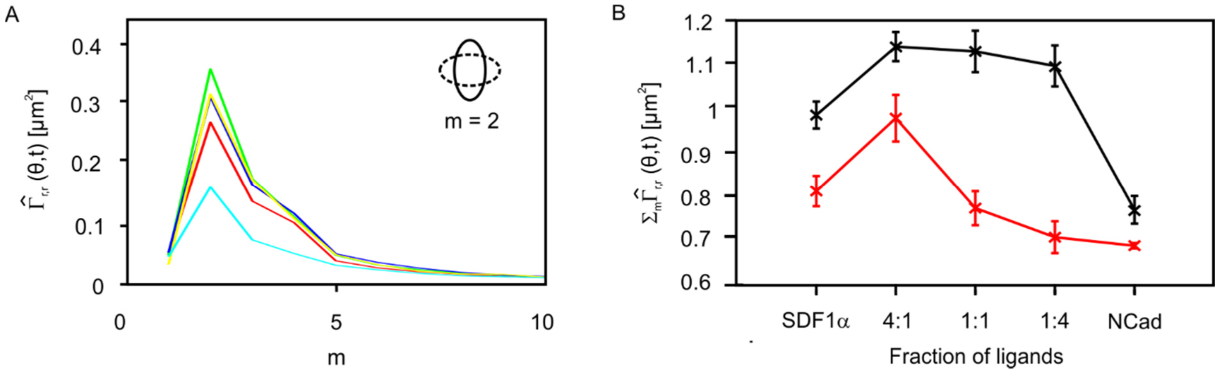

Figure 3.29 | HSPC dissipate more energy in the presence of two ligands. (A) Power spectrum of HSPC at different fractions of SDF1α and N-cadherin at <*d* > = 13 nm: Pure SDF1α (red), SDF1α:N-cad [4:1] (green) SDF1α:N-cad [1:1] (blue), SDF1α:N-cad [1:4] (yellow), pure N-cadherin (cyan). (B) Total power in the presence (red) and absence (black) of dissolved SDF1α plotted vs. different fractions of SDF1α : N-cadherin. Data points represent means ± SEM for n = 30 cells of three individual experiments.

3.3.1.3 Summary

The current approach demonstrated the synergistic effect of different ligand-receptor pairs on the adhesion and morphological dynamics of HSPC. In the simultaneous presence of N-cadherin and SDF1α, phase contrast and microinterferometry experiments revealed a pronounced polarization of HSPC which was not detected for HSPC on *in vitro* niche models displaying either N-cadherin or SDF1α. This finding was accompanied by the enhanced formation of cell protrusions. In contrast, no significant differences of the fraction of adherent cells and the adhesion area were detected. Statistical analysis of stochastic morphological dynamics revealed that HSPC motility was dominated by oscillatory deformations with simultaneous spinning motion. Moreover, HSPC dissipated higher energy in the simultaneous presence of N-cadherin and SDF1α. Surprisingly, HSPC were highly sensitive to the changes in the fractions of the two ligands SDF1α and N-cadherin. Whereas a fraction of SDF1α/N-cadherin [4:1] caused the highest cellular motility, a fraction of SDF1α/N-cadherin [1:4] led to the highest polarization of cells as indicated by increase in the aspect ratio of cells. This finding implies that actin dynamics correlate with the concentration of immobilized SDF1α. This example of 'cross-talk' between HSPC receptors suggests that chemokines might generally transduce accessory signals towards cell adhesion receptors between adjacent cells to modify their adhesion and migratory responses. Thus, triggering of cytoskeletal activity by chemokines supported by the adhesion to actin-linked cell adhesion molecules might be general strategy of the bone marrow niche to enable sustained HSPC adhesion and migration. The remaining question is how the direction and rate of cell motility control the balance between immobilization and mobilization of HSPC in the bone marrow niche, which is a key factor for the maintenance of the stem cell pool and the development of differentiated cells. Therefore, further experiments should focus on investigations of the adhesion and migration behavior of HSPC on *in vitro* niche models displaying a gradient of SDF1α in the presence and absence of different fractions of N-cadherin. As HSPC are capable of moving preferentially along a gradient of soluble and/or immobilized SDF1α[33], such experiments will allow for further statements on the synergistic role of both ligands. Moreover, further experiments should be performed in order to elucidate the role of the actin cytoskeleton in this 'crosstalk'. For example, quantifying the mean fluorescence intensity of actin-stained HSPC, after their adhesion to *in vitro* niche models displaying different fractions of N-cadherin and SDF1α, would allow for the detection of the relative amount of F-actin. Furthermore, confocal microscopy could be used to investigate the spatial distribution of F-actin in polarized cells and its correlation with the distribution of the receptors N-cadherin and CXCR4.

3.4 Impact of stem cell source and malignancy

3.4.1.1 Theoretical background

Bone marrow failure diseases comprise several severe and rare diseases which are characterized by a loss of functionality of the bone marrow niche to produce appropriate numbers of matured hematopoietic cells. Among them, acute myeloid leukemia (AML) is a clonal disorder of HSPC that have lost the ability to differentiate into cells of the myeloid lineage (Fig. 3.30A), hence leading to accumulation of undifferentiated leukemic blasts (LB) (Fig. 3.30B)[35, 36]. Symptoms are immune deficiency, fatigue and bleeding[35]. Although the current concept of AML treatment includes a chemotherapy followed by a stem cell transplantation, the four-year survival rate ranges from 30-40 % dependent on the subtype[35, 228]. Present evidence indicates that LB are derived from leukemia initiating cells (LIC)[37, 38]. These cells share common features with healthy HSPC, for example they can be identified by the same phenotype $CD34^+CD38^-$. Additionally, they are well protected from cell division by adhesion to the bone marrow niche, and thus are resistant to chemotherapy which is the main reason for remission[39]. Although HSPC and LIC reside in the microenvironment of the bone marrow, little is known about the precise molecular mechanisms and the differences in their interactions with the bone marrow niche[40]. To increase the survival rate of patients, the stem cell transplantation as well as the effectiveness of chemotherapy has to be improved. Thus, the differential adhesion of HSPC vs. LIC to the stem cell niche might be exploited for sufficient mobilization of LIC before chemotherapy followed by intensive investigations on the adhesion mechanisms of the healthy, transplantable HSPC. In the allogenic stem cell transplantation the whole hematopoietic system is reconstituted by the donation of HSPC which are collected from a healthy donor[229]. There are multiple sources of HSPC. In 1963, Thomas successfully derived HSPC from the human bone marrow which is considered as the main stem cell source[230]. Besides that, other sources of HSPC such as PB[231] or CB[232] have been identified in the 1980s. The various HSPC sources differ in the total amount of HSPC ($CD34^+$ cells) and in their proportion of long-term (LT), short-term (ST) HSPC and multi-potent progenitors (MPP) which influences their reconstitutive and immunogenic characteristics as summarized in Table 3.2[233]. The main source for allogenic stem cell transplantation are HSPC from PB which can be obtained in sufficient numbers after their mobilization from bone marrow with granulocyte colony-stimulating factor (G-CSF)[234, 235]. This treatment leads to a 16.3-fold increase of the mean peripheral blood HSPC ($CD34^+$) concentration[236].

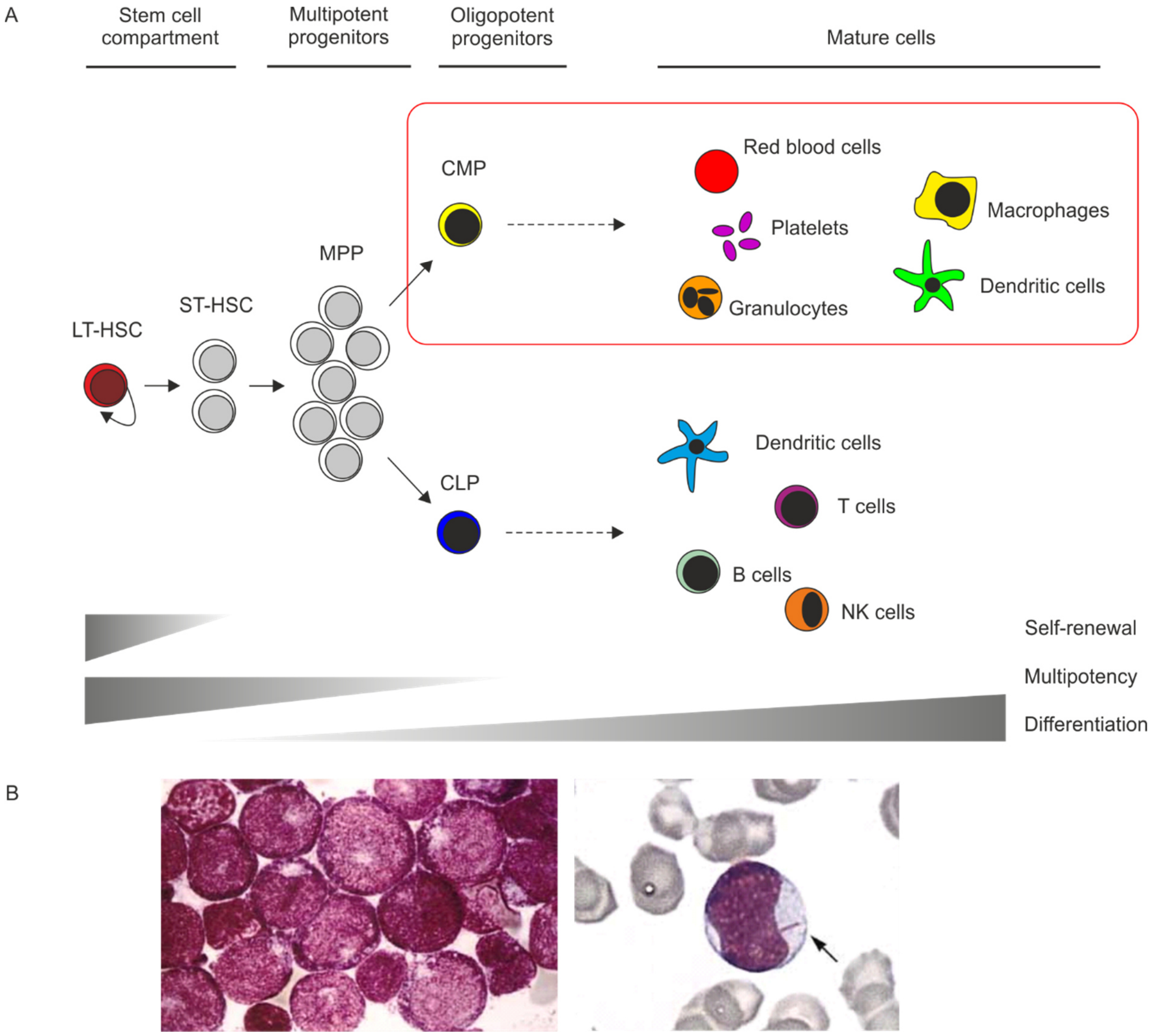

Figure 3.30 | Cytological findings caused by acute myeloid leukemia. (A) Hematopoietic and progenitor cell lineages comprise long-term (LT) and short-term (ST) HSPC which give rise to multi-potent progenitor cells (MPP). They differ in their ability to self-renew and their potency. Common myeloid progenitors (CMP) and common lymphoid progenitors (CLP) are already lineage-commited cells which give rise to all matured blood cells. In case of AML, the myeloid lineage is affected which leads to accumulation of undifferentiated leukemic blasts (B, adopted from Lowenberg *et al.*[35]).

Differences between non-mobilized and mobilized HSPC arise from the fact that G-CSF induces several side reactions which affects for example the CXCR4/SDF1α axis. Details of this regulatory process are poorly understood. It was shown that G-CSF induces the release of neutrophil elastase (NE) and matrix metalloproteinase-9 (MMP-9) into the bone marrow niche[237], which in turn down-regulates levels of SDF1α by enzymatic degradation. This finding was accompanied by the cleavage of the N-terminus of CXCR4[238] which includes the binding region for SDF1α[239]. Thus, the enforced mobilization of HSPC disrupts the interaction between the ligand-receptor pair SDF1α/CXCR4 in order to prevent the cells from homing back to the bone marrow. Based on these findings, the current project was expanded towards the quantitative characterization of the adhesion behavior of HSPC from PB of healthy donors, and LB (CD34$^+$) from AML patients in order to gain a deeper insight into the impact of the stem cell source and the effect of AML. Measurements on the fraction of adherent cells, adhesion area and adhesion strength were performed and compared to data obtained from CB HSPC for cells seeded on *in vitro* niche models displaying SDF1α at three selected distances <d> ~ 6, 11 and 18 nm. The underlying experiments were performed as described in Chapters 3.1 – 3.2.

Table 3.4 | Percentage of CD34$^+$ cells in the total nucleated cell count of different sources at steady state. In case of peripheral blood, the fraction refers to data obtained from healthy donors which did not receive mobilization agents[233].

Source	Fraction of CD34$^+$ cells [%]
Bone marrow	1.1[233]
Cord blood	0.5[240]
Peripheral blood	0.06[233]

3.4.1.2 Results and discussion

The current approach was expanded towards the analysis of the differential adhesion of HSPC from different sources. Hence, microinterferometry experiments and pressure wave assays were performed in order to gain a quantitative insight into the differences in the adhesion of healthy HSPC from CB and PB, and LB from one AML patient. Special attention has been attributed to the ligand-receptor pair SDF1α/CXCR4. For this purpose, HSPC from PB and CB as well as LB from an AML patient were seeded on *in vitro* niche models displaying SDF1α at an average intermolecular distance $<d_{SDF1\alpha}>$ ~ 6, 11 and 18 nm. These distances were selected as almost all HSPC from CB were identified as adherent in prior experiments (Chapter 3.2.1). Figure 3.31A represents the fraction of adherent cells χ of HSPC from CB and PB at t = 2 h. Whereas almost all cells adhered in case of HSPC from CB, the fraction of adhered HSPC from PB at $<d_{SDF1\alpha}>$ ~ 11 nm was only 55 % and even less for $<d_{SDF1\alpha}>$ ~ 18 nm (35 %). A similar observation was found for the adhesion area (Fig. 3.31B). The adhesion area at $<d_{SDF1\alpha}>$ ~ 11 nm corresponded to A_{Adh} = 6.0 µm^2 which is less than half of the value for HSPC from CB (A_{Adh} =16.0 nm). Again, this finding was even more pronounced at $<d_{SDF1\alpha}>$ ~ 18 µm^2. To further highlight the differences between HSPC from CB and PB, the adhesion area A_{Adh} as a function of $<d_{SDF\alpha}>$ was again fitted by the Hill equation (Equ. 3.2.25).

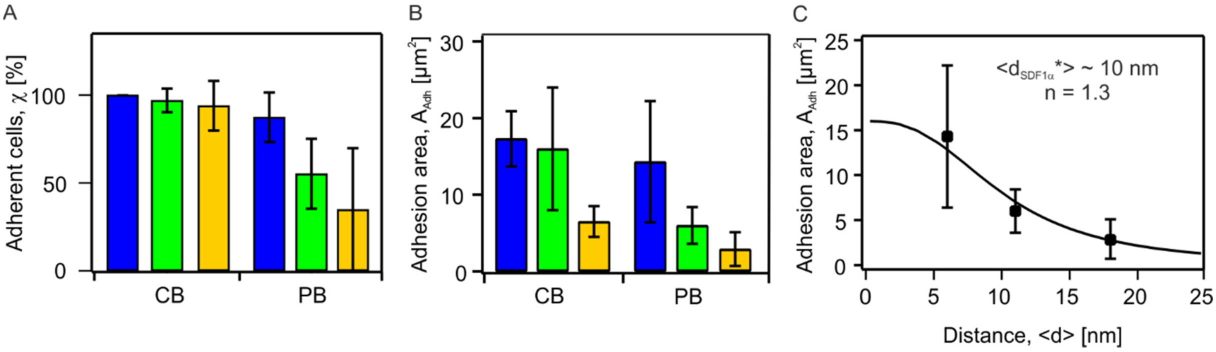

Figure 3.31 | G-CSF treatment reduced the ability of HSPC to adhere to SDF1α. (A) The fraction of adherent HSPC from CB and PB on supported membranes displaying SDF1α at $<d_{SDF1\alpha}>$ ~ 6 (blue), 11 (green) and 18 nm (yellow) at t = 2 h and (B) the corresponding values for adhesion area. Bars represent means ± SD for n = 50 cells. (C) Fitting of the data for adhesion area of HSPC from PB vs. $<d_{SDF1\alpha}>$ with the empirical Hill euqation (black line). Data points represent means ± SD for *n* = 50 cells.

A shift of the unbinding transition to a critical distance $<d_{SDF1\alpha*}>$ ~ 10 nm and a cooperativity coefficient *n* ~ 1.3 were obtained as depicted in Figure 3.31C. Both results were significantly smaller compared to the values obtained before for healthy HSPC from CB (see 3.2.1). Furthermore, the pressure wave assay revealed a critical pressure for cell detachment *P** ~ 5.8 MPa at $<d_{SDF1\alpha}>$ ~ 11 nm, which was 15 - 20 % less than the corresponding value of HSPC derived from CB (7.0 MPa). In conclusion, these results supports previous findings about the influence of G-CSF induced HSPC mobilization[237, 238]. The administration with G-CSF leads to a cleavage of the N-terminus of the CXCR4 receptor which includes the binding region for SDF1α. Thus, CXCR4 loses its ability to bind SDF1α which in turn causes a reduction of adhesion area, adhesion strength and, thus, a decrease of the fraction of adherent cells. The question arises, how long the mobilized HSPC need to recover their surface expression of CXCR4. Kollet *et al.* could show that the surface expression of CXCR4 increased again significantly 24 hours after cytokine treatment in NOD/SCID mice[241]. As our experiments are performed directly after PB cells have been collected from healthy donors, the influence of the re-expression of CXCR4 on the surface of HSPC should be negligible small. Further investigations were performed to assess potential differences in the adhesion behavior of LB from AML patients in order to quantify differences to HSPC from healthy donors. Of particular interest was the understanding of the differential adhesion of LB and HSPC from PB which serve as main stem cell source in allogenic stem cell transplantation after chemotherapy. Figure 2.32A depicts the fraction of adherent cells as a function of the average intermolecular distance $<d_{SDF1\alpha}>$ ~ 6, 11 and 18 nm.

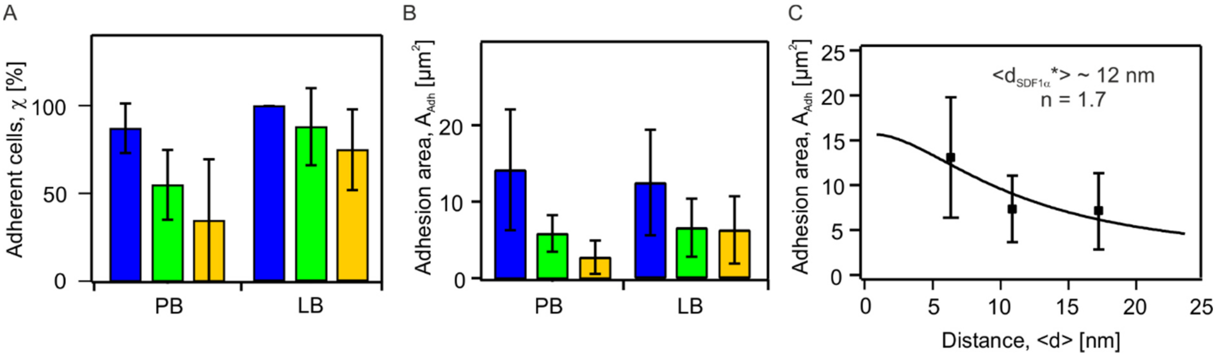

Figure 3.32 | LB adhesion is much more effective compared to the adhesion of enforced mobilized HSPC from PB. (A) The fraction of adherent HSPC from PB and LB on supported membranes displaying SDF1α at $<d_{SDF1\alpha}>$ ~ 6 (blue), 11 (green) and 18 nm (yellow) at t = 2 h and (B) the corresponding values for adhesion area. Bars represent means ± SD for n = 50 cells. (C) Fitting of the data for adhesion area vs. $<d_{SDF1\alpha}>$ with the empirical Hill euqation (black line). Data points represent means ± SD for n = 50 cells.

The fraction of adherent cells χ of LB was around 40 % higher compared to HSPC from PB at $<d_{SDF1\alpha}>$ ~ 11 and 18 nm. Data of the adhesion area as a function of $<d_{SDF1\alpha}>$ of LB almost resemble the ones for HSPC from PB (Fig. 3.32B), but fitting the data set with the empirical Hill equation revealed a higher transition point for unbinding, $<d_{SDF1\alpha}>$ ~ 12 nm, and a higher Hill coefficient, n = 1.7. These values were close to the ones for HSPC from CB. These results indicate that LB adhesion to bone marrow niche is much more significant.

3.4.1.3 Summary

The current Chapter comprised a detailed analysis of the adhesion of HSPC from PB and LB. Characteristic differences in the adhesiveness of HSPC from different sources were identified by RICM and pressure wave assay were performed. PB HSPC are used as the main stem cell source for allogenic stem cell transplantations. Thus, the current study characterized the 'homing' potential of mobilized HSPC to bone marrow after transplantation. RICM experiments of HSPC from PB on *in vitro* niche models displaying SDF1α revealed both a reduction in the fraction of adherent cells and a decrease of the adhesion area. Additionally, similar findings were made by pressure wave assay. The adhesion strength of HSPC from PB was significantly smaller compared to HSPC from CB. The obtained results support previous findings which demonstrated that G-CSF induces the release of NE and MMP-9[237, 238]. This in turn downregulates levels of SDF1α in bone marrow by enzymatic degradation, follwed by the cleavage of the N-terminus of CXCR4. Thus, the enforced mobilization of HSPC led to a substantial distortion of the interaction between the ligand-receptor pair SDF1α/CXCR4 resulting in a reduction of the fraction of adherent cells and a decrease of the adhesion area. Efficient chemotherapy requires a detailed knowledge of potential differences in the adhesion behavior of LB vs. healthy HSPC. Therefore, the current study was expanded towards the analysis of the adhesiveness of LB from an AML patient. Malignant cells showed a higher fraction of adherent cells accompanied by a slightly reduced adhesion area in comparison to HSPC from PB. Although only LB from one AML patient were tested, the present study suggests that the adhesiveness of LB is stronger compared to healthy HSPC which causes the insufficient effect of chemotherapy and the resultant remission.

4. Conclusion

This thesis presented the quantification of the relative significance of interactions between human hematopoietic stem and progenitor cells (HSPC) and bone marrow niche by a unique combination of novel experimental techniques and methods in statistical physics. Supported phospholipid membranes, that display the key ligands N-cadherin and SDF1α, were utilized as surrogate niche models in order to identify their differential roles in the maintenance of stem cell mobilization and homing.

In Chapters 2.1 and 2.2, the *in vitro* niche models based on supported membranes were characterized utilizing high energy specular X-ray reflectivity (XRR) and quartz crystal microbalance with dissipation monitoring (QCM-D). XRR yielded the thickness, roughness and scattering length density profile of supported membranes before and after the coupling of N-cadherin and SDF1α. For example, in case of membranes functionalized with the extracellular domain of N-cadherin with hexa-histidine tag, XRR confirmed the formation of a uniform protein layer with a thickness of d = 170 Å, an interfacial roughness of σ = 41 Å and a scattering length density of $\rho = 10.1\cdot10^{-6}$ Å^{-2}. QCM-D demonstrated that the coupling of N-cadherin resulted in a change in mass of Δm = 3457 ng·cm^{-2} which agrees well with similar values obtained for recombinant E-cadherin-IgG Fc fusion protein and recombinant Xenopus cadherin-11. Moreover, the modeling of QCM-D data with the Voigt-Voinova model yielded an elastic shear modulus of $\mu_{f,\ N\text{-}cadherin}$ = 0.6 MPa and a shear viscosity of $\eta_{f,N\text{-}cadherin}$ = 3.2 mPa·s. The fact that changes in mass linearly scaled with the average intermolecular distance $<d>$ of anchor lipids implies that the functionalization of membranes with recombinant proteins was quantitative, which enabled the precise control of the distance between proteins with nm accuracy.

In Chapter 3.2, label-free, live-cell imaging by reflection interference contrast microscopy (RICM) was utilized to quantitatively assess the specific binding of HSPC (CD34$^+$ cells from cord blood provided by Prof. Dr. Anthony D. Ho from the Department of Medicine V, University of Heidelberg) to the *in vitro* niche models displaying either N-cadherin or SDF1α at precisely defined average intermolecular distances $<d>$ ~ 6 – 80 nm. RICM relies on the interference of linearly polarized light reflected at the substrate surface and sensitively detects spatio-temporal changes in the height profile of a cell near the *in vitro* niche model. This allowed for the quantification of (a) the fraction of adherent cells χ and (b) the area of tight adhesion A_{Adh}. First, the specific adhesion of HSPC to the *in vitro* niche model was significantly influenced by changes in the average intermolecular distance $<d_{N\text{-}cadherin}>$ and $<d_{SDF1\alpha}>$ between ligand molecules. The contact of HSPC with the surrogate surface exhibited a clear binding/unbinding transition. In fact, the plot of A_{Adh}

vs. $<d>$ could be well fitted by the empirical Hill equation, demonstrating that the adhesion of HSPC is a positively cooperative process with cooperativity coefficients of $n_{SDF1\alpha/CXCR4}$ = 1.9 and $n_{N\text{-}cadherin/N\text{-}cadherin}$ = 1.4, respectively. Second, to gain deeper insights into the mechanical strength of cell adhesion, a novel technique utilizing ultrasonic pressure waves induced by ps laser pulses were applied to determine the critical pressure to detach HSPC from the *in vitro* niche models with high statistical reliability (100-200 cells/h) which is about two orders of magnitude larger compared to commonly used techniques like micropipette aspiration and AFM peeling. It was found that the adhesion mediated via the SDF1α/CXCR4 axis is stronger than that mediated via homophilic interactions between N-cadherins, which can be characterized by the characteristic binding/unbinding transition $<d_{SDF1\alpha}*>$ ~ 12 nm and $<d_{N\text{-}cadherin}*>$ ~ 14 nm. The results clearly demonstrated the importance of N-cadherin to bind HSPC to bone marrow niche, which is in stark contrast to previous studies that failed to detect any sign of specific functions.

Another clinical relevant question, in addition to adhesion, is how HSPC migrate in the bone marrow niche during homing and mobilization. Cell locomotion is tightly coupled to shape deformations. Since HSPC are poorly deformable cells due to the fact that their cell volume is marginally larger than that of their nuclei, the shape deformation was analyzed in Fourier space. Remarkably, the power spectrum analysis $\hat{\Gamma}(\theta,t) = \langle FT\big(r(\theta,t)\big) \cdot FT\big(r(\theta,t)\big)\rangle$ for different modes m of deformation exhibited a prominent peak at m = 2 independent from $<d_{SDF1\alpha}>$ suggesting that HSPC predominantly undergo oscillatory deformation. Moreover, the energy dissipation during cell deformation was most pronounced near $<d_{SDF1\alpha}*>$ implying that HSPC are furthest from equilibrium around this $<d_{SDF1\alpha}>$. The energy dissipation was drastically suppressed when HSPC were incubated with a physiological level of soluble SDF1α (5 ng/mL). As SDF1α is the only chemokine that induces the migration of HSPC in bone marrow, this finding suggests that the counterplay of soluble vs. immobilized SDF1α affects the mode of deformation and motion of HSPC. The significant change caused by the presence of the physiological concentration of soluble SDF1α was successfully demonstrated for the first time, which is in clear contrast to previous *in vitro* studies that used 10-100 times higher concentrations of soluble SDF1α. The obtained results clearly demonstrated that the combination of well-defined *in vitro* niche models and methods in statistical physics is a powerful tool to extract spatio-temporal patterns of stem cells hidden behind stochastic noises.

Furthermore, oscillatory deformations of HSPC on membranes displaying SDF1α were much more pronounced compared to those displaying N-cadherin which indicates different roles of ligands in HSPC migration. This raises the next question: Why does nature utilize both N-cadherin and SDF1α? To answer this question, the adhesion and morphological dynamics of HSPC on *in vitro* niche models displaying both ligands were studied (Chapter 3.4). Interestingly, HSPC dissipate more energy when both ligands coexist on the membrane surface, although both the fraction of adherent cells χ and the area of tight adhesion A_{Adh} remained almost unchanged. The distinct change in deformation and motion of HSPC caused by altering the mixing ratio could represent different molecular compositions in the endosteal and vascular niche, which are sub-niches of the bone marrow niche: HSPC are less deformable in the endosteal niche whose major constituents are N-cadherin expressing, spindle-shaped osteoblasts, while HSPC are more deformable in vascular niche with higher SDF1α expression level. Furthermore, the current findings imply a synergistic effect of N-cadherin and SDF1α.

In Chapter 3.5, the strategy established above was applied for more clinically relevant samples. First, to model the homing of allogeneic transplanted HSPC from the peripheral blood (PB) of healthy donors, the adhesion of HSPC from PB was compared to HSPC from cord blood (CB). PB-HSPC exhibited a distinctly retarded adhesion capability which could be attributed to the partial de-activation of CXCR4 caused by the enforced mobilization of HSPC from bone marrow to PB with granulocyte-colony stimulating factor prior to the HSPC harvest. Finally, the adhesion of leukemic blasts (LB) from acute myeloid leukemia patients was compared to that of PB-HSPC in order to simulate the competition between immobilization of allogeneic transplanted PB-HSPC vs. LB. Adhesion of LB mediated by the SDF1α/CXCR4 axis was found to be much more significant compared to that of PB-HSPC reflecting the difficulty of replacing LB by healthy PB HSPC.

The obtained results clearly demonstrated the power of precisely designed *in vitro* models of hematopoietic stem cell niche in bone marrow as a novel platform to investigate human HSPC towards the quantification of the functions of key ligands and new drug candidates. Many results presented in this thesis could only be obtained by the combination of novel experimental techniques and analytical methods, which are not accessible by conventional phenomenological microscopy observation. The presented strategies have large potential to replace currently used *in vitro* systems such as mouse models.

5. Perspectives

The current thesis successfully demonstrated the use of a precisely defined *in vitro* niche model based on N-cadherin and/or SDF1α functionalized membranes on solid support for quantitative characterizations of adhesion and morphological dynamics of HSPC.

However, the exact mechanism of HSPC immobilization and mobilization remains to be ascertained as cell adhesion molecules and chemokines are not equally distributed in bone marrow niche. For example, the mobilization and immobilization of HSPC is governed by a dynamic concentration gradient of the chemoattractant SDF1α[242]. This gradient is based on a distinct spatial distribution of cells in bone marrow niche which display or secret this chemoattractant as ECM-anchored[29] or soluble molecule stimulated by signals from the sympathetic nervous system[15]. To define the influence of a membrane-coupled concentration gradient of SDF1α on adhesion and migration of HSPC, it is essential to design a highly controllable model system which allows for quantitative investigations on the morphological dynamics and modes of motion *in vitro*. In order to refine the utilized *in vitro* niche model, a second type of *in vitro* niche model has to be developed which is based on a solid-supported membrane displaying SDF1α as a lateral concentration gradient. Supported membranes displaying a concentration gradient of proteins can be fabricated by membrane electrophoresis (Fig. 5.1).

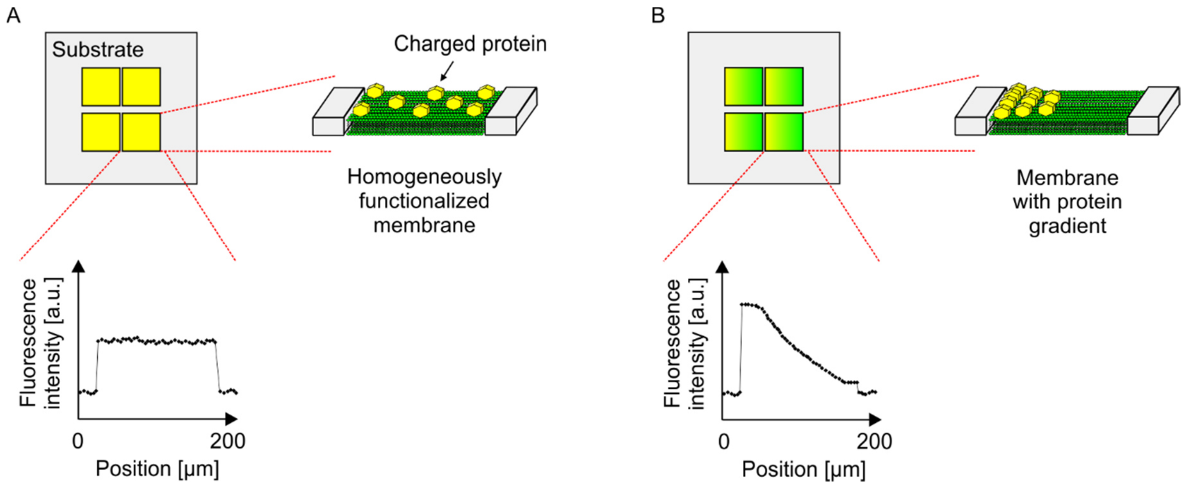

Figure 5.1 | Protein gradients on solid-supported membranes prepared by electrophoresis. (A) Schematic illustration of a micropatterned glass substrates after the deposition of a supported membrane and subsequent functionalization with charged proteins. (B) The application of an external electrical field parallel to the fluid surface can be used to create field induced concentration profiles of the coupled protein. The successful preparation can be followed by the use of dye-labelled proteins as indicated by the progression of the detectable fluorescence intensity.

In detail, membrane electrophoresis allows for the lateral separation and accumulation of charged amphiphiles or proteins in or on top of a supported membrane by the application of an external electrical field parallel to the fluid surface in order to create field-induced concentration profiles. In 1995, Groves and Boxer refined this technique by the use of micro-patterned substrates[243]. These developments provided the basis for the first preparation of concentration gradients of membrane-anchored proteins described by Groves in 1996[244]. Recent reports demonstrated the fabrication of concentration gradients of tethered vesicles[245, 246], membrane-anchored DNA[247, 248] and proteins[249].

Another future aspect would be to investigate the actin dynamics of HSPC and its correlation with the re-distribution of receptors along the adhesion area of HSPC. The current thesis provided first evidence for synergistic effects of the cell adhesion molecule N-cadherin and the chemokine SDF1α on the migration and adhesion of HSPC. Mechanistic investigations on molecular level should be performed to further investigate the correlation of both ligand-receptor pairs with the actin dynamics of HSPC. The ability of HSPC to respond to chemoattractants is essential for their homing efficiency after stem cell transplantation as well as their drug-induced mobilization from bone marrow across the bone marrow endothelium into the peripheral blood. Voermans *et al.* demonstrated that the stimulation of HSPC with SDF1α induces actin polymerization by the simultaneous induction of cell migration[162]. The response of the HSPC is accompanied by the redistribution of surface receptors. For example, Avigdor *et al.* demonstrated that the receptor CD44, which is a receptor for hyaluronic acid, was asymmetrically distributed after the incubation of HSPC with SDF1α[250]. Moreover, Giebel *et al.* found that CXCR4 appeared as a gradient along a migrating HSPC with its highest expression in the leading edge[227]. Zhang *et al.* reported the asymmetric expression of N-cadherin by LT-HSPC, which were found in close proximity to N-cadherin expressing, spindle-shaped osteoblasts[11]. Therefore, the quantitative analysis of actin dynamics in correlation with the spatial distribution of N-cadherin and CXCR4 along the adhesion area of HSPC would provide a detailed understanding of the synergistic effects of N-cadherin and SDF1α on HSPC adhesion and migration. Live-cell imaging with a focus on actin dynamics would be possible by live-cell staining of HSPC with silicon-rhodamine (SiR) actin[251]. The derivative of desbromo-desmethyl-jasplakinolide binds to actin with minimal cytotoxicity and has a high photo stability.

6. Appendix I

6.1 Fine structures and water permeability of fullerence based vesicles[†]

6.1.1 Introduction

Nanometer-sized compartment structures like vesicles based on synthetically derived amphiphilic molecules are of high interest in life sciences due to their ability to function as nano-carriers. Inspired by nature, such vesicular structures mimic liposomes and are based on amphiphilic molecules that contain a polar head/nonpolar tail motif[252-254]. Driven by the hydrophobic effect, amphiphiles cluster together in aqueous solution and form bilayers to reduce the contact sides between the hydrophobic parts of the molecules and water[67, 255, 256]. This polymorphic structure leads to characteristic properties like mechanical stability and water permeability and discloses the possibility of encapsulating various hydrophilic molecules inside the vesicle[103]. These vesicles can be used as nano-carriers for drug-delivery and delivery systems in diagnostic and cosmetic fields[257]. In contrast to liposomes[258], nano-carriers based on synthetically derived molecules shall overcome drawbacks like low chemical and physical stability during their use and storage, short blood circulation half-times, poor encapsulation efficiency and low manufacturability on an industrial scale[257]. One further development of these amphiphilic structures are molecules with a nonpolar/polar/nonpolar (n-p-n′) motif[259]. The group of Nakamura reported the synthesis of 18 new fullerene derivatives (Rf8K) bearing alkyl and perfluoroalkyl side chains (n, n′-part) connected at a cyclopentadienide anion (p-part) of the fullerene (Fig. 6.1)[260, 261]. With the counter ion potassium, the resultant solvent-separated ion pair enables water penetration into the hydrophobic side chains and discloses the possibility of vesicle formation[262]. A major advantage of vesicles based on fullerene derivatives are their high stability in keeping their shape upon heating to 90 °C, on a solid substrate, in air or under vacuum[260]. The primary aim of this study is to investigate the structural properties of vesicles with (n-p-n′) motif based on the fullerene derivative Rf8K (Fig. 6.1). In the current thesis, small-angle neutron scattering (SANS) was utilized to investigate the fine structures of the fluorous fullerene vesicles in solution perpendicular to their surface plane.

[†] Dr. W. Abuillan (Institute of Physical Chemistry, University of Heidelberg, Germany) equally contributed to the experiments and data presented in this Chapter.

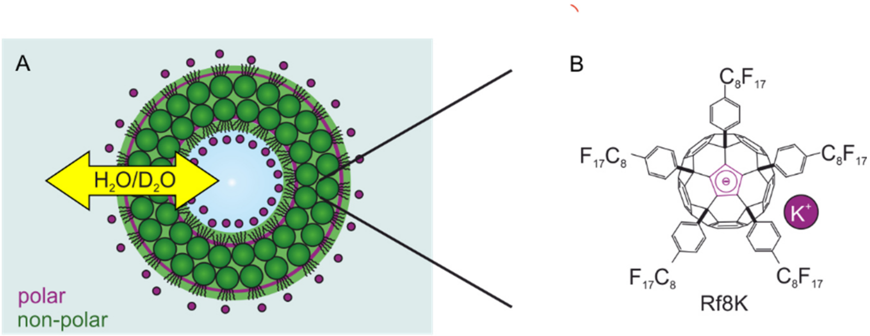

Figure 6.1 | Schematic illustration of the vesicular and molecular structure of Rf8K vesicles. (A) Schematic model of a Rf8K vesicle. (B) Chemical structure of the potassium complex of fullerene anions.

The fullerene derivative Rf8K was kindly provided by Assoc. Prof. Koji Harano from the laboratory of Prof. Dr. Eiichi Nakamura (Department of Chemistry, Graduate School of Science, University of Tokyo, Tokyo, Japan). As depicted in Figure 6.1B, Rf8K consists of a pentakis(*p*-perfluorooctyl)phenyl moiety which is covalently linked to a cyclopentadienide anion on a fullerene molecule. SANS is widely used to reveal the fine structure of nanoparticles made of soft biomaterials or hard matter in solution or in matrix by measuring the momentum transfer of an elastically scattered neutrons close to the direct beam[263-265]. An important feature of neutron scattering techniques is the contrast variation method based on the different scattering length *b* of isotopes[266, 267]. This technique allowed for the quantitative determination of the water permeability coefficient of Rf8K vesicles in aqueous solution beside the structural information of the vesicles.

6.1.2 Experimental realization

6.1.2.1 Synthesis of Rf8K and vesicle formation in water

The fullerene derivative Rf8K was kindly provided by K. Harano (Prof. Eiichi Nakamura, Department of Chemistry, Graduate School of Science, University of Tokyo, Tokyo, Japan). Their synthesis was based on the following steps: Rf8K vesicles were obtained as described previously[261]. Briefly, the fullerene derivative Rf8H was synthesized by 5-fold addition of a 4-substituted phenylcopper reagent to the fullerene C60 (81-98%). Rf8H was treated with potassium tert-butoxide in tetrahydrofuran (THF) to form a homogeneous solution of Rf8K, which was injected in either H_2O (0.80 mM) or D_2O (0.89 mM). Remaining THF was removed under reduced pressure resulting in the formation of a homogeneous vesicle solution of the potassium fullerene. The prepared vesicle suspension was orange, homogeneous, and clear without further purification. The preparative success was tested by dynamic light scattering (DLS) resulting in the size and homogeneity of the sample.

6.1.2.2 SANS experiments

SANS experiments were carried out at the large scale structure diffractometer D22 of the Institute Laue-Langevin (ILL, Grenoble, France). As depicted in Figure 6.2, samples were irradiated with a monochromatic neutron beam with a wavelength λ of 6 Å and a wavelength spread (fwhm) of $\Delta\lambda$ = 10%. The beam size was 0.7 cm^2 at the sample position. The data were recorded at two different sample-detector distances of 2.0 m and 14.0 m using a ^{3}He detector with 128 x 128 pixels and a pixel size of 8 x 8 mm^2 together with two collimation lengths (4.0 and 14.4 m) resulting in a q range of $0.0031 < q < 0.4971$ Å. The wave vector is defined as $q = 4\pi \sin\theta/\lambda$, where 2θ is the scattering angle. The samples were kept in quartz cells (Hellma Analytics, Müllheim, Germany) with path lengths of 1 cm. The data were background subtracted and absolute scale intensities (cm^{-1}) were obtained by calibration using the incoherent scattering signal from a 1-cm thick water sample. Furthermore, the data were normalized by the transmission and sample thickness. SANS measurements for Rf8K vesicles in H_2O and D_2O were performed with concentrations of 0.80 mM and 0.89 mM, respectively.

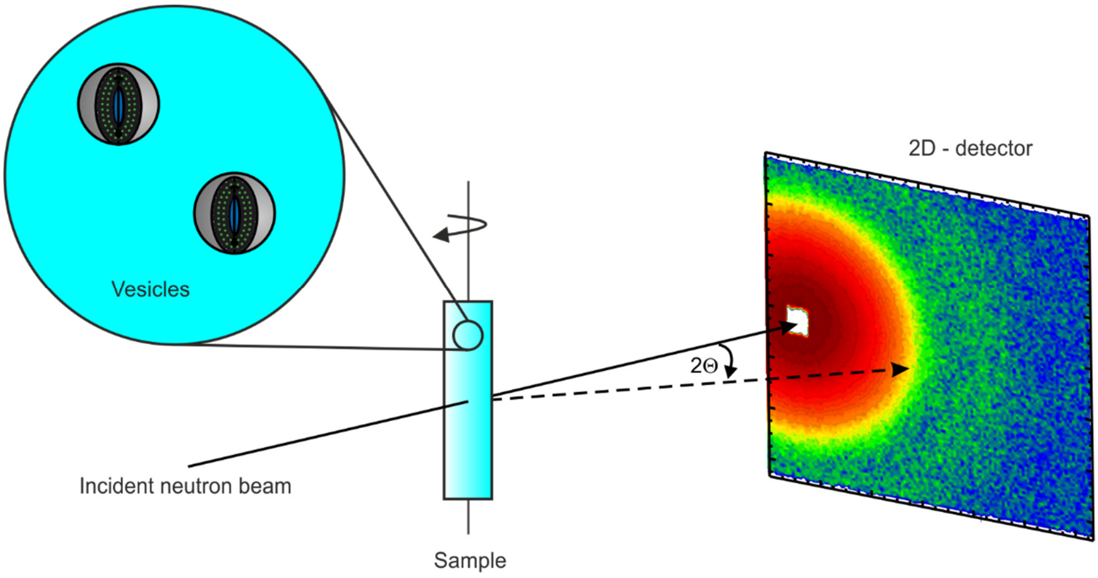

Figure 6.2 | Measurement geometry of SANS. Schematic illustration of the scattering geometry used in SANS experiments. Rf8K vesicles in aqueous solution were kept in quartz cells. The data is recorded with a two-dimensional ^{3}He detector.

6.1.2.3 Neutron contrast variation study

Neutron contrast variation studies were performed for Rf8K vesicles in different H_2O/D_2O mixtures. In the first step, Rf8K vesicles were prepared in pure H_2O and D_2O solutions. Then, the Rf8K vesicle suspensions in pure solvent were diluted by adding different amounts of D_2O and H_2O resulting in 20:80, 40:60, 60:40 and 80:20 vol% mixtures, respectively. Thereafter, SANS profiles were recorded for each sample repeatedly for up to 14 h. Data treatment was performed as described above.

6.1.2.4 SANS data fitting and analysis

For determination of the fine structure of Rf8K vesicles, SANS measurements were performed recording the scattering intensity $I(q)$ as a function of the magnitude of the scattering vector q. In case of a dilute, polydisperse system of non-interacting particles with a size distribution $f(r)$, $I(q)$ is defined as given by

$$I(q) = \frac{N}{V}(\rho_{solv} - \rho_p)^2 \int_0^\infty f(r)(A(q,r))^2 dr\,, \tag{6.1.1}$$

where N/V represents the number density of the particles and ρ_{solv} and ρ_p are the scattering length densities of the solvent and the particles, respectively[268]. $A(q)$ describes the form amplitude and is related to the form factor by $P(q,r) = |A(q,r)|^2$ representing the Fourier transform of the contrast $\Delta\rho(r)$ between the between coherent neutron-scattering length density of the vesicular bilayer and the solvent. For basic analysis, the natural logarithm of the scattered intensity was plotted as a function of the square of the scattering vector q to obtain information on the radius of gyration R_g which can be fitted using the Guinier approximation according to

$$\ln(I_q) = \ln(\mathrm{I_0}) - \left(\frac{\mathrm{Rg}^2}{3}\right) * \ln(\mathrm{q}^2)\,, \tag{6.1.2}$$

where I_q describes the scattering intensity as a function of the wave vector q[269]. I_0 represents the scattering intensity at q = 0. The average radius R of the Rf8K vesicles is estimated from the radius of gyration as given by

$$\mathrm{R} = \left({}^{5}/_{3}\right)^{0.5} \mathrm{R_g}\,. \tag{6.1.3}$$

Fitting of SANS data were performed using the open source software SasView.[270] In case of vesicles, the 1D scattering intensity of the SANS profiles, $I(q)$, as a function of the wave vector q is described by a core-shell model and is given by

$$\begin{aligned}(A(q,r))^2 = \frac{scale}{V_s}\Bigg[3V_c(p_c - p_s)\frac{[\sin(qr_c) - qr_c\cos(qr_c)]}{(Qr_c)^3} + 3V_s(\rho_s \\ - \rho_{solv})\frac{[\sin(qr_{ss}) - qr\cos(qr_s)]}{(qr_s)^3}\Bigg]^2 - bkg\,, \end{aligned} \tag{6.1.4}$$

where scale is a scale factor, V_s and ρ_s are the volume and the SLD of the outer shell[269]. V_c, r_c and ρ_c represent the volume, the radius and the SLD of the vesicle core, respectively. ρ_{solv} corresponds to the SLD of the surrounding solvent. As the vesicle membrane consists of layers with different SLD, the present model has to be expanded to a core-multishell model. In the described model, the core and each shell are assumed to have uniform scattering length densities. As the experimental scattering intensity $I(q)$ is influenced by instrumental resolution parameters, dI and dq values were taken into account for data fitting.[271] To account for polydispersity *PD*, each size distribution of the shells were taken into account by convolution based on the Schulz equation[272] as given by

$$f(x) = \frac{1}{Norm}((z+1)^{z+1})(x/x_{mean})^z\,\frac{exp[-(z+1)\,x/x_{mean}]}{x_{mean}\Gamma(z+1)}\,, \tag{6.1.5}$$

$$with\ PD = {}^{\sigma}\!/_{x_{mean}}\ . \tag{6.1.6}$$

x_{mean} corresponds to the mean of the distribution. *Norm* is a normalization factor which is obtained during the numerical calculation. As a consequence of sample *PD*, the oscillations in the SANS profile vanish and the first minima is shifted to higher Q-values.[273] Therefore, neglecting *PD* leads to the overestimation of the vesicle size.

6.1.3 Fine structures of Rf8K vesicles

In Figures 6.2A and B, the SANS profiles of Rf8K vesicles in pure H_2O and D_2O at 25 °C are depicted, respectively. The red solid lines correspond to the best fit of the scattering intensity $I(q)$. Differences in the scattering intensity $I(q)$ between the H_2O and D_2O sample are caused by an increase in the background level owing to the replacement of heavy water by light water. In case of Rf8K vesicles in H_2O (Fig. 6.2A), a core-multishell model was applied for data modeling in which the membrane structure of the vesicle is described by three shells representing the fullerene core by one shell surrounded by the perfluoroalkyl chains as outer and inner shells and the core is assigned for H_2O. In case of Rf8K vesicles in D_2O, the best fit could only be achieved by the use of a core shell model describing the vesicle structure by one shell including a core of D_2O. As the perfluoroalkyl chains were hydrated, the presence of D_2O led to a partial convergence of the SLD of all layers and thus the SLD contrast became less. Both fitting procedures yielded parameters for the thickness d and the scattering length density ρ of the shells. During the refinement of the SANS analysis, the SLD of H_2O and D_2O were set constant to $-5.61\cdot10^{-7}$ Å^{-2} and $6.38\cdot10^{-6}$ Å^{-2}, respectively. The parameters corresponding to the best fit results are summarized in Table 1. For Rf8K vesicles in H_2O, the data fitted well to the core-multishell model describing the vesicle membrane by three shells (Fig. 6.3A). The overall radius of Rf8K vesicles in H_2O corresponded to 141.4 Å and was consistent with the value obtained by basic Guinier analysis R = 143 ± 7 Å (Appendix II, Fig. 7.3A). Furthermore, data modeling revealed a fullerene shell thickness of 23.8 Å and a SLD of $\rho_f = 2.55\cdot10^{-6}$ Å^{-2}. As the van-der-Waals diameter of a fullerene molecule corresponds to 11 Å[274], this thickness suggests that the fullerene shell was composed of a molecular double layer. Previous DLS experiments based on the estimation of the area per Rf8K molecule from their size and molecular weight suggested that the amphiphilic Rf8K molecules form an interdigitated layer. However, this scenario was excluded from our current SANS results which provides structural information at the molecular level with Å resolution, as the scattering function of a vesicle cannot be fitted by an interdigitated layer.[261] Furthermore, previous studies indicated that fluorocarbon chains have an area per molecule of 0.3 nm^2/chain[275] which in turn forces the total area of five perfluoroalkyl side chains to be higher than 1.5 nm^2. Thus, the total area per Rf8K molecule is not determined by the area of the fullerene moiety but by the total area of the perfluoroalkyl side chains. The obtained SLD of the fullerene shell, $\rho_f = 2.55\cdot10^{-6}$ Å^{-2}, is significantly smaller compared to the values of the pure compound and suggest a less dense packing. Avdeev *et al.* reported a value of $\rho_{coll} = 5.44\cdot10^{-6}$ Å^{-2} for molecular-colloidal solutions of C_{60} in water[276], which is close to that calculated for the crystalline state of fullerenes, $\rho_{crys} = 5.62\cdot10^{-6}$ Å^{-2} [274]. Based on the value obtained by Avdeev *et al.*, the volume fraction of fullerene molecules in the shell was calculated according to

$$\phi = \frac{\rho_f}{\rho_{crys}} = 0.47. \tag{6.1.7}$$

This volume fraction is close to the packing density of a primitive-cubic crystal system with a volume fraction of $\phi = 0.52$. The thickness of the shells consisting of perfluoroalkyl chains is rather different from each other. Whereas the inner layer has a thickness of 29.9 Å, the thickness of the outer layer is 44.8 Å. This can be explained by more water hydration into the outer, less compressed shell compared to more compact perfluoroalkyl chains in the inner shell. This fact is reflected by the lower SLD of outer shell of perfluoroalkyl chains $\rho_{outer} = 1.51 \cdot 10^{-6}$ Å^{-2} which is half the value of the inner shell $\rho_{inner} = 3.10 \cdot 10^{-6}$ Å^{-2}. Due to the hydrophilic centrally located cyclopentadienide anion of the fullerene and its counter ion potassium causing a solvent-separated ion pair, water molecules are able to penetrate into the perfluoroalkyl chains which is additionally facilitated by a less dense shell. Moreover, the obtained thicknesses suggested that both shells included not only the perfluoroalkyl chains but also the potassium ions due the formation of a solvent-separated ion pair with the cyclopentadienide as indicated in Fig. 6.1A. This finding is supported by a previous study of Kaindl *et al.*, who reported total lengths of the fluorinated lipids with $C_{10}F_{21}$ - and $C_{17}F_{35}$ - side chains of 12.8 Å and 21.9 Å, respectively[277]. For Rf8K vesicles in D_2O, the SANS curve show a shallow minimum at lower *q*-values compared to the H_2O sample which is due to the larger size of the Rf8K vesicles within this sample (Fig. 3B). The total radius of the Rf8K vesicles is obtained to be 171.0 Å (Table 6.1) which is slightly smaller from the value obtained by basic Guinier analysis, R = 190.5 ± 12.8 Å (Appendix II, Fig. 7.3B). In D_2O, the membrane thickness is 122.7 Å which is around 20 % thicker compared to the H_2O sample but with higher polydispersity index (Table 6.1) suggesting that water incorporation into the vesicle bilayer has an impact on the fine structure of Rf8K vesicles. The scattering length density of the membrane was obtained as $3.20 \cdot 10^{-6}$ Å^{-2}.

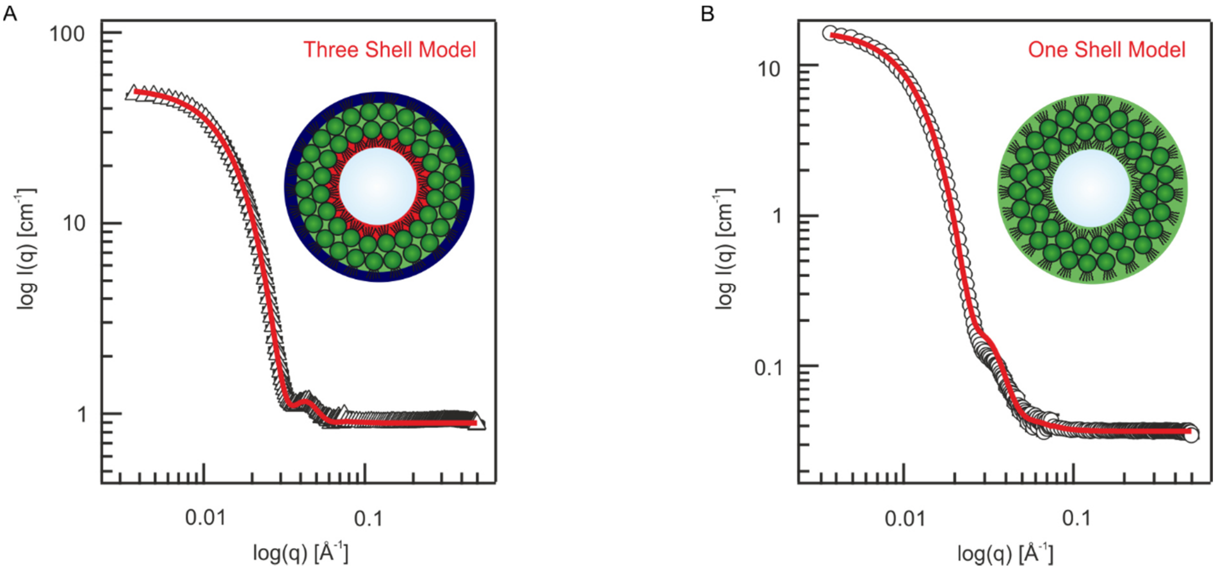

Figure 6.3 | SANS profiles for Rf8K vesicles in pure H_2O (A) and D_2O (B). The best fits are shown in red yielding a total shell thickness *d* = 141 Å and a core radius *R* = 43 Å for Rf8K in H_2O, and a total shell thickness *d* = 123 Å, a core radius *R* = 48 nm for Rf8K vesicles in D_2O. Insets represent the underlying model of the best fit. Rf8K vesicles in H_2O are fitted based on a multi-core shell model while for D_2O a core shell model is applied. For both data sets, the polydispersity was taken into account assuming a Schulz distribution of each shell of the vesicle.

Table 6.1 | Fitting of SANS experiments for Rf8K vesicles in H_2O and D_2O provides information about the thickness *d*, the SLD *ρ* and the polydispersity index PD of the sample.

Rf8K in H_2O	**Core multishell model**		
	d [Å]	**ρ [$\cdot 10^{-6}$ Å^{-2}]**	**PD**
Fluorinated alkyl chains	44.8	1.51	0.09
Fullerene layer	23.8	2.55	0.11
Fluorinated alkyl chains	29.9	3.10	0.16
Vesicle core	85.8	-0.56	0.19

Rf8K in D_2O	**Core shell model**		
	d [Å]	**ρ [$\cdot 10^{-6}$ Å^{-2}]**	**PD**
Membrane	122.7	3.20	0.23
Vesicle core	96.6	6.38	0.01

6.1.4 Water permeability

For quantitative investigations on the permeation of H_2O/D_2O across the vesicular bilayer of Rf8K molecules, a contrast variation method was applied. In case of a water permeable membrane, the addition of a defined amount of D_2O or H_2O to a Rf8K vesicle suspension of pure H_2O or D_2O leads to a continuous change in the SLD of the vesicle core caused by osmosis of water molecules. As a consequence of the large excess of the extravesicular volume, the SLD of the external solvent remains constant. Hence, the exchange rate k_{ex} of water molecules across the membrane can be determined, followed by the calculation of the permeability coefficient P_d. In Figure 6.4, two series of SANS profiles for Rf8K vesicles in H_2O:D_2O mixtures of 80:20 and 20:80 vol% for an incubation time of t = 0 – 14 h are shown. The black solid lines correspond to the best fit matching the experimental results. The start time of the measurements, t = 0 min, denotes the time point of the preparation of the different solvent mixtures. Based on the previous assumptions, a core multishell model was applied for the consecutive modeling of the SANS profiles at all time points during the incubation of the original H_2O sample in the presence of 20 vol% D_2O (Fig. 6.3A). The SLD of the solvent mixture ρ_{mix} was set constant to a value calculated as follows

$$\rho_{mix} = \phi\, \rho_{H_2O} + (1-\phi) y\, \rho_{D_2O}\,, \tag{6.1.8}$$

where ϕ represents the volume percentage of the H_2O solvent. The structural parameters obtained from the previous fitting (Table 1) served as basis for the refinement of each SANS profile. The first step of the modeling included the adjustment of the background value in order to account for the different scattering level of the pure solvent and the mixture of heavy and light water. Thereafter, all membrane parameters of the vesicle were fitted. In general, the addition of 20 vol% of heavy water to Rf8K vesicles in light water led to an increase of the scattering intensity (Fig. 6.3A). This change is caused by continuous exchange of water molecules between the vesicle core and the surrounding medium leading to a higher contrast between the aqueous medium and the vesicular membrane. During the incubation time of t = 14 h, the SLD of the core ρ_{core} gradually reached the value of the surrounding solvent mixture (Fig 6.3A, inset). Additionally, the SLD of the outer perfluoroalkyl chains ρ_{core} changed slightly from 1.5 to 1.7 within a time frame of 200 min (Appendix II, Fig. 7.5A, blue).

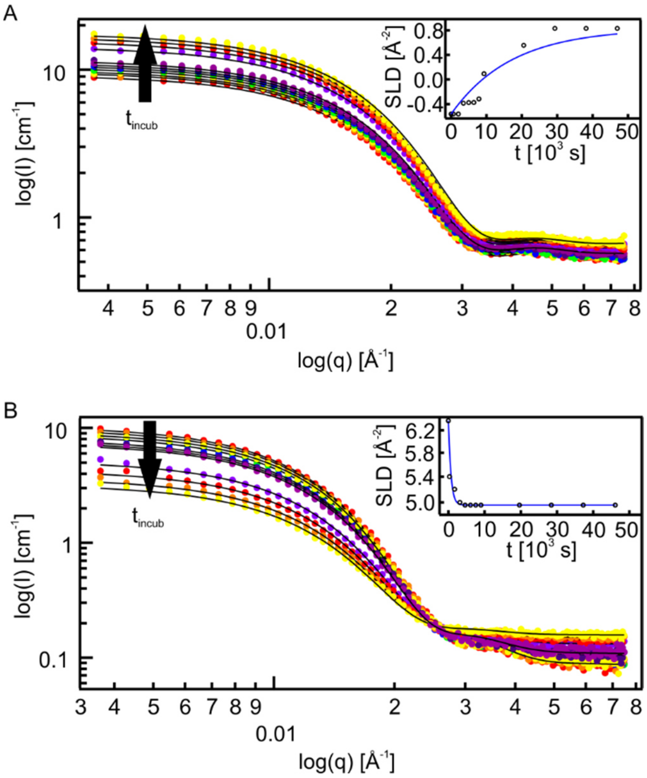

Figure 6.4 | Neutron contrast variation of Rf8K vesicles in H_2O:D_2O mixtures. SANS profiles of (A) 80:20 and (B) 20:80 mixtures and their best fits (black lines). The black arrow indicates the decrease on I_0 during the incubation time of vesicles in the corresponding solvent mixture. Insets represent the SLD of the vesicle core in H_2O:D_2O mixtures at an incubation time of t = 0 – 14 h and its best fit (blue line), yielding the permeability coefficients P_d of solvent molecules across the Rf8K bilayer.

On the other hand, the SLD of the inner shell and the fullerene core was not affected during the 14 h of incubation due to their compact structure and thus less hydrated state (Appendix II, Fig. 7.5, black and red). For comparison, a time-dependent series of SANS profiles of the incubation of Rf8K vesicles in 20 % H_2O was recorded (Fig. 6.3B). In general, the addition of 20 % H_2O led to a continuous decrease of the scattering intensity accompanied by a decrease of the maximum in the mid-q range. The latter phenomena was not present in case of the sample containing Rf8K in 80 % H_2O and is caused by a drop in scattering contrast. As described for the sample containing Rf8K vesicles in pure D_2O, data modeling is based on a core shell model describing the vesicular membrane by only one shell. The SLD of the core ρ_{core} reached the value of the surrounding solvent mixture $p = 4.96 \cdot 10^{-6}$ Å^{-2} during the incubation (Fig. 6.3B inset). Due to the fact, that only a simple core shell model could be applied to the obtained data set, modeling of the SANS profiles results in an ensemble information about the influence of the water molecules on the vesicular membrane. In this particular case, there was no change of the scattering length density ρ of the membrane caused by the addition of H_2O to Rf8K vesicles in D_2O. Nevertheless, it should be noted that the use of this oversimplified model may underestimate the influence of the presence of H_2O/ D_2O on the vesicular membrane. In addition, neutron contrast variation studies corresponding to 40:60 and 60:40 vol% mixtures were carried out and are represented together with their best fits in the Appendix (Fig. 7.5). The overall observed trends are consistent with tendencies presented here. For all measurements, the exchange rate k_{ex} was calculated by fitting the change of the SLD of the core ρ_{core} as a function of the incubation time t by an exponential function according to (insets in Fig. 6.3A and 6.3B, blue curves)

$$\rho(t) = \rho_{core,\,t=0} + \Delta\rho[1 - exp(-k_{ex}t)]\,. \tag{6.1.9}$$

$\rho_{core,\ t=0}$ represents the SLD of the core before mixing the solvents and t denotes the incubation time of vesicles in the solvent mixture. $\Delta\rho$ corresponds to the difference between the SLD of the core at t = 0 h and at time of the saturation level. The insets in Figure 6.3 represent the SLD of the core as a function of the incubation time of RF8K vesicles in 20:80 and 80:20 vol% mixtures and their best fits are superimposed by a blue line. The permeability coefficient P_d can then be calculated according to

$$P_d = k_{ex}\frac{V}{A} = k_{ex}\frac{4\pi r^3}{12\pi r^2} = k_{ex}\frac{1}{3}r\,, \tag{6.1.10}$$

where V/A is the volume-to-surface ratio of the Rf8K vesicle and r is its radius. Both values are obtained from the structural parameters of the Rf8K vesicles presented in table 1. The obtained results are shown in Table 2. At room temperature an exchange rate for D_2O of k_{ex} ~ $0.6 \cdot 10^{-4}$ s^{-1} was calculated for 60:40 and 80:40 vol% of H_2O:D_2O mixtures. In case of 20:80 and 40:60 vol% mixtures, the exchange of H_2O was 1-2 magnitudes higher. Calculation of the permeability coefficients P_d resulted in a value of ~$3 \cdot 10^{-13}$ m/s for 60:40 and 80:20 vol% sample and $12 \cdot 10^{-13}$ m/s and $57 \cdot 10^{-13}$ m/s for 40:60 and 20:80 vol% H_2O:D_2O mixtures, respectively. These findings indicate a significant difference in H_2O vs. D_2O diffusion across a Rf8K membrane. Homma *et al.* determined the permeability coefficient for Rf8K vesicles by a ^{17}O NMR relaxation time measurement to be $(3.01 \pm 0.09) \cdot 10^{-7}$ m/s [261]. Note that the direct comparison between P_d values obtained here and those obtained by ^{17}O NMR method[278, 279] is hardly possible due to the fact that the latter ones are based on measurements of water diffusion in the presence of a salt concentration gradient. There, the existent osmotic pressure accelerates water diffusion across a membrane and thus increases the water permeability coefficient. In general, the obtained water permeability coefficient P_d for Rf8K vesicles are remarkable low. For comparison, lipid bilayers consisting of pure phosphatidylcholine molecules have a permeability coefficient of 10^{-4} – 10^{-6} m/s.[280] In case of red blood cells, Mlekoday *et al.* obtained a value of $2 \cdot 10^{-4}$ m/s.[281] Note, the later value was again determined in the presence of an osmotic pressure.

Table 6.2 | Determination of exchange rate k_{ex} and permeability coefficient P_d of H_2O and D_2O for Rf8K vesicles. Parameters and results.

H_2O : D_2O [vol%]	80:20	60:40	40:60	20:80
$\rho_{mix,\ t=0}$ [$\cdot 10^{-6}$ Å^{-2}]	8.30	1.38	3.59	4.96
$\rho_{core,\ t=0\ h}$ [$\cdot 10^{-6}$ Å^{-2}]	-0.56	-0.56	6.38	6.38
$\rho_{core,\ t=14\ h}$ [$\cdot 10^{-6}$ Å^{-2}]	8.30	1.38	3.59	4.96
$\Delta\rho$ [$\cdot 10^{-6}$ Å^{-2}]	1.39	1.95	-2.79	-1.42
k_{ex} [$\cdot 10^{-4}$ 1/s]	0.55 ± 0.09	0.58 ± 0.17	2.16 ± 0.43	10.00 ± 0.04
P_d [$\cdot 10^{-13}$ m/s]	2.58 ± 0.48	2.73 ± 0.82	12.30 ± 2.62	57.00 ± 4.98

6.1.5 Summary

Neutron scattering experiments were performed to determine the fine structures of vesicles based on the amphiphilic fullerene derivative Rf8K bearing perfluoroalkyl side chains connected to a cyclopentadienide anion of the fullerene moiety. A combination of SANS and neutron contrast variation measurements allowed for the determination of permeability coefficient of the Rf8K membrane.

First, a fitting procedure of the SANS data by a core-multishell model confirmed a membrane structure with a (n-p-n') motif[260] consisting of a fullerene layer inside the membrane and two perfluoroalkyl side chain layers pointing to the outside of the membrane. In contrast to the findings of Homma *et al.*[261], the current findings revealed that the spontaneous formation of vesicles by Rf8K molecules water led to a molecular double layer of Rf8K molecules with a total thickness of 98.5 Å instead of an interdigitated layer. In detail, the inner shell of Rf8K vesicles consisted of a fullerene double layer with a thickness of 23.8 Å which is in well agreement with literature values of the van-der-Waals diameter of fullerene molecules[274]. Second, a contrast variation study enabled the quantification of the permeability coefficients of the Rf8K membrane for light and heavy water. In both cases, remarkable low values were obtained which are in the range of $P_d = 10^{-13} - 10^{-12}$ m/s and thus six orders of magnitude smaller compared to artificial phospholipid membranes or cell membranes[280-282]. Such a low permeability coefficient suggests the possibility to utilize the Rf8K vesicles as nano-carriers for aqueous solutions of hydrophilic compounds. The obtained results demonstrated that the unique combination of SANS and neutron contrast variation measurements enabled the quantification of not only the structural properties with Å accuracy but also the water permeability coefficient of membranes based on synthetic amphiphiles.

7. Appendix II

7.1 List of Abbreviations

AC	Alternating current
AML	Acute myeloid leukemia
AR	Aspect ratio
Biotin-DOPE	1,2-dioleoyl-*sn*-glycero-3-phosphoethanolamine-N-(cap biotinyl) (sodium salt)
BM	Bone marrow
BMEC	Bone marrow endothelial cells
$CaCl_2$	Calcium(II)chloride
C-cadherin	Classical cadherin
CAM	Cell adhesion molecules
CB	Cord blood
CD	Cluster of differentiation
$CHCl_3$	Chloroform
CLP	Common lymphoid progenitors
CMP	Common myeloid progenitors
CXCR4	C-X-C chemokine receptor type 4
C_{60}	(C_{60}-I_h)[5,6]fullerene
$<d>$	Average intermolecular distance
DGS-NTA	1,2-dioleoyl-*sn*-glycero-3-[(N-(5-amino-1-carboxypentyl) iminodiacetic acid)succinyl] (nickel salt)
EC	Ectodomain (of cadherins)
E-cadherin	Cadherins from epithelia
G-CSF	Granulocyte-colony stimulating factor
HBS	Hepes buffered saline
Hepes	4-(2-hydroxyethyl)-1-piperazineethanesulfonic acid
H_2O	Water
H_2O_2	Hydrogen peroxide
HSPC	Hematopoietic stem and progenitor cells
LB	Leukemic blasts
LIC	Leukemia initiating cells
LT-HSPC	Long-term hematopoietic stem cells
M	Molar concentration
mM	Millimolar

MPP	Multipotent progenitor cells
MSC	Mesenchymal stem cells
NaCl	Sodium chloride
N-cadherin	Neural cadherin
NH_4OH	Aqueous solution of ammonia
$NiCl_2$	Nickel(II)chloride
P	Polarizer
PB	Peripheral blood
QCM-D	Quartz crystal microbalance with dissipation monitoring
RICM	Reflection interference contrast microscopy
SDF1α	Stromal cell-derived factor 1α (also known as C-X-C motif chemokine 12 (CXCL12))
SDS	Sodium dodecyl sulfate
SLD	Scattering length density
SUV	Small unilamellar vesicles
SOPC	1-stearoyl-2-oleoyl-*sn*-glycero-3-phosphocholine
ST-HSPC	Short-term hematopoietic stem cells
vs.	Versus
XRR	High-energy specular X-ray reflectivity

7.2 Supplementary information

7.2.1 Full QCM-D data sets

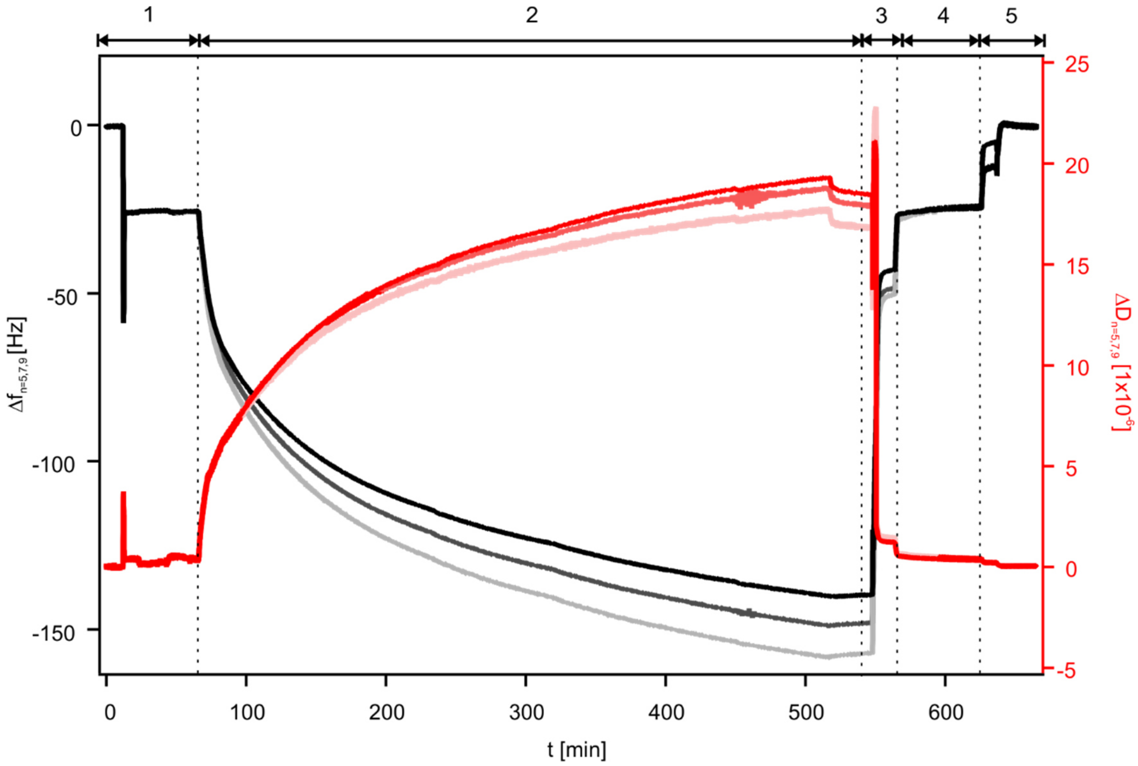

Figure 7.1 | Deposition of a supported membrane containing 2 mol% DGS-NTA and functionalization with His6 N-cadherin. Changes in resonant frequency *Δf* (light grey, grey, black) and dissipation *ΔD* (beige, light red, red) monitored at 25, 35 and 45 MHz (n = 5, 7, 9), respectively, during (1) the formation of planar membrane consisting of 2 mol% DOGS-NTA in SOPC on SiO_2 substrates and (2) the subsequent functionalization with His6 N-cadherin. Decoupling of His6 N-cadherin from the supported membrane by 100 mM aqueous EDTA (3) led back to levels of *Δf* and *ΔD* for a pure supported membrane (4). The supported membrane was removed from the SiO_2 substrate by 20 mM aqueous SDS (5).

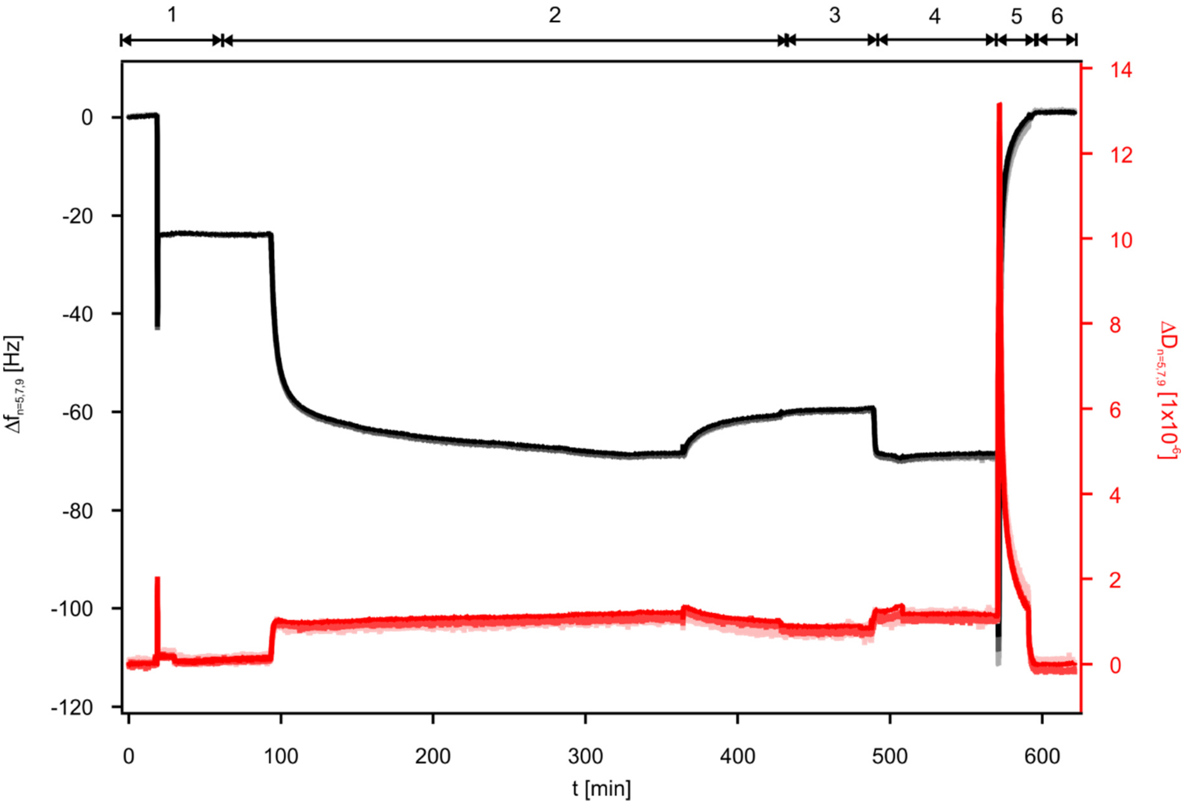

Figure 7.2 | Deposition of a supported membrane containing 0.5 mol% biotin-DOPE and successive functionalization with neutravidin and biotin-SDF1α. Changes in resonant frequency *Δf* (light grey, grey, black) and dissipation *ΔD* (beige, light red, red) monitored at 25, 35 and 45 MHz (n = 5, 7, 9), respectively, during (1) the formation of planar membrane consisting of 0.5 mol% biotin-DOPE in SOPC on SiO_2 substrates and (2) the subsequent functionalization with neutravidin. Electrostatically bound neutravidin was removed by (3) 100 mM glycine hydrochloride (pH 2.5) followed by the coupling of biotin-SDF1α to neutravidin. The complete *in vitro* niche model was removed from the SiO_2 substrate by 20 mM aqueous SDS (5).

7.2.2 Basic analysis of SANS data of Rf8K vesicles

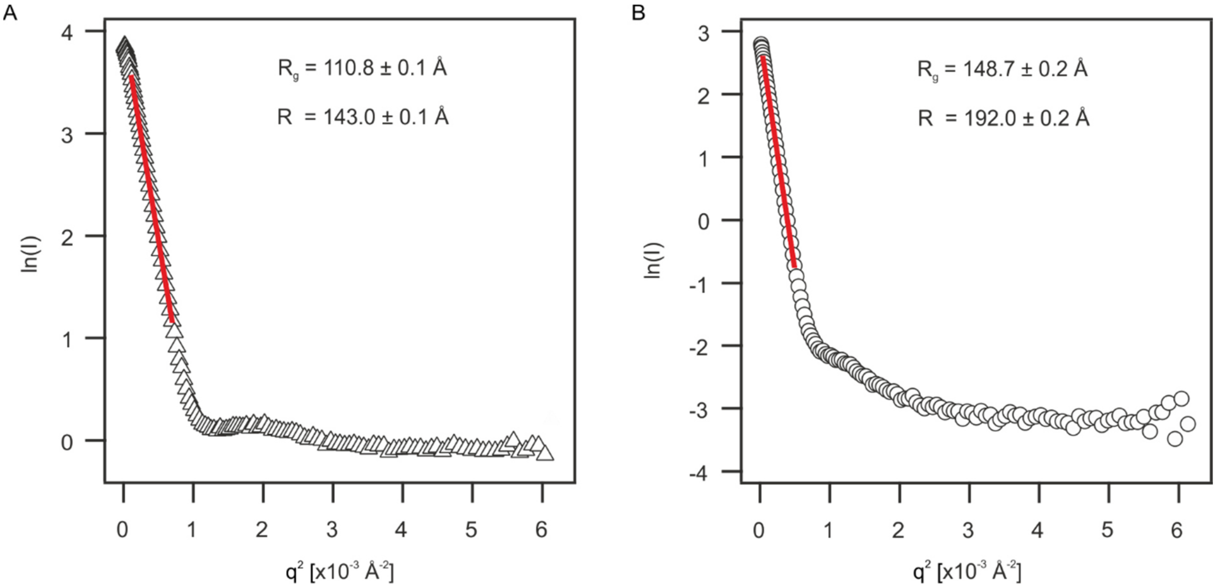

Figure 7.3 | Guinier plot for Rf8K vesicles in pure (A) H_2O and (B) D_2O. The solid lines represent the best fits according to Guinier approximation resulting in a radius of gyration R_g of 110.8 Å and 148.7 Å, respectively.

Basic analysis of SANS profiles for Rf8K in H_2O and D_2O was performed according to the Guinier approximation[269]. The natural logarithm of the scattered intensity *I(q)* was plotted as a function of the square of the scattering vector *q* to obtain information on the radius of gyration R_g which can be fitted using the Guinier approximation[269] according to

$$\ln(I_q) = \ln(\mathrm{I_0}) - \left(\frac{\mathrm{Rg}^2}{3}\right) * \ln(\mathrm{q}^2)\,, \tag{7.2.1}$$

where I_q describes the scattering intensity as a function of the wave vector q. I_0 represents the scattering intensity at q = 0. The average radius *R* of the Rf8K vesicles is estimated from the radius of gyration as given by

$$\mathrm{R} = \left({}^{5}/_{3}\right)^{0.5} \mathrm{R_g}\,. \tag{7.2.2}$$

A radius of gyration R_g for Rf8K in H_20 and D_2O was obtained as 110.8 Å and 148.7 Å, respectively (Appendix II, Figure 7.3A und B).

7.2.3 Neutron contrast variation study of Rf8K vesicles

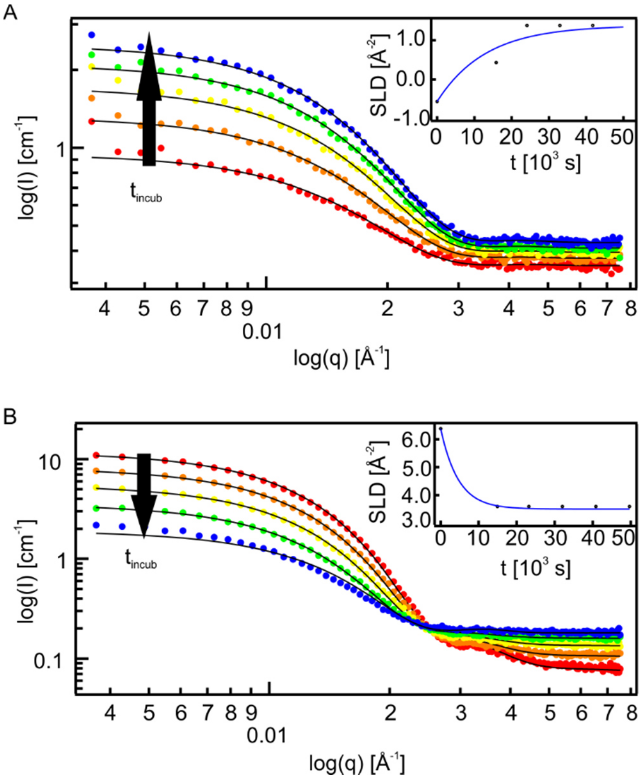

Figure 7.4 | Neutron contrast variation experiment of Rf8K vesicles in H_2O:D_2O mixtures. SANS profiles of (A) 60:40 and (B) 40:60 mixtures and their best fits (black lines). The black arrow indicates the decrease on I_0 during the incubation time of vesicles in the corresponding solvent mixture. Insets represent the SLD of the vesicle core in H_2O:D_2O mixtures at an incubation time of t = 0 – 14 h and its best fit (blue line), yielding the permeability coefficients P_d of solvent molecules across the Rf8K shell.

7.2.4 Change in the scattering length density of the vesicle shells

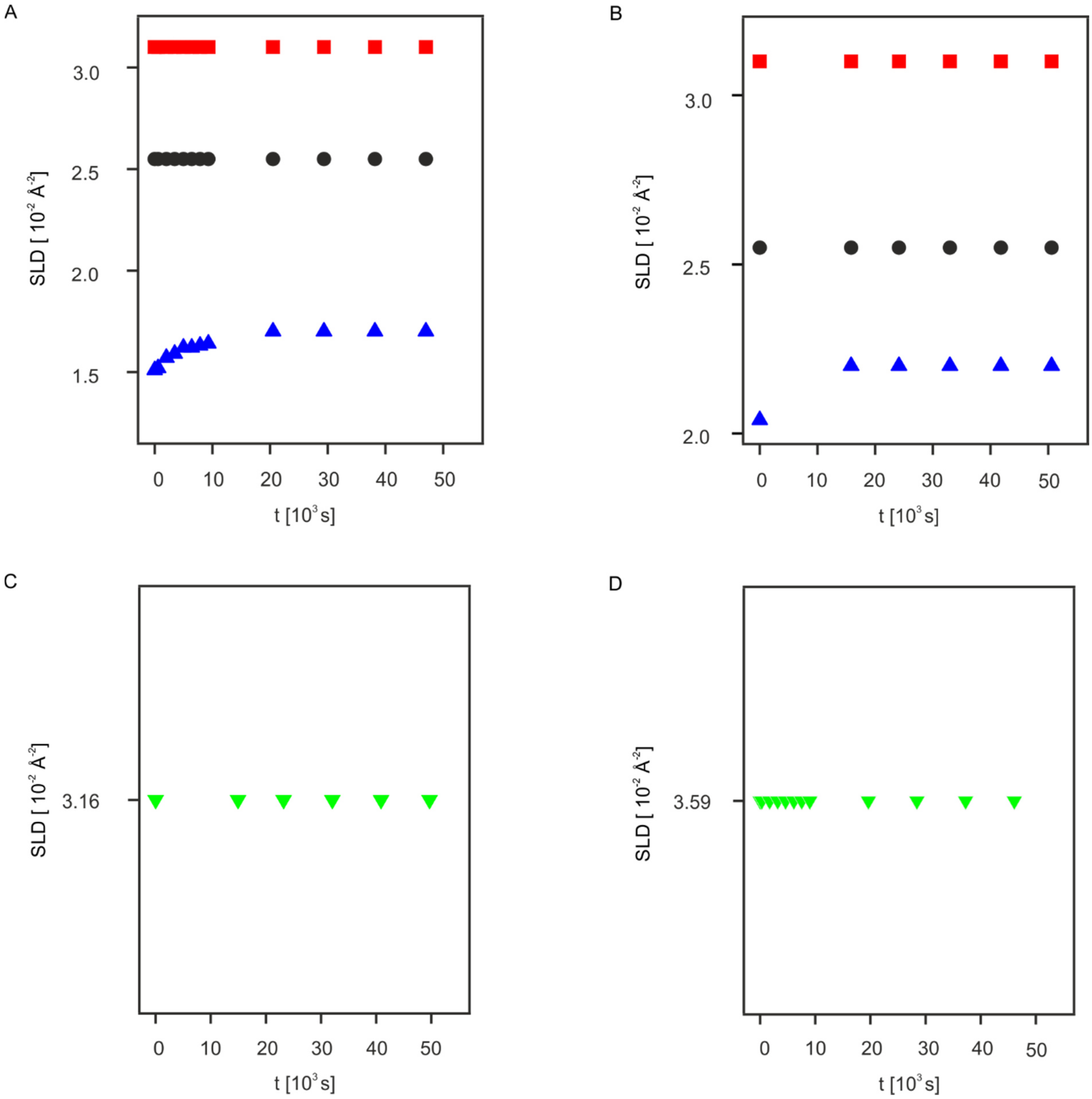

Figure 7.5 | Changes in the SLD as a function of the incubation time *t* of the inner perfluoroalkyl chains (red), fullerene layer (black) and the outer perfluoroalkyl chains (blue) for Rf8K vesicles in 80:20 (A) and 60:40 (B) mixtures. Only the SLD of the outer perfluoroalkyl chains changes indicating that there are almost no water molecules present in the fullerene and inner fluorocarbon shells. Changes in the SLD of the total vesicle shell of Rf8K vesicles in 20:80 (C) and 40:60 (D) mixtures [H_2O:D_2O].

8. Bibliography

1. Maximow AA. *Der Lymphozyt als gemeinsame Stammzelle der verschiedenen Blutelemente in der embryonalen Entwicklung und im postfetalen Leben der Säugetiere* (1909).

2. Till JE, McCulloch EA. A direct measurement of the radiation sensitivity of normal mouse bone marrow cells. *Radiation Research* **14**, 213-222 (1961).

3. Becker AJ*, et al.* Cytological Demonstration of the Clonal Nature of Spleen Colonies Derived from Transplanted Mouse Marrow Cells. *Nature* **197**, 452-454 (1963).

4. Siminovitch L*, et al.* The distribution of colony-forming cells among spleen colonies. *Journal of Cellular and Comparative Physiology* **62**, 327-336 (1963).

5. Celso CL*, et al.* Live-animal tracking of individual haematopoietic stem/progenitor cells in their niche. *Nature* **457**, 92-96 (2009).

6. Als-Nielsen J, McMorrow D. *Elements of modern X-ray physics*. John Wiley & Sons (2011).

7. MacArthur BD*, et al.* Systems biology of stem cell fate and cellular reprogramming. *Nature Reviews Molecular Cell Biology* **10**, 672-681 (2009).

8. Moore KA, Lemischka IR. Stem cells and their niches. *Science* **311**, 1880-1885 (2006).

9. Wilson A, Trumpp A. Bone-marrow haematopoietic-stem-cell niches. *Nature Reviews Immunology* **6**, 93-106 (2006).

10. Schofield R. The relationship between the spleen colony-forming cell and the haemopoietic stem cell. *Blood Cells* **4**, 7-25 (1977).

11. Calvi L*, et al.* Osteoblastic cells regulate the haematopoietic stem cell niche. *Nature* **425**, 841-846 (2003).

12. Zhang J*, et al.* Identification of the haematopoietic stem cell niche and control of the niche size. *Nature* **425**, 836-841 (2003).

13. Kiel MJ*, et al.* SLAM family receptors distinguish hematopoietic stem and progenitor cells and reveal endothelial niches for stem cells. *Cell* **121**, 1109-1121 (2005).

14. Mendez-Ferrer S*, et al.* Mesenchymal and haematopoietic stem cells form a unique bone marrow niche. *Nature* **466**, 829-834 (2010).

15. Katayama Y*, et al.* Signals from the sympathetic nervous system regulate hematopoietic stem cell egress from bone marrow. *Cell* **124**, 407-421 (2006).

16. Dexter TM*, et al.* Conditions controlling the proliferation of haemopoietic stem cells in vitro. *Journal of Cellular Physiology* **91**, 335-344 (1977).

17. Taichman R*, et al.* Human osteoblasts support human hematopoietic progenitor cells in. *Blood* **87**, 518-524 (1996).

18. Wagner W*, et al.* Adhesion of hematopoietic progenitor cells to human mesenchymal stem cells as a model for cell– cell interaction. *Experimental Hematology* **35**, 314-325 (2007).

19. Wagner W*, et al.* Molecular and secretory profiles of human mesenchymal stromal cells and their abilities to maintain primitive hematopoietic progenitors. *Stem Cells* **25**, 2638-2647 (2007).

20. Wein F*, et al.* N-cadherin is expressed on human hematopoietic progenitor cells and mediates interaction with human mesenchymal stromal cells. *Stem Cell Research* **4**, 129-139 (2010).

21. Puch S*, et al.* N-cadherin is developmentally regulated and functionally involved in early hematopoietic cell differentiation. *Journal of Cell Science* **114**, 1567-1577 (2001).

22. Hosokawa K*, et al.* Knockdown of N-cadherin suppresses the long-term engraftment of hematopoietic stem cells. *Blood* **116**, 554-563 (2010).

23. Kiel MJ*, et al.* Lack of evidence that hematopoietic stem cells depend on N-cadherin-mediated adhesion to osteoblasts for their maintenance. *Cell Stem Cell* **1**, 204-217 (2007).

24. Kiel MJ*, et al.* Hematopoietic Stem Cells Do Not Depend on N-Cadherin to Regulate Their Maintenance. *Cell Stem Cell* **4**, 170-179 (2009).

25. Greenbaum AM*, et al.* N-cadherin in osteolineage cells is not required for maintenance of hematopoietic stem cells. *Blood* **120**, 295-302 (2012).

26. Bromberg O*, et al.* Osteoblastic N-cadherin is not required for microenvironmental support and regulation of hematopoietic stem and progenitor cells. *Blood* **120**, 303-313 (2012).

27. Méndez-Ferrer S*, et al.* Haematopoietic stem cell release is regulated by circadian oscillations. *Nature* **452**, 442-447 (2008).

28. Greenbaum A*, et al.* CXCL12 in early mesenchymal progenitors is required for haematopoietic stem-cell maintenance. *Nature* **495**, 227-230 (2013).

29. Netelenbos T*, et al.* Proteoglycans on bone marrow endothelial cells bind and present SDF-1 towards hematopoietic progenitor cells. *Leukemia* **17**, 175-184 (2003).

30. Sugiyama T*, et al.* Maintenance of the hematopoietic stem cell pool by CXCL12-CXCR4 chemokine signaling in bone marrow stromal cell niches. *Immunity* **25**, 977-988 (2006).

31. Lataillade J-J*, et al.* Chemokine SDF-1 enhances circulating CD34+ cell proliferation in synergy with cytokines: possible role in progenitor survival. *Blood* **95**, 756-768 (2000).

32. Hattori K*, et al.* Plasma elevation of stromal cell–derived factor-1 induces mobilization of mature and immature hematopoietic progenitor and stem cells. *Blood* **97**, 3354-3360 (2001).

33. Aiuti A*, et al.* The chemokine SDF-1 is a chemoattractant for human CD34+ hematopoietic progenitor cells and provides a new mechanism to explain the

mobilization of CD34+ progenitors to peripheral blood. *The Journal of Experimental Medicine* **185**, 111-120 (1997).

34. Faber A*, et al.* The many facets of SDF-1 α, CXCR4 agonists and antagonists on hematopoietic progenitor cells. *BioMed Research International* **2007**, (2007).

35. Lowenberg B*, et al.* Acute myeloid leukemia. *New England Journal of Medicine* **341**, 1051-1062 (1999).

36. Estey E, Döhner H. Acute myeloid leukaemia. *The Lancet* **368**, 1894-1907 (2006).

37. Lapidot T*, et al.* A cell initiating human acute myeloid leukaemia after transplantation into SCID mice. *Nature* **367**, 645-648 (1994).

38. Hope KJ*, et al.* Acute myeloid leukemia originates from a hierarchy of leukemic stem cell classes that differ in self-renewal capacity. *Nature Immunology* **5**, 738-743 (2004).

39. Ishikawa F*, et al.* Chemotherapy-resistant human AML stem cells home to and engraft within the bone-marrow endosteal region. *Nature Biotechnology* **25**, 1315-1321 (2007).

40. Lane SW*, et al.* The leukemic stem cell niche: current concepts and therapeutic opportunities. *Blood* **114**, 1150-1157 (2009).

41. Matsunaga T*, et al.* Interaction between leukemic-cell VLA-4 and stromal fibronectin is a decisive factor for minimal residual disease of acute myelogenous leukemia. *Nature Methods* **9**, 1158-1165 (2003).

42. Rombouts EJ*, et al.* Relation between CXCR-4 expression, Flt3 mutations, and unfavorable prognosis of adult acute myeloid leukemia. *Blood* **104**, 550-557 (2004).

43. Krause D*, et al.* CD34: structure, biology, and clinical utility. *Blood* **87**, 1-13 (1996).

44. Ran D*, et al.* Heterogeneity of leukemia stem cell candidates at diagnosis of acute myeloid leukemia and their clinical significance. *Experimental Hematology* **40**, 155-165. e151 (2012).

45. Øyan AM*, et al.* CD34 expression in native human acute myelogenous leukemia blasts: differences in CD34 membrane molecule expression are associated with different gene expression profiles. *Cytometry Part B: Clinical Cytometry* **64**, 18-27 (2005).

46. Sackmann E, Tanaka M. Supported membranes on soft polymer cushions: fabrication, characterization and applications. *Trends in Biotechnology* **18**, 58-64 (2000).

47. Tanaka M, Sackmann E. Polymer-supported membranes as models of the cell surface. *Nature* **437**, 656-663 (2005).

48. Singer S, Nicolson GL. The fluid mosaic model of the structure of cell membranes. *Science* **175**, 720-731 (1972).

49. Yoshikawa HY*, et al.* Quantitative Evaluation of Mechanosensing of Cells on Dynamically Tunable Hydrogels. *Journal of the American Chemical Society* **133**, 1367-1374 (2011).

50. Röntgen WC. Über eine neue Art von Strahlen. *Annalen der Physik* **300**, 1-11 (1898).

51. Compton AH. A quantum theory of the scattering of X-rays by light elements. *Physical Review* **21**, 483 (1923).

52. Tolan M. Reflectivity of x-rays from surfaces. *X-Ray Scattering from Soft-Matter Thin Films: Materials Science and Basic Research*, 5-31 (1999).

53. Russell T. X-ray and neutron reflectivity for the investigation of polymers. *Materials Science Reports* **5**, 171-271 (1990).

54. Helm C*, et al.* Phospholipid monolayer density distribution perpendicular to the water surface. A synchrotron X-ray reflectivity study. *Europhysics Letters* **4**, 697 (1987).

55. Koerner A*, et al.* Cell differentiation of pluripotent tissue sheets immobilized on supported membranes displaying cadherin-11. *PloS One* **8**, e54749 (2013).

56. Abuillan W*, et al.* Quantitative determination of the lateral density and intermolecular correlation between proteins anchored on the membrane surfaces using grazing incidence small-angle X-ray scattering and grazing incidence X-ray fluorescence. *The Journal of Chemical Physics* **137**, 204907 (2012).

57. Salditt T*, et al.* X-ray reflectivity of solid-supported, multilamellar membranes. *The European Physical Journal E* **7**, 105-116 (2002).

58. Born M, Wolf E. *Principles of optics: electromagnetic theory of propagation, interference and diffraction of light*. Cambridge university press (1999).

59. Gibaud A. Specular reflectivity from smooth and rough surfaces. In: *X-ray and neutron reflectivity: principles and applications*. Springer (1999).

60. Parratt LG. Surface studies of solids by total reflection of X-rays. *Physical Review* **95**, 359 (1954).

61. Abelés F. Recherches sur la propagation des ondes électromagnétiques sinusoidales dans les milieux stratifiés. Application aux couches minces. *Annales de Physique* **5**, 569-639 (1950).

62. Kern W. Cleaning solutions based on hydrogen peroxide for use in silicon semiconductor technology. *RCA Review* **31**, 187-206 (1970).

63. Nelson A. Co-refinement of multiple-contrast neutron/X-ray reflectivity data using MOTOFIT. *Journal of Applied Crystallography* **39**, 273-276 (2006).

64. Hochrein MB*, et al.* Structure and Mobility of Lipid Membranes on a Thermoplastic Substrate. *Langmuir* **22**, 538-545 (2006).

65. Nováková E*, et al.* Structure of two-component lipid membranes on solid support: An x-ray reflectivity study. *Physical Review E* **74**, 051911 (2006).

66. Miller CE*, et al.* Characterization of biological thin films at the solid-liquid interface by X-ray reflectivity. *Physical Review Letters* **94**, 238104 (2005).

67. Israelachvili JN. *Intermolecular and surface forces: revised third edition*. Academic Press (2011).

68. Merkel R*, et al.* Molecular friction and epitactic coupling between monolayers in supported bilayers. *Journal de Physique* **50**, 1535-1555 (1989).

69. Málková Š*, et al.* X-Ray Reflectivity Studies of cPLA 2 α-C2 Domains Adsorbed onto Langmuir Monolayers of SOPC. *Biophysical Journal* **89**, 1861-1873 (2005).

70. Seitz PC*, et al.* Modulation of Substrate–Membrane Interactions by Linear Poly (2-methyl-2-oxazoline) Spacers Revealed by X-ray Reflectivity and Ellipsometry. *Chemphyschem* **10**, 2876-2883 (2009).

71. Hochuli E*, et al.* New metal chelate adsorbent selective for proteins and peptides containing neighbouring histidine residues. *Journal of Chromatography A* **411**, 177-184 (1987).

72. Harrison OJ*, et al.* The Extracellular Architecture of Adherens Junctions Revealed by Crystal Structures of Type I Cadherins. *Structure* **19**, 244-256 (2011).

73. Pokutta S*, et al.* Conformational changes of the recombinant extracellular domain of E-cadherin upon calcium binding. *European Journal of Biochemistry* **223**, 1019-1026 (1994).

74. Martel L*, et al.* X-ray reflectivity investigations of two-dimensional assemblies of C-cadherins: First steps in structural and functional studies. In: *Journal de Physique IV (Proceedings)* (ed^(eds). EDP sciences (2002).

75. Rosano C*, et al.* The X-ray three-dimensional structure of avidin. *Biomolecular Engineering* **16**, 5-12 (1999).

76. Pugliese L*, et al.* Crystal structure of apo-avidin from hen egg-white. *Journal of Molecular Biology* **235**, 42-46 (1994).

77. Orelma H*, et al.* Generic method for attaching biomolecules via avidin–biotin complexes immobilized on films of regenerated and nanofibrillar cellulose. *Biomacromolecules* **13**, 2802-2810 (2012).

78. Ohnishi Y*, et al.* Crystal structure of recombinant native SDF-1α with additional mutagenesis studies: An attempt at a more comprehensive interpretation of accumulated structure-activity relationship data. *Journal of Interferon & Cytokine Research* **20**, 691-700 (2000).

79. Dealwis C*, et al.* Crystal structure of chemically synthesized [N33A] stromal cell-derived factor 1α, a potent ligand for the HIV-1 "fusin" coreceptor. *Proceedings of the National Academy of Sciences of the United States of America* **95**, 6941-6946 (1998).

80. Janshoff A*, et al.* Piezoelectric Mass-Sensing Devices as Biosensors: An Alternative to Optical Biosensors? *Angewandte Chemie International Edition* **39**, 4004-4032 (2000).

81. Ward MD, Buttry DA. In situ interfacial mass detection with piezoelectric transducers. *Science* **249**, 1000-1007 (1990).

82. Rodahl M*, et al.* Quartz crystal microbalance setup for frequency and Q-factor measurements in gaseous and liquid environments. *Review of Scientific Instruments* **66**, 3924 (1995).

83. Sauerbrey G. Verwendung von Schwingquarzen zur Wägung dünner Schichten und zur Mikrowägung. *Zeitschrift fur Physik* **155**, 206-222 (1959).

84. Curie J, Curie P. Développement, par pression, de l'électricité polaire dans les cristaux hémièdres à faces inclinées. *Comptes Rendus* **91**, 294-295 (1880).

85. Bruckenstein S, Shay M. Experimental aspects of use of the quartz crystal microbalance in solution. *Electrochimica Acta* **30**, 1295-1300 (1985).

86. Sauerbrey G. Use of quartz vibration for weighing thin films on a microbalance. *Zeitschrift fur Physik* **155**, 206-212 (1959).

87. Oberg P, Lingensjo J. Crystal Film Thickness Monitor. *Review of Scientific Instruments* **30**, 1053-1053 (1959).

88. Nomura T, Okuhara M. Frequency shifts of piezoelectric quartz crystals immersed in organic liquids. *Analytica Chimica Acta* **142**, 281-284 (1982).

89. Martin SJ*, et al.* Characterization of a quartz crystal microbalance with simultaneous mass and liquid loading. *Analytical Chemistry* **63**, 2272-2281 (1991).

90. Rodahl M*, et al.* QCM Operation in Liquids: An Explanation of Measured Variations in Frequency and Q Factor with Liquid Conductivity. *Analytical Chemistry* **68**, 2219-2227 (1996).

91. Voinova MV*, et al.* Viscoelastic acoustic response of layered polymer films at fluid-solid interfaces: continuum mechanics approach. *Physica Scripta* **59**, 391 (1999).

92. Sackmann E. Supported membranes: scientific and practical applications. *Science* **271**, 43-48 (1996).

93. Malmstrom J*, et al.* Viscoelastic modeling of highly hydrated laminin layers at homogeneous and nanostructured surfaces: quantification of protein layer properties using QCM-D and SPR. *Langmuir* **23**, 9760-9768 (2007).

94. Richter R*, et al.* Pathways of lipid vesicle deposition on solid surfaces: a combined QCM-D and AFM study. *Biophysical Journal* **85**, 3035-3047 (2003).

95. Frenkel N*, et al.* Mechanistic Investigation of Interactions between Steroidal Saponin Digitonin and Cell Membrane Models. *The Journal of Physical Chemistry B* **118**, 14632-14639 (2014).

96. Keller CA*, et al.* Formation of supported membranes from vesicles. *Physical Review Letters* **84**, 5443-5446 (2000).

97. Sakai S*, et al.* Adsorption behaviors of recombinant E-cadherin-IgG Fc fusion protein on polystyrene surface. *Colloids and Surfaces B: Biointerfaces* **94**, 192-198 (2012).

98. Larsson C*, et al.* Characterization of DNA Immobilization and Subsequent Hybridization on a 2D Arrangement of Streptavidin on a Biotin-Modified Lipid Bilayer Supported on SiO2. *Analytical Chemistry* **75**, 5080-5087 (2003).

99. Höök F*, et al.* Variations in Coupled Water, Viscoelastic Properties, and Film Thickness of a Mefp-1 Protein Film during Adsorption and Cross-Linking: A Quartz

Crystal Microbalance with Dissipation Monitoring, Ellipsometry, and Surface Plasmon Resonance Study. *Analytical Chemistry* **73**, 5796-5804 (2001).

100. Wolny PM*, et al.* On the adsorption behavior of biotin-binding proteins on gold and silica. *Langmuir* **26**, 1029-1034 (2009).

101. Fischer H*, et al.* Average protein density is a molecular-weight-dependent function. *Protein Science* **13**, 2825-2828 (2004).

102. Fukuto M*, et al.* Effects of surface ligand density on lipid-monolayer-mediated 2D assembly of proteins. *Soft Matter* **6**, 1513-1519 (2010).

103. Lipowsky R, Sackmann E. *Structure and dynamics of membranes: I. from cells to vesicles/II. generic and specific interactions*. Elsevier (1995).

104. Dexter T, Moore M. In vitro duplication and 'cure'of haemopoietic defects in genetically anaemic mice. *Nature* **269**, 412 - 414 (1977).

105. McConnell H*, et al.* Supported planar membranes in studies of cell-cell recognition in the immune system. *Biochimica et Biophysica Acta (BBA)-Reviews on Biomembranes* **864**, 95-106 (1986).

106. Halbleib JM, Nelson WJ. Cadherins in development: cell adhesion, sorting, and tissue morphogenesis. *Genes & Development* **20**, 3199-3214 (2006).

107. Bell GI*, et al.* Cell adhesion. Competition between nonspecific repulsion and specific bonding. *Biophysical Journal* **45**, 1051 (1984).

108. Bruinsma R*, et al.* Adhesive switching of membranes: experiment and theory. *Physical Review E* **61**, 4253 (2000).

109. Albersdorfer A*, et al.* Adhesion-induced domain formation by interplay of long-range repulsion and short-range attraction force: A model membrane study. *Biophysical Journal* **73**, 245-257 (1997).

110. Bell GI. Models for the specific adhesion of cells to cells. *Science* **200**, 618-627 (1978).

111. Rädler JO*, et al.* Fluctuation analysis of tension-controlled undulation forces between giant vesicles and solid substrates. *Physical Review E* **51**, 4526 (1995).

112. Weikl TR*, et al.* Adhesion of membranes with competing specific and generic interactions. *The European Physical Journal E* **8**, 59-66 (2002).

113. Sackmann E, Bruinsma RF. Cell Adhesion as Wetting Transition? *Chemphyschem* **3**, 262-269 (2002).

114. Sengupta K, Limozin L. Adhesion of soft membranes controlled by tension and interfacial polymers. *Physical Review Letters* **104**, 088101 (2010).

115. Rädler J, Sackmann E. Imaging optical thicknesses and separation distances of phospholipid vesicles at solid surfaces. *Journal de Physique II* **3**, 727-748 (1993).

116. Limozin L, Sengupta K. Quantitative reflection interference contrast microscopy (RICM) in soft matter and cell adhesion. *Chemphyschem* **10**, 2752-2768 (2009).

117. Zilker A*, et al.* Dynamic reflection interference contrast (RIC-) microscopy: a new method to study surface excitations of cells and to measure membrane bending elastic moduli. *Journal De Physique* **48**, 2139-2151 (1987).

118. Monzel C*, et al.* Probing Biomembrane Dynamics by Dual-Wavelength Reflection Interference Contrast Microscopy. *Chemphyschem* **10**, 2828-2838 (2009).

119. Ploem J. Reflection-contrast microscopy as a tool for investigation of the attachment of living cells to a glass surface. *Mononuclear phagocytes in immunity, infection and pathology Blackwell, Oxford*, 405-421 (1975).

120. Wiegand G*, et al.* Microinterferometry: three-dimensional reconstruction of surface microtopography for thin-film and wetting studies by reflection interference contrast microscopy (RICM). *Applied Optics* **37**, 6892-6905 (1998).

121. Brian AA, McConnell HM. Allogeneic stimulation of cytotoxic T cells by supported planar membranes. *Proceedings of the National Academy of Sciences of the United States of America* **81**, 6159-6163 (1984).

122. Marlin SD, Springer TA. Purified intercellular adhesion molecule-1 (ICAM-1) is a ligand for lymphocyte function-associated antigen 1 (LFA-1). *Cell* **51**, 813-819 (1987).

123. Dustin ML, Springer TA. Lymphocyte function-associated antigen-1 (LFA-1) interaction with intercellular adhesion molecule-1 (ICAM-1) is one of at least three mechanisms for lymphocyte adhesion to cultured endothelial cells. *The Journal of Cell Biology* **107**, 321-331 (1988).

124. Chan P-Y*, et al.* Influence of receptor lateral mobility on adhesion strengthening between membranes containing LFA-3 and CD2. *The Journal of Cell Biology* **115**, 245-255 (1991).

125. Qi S*, et al.* Synaptic pattern formation during cellular recognition. *Proceedings of the National Academy of Sciences of the United States of America* **98**, 6548-6553 (2001).

126. Kaindl T*, et al.* Spatio-temporal patterns of pancreatic cancer cells expressing CD44 isoforms on supported membranes displaying hyaluronic acid oligomers arrays. *PloS One* **7**, e42991 (2012).

127. Eakin RE*, et al.* The concentration and assay of avidin, the injury protein in raw egg white. *Journal of Biological Chemistry* **140**, 535-543 (1941).

128. Livnah O*, et al.* Three-dimensional structures of avidin and the avidin-biotin complex. *Proceedings of the National Academy of Sciences of the United States of America* **90**, 5076-5080 (1993).

129. Helm CA*, et al.* Measurement of ligand-receptor interactions. *Proceedings of the National Academy of Sciences of the United States of America* **88**, 8169-8173 (1991).

130. Schmitt L*, et al.* Synthesis and Characterization of Chelator-Lipids for Reversible Immobilization of Engineered Proteins at Self-Assembled Lipid Interfaces. *Journal of the American Chemical Society* **116**, 8485-8491 (1994).

131. Dorn IT*, et al.* Orientation and two-dimensional organization of proteins at chelator lipid interfaces. *Biological Chemistry* **379**, 1151-1160 (1998).

132. Dietrich C*, et al.* Functional Immobilization of a DNA-Binding Protein at a Membrane Interface via Histidine Tag and Synthetic Chelator Lipids. *Biochemistry* **35**, 1100-1105 (1996).

133. Takeichi M. The cadherins: cell-cell adhesion molecules controlling animal morphogenesis. *Development* **102**, 639-655 (1988).

134. Gumbiner BM. Regulation of cadherin-mediated adhesion in morphogenesis. *Nature Reviews: Molecular Cell Biology* **6**, 622-634 (2005).

135. Leckband D, Prakasam A. Mechanism and dynamics of cadherin adhesion. *Annual Review of Biomedical Engineering* **8**, 259-287 (2006).

136. Häussinger D*, et al.* Proteolytic E-cadherin activation followed by solution NMR and X-ray crystallography. *The EMBO Journal* **23**, 1699-1708 (2004).

137. Shapiro L*, et al.* Considerations on the folding topology and evolutionary origin of cadherin domains. *Proceedings of the National Academy of Sciences of the United States of America* **92**, 6793-6797 (1995).

138. Alattia J-R*, et al.* Lateral self-assembly of E-cadherin directed by cooperative calcium binding. *FEBS Letters* **417**, 405-408 (1997).

139. Koch AW*, et al.* Homophilic adhesion by cadherins. *Current Opinion in Structural Biology* **9**, 275-281 (1999).

140. Nagar B*, et al.* Structural basis of calcium-induced E-cadherin rigidification and dimerization. *Nature* **380**, 360 - 364 (1996).

141. Tomschy A*, et al.* Homophilic adhesion of E-cadherin occurs by a co-operative two-step interaction of N-terminal domains. *The EMBO Journal* **15**, 3507 (1996).

142. Chen CP*, et al.* Specificity of cell–cell adhesion by classical cadherins: Critical role for low-affinity dimerization through β-strand swapping. *Proceedings of the National Academy of Sciences of the United States of America* **102**, 8531-8536 (2005).

143. Dealwis C*, et al.* Crystal structure of chemically synthesized [N33A] stromal cell-derived factor 1alpha, a potent ligand for the HIV-1 "fusin" coreceptor. *Proceedings of the National Academy of Sciences of the United States of America* **95**, 6941-6946 (1998).

144. Lilien J*, et al.* The juxtamembrane domain of cadherin regulates integrin-mediated adhesion and neurite outgrowth. *Journal of Neuroscience Research* **58**, 727-734 (1999).

145. Leckband DE*, et al.* Mechanotransduction at cadherin-mediated adhesions. *Current Opinion in Cell Biology* **23**, 523-530 (2011).

146. Chappuis-Flament S*, et al.* Multiple cadherin extracellular repeats mediate homophilic binding and adhesion. *The Journal of Cell Biology* **154**, 231-243 (2001).

147. Bayas MV*, et al.* Lifetime measurements reveal kinetic differences between homophilic cadherin bonds. *Biophysical Journal* **90**, 1385-1395 (2006).

148. Florin E-L*, et al.* Adhesion forces between individual ligand-receptor pairs. *Science* **264**, 415-417 (1994).

149. Leckband D, de Rooij J. Cadherin adhesion and mechanotransduction. *Annual Review of Cell and Developmental Biology* **30**, 291-315 (2014).

150. Ladoux B*, et al.* Strength Dependence of Cadherin-Mediated Adhesions. *Biophysical Journal* **98**, 534-542 (2010).

151. Crump MP*, et al.* Solution structure and basis for functional activity of stromal cell-derived factor-1; dissociation of CXCR4 activation from binding and inhibition of HIV-1. *The EMBO Journal* **16**, 6996-7007 (1997).

152. Loetscher M*, et al.* Cloning of a human seven-transmembrane domain receptor, LESTR, that is highly expressed in leukocytes. *Journal of Biological Chemistry* **269**, 232-237 (1994).

153. Ji TH*, et al.* G protein-coupled receptors I. Diversity of receptor-ligand interactions. *Journal of Biological Chemistry* **273**, 17299-17302 (1998).

154. Zou Y-R*, et al.* Function of the chemokine receptor CXCR4 in haematopoiesis and in cerebellar development. *Nature* **393**, 595-599 (1998).

155. Vega B*, et al.* Technical Advance: Surface plasmon resonance-based analysis of CXCL12 binding using immobilized lentiviral particles. *Journal of Leukocyte Biology* **90**, 399-408 (2011).

156. Staudinger R, Bandres JC. Solubilization of the chemokine receptor CXCR4. *Biochemical and Biophysical Research Communications* **274**, 153-156 (2000).

157. Bereiter-Hahn J*, et al.* Quantitative reflection contrast microscopy of living cells. *The Journal of Cell Biology* **82**, 767-779 (1979).

158. Coelho Neto J*, et al.* Measuring optical and mechanical properties of a living cell with defocusing microscopy. *Biophysical Journal* **91**, 1108-1115 (2006).

159. Hill AV. The possible effects of the aggregation of the molecules of haemoglobin on its dissociation curves. *The Journal of Physiology* **40**, 4-7 (1910).

160. Förster R*, et al.* Intracellular and surface expression of the HIV-1 coreceptor CXCR4/fusin on various leukocyte subsets: rapid internalization and recycling upon activation. *The Journal of Immunology* **160**, 1522-1531 (1998).

161. Tai C-Y*, et al.* Activity-Regulated N-Cadherin Endocytosis. *Neuron* **54**, 771-785 (2007).

162. Voermans C*, et al.* SDF-1–induced actin polymerization and migration in human hematopoietic progenitor cells. *Experimental Hematology* **29**, 1456-1464 (2001).

163. Shao JY, Hochmuth RM. Micropipette suction for measuring piconewton forces of adhesion and tether formation from neutrophil membranes. *Biophysical Journal* **71**, 2892-2901 (1996).

164. Hochmuth RM. Micropipette aspiration of living cells. *Journal of Biomechanics* **33**, 15-22 (2000).

165. Binnig G*, et al.* Atomic Force Microscope. *Physical Review Letters* **56**, 930-933 (1986).

166. Benoit M*, et al.* Discrete interactions in cell adhesion measured by single-molecule force spectroscopy. *Nature Cell Biology* **2**, 313 (2000).

167. Puech P-H*, et al.* A new technical approach to quantify cell–cell adhesion forces by AFM. *Ultramicroscopy* **106**, 637-644 (2006).

168. Neuman KC, Nagy A. Single-molecule force spectroscopy: optical tweezers, magnetic tweezers and atomic force microscopy. *Nature Methods* **5**, 491-505 (2008).

169. Walter N*, et al.* Cellular Unbinding Forces of Initial Adhesion Processes on Nanopatterned Surfaces Probed with Magnetic Tweezers. *Nano Letters* **6**, 398-402 (2006).

170. Sagvolden G*, et al.* Cell adhesion force microscopy. *Proceedings of the National Academy of Sciences of the United States of America* **96**, 471-476 (1999).

171. Butt H-J, Jaschke M. Calculation of thermal noise in atomic force microscopy. *Nanotechnology* **6**, 1 (1995).

172. Yoshikawa HY*, et al.* Quantitative Evaluation of Adhesion of Osteosarcoma Cells to Hydrophobic Polymer Substrate with Tunable Elasticity. *The Journal of Physical Chemistry B* **116**, 8024-8030 (2012).

173. Vogel A*, et al.* Optical and acoustic investigations of the dynamics of laser-produced cavitation bubbles near a solid boundary. *Journal of Fluid Mechanics* **206**, 299-338 (1989).

174. Yamamoto A*, et al.* A new technique for direct measurement of the shear force necessary to detach a cell from a material. *Biomaterials* **19**, 871-879 (1998).

175. Francis G*, et al.* Direct measurement of cell detachment force on single cells using a new electromechanical method. *Journal of Cell Science* **87**, 519-523 (1987).

176. Pierrat S*, et al.* Enforced detachment of red blood cells adhering to surfaces: Statics and dynamics. *Biophysical Journal* **87**, 2855-2869 (2004).

177. Ingber DE. Mechanobiology and diseases of mechanotransduction. *Annals of Medicine* **35**, 564-577 (2003).

178. Janmey PA, Weitz DA. Dealing with mechanics: mechanisms of force transduction in cells. *Trends in Biochemical Sciences* **29**, 364-370 (2004).

179. Gether U. Uncovering molecular mechanisms involved in activation of G protein-coupled receptors. *Endocrine Reviews* **21**, 90-113 (2000).

180. Shapiro L, Weis WI. Structure and biochemistry of cadherins and catenins. *Cold Spring Harbor Perspectives in Biology* **1**, a003053 (2009).

181. Friedl P, Gilmour D. Collective cell migration in morphogenesis, regeneration and cancer. *Nature Reviews Molecular Cell Biology* **10**, 445-457 (2009).

182. Martin P. Wound healing--aiming for perfect skin regeneration. *Science* **276**, 75-81 (1997).

183. Yamaguchi H*, et al.* Cell migration in tumors. *Current Opinion in Cell Biology* **17**, 559-564 (2005).

184. Friedl P, Weigelin B. Interstitial leukocyte migration and immune function. *Nature Immunology* **9**, 960-969 (2008).

185. Lauffenburger DA, Horwitz AF. Cell Migration: A Physically Integrated Molecular Process. *Cell* **84**, 359-369 (1996).

186. Knight B*, et al.* Visualizing muscle cell migration in situ. *Current Biology* **10**, 576-585 (2000).

187. Thiery JP. Epithelial–mesenchymal transitions in tumour progression. *Nature Reviews Cancer* **2**, 442-454 (2002).

188. Coates TD*, et al.* Relationship of F-actin distribution to development of polar shape in human polymorphonuclear neutrophils. *The Journal of Cell Biology* **117**, 765-774 (1992).

189. Sullivan SJ*, et al.* Asymmetric distribution of the chemotactic peptide receptor on polymorphonuclear leukocytes. *The Journal of Cell Biology* **99**, 1461-1467 (1984).

190. Etienne-Manneville S, Hall A. Rho GTPases in cell biology. *Nature* **420**, 629-635 (2002).

191. Raftopoulou M, Hall A. Cell migration: Rho GTPases lead the way. *Developmental Biology* **265**, 23-32 (2004).

192. Einstein A. Über die von der molekularkinetischen Theorie der Wärme geforderte Bewegung von in ruhenden Flüssigkeiten suspendierten Teilchen. *Annalen der Physik* **4**, (1905).

193. Einstein A. Zur Theorie der Brownschen Bewegung. *Annalen der Physik* **19**, 317 (1906).

194. Przibram K. Über die ungeordnete Bewegung niederer Tiere. *Pflügers Archiv European Journal of Physiology* **153**, 401-405 (1913).

195. Fürth R. Die brownsche Bewegung bei Berücksichtigung einer Persistenz der Bewegungsrichtung. mit Anwendungen auf die Bewegung lebender Infusorien. *Zeitschrift für Physik A Hadrons and Nuclei* **2**, 244-256 (1920).

196. Gail MH, Boone CW. The locomotion of mouse fibroblasts in tissue culture. *Biophysical Journal* **10**, 980 (1970).

197. Li L*, et al.* Persistent cell motion in the absence of external signals: a search strategy for eukaryotic cells. *PloS One* **3**, e2093 (2008).

198. Harms BD*, et al.* Directional persistence of EGF-Induced cell migration is associated with stabilization of lamellipodial protrusions. *Biophysical Journal* **88**, 1479-1488 (2005).

199. Wright A*, et al.* The differential effect of endothelial cell factors on in vitro motility of malignant and non-malignant cells. *Annals of Biomedical Engineering* **36**, 958-969 (2008).

200. Stokes CL*, et al.* Migration of individual microvessel endothelial cells: stochastic model and parameter measurement. *Journal of Cell Science* **99**, 419-430 (1991).

201. Weeks ER*, et al.* Anomalous diffusion in asymmetric random walks with a quasi-geostrophic flow example. *Physica D: Nonlinear Phenomena* **97**, 291-310 (1996).

202. Coscoy S*, et al.* Statistical analysis of sets of random walks: how to resolve their generating mechanism. *Bulletin of Mathematical Biology* **69**, 2467-2492 (2007).

203. Viswanathan GM*, et al.* Lévy flight search patterns of wandering albatrosses. *Nature* **381**, 413-415 (1996).

204. Shapere A, Wilczek F. Self-propulsion at low Reynolds number. *Physical Review Letters* **58**, 2051 (1987).

205. Ohta T, Ohkuma T. Deformable Self-Propelled Particles. *Physical Review Letters* **102**, 154101 (2009).

206. Tarama M, Ohta T. Spinning motion of a deformable self-propelled particle in two dimensions. *Journal of Physics: Condensed Matter* **24**, 464129 (2012).

207. Itino Y, Ohta T. Dynamics of deformable self-propelled particles with repulsive interaction. *Journal of the Physical Society of Japan* **81**, 104007 (2012).

208. Keren K*, et al.* Mechanism of shape determination in motile cells. *Nature* **453**, 475-480 (2008).

209. Bosgraaf L, Van Haastert PJ. The ordered extension of pseudopodia by amoeboid cells in the absence of external cues. *PloS One* **4**, e5253 (2009).

210. Maeda YT*, et al.* Ordered patterns of cell shape and orientational correlation during spontaneous cell migration. *PloS One* **3**, e3734 (2008).

211. Partin AW, *et al.* Fourier analysis of cell motility: correlation of motility with metastatic potential. *Proceedings of the National Academy of Sciences of the United States of America* **86**, 1254-1258 (1989).

212. Jacobson L*, et al.* The influence of the spleen on hematopoietic recovery after irradiation injury. *Experimental Biology and Medicine* **73**, 455-459 (1950).

213. Magnon C, Frenette PS. Hematopoietic stem cell trafficking. *Annals of the New York Academy of Sciences* **1116**, 392-413 (2007).

214. van Buul JD*, et al.* Migration of human hematopoietic progenitor cells across bone marrow endothelium is regulated by vascular endothelial cadherin. *The Journal of Immunology* **168**, 588-596 (2002).

215. Abràmoff MD*, et al.* Image processing with ImageJ. *Biophotonics International* **11**, 36-42 (2004).

216. Ponti A*, et al.* Two distinct actin networks drive the protrusion of migrating cells. *Science* **305**, 1782-1786 (2004).

217. Theriot JA, Mitchison TJ. Actin microfilament dynamics in locomoting cells. *Nature* **352**, 126-131 (1991).

218. Mitchison T, Cramer L. Actin-based cell motility and cell locomotion. *Cell* **84**, 371-379 (1996).

219. Hall A. Rho GTPases and the Actin Cytoskeleton. *Science* **279**, 509-514 (1998).

220. Yang FC*, et al.* Rac and Cdc42 GTPases control hematopoietic stem cell shape, adhesion, migration, and mobilization. *Proceedings of the National Academy of Sciences of the United States of America* **98**, 5614-5618 (2001).

221. Henschler R*, et al.* SDF-1α-induced intracellular calcium transient involves Rho GTPase signalling and is required for migration of hematopoietic progenitor cells. *Biochemical and Biophysical Research Communications* **311**, 1067-1071 (2003).

222. Fukuda S*, et al.* Flt3 ligand and the Flt3 receptor regulate hematopoietic cell migration by modulating the SDF-1α (CXCL12)/CXCR4 axis. *Blood* **105**, 3117-3126 (2005).

223. Schaller MD. Paxillin: a focal adhesion-associated adaptor protein. *Oncogene* **20**, 6459-6472 (2001).

224. Yano H*, et al.* Roles played by a subset of integrin signaling molecules in cadherin-based cell–cell adhesion. *The Journal of Cell Biology* **166**, 283-295 (2004).

225. Atilgan E*, et al.* Mechanics and dynamics of actin-driven thin membrane protrusions. *Biophysical Journal* **90**, 65-76 (2006).

226. Sánchez-Madrid F, del Pozo MA. Leukocyte polarization in cell migration and immune interactions. *The EMBO Journal* **18**, 501-511 (1999).

227. Giebel B*, et al.* Segregation of lipid raft markers including CD133 in polarized human hematopoietic stem and progenitor cells. *Blood* **104**, 2332-2338 (2004).

228. van Rhenen A*, et al.* High Stem Cell Frequency in Acute Myeloid Leukemia at Diagnosis Predicts High Minimal Residual Disease and Poor Survival. *Clinical Cancer Research* **11**, 6520-6527 (2005).

229. Thomas ED*, et al.* Intravenous infusion of bone marrow in patients receiving radiation and chemotherapy. *New England Journal of Medicine* **257**, 491-496 (1957).

230. Thomas ED, Storb R. Technique for human marrow grafting. *Blood* **36**, 507-515 (1970).

231. Körbling M*, et al.* Successful engraftment of blood derived normal hemopoietic stem cells in chronic myelogenous leukemia. *Experimental Hematology* **9**, 684-690 (1981).

232. Gluckman E*, et al.* Hematopoietic Reconstitution in a Patient with Fanconi's Anemia by Means of Umbilical-Cord Blood from an HLA-Identical Sibling. *New England Journal of Medicine* **321**, 1174-1178 (1989).

233. Korbling M, Anderlini P. Peripheral blood stem cell versus bone marrow allotransplantation: does the source of hematopoietic stem cells matter? *Blood* **98**, 2900-2908 (2001).

234. Kessinger A*, et al.* Allogeneic transplantation of blood-derived, T cell-depleted hemopoietic stem cells after myeloablative treatment in a patient with acute lymphoblastic leukemia. *Bone Marrow Transplantation* **4**, 643-646 (1989).

235. Russell N*, et al.* Peripheral blood stem cells as an alternative to marrow for allogeneic transplantation. *The Lancet* **341**, 1482 (1993).

236. Korbling M*, et al.* Allogeneic blood stem cell transplantation: peripheralization and yield of donor-derived primitive hematopoietic progenitor cells (CD34+ Thy-1dim) and lymphoid subsets, and possible predictors of engraftment and graft-versus-host disease. *Blood* **86**, 2842-2848 (1995).

237. Petit I*, et al.* G-CSF induces stem cell mobilization by decreasing bone marrow SDF-1 and up-regulating CXCR4. *Nature Imunology* **3**, 687-694 (2002).

238. Lévesque J-P*, et al.* Disruption of the CXCR4/CXCL12 chemotactic interaction during hematopoietic stem cell mobilization induced by GCSF or cyclophosphamide. *Journal of Clinical Investigation* **111**, 187-196 (2003).

239. Brelot A*, et al.* Identification of residues of CXCR4 critical for human immunodeficiency virus coreceptor and chemokine receptor activities. *Journal of Biological Chemistry* **275**, 23736-23744 (2000).

240. Broxmeyer HE. Primitive hematopoietic stem and progenitor cells in human umbilical cord blood: an alternative source of transplantable cells. In: *Molecular Genetics and Therapy of Leukemia*. Springer (1996).

241. Kollet O*, et al.* Human CD34+CXCR4− sorted cells harbor intracellular CXCR4, which can be functionally expressed and provide NOD/SCID repopulation. *Blood* **100**, 2778-2786 (2002).

242. Dar A*, et al.* Mutual, reciprocal SDF-1/CXCR4 interactions between hematopoietic and bone marrow stromal cells regulate human stem cell migration and development in NOD/SCID chimeric mice. *Experimental Hematology* **34**, 967-975 (2006).

243. Groves JT, Boxer SG. Electric field-induced concentration gradients in planar supported bilayers. *Biophysical Journal* **69**, 1972-1975 (1995).

244. Groves JT*, et al.* Electrical manipulation of glycan phosphatidyl inositol tethered proteins in planar supported bilayers. *Biophysical Journal* **71**, 2716-2723 (1996).

245. Yoshina-Ishii C, Boxer SG. Arrays of mobile tethered vesicles on supported lipid bilayers. *Journal of the American Chemical Society* **125**, 3696-3697 (2003).

246. Yoshina-Ishii C, Boxer SG. Controlling two-dimensional tethered vesicle motion using an electric field: interplay of electrophoresis and electro-osmosis. *Langmuir* **22**, 2384-2391 (2006).

247. Olson DJ*, et al.* Electrophoresis of DNA adsorbed to a cationic supported bilayer. *Langmuir* **17**, 7396-7401 (2001).

248. Galneder R*, et al.* Microelectrophoresis of a bilayer-coated silica bead in an optical trap: application to enzymology. *Biophysical Journal* **80**, 2298-2309 (2001).

249. Tanaka M*, et al.* Frictional drag and electrical manipulation of recombinant proteins in polymer-supported membranes. *Langmuir* **23**, 5638-5644 (2007).

250. Avigdor A*, et al.* CD44 and hyaluronic acid cooperate with SDF-1 in the trafficking of human CD34+ stem/progenitor cells to bone marrow. *Blood* **103**, 2981-2989 (2004).

251. Lukinavicius G*, et al.* Fluorogenic probes for live-cell imaging of the cytoskeleton. *Nature Methods* **11**, 731-733 (2014).

252. Samad A*, et al.* Liposomal Drug Delivery Systems: An Update Review. *Current Drug Delivery* **4**, 297-305 (2007).

253. Uchegbu L. *Synthetic surfactant vesicles: niosomes and other non-phospholipid vesicular systems*. CRC Press (2003).

254. van Hest JCM*, et al.* Polystyrene-Dendrimer Amphiphilic Block Copolymers with a Generation-Dependent Aggregation. *Science* **268**, 1592-1595 (1995).

255. Tanford C. The hydrophobic effect and the organization of living matter. *Science* **200**, 1012-1018 (1978).

256. Tanford C. *The Hydrophobic Effect: Formation of Micelles and Biological Membranes 2d Ed*. J. Wiley. (1980).

257. Lasic DD, Papahadjopoulos D. *Medical Applications of Liposomes*. Elsevier (1998).

258. Bangham A. Liposomes: the Babraham connection. *Chemistry and Physics of Lipids* **64**, 275-285 (1993).

259. Zhou S*, et al.* Spherical bilayer vesicles of fullerene-based surfactants in water: a laser light scattering study. *Science* **291**, 1944-1947 (2001).

260. Homma T*, et al.* Nanometer-Sized Fluorous Fullerene Vesicles in Water and on Solid Surfaces. *Angewandte Chemie International Edition* **49**, 1665-1668 (2010).

261. Homma T*, et al.* Preparation and Properties of Vesicles Made of Nonpolar/Polar/Nonpolar Fullerene Amphiphiles. *Journal of the American Chemical Society* **133**, 6364-6370 (2011).

262. Matsuo Y*, et al.* X-ray Crystallographic Characterization of Potassium Pentaphenyl[60]fullerene. *Chemistry Letters* **34**, 1078-1079 (2005).

263. Stuhrmann H. Neutron small-angle scattering of biological macromolecules in solution. *Journal of Applied Crystallography* **7**, 173-178 (1974).

264. Boué F*, et al.* Small angle scattering from soft matter—application to complex mixed systems. *Comptes Rendus Physique* **8**, 821-844 (2007).

265. Guimer A, Fournet G. *Small angle scattering of X-rays* (1955).

266. Stuhrmann HB, Duee ED. The determination of the scattering density distribution of polydisperse solutions by contrast variation: a neutron scattering study of ferritin. *Journal of Applied Crystallography* **8**, 538-542 (1975).

267. Ibel K, Stuhrmann H. Comparison of neutron and X-ray scattering of dilute myoglobin solutions. *Journal of Molecular Biology* **93**, 255-265 (1975).

268. Feigin L*, et al.* Determination of the integral parameters of particles. In: *Structure Analysis by Small-Angle X-ray and Neutron Scattering*. Springer (1987).

269. Guinier A*, et al.* Small-angle scattering of X-rays. (1955).

270. Love AEH. *A treatise on the mathematical theory of elasticity*. Cambridge University Press (2013).

271. Grillo I. Effect of instrumental resolution and polydispersity on ideal form factor in Small Angle Neutron Scattering. (ed^(eds). ILL Technical Report No. ILL01GR08T (2000).

272. Aragon SR, Pecora R. Theory of Dynamic Light-Scattering from Polydisperse Systems. *Journal of Chemical Physics* **64**, 2395-2404 (1976).

273. Kotlarchyk M, Chen S-H. Analysis of small angle neutron scattering spectra from polydisperse interacting colloids. *The Journal of Chemical Physics* **79**, 2461 (1983).

274. Kratschmer W*, et al.* Solid C60: a new form of carbon. *Nature* **347**, 354-358 (1990).

275. Oelke J*, et al.* Highly uniform, strongly correlated fluorinated lipid nanodomains embedded in biological membrane models. *Applied Physics Letters* **93**, 213901 (2008).

276. Avdeev MV*, et al.* Structural Features of Molecular-Colloidal Solutions of C60 Fullerenes in Water by Small-Angle Neutron Scattering. *Langmuir* **20**, 4363-4368 (2004).

277. Kaindl T*, et al.* Regulation of adhesion behavior of murine macrophage using supported lipid membranes displaying tunable mannose domains. *Journal of Physics: Condensed Matter* **22**, 285102 (2010).

278. Haran N, Shporer M. Study of water permeability through phospholipid vesicle membranes by 17 O NMR. *Biochimica et Biophysica Acta (BBA)-Biomembranes* **426**, 638-646 (1976).

279. Isobe H*, et al.* Energetics of water permeation through fullerene membrane. *Proceedings of the National Academy of Sciences of the United States of America* **104**, 14895-14898 (2007).

280. Finkelstein A. Water and nonelectrolyte permeability of lipid bilayer membranes. *Journal of General Physiology* **68**, 127-135 (1976).

281. Mlekoday HJ*, et al.* Osmotic Water Permeability of the Human Red-Cell - Dependence on Direction of Water-Flow and Cell-Volume. *Journal of General Physiology* **81**, 213-220 (1983).

282. Levitt DG, Mlekoday HJ. Reflection coefficient and permeability of urea and ethylene glycol in the human red cell membrane. *Journal of General Physiology* **81**, 239-253 (1983).